Synthesis, Characterization and Photophysics of Novel Cholesterol Analogues and their Potential as Cell Membrane Probes.

JACINTA DREW

THESIS SUBMITTED TO
THE SCHOOL OF GRADUATE STUDIES AND RESEARCH
IN PARTIAL FULFILLMENT OF THE REQUIREMENTS FOR THE DEGREE OF
DOCTOR OF PHILOSOPHY IN CHEMISTRY

University of Ottawa

Abstract

Fluorescent sterols, which resemble cholesterol closely in both molecular geometry and amphipathic nature have been synthesized by the introduction of hydrophobic sidechains embodying aryl diene or triene units. A direct synthesis of one of these fluorescent cholesterol analogues, containing a diene phenyl chromophore (**4a**), was possible by a phosphonate Wittig reaction on pregnenolone protected at C-3. Two other cholesterol analogues, with a triene phenyl (**5a**) or diene 2′-naphthyl (**6a**) chromophore, were prepared by phosphorane and phosphonate Wittig reactions on the more reactive and less sterically hindered 20(22)E-α,β-unsaturated aldehyde (**3a**), which was obtained from pregnenolone by two different routes. The first route involved a Grignard reaction with vinylmagnesium bromide followed by oxidative rearrangement with pyridinium chlorochromate, which resulted in an 80:20 ratio of the diastereomeric aldehydes **3a**/**3b**. A more stereoselective synthesis of **3a** over **3b** (96:4) was achieved by a phosphonate Wittig reaction with the carbanion generated from diethyl [2-(cyclohexylimino)vinyl]phosphonate.

The geometry of the fluorescent olefinic sterols was determined by high resolution nuclear magnetic resonance (NMR) spectroscopy, in particular on the basis of ^{1}H-^{1}H shift-correlated spectra (COSY) and nuclear Overhauser effect difference spectra (nOe), and the *all-trans* diastereomers were investigated for their potential as cell membrane probes. A complete ring proton resonance assignment and coupling constant analysis was also performed for the triene phenyl cholesterol analogue and represents one of the first total analyses of the ^{1}H NMR spectrum of a steroid nucleus.

Time-resolved fluorescence studies at room and low temperatures, as well as molecular orbital calculations and nOe spectra, determined that the photophysical behaviour of the diene 2′-naphthyl cholesterol analogue is a consequence of both a

ground state and an excited state conformational equilibrium. In the ground state, evidence is presented for the existence of a nonplanar C-22,C-23 *s-trans*, C-24,C-2′ *s-cis* (*tc*) rotamer as well as the more stable *s-trans*, *s-trans* (*tt*) rotamer. This ground state equilibrium could prove useful in monitoring changes in membrane order at constant temperature. In the excited state, the nonplanar *tc*-rotamer undergoes a small amplitude conformational change to a planar *tc*-rotamer. This viscosity dependent process has the potential to be exploited for studies of membrane dynamics. The photophysical behaviour of the triene phenyl cholesterol analogue is a result of an equilibrium between its two lowest excited electronic states. This excited state equilibrium is also found to be viscosity dependent, most probably due to different viscosity dependencies of the nonradiative processes from the two states, so this molecule also has potential as a probe of membrane dynamics. In addition, its absorption spectral characteristics make it ideal for resonance energy transfer studies with tryptophan and tyrosine, the intrinsic fluorophores of proteins. The diene phenyl cholesterol analogue proved to be unsuitable as a membrane probe due to its low fluorescence quantum yield and very short fluorescence lifetimes.

Preliminary model membrane studies are presented which indicate that the diene 2′-naphthyl and triene phenyl cholesterol analogues are sensitive to the phase state and cholesterol content of lipid bilayers. These two fluorescent sterol probes hold great promise as a means to attain a better understanding of the role of cholesterol in membrane structure and function.

Acknowledgements

Due to the multidisciplinary nature of the research described herein, there are many people who need to be thanked for their scientific contributions to this Ph.D. thesis. My supervisors Prof. Peter Morand (University of Ottawa) and Dr. Arthur Szabo (National Research Council of Canada) first kindled my interest in this project and then allowed me the freedom to pursue it along my own lines of thought. Both of them supported my wish to present portions of this work at various national and international conferences, which gave me the opportunity to meet top researchers, particularly in the field of fluorescence spectroscopy. These contacts will no doubt be of importance once I return to Australia.

Marie Letellier, during her term as a summer student at NRC, assisted with the synthetic and purification procedures detailed in Chapter 2. Dr. Jean-Robert Brisson (NRC) measured the high resolution NMR spectra reported in Chapter 3, and was very generous with his own time and with the acquisition time he allotted to my samples on the 500 MHz spectrometer. Dr. Francesco Zerbetto (NRC) performed the molecular orbital calculations presented in Chapter 4 and I also thank him for helpful discussions.

The indirect method of obtaining excitation decay associated spectra was first brought to my attention by Dr. Jay Knutson (NIH), and subsequent discussions with Dr. Michael Zuker (NRC) and Dr. Szabo, as well as the computer programming assistance of Joanne Ridgeway (NRC), led to the development of a linear least squares method which was used to obtain the IEDAS presented in Chapter 4. I also thank Dr. Knutson for access to ADAS computer programs in his laboratory. In addition, both Joanne Ridgeway and Lise Bramall (NRC) could always be called upon to help with day-to-day problems in fluorescence decay data analysis. Special mention must also be made of the technical expertise of Don Krajcarski (NRC),

which has no doubt contributed to the reputation of Dr. Szabo's laboratory as a centre of excellence in fluorescence instrumentation.

Several people provided spectral or analytical services throughout the course of this work. These include Dr. Clem Kazakoff (U. of O., mass spectra), Raj Capoor (U. of O., 300 MHz NMR spectra), Hector Séguin (NRC, elemental analyses) and Dr. David Brown, Anne Kroeker and Martha Julien (Ottawa-Carleton Resource Centre for Biological Microscopy, electron microscopy).

Regarding the production of this document, I thank Allan Kamen for typing and formatting, and Marie Letellier, Chris Hoag, Eva Szabo and Tammy White for assistance with the diagrams.

I am deeply grateful to my friends and colleagues for their encouragement and support, especially Anita MacEachern, Myrna Monck, Alain Richer, Xavier Lee, Cindy Hutnik and John Baenziger. Their contribution to this thesis, as well as that of the Legere family of Toronto and Elgin, is immeasurable. Of course, the financial support of the Association of Universities and Colleges of Canada (AUCC) over the past five years, through their Commonwealth Scholarship plan, was also invaluable.

Finally, I thank my family without whose support, throughout all of my years of study, the realization of this thesis would not have been possible.

Contents

List of Tables

List of Figures

List of Abbreviations

Only the most frequently used abbreviations appear here, or those whose definitions are so long that they were not included in the main body of the thesis.

ADC	Analogue-to-Digital Converter
BPE	3-Styrylidenebenz[e]indane
CHORTLE	Carbon hydrogen correlations from one- dimensional polarization transfer spectra by least-squares analysis
CNDO/S	Complete Neglect of Differential Overlap/ Spectroscopic
COSY	Shift-correlated spectrum
DAS	Decay Associated emission Spectrum
DCM	4-Dicyanomethylene-2-methyl-6-dimethylaminostyryl-4H-pyran
DMF	Dimethylformamide
DMPC	1,2-dimyristoyl-*sn*-glycero-3-phosphocholine
DNC	Diene 2′-Naphthyl Cholesterol analogue
DPC	Diene Phenyl Cholesterol analogue
DPH	1,6-Diphenyl-1,3,5-hexatriene
DSC	Differential Scanning Calorimetry
EPR	Electron Paramagnetic Resonance
FRAP	Fluorescence Recovery After Photobleaching
FWHM	Full Width at Half Maximum

H1L1, H3L1, H1L0, H0L1	Mixtures of heavy and light mineral oils in 1:1, 3:1, 1:0 and 0:1 ratios respectively.
HPLC	High Performance Liquid Chromatography
IEDAS	Indirect Excitation Decay Associated Spectrum
KDP	Potassium dihydrogen phosphate
LDL	Low Density Lipoprotein
LUV	Large Unilamellar Vesicle
MCA	Multichannel Analyzer
MCH	Methylcyclohexane
MLV	Multilamellar Vesicle
MPE	1-Phenyl-2-(3′-methyl-2′-naphthyl)ethene
NBD	2′-Naphthyl-1,3-butadiene
NEER	Non-Equilibration of Excited Rotamers
nOe	nuclear Overhauser effect
PCC	Pyridinium Chlorochromate
PHT	Phenyl-1,3,5-hexatriene
PNE	1-Phenyl-2-(2′-naphthyl) ethene
SAS	Species Associated emission Spectrum
SUV	Small Unilamellar Vesicle
SVR	Serial Variance Ratio
TAC	Time-to-Amplitude Converter
TCSPC	Time-Correlated Single Photon Counting
THF	Tetrahydrofuran
TMP	2,2,4-trimethylpentane
TPC	Triene Phenyl Cholesterol analogue
TRIS	Tris(hydroxymethyl)aminomethane

Chapter 1

Introduction

1.1 Membrane Structure and Function

Biological or cell membranes are important components of living systems[1-5]. Both eucaryotic cells which are found in plants and animals, and procaryotic or bacteria cells, possess outer or plasma membranes which, among their many important functions, serve to define the boundary of the cell and hence maintain its structural integrity. In addition, the complex eucaryotic cells can contain internal membranes which separate or compartmentalize particular organelles, such as chloroplasts or mitochondria, from the rest of the cell.

Membranes act as highly selective permeability barriers, regulating the transport of molecules and ions between a cell/organelle and its environment. These transport processes are very important to the function and survival of a cell/organelle. For example, most animal cells have a high concentration of K^+ and a low concentration of Na^+ with respect to the external medium. This ionic gradient is essential in rendering nerves and muscle cells electrically excitable, in controlling cell volume, and it also drives the active transport of sugars and amino acids. Membranes also provide non-aqueous environments where enzymes can catalyze essential chemical reactions that could not occur in aqueous solution. In addition, many cell membranes have specific recognition or receptor sites on their outer surface for the purposes of, for instance, recognizing other cells or binding hormones.

Membranes are composed largely of proteins and lipids, arranged together in a noncovalent assembly. Proteins are large molecules consisting of sequences of amino acids (they can also contain carbohydrate residues), and typically have molecular weights ~10,000–100,000. Lipids, on the other hand, are smaller with molecular weights <1000. They are amphipathic molecules since they possess both a hydrophilic or polar portion, and a hydrophobic or nonpolar portion. The most abundant membrane lipids are the phospholipids and, in particular, those based on a glycerol backbone (Figure 1.1).

The phosphate ester with its associated substituent R^1, which is polar and often charged, constitutes what is referred to as the headgroup region of the lipid molecule, and is the hydrophilic portion. The R^2, R^3 substituents make up the hydrophobic

portion as they are saturated or unsaturated hydrocarbons usually attached to the glycerol backbone via a carboxyl group. For this reason, this is usually referred to as the acyl chain region of the lipid molecule.

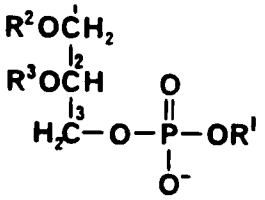

Figure 1.1: A glycero-phospholipid

A model for the structure of membranes was put forward by Singer and Nicholson in 1972, and is termed the **fluid mosaic model**[6]. This model was found to qualitatively account for a number of the properties and experimental observations made of membranes. In this model, the lipid molecules are depicted as adopting a bilayer structure. They align in layers which are two molecules thick, with their polar headgroups facing outward towards the aqueous environment, thereby maximizing hydrophilic interactions, while the nonpolar acyl chains are sequestered away from the water toward the interior of the bilayer, thereby maximizing hydrophobic interactions. Such a bilayer structure is consistent with X-ray diffraction studies of membranes which indicate that there is high electron density at the two peripheries of the membrane and low electron density at the centre of the membrane. The thickness of membranes, determined by electron microscopy to be ~6–9 nm, is also indicative of a lipid bilayer structure.

The proteins in the fluid mosaic model of a membrane are classified into two types, in order to account for the observation that some proteins are easily dissociated free of lipids from the membrane, while others require much more drastic conditions to effect dissociation and are often associated with lipids when isolated. Peripheral or easily dissociated proteins, are considered to interact only with the surface of the lipid bilayer and not to have an appreciable effect on the membrane structure. The more highly associated or integral proteins, however, are depicted to be embedded in the lipid bilayer, and to be critical to the structural integrity of membranes. Freeze-fracture electron microscopy of membranes has shown that these integral proteins can either be partially embedded, or can span the bilayer. The degree of insertion is postulated by the fluid mosaic model to depend on the

amino acid sequence and conformation of the protein. Polar amino acid residues will preferentially associate with either the aqueous environment or the hydrophilic headgroup region of the lipid bilayer, while the nonpolar residues will align so as to maximize hydrophobic interactions with the nonpolar lipid acyl chains. The distribution of proteins in a membrane, with respect to the plane of the bilayer, however, is known to be asymmetric. In order to accommodate this, it was proposed that the two-dimensional long range distribution of integral proteins in the plane of the membrane is random.

The static mosaic structure described so far for a membrane cannot account for known specific protein-lipid interactions, nor for the fact that membranes perform many complex dynamic functions, most notably the selective transport of ions and molecules into and out of cells. This led to the emergence of the concept of membrane fluidity as the missing link in the correlation of membrane structure and function[6-13]. Thus, the function of a membrane is considered to be mediated by its specific protein composition, while the lipid molecules provide the 'appropriate' environment for the membrane process to occur. Specific protein-lipid interactions can then be rationalized if the optimal functioning of a protein, for example the ability of an enzyme to adopt its active conformation, is dependent on the fluidity of the surrounding lipid.

1.2 Membrane Fluidity

1.2.1 Static and Dynamic Aspects

The concept of membrane fluidity is still evolving[7-13], but is generally recognized to encompass both static and dynamic aspects. The static aspect is considered to be largely related to the packing of the lipid molecules, in particular to the relative orientation or order of their acyl chains, with respect to the bilayer normal. The dynamic aspect is related to the translational and rotational diffusion or mobility of the lipids, which in turn can induce protein mobility. Often, however, the motion of membrane proteins is restricted through association with other membrane or cytoskeletal proteins.

The dynamics of membrane lipids and proteins is complex since their translational and rotational properties differ in directions parallel and perpendicular to the membrane plane. The observed asymmetry of lipid/protein composition between the intra- and extracellular surfaces of a membrane, for example, can be rationalized by very slow rates of out-of-plane rotations or transverse motions ('flip-flop') of both lipids and proteins, consistent with the energetically unfavourable migration of polar headgroups or residues through a nonpolar membrane interior. In contrast, in-plane rotations about C-C bonds in lipids are rapid ($\sim$0.1 ns)[14] while in-plane rotational diffusion of membrane proteins has been observed on the millisecond timescale[15]. Both in-plane (lateral) and out-of-plane (vertical) translational diffusion of lipids and proteins occur. In the case of proteins, these movements are usually in response to local lipid fluidity changes and are of physiological significance, for instance, in the formation of active protein aggregates (lateral diffusion), or in the control of accessibility of receptors/enzymes to ligand/substrate binding (vertical diffusion).

It is clear from the above discussion that membrane fluidity is largely determined by the physical state of the lipids. For this reason, many studies have been made of model membranes containing solely lipid molecules, in order to gain some insight into the intrinsic properties of lipid bilayers which affect their fluidity. Model membranes composed of a single type of lipid molecule have been shown by differential

scanning calorimetry (DSC) to undergo a very sharp endothermic phase transition, at a temperature T_m characteristic of the length and degree of saturation of the acyl chains, as well as the type of headgroup[16]. X-ray diffraction studies indicate that there is crystalline-like packing of the lipids below T_m, as evidenced by sharp reflections at 4.15Å, while above T_m there is a broad reflection at ~4.5Å indicating that the lipids are in a more fluid state[17]. However, the enthalpy change (and hence the entropy change) associated with the transition is less than that observed for the melting of the corresponding fatty acids, which demonstrates that the acyl chains in the lipid bilayer structure retain some order in their fluid state[18]. NMR[19], EPR[20,21] and fluorescence[22,23] spectroscopies have provided insight into the changes associated with this gel-liquid crystalline phase transition of lipid bilayers on the molecular level. These techniques can give information on both the order and the dynamics of the lipid acyl chains. The order is usually quantified in terms of an order parameter, S, which is related to the time-averaged orientation of the particular region or segment of the acyl chain being monitored (equation 1.1).

$$S = \frac{1}{2}(3\overline{\cos^2\theta} - 1) \tag{1.1}$$

θ = instantaneous angle between the acyl chain segment/region and the bilayer normal; the bar indicates a time average.

If the acyl chains lie parallel to the bilayer normal (i.e. $\theta = 0°$), then S = 1 and the acyl chains are in a state of maximum order. A complete random distribution of the molecular axes (disorder) corresponds to S = 0. The dynamics of the acyl chains is most often quantified in terms of a rotational correlation time, τ_c, or a lateral diffusion coefficient, D_L.

The various spectroscopic techniques, mentioned earlier, indicate that the gel-liquid crystalline phase transition of a single lipid component model membrane is associated with an increase in the disorder of the lipid acyl chains[24,25]. This has been attributed to the presence of an increased number of gauche-, as opposed to anti-, conformers about the C–C bonds in the liquid crystalline phase. Concomitant with the increase in disorder is an increase in the motions of the acyl chains, as evidenced by a decrease in τ_c through the phase transition[24,25].

The degree of order and dynamical freedom of a lipid molecule is found not only

to vary with the phase state of a lipid bilayer, but also with respect to position along the acyl chain. This has been most elegantly demonstrated by both ^{2}H and ^{13}C NMR spectroscopy employing selectively ^{2}H or ^{13}C labelled lipids[26]. The order parameters and rotational correlations times obtained are thus appropriate to a very localized portion of the acyl chain, and have shown that there is a fluidity gradient from a relatively highly ordered and immobile segment (C-2 to C-11) near the lipid headgroup, to a disordered and more mobile segment at the methyl terminal end of the molecule.

1.2.2 Factors Affecting Membrane Fluidity

A number of physiological conditions can affect lipid fluidity in membranes, and consequently the optimal functioning of enzymes, receptors and transport proteins in the membrane[10]. The main modulators of inherent membrane lipid fluidity are the serum lipid composition, which is largely determined by the functioning of the liver (and to a lesser extent by diet), and the intracellular lipid metabolism. Membranes have at their disposal a number of mechanisms by which they can maintain optimal fluidity and functioning in response to perturbations by such factors. The two main mechanisms involve changes in cholesterol level and/or the composition of lipid acyl chains.

Degree of Unsaturation of Lipid Acyl Chains

Introduction of a single *cis*-double bond into a lipid acyl chain results in a lowering of the gel-liquid crystalline phase transition temperature, T_m, by ~50°C. It is proposed that this is because the packing of surrounding lipid molecules is disturbed by the presence of the inflexible bend in the chain. Deuterium magnetic resonance studies have shown that there is an associated disordering of the lipid acyl chains while early EPR studies indicated a concomitant increase in mobility[27]. Hence, the introduction of unsaturation was considered to increase membrane fluidity. However, while recent fluorescence depolarization and EPR experiments have confirmed the disordering effect, diffusion coefficients (and thus mobilities) were found to be lower in lipid multibilayers composed of a monounsaturated lipid as opposed to a saturated lipid[28,29]. Further increases in degree of lipid unsaturation provide only

small extra decreases in order and T_m[30,31]. This suggests that high levels of such polyunsaturated lipids in some membranes must be of other physiological significance, possibly in specific protein-lipid or sterol-lipid interactions[9].

Level of Cholesterol

Incorporation of cholesterol into a membrane under physiological conditions induces an ordering of the normally fluid lipid acyl chains, which is the opposite trend to that observed upon increasing the degree of lipid unsaturation. The ordering effect is greatest in the C-2 to C-11 portion of the lipid acyl chain, corresponding to interaction with the fused ring system of cholesterol[35]. Towards the end of the acyl chains, cholesterol only induces a small increase in order[35]. In addition, the presence of cholesterol has only a small influence on T_m of a lipid bilayer. However, the enthalpy change associated with the gel-liquid crystalline transition is gradually lowered until at a cholesterol phospholipid ratio of 1:1, a phase transition is no longer detectable by DSC[36,37]. This is an indication that at these cholesterol levels, the degree of order between the formal gel and liquid crystalline phases is very similar such that there is no longer any entropy (and enthalpy) change upon passing through T_m of the lipid. In the gel phase, cholesterol induces disorder of lipid acyl chains[32–34] in contrast to what is observed in the liquid crystalline phase, so this accounts for the zero entropy change at high cholesterol levels.

Although cholesterol is essential for the normal growth and functioning of all mammalian cells, it can also lead to a pathological state known as atherosclerosis[38]. This disease involves the accumulation of cholesterol in the form of plaques, in the walls of arteries. These plaques inhibit blood flow and can eventually lead to formation of a blood clot resulting in obstruction of an artery, causing a heart attack or stroke. The mechanism of this plaque formation is not clearly understood. It is known that the cholesterol found in these plaques originates from low density lipoprotein (LDL) particles circulating in the blood, so the factors affecting the number of LDL receptors in the plasma membranes of cells, and hence the LDL levels in the bloodstream, are the subject of active research[39]. Considerable effort has also been directed towards an understanding of the normal functioning of cholesterol in plasma and other membranes[32–34,40]. A brief account follows of the current

appreciation of the role of cholesterol in the structure and function of membranes.

1.3 The Role of Cholesterol in Membranes

1.3.1 The Location of Cholesterol in Membranes and Cells

Sterols are one of the major classes of lipids found in eucaryotic cells, with cholesterol being the most abundant sterol in mammalian cells. Cholesterol is amphipathic due to its hydrophilic 3β-OH group (Figure 1.2) and its hydrophobic ring system and sidechain. Its location in a lipid bilayer, with respect to the bilayer normal, has been determined by neutron diffraction experiments on egg lecithin multilayers incorporated with cholesterol selectively labelled at C-3 with deuterium[41]. The deuterium label was found to be at the position of the ester bonds of the adjacent lipid acyl chains. So it was concluded that cholesterol intercalates between lipid hydrocarbon chains with its alkyl sidechain pointing towards the hydrophobic bilayer interior, and its hydrophilic 3β-OH group residing closest to the polar headgroup region, in the vicinity of the lipid acyl linkage. Freeze-fracture electron microscopy of plasma membranes has shown, however, that the distribution of cholesterol in the plane of the bilayer (i.e. lateral distribution) is not uniform, similar to what was observed for integral proteins[13,33]. In addition, cholesterol occurs in much higher concentrations in plasma membranes (~30–50 mole percent) than in many of the intracellular membranes, including the endoplasmic reticulum membrane (~12 mole percent) in which it is biosynthesized[13,33]. Any unifying picture of the role of cholesterol in membranes must account for its asymmetric inter- and intramembrane distribution, as well as its already cited abolition of phospholipid gel-liquid crystalline phase transitions, and its ordering effect on lipid acyl chains under physiological conditions.

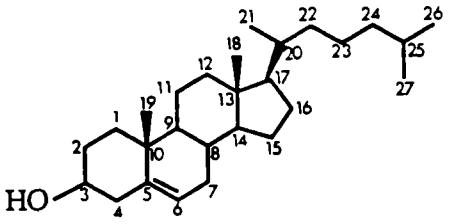

Figure 1.2: Cholesterol with carbon atom numberings

1.3.2 Structural Features of the Cholesterol Molecule Necessary for its Effects on Membranes

One approach has been to gain insight into cholesterol-phospholipid interactions through examining the effect of modifications of the cholesterol structure on the phase transition and order of phospholipid acyl chains. Cholest-5-ene, which has the same structure as cholesterol except for the absence of the 3β-OH group, has very little ordering effect on lipid acyl chains above T_m, judging by order parameters obtained from fluorescence depolarization experiments[42]. Similarly, absence of the C-5,C-6 double bond in cholestan-3β-ol, results in less efficient ordering of acyl chains as monitored by both ^{13}C NMR and fluorescence depolarization[42,43]. It has been postulated that the importance of the C-5,C-6 double bond originates in the twist it gives to the fused ring system, making the cholesterol molecule more cylindrical, which could be important in its intercalation between the acyl chains. Also, the orientation of the C-O bond of the 3β-OH group with respect to the remainder of the molecule differs between cholestan-3β-ol and cholesterol. Indeed, it has been ascertained that not only is the presence of a C-3 hydroxyl group crucial to cholesterol's function in a membrane, but that its spatial arrangement is also critical. Epicholesterol, the 3α-OH analogue of cholesterol in which the hydroxy group lies below the plane of the fused ring system, instead of above, fails to induce the same extent of acyl chain ordering as cholesterol[42,44]. A deuterium NMR study of the orientation of $3d_1$-cholesterol and $3d_1$-epicholesterol in a phospholipid model membrane[44] has shown that cholesterol is tilted with respect to the acyl chains such

that its 3β-OH group lies parallel to the bilayer normal, both above and below T_m of the lipid. In contrast, epicholesterol is aligned parallel to the bilayer normal below T_m, resulting in the 3α-OH group being essentially perpendicular to the bilayer normal. Above T_m, epicholesterol is tilted at a similar angle to the acyl chains as is cholesterol, but the 3α-OH group points in towards the hydrophobic region of the bilayer.

Due to the specific requirement of a 3β-OH group for mediation of the membrane functions of cholesterol, as well as the known location of the 3β-OH group near the carbonyl group of the adjacent lipid acyl chain from neutron scattering experiments, the possibility of hydrogen bond formation between cholesterol and phospholipids has been widely investigated. Initially, steric arguments were used to explain how the 3β-OH group of cholesterol, but not the 3α-OH group of epicholesterol, could participate in H-bonding with the carbonyl oxygen atom of adjacent lipid acyl chains. On one hand it was postulated that cholesterol was H-bonded to the carbonyl group of the acyl chain attached to C-2 of the glycerol backbone (see Figure 1.1), possibly indirectly through the involvement of water molecules[45]. A later study proposed that the H-bond occurred to the carbonyl group of the C-1 acyl chain, and that it was a direct H-bond as this would maximize hydrophobic interactions between the cholesterol nucleus and the lipid acyl chains[45]. In any case, existence of a H-bond between cholesterol and phospholipids was cited as an underlying reason for the unique ordering properties of cholesterol. More recent evidence from ^{13}C NMR, however, indicates that the carbonyl ^{13}C signal from a cholesterol/phospholipid model membrane was not shifted downfield by 2 ppm as would be expected upon H-bonding[46]. Results of subsequent infrared (IR) and Raman spectroscopic studies, in particular the absence of a Raman transition between 1700–1710 cm^{-1}, provided further evidence against the existence of a H-bond[48]. Permeability studies on model membranes composed of phospholipids with either diester, diether, or dialkyl chains showed that incorporation of cholesterol reduced bilayer permeability to very similar extents in all three cases[49]. Thus, it was concluded that there is no specific hydrophilic interaction such as H-bonding between the 3β-OH group of cholesterol and a carbonyl group of an adjacent lipid chain. H-bonding is now considered by most researchers (see ref. 50 for an exception) not

to be a contributing factor in the effects of cholesterol on lipid bilayers.

Spectroscopic studies of model membranes containing sterols modified from the cholesterol structure in either the ring system or the sidechain, have provided some insight into the hydrophobic interactions between cholesterol and phospholipids. Lanosterol, a precursor of cholesterol in the biosynthetic pathway, does not induce any change in order at C-9 and C-10 positions of lipid acyl chains as monitored by ^{2}H NMR, in contrast to the effect of cholesterol at this depth in the bilayer[51]. This difference in behaviour has been attributed to the presence of a methyl substituent at C-14 in lanosterol (see Figure 1.2), which projects out of the normally planar α-face of the fused ring system. Thus it appears that the planar α-face of cholesterol is necessary for its effects on lipid acyl chains. In addition, the presence of a nonpolar sidechain is crucial. 5α-Androstan-3β-ol, an analogue of cholesterol with no sidechain and also no C-5,C-6 double bond, is found to have a substantially lower ordering effect on model membranes than either cholesterol or cholestan-3β-ol (no C-5,C-6 double bond)[42]. Sterols with C_8 sidechains, as present in cholesterol, which are substituted with polar functional groups such as hydroxy or keto, also do not mimic cholesterol's effects on phospholipids[42].

In summary, the 3β-OH group, the C-5,C-6 double bond, the planar α-face and the nonpolar sidechain are all functionally important components of the cholesterol structure. However, there are still many aspects of cholesterol's role in membranes which remain to be elucidated. These include the effect of cholesterol on lipid acyl chain dynamics, the molecular details of the phase behavior of phospholipid-cholesterol bilayers, and details of cholesterol's interaction with membrane proteins.

1.3.3 Cholesterol-Phospholipid Interactions

While it is generally recognized that cholesterol promotes acyl chain mobility in the gel phase[32–34], there is controversy as to its effect above T_m, i.e. under physiologically relevant conditions. Diffusion coefficients determined by the technique of fluorescence recovery after photobleaching (FRAP)[52,53] have been found to decrease at higher cholesterol levels, as have some diffusion coefficients determined by EPR spectroscopy[54–56]. Some studies have indicated that cholesterol has very little effect on phosopholipid diffusion[57,58], while others demonstrate that lipid dynamical

freedom is enhanced in the presence of cholesterol[28,29,59,60]. Possible sources of these discrepancies include the variety of models used to obtain the motional parameters, as well as potential perturbation of the phosopholipid-cholesterol bilayers by the spectroscopic probe molecules. Also, the region of the bilayer that is being probed must be considered, since one study has indicated that cholesterol has opposite effects on lipid chain mobility near the glycerol backbone as opposed to the methyl terminal end[61].

Another controversy surrounds the rationalization of changes in a number of physical properties of phospholipid-cholesterol model membranes with mole percent cholesterol content. In particular, many of these properties such as the endotherm for the gel-liquid crystalline transition[37], X-ray and electron diffraction spacings and linewidths[62], lateral diffusion coefficients[52,53], and partitioning with respect to water of a spin-label probe[63], change abruptly at a cholesterol level of approximately 20 mole percent. In the gel phase, additional pivotal cholesterol levels appear to be ~5%, 33%, and/or 50%[37,62,64] depending on the parameter being measured. Phase diagrams, with phase boundaries at some or all of the cholesterol levels mentioned above[63,66], have been invoked to explain this host of observations. Alternatively, the results have been interpreted in terms of a single phase, with a continuous change of structure as microdomains of phospholipid:cholesterol complexes with 2:1[13,50], 1:1[50], or no specific[62] stoichiometry are formed. Clearly, this aspect of cholesterol's interaction with phospholipids requires clarification because of its implication in understanding the role of cholesterol in membrane functions such as transport.

1.3.4 Techniques for Studying Cholesterol's Effects on Membranes

A major contributing factor to the confusion surrounding the details of cholesterol's interactions with other membrane components arises from the fact that very few methods can detect the intrinsic properties of cholesterol when it is in a membrane environment. Bulk effects of cholesterol on a membrane can be measured by techniques such as DSC, electron microscopy and X-ray diffraction. However, an appreciation on the molecular level requires the use of spectroscopic techniques.

As mentioned earlier, the most commonly used spectroscopies are NMR, EPR and fluorescence. Each of these methods has advantages and disadvantages in the study of biologically important systems such as membranes.

NMR and EPR Spectroscopies

NMR has the widest applicability because of the number of nuclei which possess a net nuclear spin. The natural abundance of these NMR-active nuclei, however, is usually too low for biological studies so isotopic enrichment, for example of ^{13}C or ^{2}H, is often necessary. It is not expected that isotopic enrichment of natural membrane constituents such as cholesterol or phospholipids would significantly affect membrane properties except that, due to the relative insensitivity of the NMR technique, millimolar concentrations of probe are required.

EPR spectroscopy is more sensitive than NMR but is the least attractive probe technique since the spin labels must bear unpaired electrons. The structures of two EPR probes based on the cholesterol structure are shown in Figure 1.3. They are rendered EPR-active through the presence of a nitroxide group. These two probes have been used extensively in studies of the order and dynamics of cholesterol-containing membranes[20,21,67,68] despite the general recognition that they induce perturbations of membrane properties[20,21], most notably the 'melting' of phospholipid chains at temperatures below T_m[67].

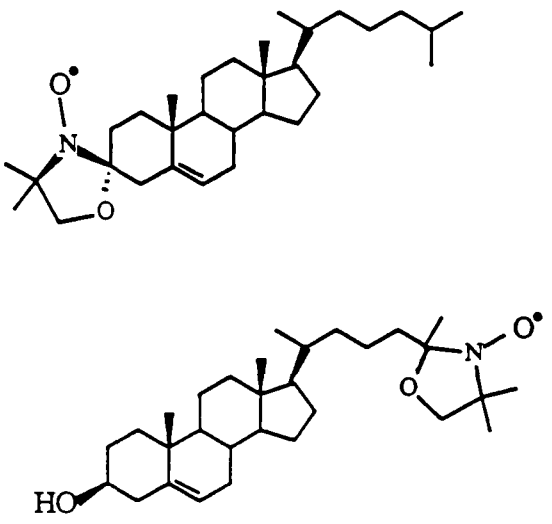

Figure 1.3: Cholesterol analogue electron paramagnetic resonance (EPR) probes.

Fluorescence Spectroscopy

Fluorescence is the most sensitive spectroscopic probe technique, and this coupled with the fact that it can monitor fast dynamical motions on the nanosecond or picosecond timescales, has resulted in its widespread use in studies of biological systems[22]. Its disadvantage is that there are only a limited number of intrinsic fluorophores. While the fluorescent aromatic amino acids tyrosine and tryptophan have enabled many studies of protein and peptide conformation and dynamics[69], membrane studies have been restricted to the use of extrinsic fluorescence probes[22,23]. The most commonly used membrane probe is 1,6-diphenyl-1,3,5-hexatriene (DPH) which bears no resemblance to any natural membrane constituent (see Figure 1.4). Moreover, the precise location of DPH in a membrane is unknown and it has been demonstrated that it adopts orientations both parallel and perpendicular to the bilayer normal in model membranes[28,29].

Fluorescent Sterol Membrane Probes

Several fluorescent probes based on the cholesterol structure have been utilized in studies of cholesterol effects on membane order and dynamics[70]. These fall into

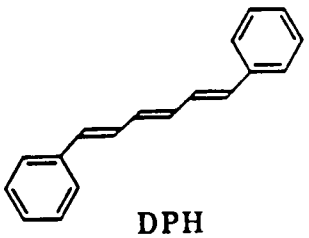

DPH

Figure 1.4: DPH

three categories depending on whether they have been modified at the C-3 position (Figure 1.5)[71,72], in the fused ring system (Figure 1.6)[73–78] or in the sidechain (Figure 1.7)[79–81]. Those probes used in the FRAP experiments outlined earlier, in the determination of lateral diffusion coefficients, were various 3β-ester derivatives[53], and are expected to interact quite differently than cholesterol with the phospholipid headgroups. In fact the DPH-ester derivative shown in Figure 1.5 intercalates between the lipid acyl chains in the opposite direction to cholesterol, with the now significantly nonpolar 3β-substituent pointing towards the bilayer interior[71]. The conjugated unsaturation introduced into the steroid nucleus in the probes dehydroergosterol and cholesta-5,7,9(11)-trien-3β-ol (Figure 1.6)[73–78] render the fused ring system more planar, and distort the positions of the 18- and 19-angular methyl groups. Since cholesterol has its greatest ordering effect on C-2 to C-11 of the lipid acyl chains, corresponding to interaction with the steroid nucleus, a change in geometry in this region of a fluorescent sterol probe is likely to perturb the normal packing of lipid/cholesterol bilayers. The sidechain modified cholesterol analogues (Figure 1.7)[79–81] all contain heteroatoms in their sidechains, which greatly alters their hydrophobicity and hence the amphipathic nature of the molecules.

It was decided to synthesize fluorescent cholesterol analogues modified in the sidechain with hydrophobic fluorophores. This was achieved through the introduction of conjugated unsaturation in the form of aryl polyenes; either a diene phenyl, a triene phenyl or a diene 2′-naphthyl moiety (Figure 1.8). Note that *all-trans* geometries of the polyenes is specified. This was in order to minimize photodegradation of the probes which not only complicates their photophysics, but the photoproducts could be toxic to the membranes under study. *Cis*-polyenes are more reactive than their *trans* diastereomers due to their increased susceptibility to addition across the

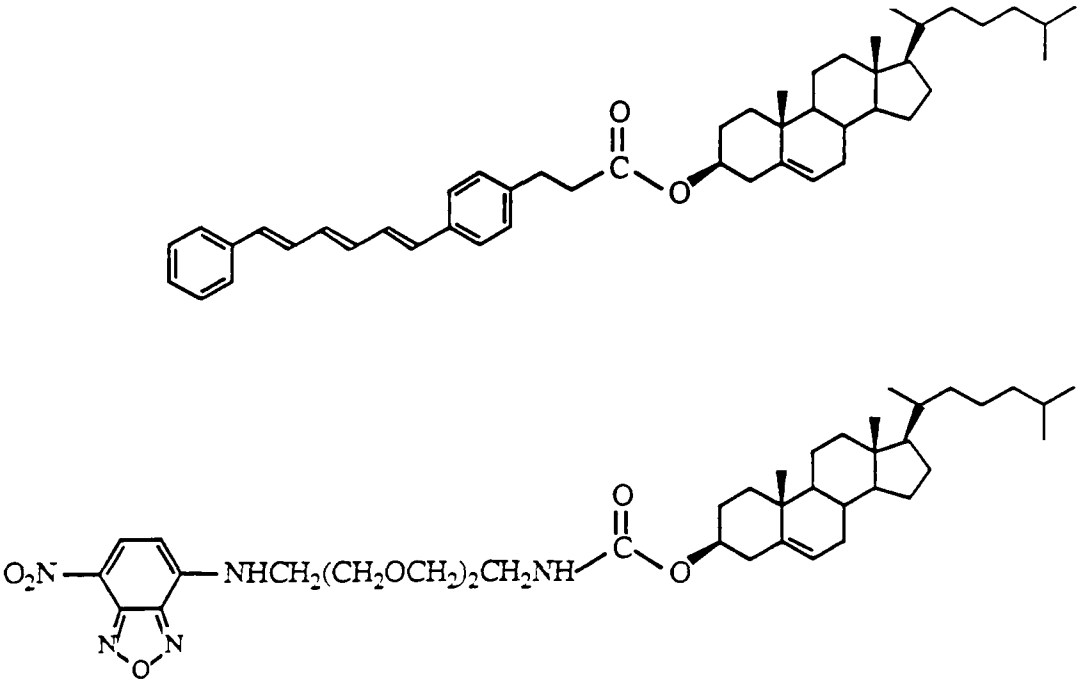

Figure 1.5: Cholesterol-based fluorescence probes modified at C-3.

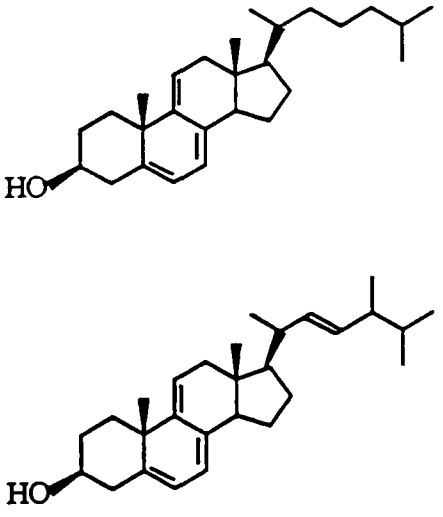

Figure 1.6: Ring-unsaturated fluorescent sterol probes.

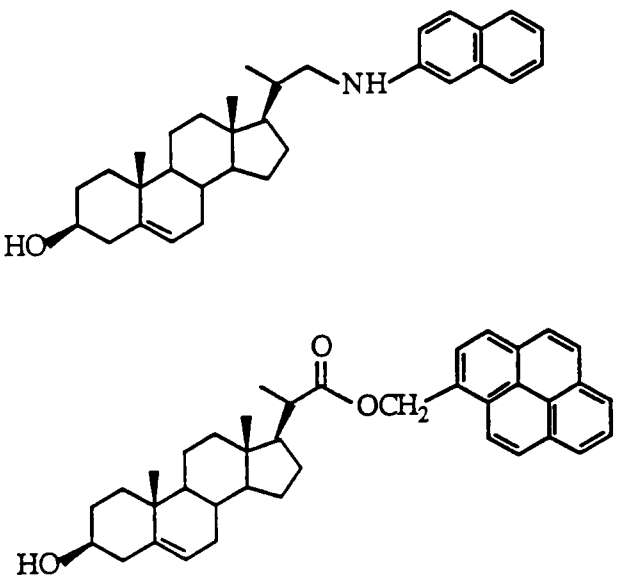

Figure 1.7: Sidechain-modified fluorescent cholesterol analogue probes.

double bond.

Inspection of space filling models shows that the diene phenyl analogue has the closest geometrical structure to that of cholesterol (Figure 1.9). It is expected that all three probes will prove to be close analogues of cholesterol. This view is supported by deuterium NMR studies of various deuteriated cholesterol derivatives incorporated into phospholipid model membranes, which have shown that the sidechain of cholesterol, up to C-22, is as rigid as the ring system, as measured by the molecular order parameter S_{mol}=0.80[82]. Even at C-24, the sidechain was found to be highly ordered with S_{mol}=0.66.

This thesis describes the synthesis and purification of these fluorescent sterols (Chapter 2), the characterization of their double bond geometries and the assignment of ^{1}H and ^{13}C resonances by high resolution NMR (Chapter 3), the characterization of their photophysical properties in isotropic solvents and hence their potential as fluidity probes (Chapter 4), and lastly some preliminary model membrane studies are presented and ideas for future experiments are discussed (Chapter 5). Although a better understanding of the role of cholesterol in membranes will come from combining the information obtained from a variety of techniques, an important contribution could be made through the use of these fluorescent cholesterol analogues as cell membrane probes.

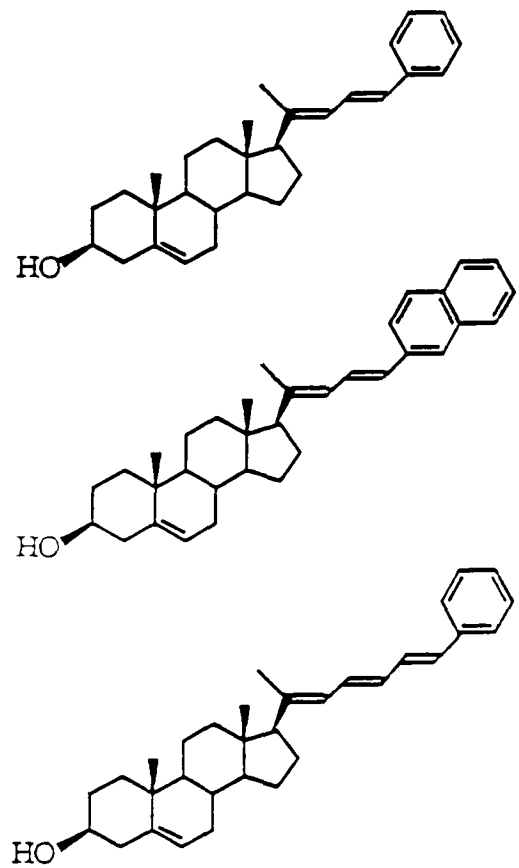

Figure 1.8: Fluorescent sterol probes, with unsaturated sidechains, synthesized in this work.

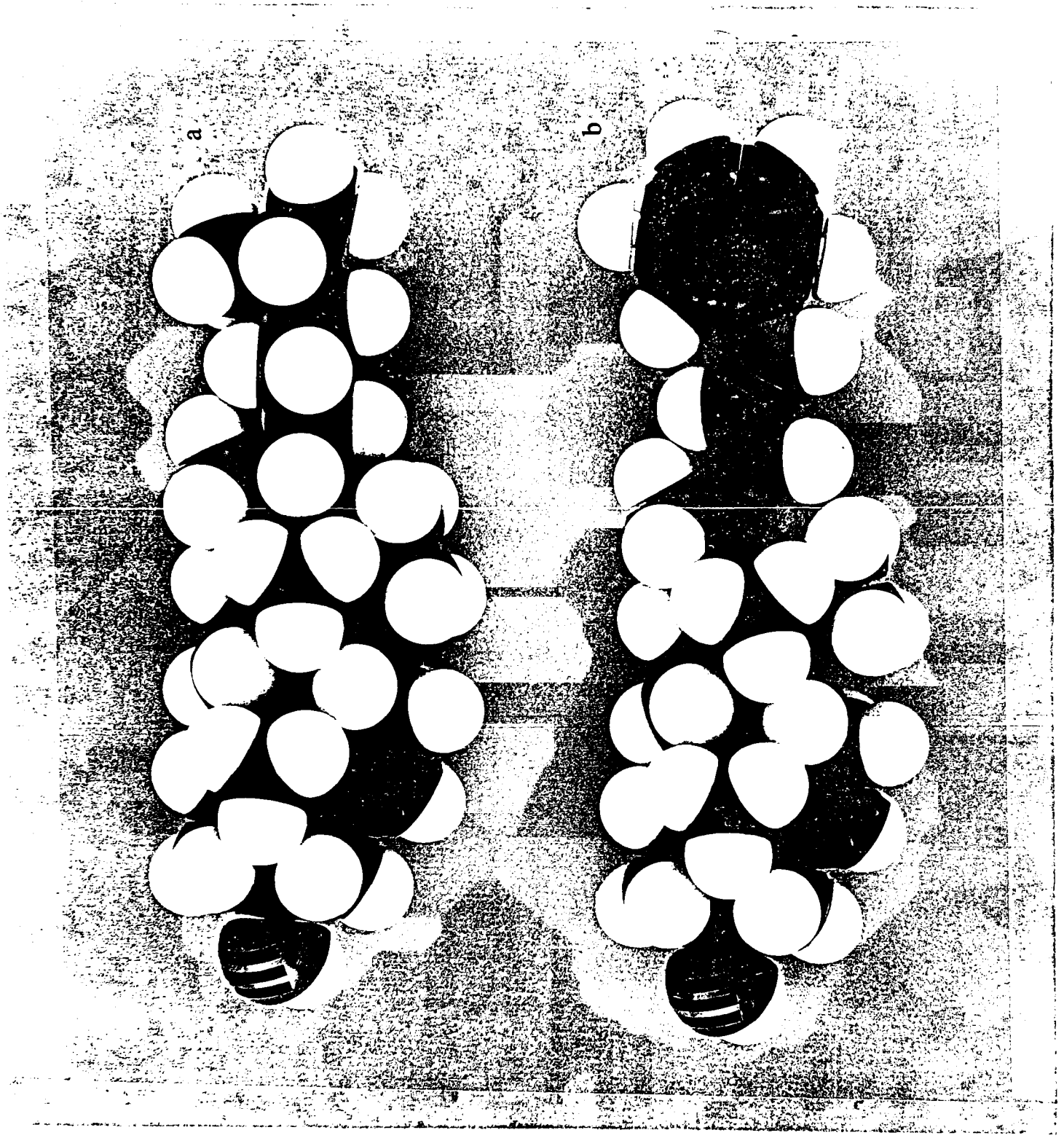

Figure 1.9: Space-filling models of (a) cholesterol and (b) the diene phenyl cholesterol analogue synthesized in this work.

1.4 References

1. L. Stryer, *"Biochemistry"*, 2nd ed., W.H. Freeman, San Francisco, **1981**.

2. A.L. Lehninger, *"Principles of Biochemistry"*, Worth, New York, **1982**.

3. D.E. Metzler, *"Biochemistry. The Chemical Reactions of Living Cells"*, Academic, New York, **1977**.

4. G. Zubay, *"Biochemistry"*, Addison-Wesley, Massachusetts, 1983.

5. R.N. Robertson, *"The Lively Membranes"*, Cambridge University Press, Cambridge, **1983**.

6. S.J. Singer and G.L. Nicholson, *Science*, **1972**, *175*, 720–731.

7. F. Jähnig, *Biophys. J.*, **1981**, *36*, 347–357.

8. D. Chapman, in *"Membrane Fluidity in Biology"*, R.C. Aloia ed., Academic. New York, **1983**, Vol. 2, pp. 5–42.

9. C.D. Stubbs in *"Essays in Biochemistry"*, New York, P.N. Campbell and R.D. Marshall eds., Academic, **1983**, Vol. 19, pp. 1–39.

10. M. Shinitzky, in *"Physiology of Membrane Fluidity"*, M. Shinitzky ed., CRC, Florida, **1984**, Vol. 1, pp. 1–51.

11. W. van der Meer, in *"Physiology of Membrane Fluidity"*, M. Shinitzky ed., CRC, Florida, **1984**, Vol. 1, pp. 53–71.

12. G. Lenaz and G.P. Castelli, in *"Structure and Properties of Cell Membranes"*, G. Benga ed., CRC, Florida, **1985**, Vol. 1, pp. 93–136.

13. M.K. Jain, *"Introduction to Biological Membranes"*, 2nd ed., Wiley, New York, **1988**.

14. J. Seelig and A. Seelig, *Q. Rev. Biophys.*, **1980**, *13*, 19–61.

15. T.M. Jovin, M. Bartholdi, W.L.C. Vaz and R.H. Austin, *Ann. N.Y Acad. Sci.*, **1981**, 366, 176–196.

16. S. Mabrey-Gaud, in *"Liposomes: From Physical Structure to Therapeutic Applications"*, C.G. Knight ed., Elsevier, Amsterdam, **1981**, pp. 105–138.

17. A.E. Blaurock, *Biochim. Biophys. Acta*, **1981**, *650*, 167–207.

18. M.C. Phillips, R.M. Williams and D. Chapman, *Chem. Phys. Lipids*, **1969**, *3*, 234–244.

19. I.C.P. Smith in *"Structure and Properties of Cell Membranes"*, G. Benga ed., CRC, Florida, **1985**, Vol. 3, pp. 237–260.

20. P.D. Morse, in *"Structure and Properties of Cell Membranes"*, G. Benga. ed., CRC, Florida, **1985**, Vol. 3., pp. 195–236.

21. S. Schreier, C.F. Polnaszek and I.C.P. Smith, *Biochim. Biophys. Acta*, **1978**. *515*, 375–436.

22. B.S. Hudson. D.L. Harris, R.D. Ludescher, A. Ruggiero, A. Cooney-Freed and S.A. Cavalier, in *"Applications of Fluorescence in the Biomedical Sciences"*, D.L. Taylor ed., Alan R. Liss, New York, **1986**, pp. 159–202.

23. F. Schroeder, in *"Subcellular Biochemistry"*, D.B. Roodyn ed., Plenum, New York, **1986**, Vol. 11, pp. 51–101.

24. Y. Lange, in ***"The Physical Chemistry of Lipids: From Alkanes to Phospholipids"***, D.M. Small ed., Plenum, New York, **1986**, pp. 523–554 and references therein.

25. G. Cevc and D. Marsh, ***"Phospholipid Bilayers. Physical Principles and Models"***, Wiley, New York, **1987**.

26. J. Seelig and A. Seelig, *Q. Rev. Biophys.*, **1980**, *13*, 19–61 and references therein.

27. A. Seelig and J. Seelig, *Biochem.*, **1977**, *16*, 45–50.

28. G. van Ginkel, L.J. Korstanje, H. van Langen and Y.K. Levine, *Faraday Diss. Chem. Soc.*, **1986**, *81*, 49–61.

29. G. Deinum, H. van Langen, G. van Ginkel and Y.K. Levine, *Biochem.*, **1988**, *27*, 852–860.

30. C.D. Stubbs, T. Kouyama, K. Kinoshita and A. Ikegami, *Biochem.*, **1981**, *20*, 4257–4262.

31. K.P Coolbear, C.B. Berde and K.M.W. Keough, *Biochem.*, **1983**, *22*, 1466–1473.

32. R.A. Demel and B. De Kruyff, *Biochem. Biophys. Acta*, **1976**, *457*, 109–132.

33. P.L. Yeagle, *Biochim. Biophys. Acta*, **1985**, *822*, 267–287.

34. F.T. Presti, in *"Membrane Fluidity in Biology"*, R.C. Aloia and J.M. Boggs eds., Academic, New York, **1985**, Vol. 4, pp. 97–146.

35. G.W. Stockton and I.C.P. Smith, *Chem. Phys. Lipids*, **1976**, *17*, 251–263.

36. B.D. Ladbrooke, R.M. Williams and D. Chapman, *Biochim. Biophys. Acta*, **1968**, *150*, 333–340.

37. S. Mabrey, P.L. Mateo and J.L. Sturtevant, *Biochem.*, **1978**, *17*, 2464–2468.

38. M.S. Brown and J.L. Goldstein, *Sci. Am.*, **1984**, *251(5)*, 58–66.

39. M.S. Brown and J.L. Goldstein, *Ann. Rev. Biochem.*, **1983**, *52*, 223–261.

40. R.A. Cooper and J.F. Strauss in *"Physiology of Membrane Fluidity"*, M. Shinitzky ed., CRC, Florida, **1984**, Vol. 1, pp. 73–97.

41. D.L. Worchester and N.P. Franks, *J. Mol. Biol.*, **1976**, *100*, 359–378.

42. M. Vincent and J. Gallay, *Biochem. Biophys. Res. Commun.*, **1983**, *113*, 799–810.

43. L.S. Ramsammy, P.A. Merz and H. Brockerhoff, *Chem. Phys. Lipids*, **1984**, *34*, 127–138.

44. R. Murari, M.P. Murari and W.J. Baumann, *Biochem.*, **1986**, *25*. 1062–1067.

45. H. Brockerhoff, *Lipids*, **1974**, *9*, 645–650.

46. C-H. Huang, *Lipids*, **1977**, *12*, 348–356.

47. A.K. Lala, *Int. J. Quant. Chem.*, **1981**, *20*, 93–97.

48. S.F. Bush, H. Levin and I.W. Levin, *Chem. Phys. Lipids*, **1980**, *27*, 101–111.

49. S. Clejan, R. Bittman, P.W. Deroo, Y.A. Issacson and A.F. Rosenthal, *Biochem.*, **1979**, *18*, 2118–2125.

50. F.T. Presti, R.J. Pace and S.I. Chan, *Biochem.*, **1982**. *21*, 3831–3835.

51. P.L. Yeagle, *Biochim. Biophys. Acta*, **1985**, *815*, 33–36.

52. J.L.R. Rubinstein, B.A. Smith and H.M. McConnell, *Proc. Natl. Acad. Sci. USA*, **1979**, *76*, 15–18.

53. M.R. Alecio, D.E. Golan, W.R. Veatch and R.R. Rando, *Proc. Natl. Acad. Sci. USA*, **1982**, *79*, 5171–5174.

54. M.A. Hemminga, *Chem. Phys. Lipids*, **1975**, *14*, 141–150.

55. A. Kusumi, W.K. Subszynski, M. Pasenkiewicz-Gierula, J.S. Hyde and H. Merkle, *Biochim. Biophys. Acta*, **1986**, *854*, 307–317.

56. A. Kusumi and M. Pasenkiewicz-Gierula, *Biochem.*, **1988**, *27*, 4407–4415.

57. K. Kinoshita and A. Ikegami, *Biochim. Biophys. Acta*, **1984**, *769*, 523–527.

58. G. Lindblom, L.B.-Å. Johansson and G. Arvidson, *Biochem.*, **1981**, *20*, 2204–2207.

59. R. Ghosh and J. Seelig, *Biochim. Biophys. Acta*, **1982**, *691*, 151–160.

60. M. Straume and B.J. Litman, *Biochem.*, **1987**, *26*, 5121–5126.

61. H. Kutchai, L.H. Chandler and G.B. Zavoico, *Biochem. Biophys. Acta*, **1983**, *736*, 137–149.

62. S.W. Hui and N-B. He, *Biochem.*, **1983**, *22*, 1159–1164.

63. W. Knoll, G. Schmidt, K. Ibel and E. Sackmann, *Biochem.*, **1985**, *24*, 5240–5246.

64. D.J. Rectenwald and H.M. McConnell, *Biochem.*, **1981**, *20*, 4505–4510.

65. B.R. Lentz, D.A. Barrow and M. Hoechli, *Biochem.*, **1980**, *19*, 1943–1954.

66. J.H. Ipsen, G. Karlström, O.G. Mouritsen, H. Wennerström and M.J. Zuckermann, *Biochim. Biophys. Acta*, **1987**, *905*, 162–172.

67. F.T. Presti and S.I. Chan, *Biochem.*, **1982**, *21*, 3821–3830.

68. G. Morot, J-F. Bureau, M. Roux, L. Maurin, E. Favre and P.F. Devaux, *Biochim. Biophys. Acta*, **1987**, *897*, 341–345.

69. A.G. Szabo, in *"The Enzyme Catalysis Process: Energetics, Structure and Dynamics"*, A. Cooper and J. Houben eds., Plenum, in press.

70. F. Schroeder, *Prog. Lipid Res.*, **1984**, *23*, 97–113.

71. M. Cranney, R.B. Cundall, G.R. Jones, J.T. Richards and E.W Thomas. *Biochim. Biophys. Acta*, **1983**, *735*, 418–425.

72. R.R. Rando, F.W. Bangerter and M.R. Alecio, *Biochim. Biophys. Acta*, **1982**, *684*, 12–20.

73. R.J.M. Smith and C. Creen, *Biochem. J.*, **1974**, *137*, 413–415.

74. J. Rogers, A.G. Lee and D.C. Wilton, *Biochim. Biophys. Acta*, **1979**, *552*, 23–37.

75. R.J. Bergeron and J. Scott, *J. Lipid Res.*, **1982**, *23*, 391–404.

76. G. Smutzer and P.L. Yeagle, *Biochim. Biophys. Acta*, **1985**, *814*, 274–280.

77. P.L-G. Chong and T.E. Thompson, *Biochim. Biophys. Acta*, **1986**, *863*, 53–62.

78. F. Schroeder, Y. Barenholz, E. Gratton and T.E. Thompson, *Biochem.*, **1987**, *26*, 2441–2448.

79. Y.J. Kao, A.K. Soutar, K-Y. Hong, H.J. Pownall, and L.C. Smith, *Biochem.*, **1978**, *17*, 2689–2696.

80. I.F. Craig, D.P. Via, W.W. Mantulin, H.J. Pownall, A.M. Gotto and L.C. Smith, *J. Lipid Res.*, **1981**, *22*, 687–696.

81. Y.J. Kao, M.C. Doody and L.C. Smith, *J. Lipid Res.*, **1986**, *27*, 781–785.

82. E.J. Dufourc, E.J. Parish, S. Chitrakorn and I.C.P. Smith, *Biochem.*, **1984**, *23*, 6062–6071.

Chapter 2

Synthesis from Pregnenolone of Fluorescent Cholesterol Analogue Probes with Aryl Polyene Sidechains

2.1 Introduction

The desired cholesterol analogue probes **4a**, **5a** and **6a** with their aryl polyene sidechains could be synthesized directly from the available C-20 steroidal ketone 3β-hydroxypregn-5-en-20-one (pregnenolone **1**,R=H) via a Wittig reaction. This reaction has the advantage over the other olefin synthetic procedures in that a double bond is formed exclusively between the nucleophilic carbon atom adjacent to the phosphorous atom in the Wittig reagent, and the carbonyl carbon atom of the starting material. However, the Wittig reaction can lead to formation of Z or E alkenes, or mixtures thereof. For the proposed fluorescence application of the desired sterols, *all-trans* or E,E,(E) polyene geometry was preferred, as discussed in Chapter 1. By adjustment of reaction conditions such as solvent and base, and by the use of structurally suitable reactants, some steric control over the Wittig reaction can be achieved.

2.1.1 Stereochemistry of the Phosphorane Wittig Reaction

Effect of Phosphorane Structure

The single most important parameter which can determine the steric course of the phosphorane Wittig reaction is the structure of the reagent of general formula

$$\underset{\text{phosphorane}}{R^1R^2R^3P{=}CR^4R^5} \longleftrightarrow \underset{\text{ylid}}{R^1R^2R^3P^+C^-R^4R^5}$$

where R^1, R^2 and R^3 are alkyl or aryl groups and often $R^1 = R^2 = R^3$. Wittig reagents have been classified into three categories depending on the ability of the R^4 or R^5 substituents to stabilize a negative charge on the carbon atom adjacent to the phosphorous atom (hereafter referred to as the α-carbon atom). These categories are :

1. 'stabilized', when R^4 or R^5 is an electron-withdrawing group such as CO_2R or CN;

2. 'semi-stabilized' or 'moderate', when R^4 or R^5 is a weakly electron-withdrawing group such as aryl or alkenyl;

3. 'unstabilized', when R^4 or R^5 is an electron-donating group such as alkyl or alkoxy.

In general (although other factors can be important, see later), stabilized ylids will react with aldehydes to give predominantly E olefins[1-7], while reactions with unstabilized ylids yield Z olefins[1-3,6,8,9] and approximately 1:1 mixtures of E:Z olefins are obtained with reactions of semi-stabilized ylids[1-3,6,10,11].

Appropriate phosphorane reagents for generation of the sterol probes **4a**, **5a** and **6a** from pregnenolone (**1**, R=H) are shown in Scheme 2.1, although the triphenyl substituents on the phosphorous atom could potentially be replaced by any combination of three alkyl groups.

Scheme 2.1

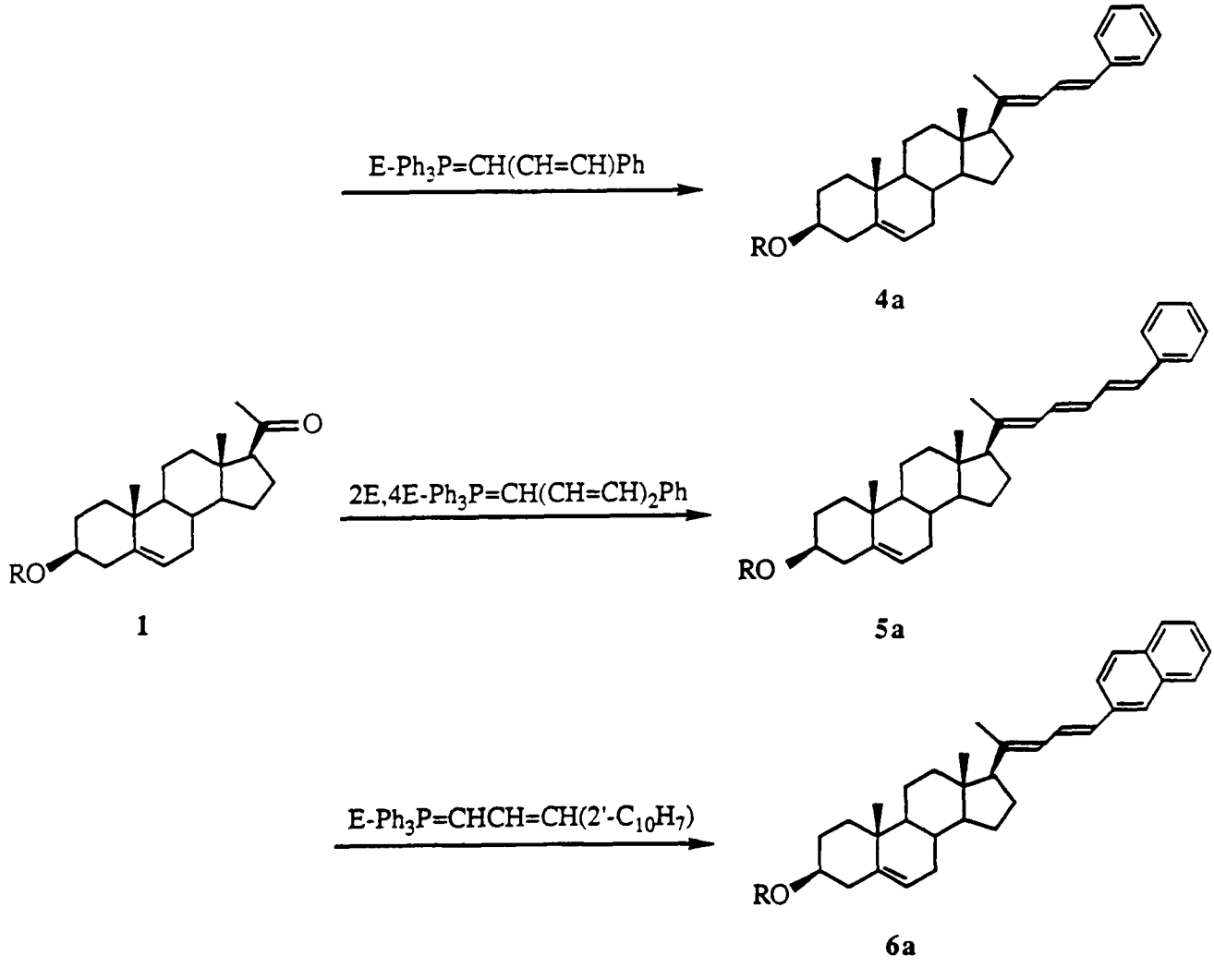

These phosphoranes fall into the 'semi-stabilized' category of Wittig reagents, so 1:1 mixtures of alkenes are to be expected in the absence of other factors.

In order to gain some understanding of why the stereochemistry of the phosphorane Wittig reaction is dependent on the nature of the group being added to the aldehyde or ketone (i.e. on the nature of the substituents R^4, R^5 in the phosphorane), it is necessary to take stock of what is known about the mechanism of the reaction. The first step of the phosphorane Wittig reaction is generation of the phosphorane/ylid reagent by treatment of the corresponding phosphonium halide salt with one equivalent of base (equation 2.1).

$$\underset{\text{phosphonium halide}}{R^1R^2R^3P^+CHR^4R^5X^-} \xrightarrow{B^-M^+} \underset{\text{phosphorane}}{R^1R^2R^3P=CR^4R^5} + M^+X^- + BH \qquad (2.1)$$

$$\updownarrow$$

$$R^1R^2R^3P^+C^-R^4R^5$$

ylid

In a 'classical' look at the mechanism of the reaction (Figure 2.1), there is then nucleophilic attack of the ylid on the carbonyl carbon atom to yield diastereomeric *erythro-* and *threo-* betaines which cyclize to the *erythro-* and *threo-* oxaphosphetanes. Syn elimination[6] of a trialkyl phosphine from the oxaphosphetanes leads to the Z and E olefins respectively.

The presence of electron-donating groups R^4, R^5 on the α-carbon atom of the phosphorane (i.e. use of an unstabilized reagent) has been found to result in high yields of Z olefin. On the other hand, use of a stabilized Wittig reagent, with its electron withdrawing R^4, R^5 substituents, leads to predominantly E olefin. This observation has been explained by considering the tendency of the intermediate oxaphosphetanes to equilibriate via the starting materials in a 'retro-Wittig' process, which would give rise to a higher proportion of the thermodynamically more stable *threo-* oxaphosphetane and hence a higher percentage of E olefin in the product. Electron-withdrawing R^4, R^5 substituents can be seen to enhance the retro-Wittig process (Figure 2.2), thus accounting for the higher E:Z alkene ratios observed in phosphorane Wittig reactions with stabilized as opposed to unstabilized reagents.

Reactions involving semi-stabilized phosphoranes, such as we are concerned with in the synthesis of sterol probes **4a**, **5a** and **6a**, lie somewhere between the two cases

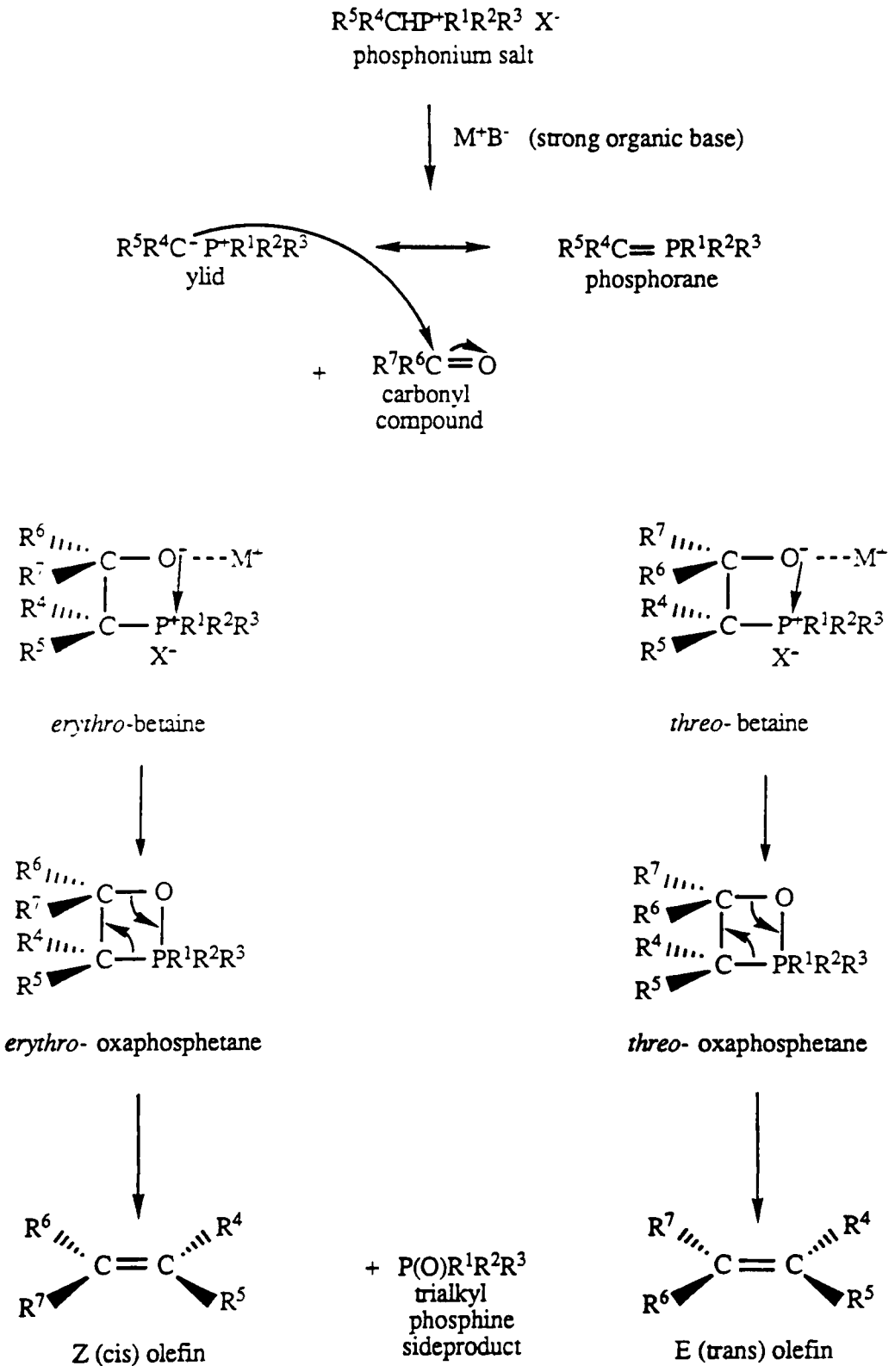

Figure 2.1: 'Classical' mechanism of the phosphorane Wittig reaction.

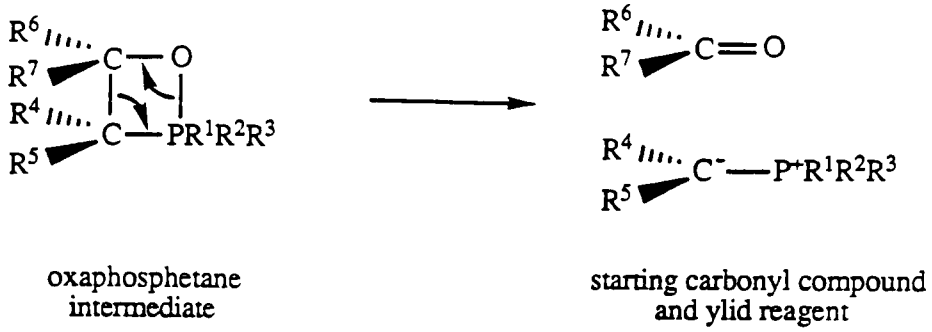

Figure 2.2: 'Retro–Wittig' process.

presented above and hence it is not surprising that generally 1:1 mixtures of E:Z olefins are obtained using this class of Wittig reagent.

It has been found that by changing the nature of the alkyl groups R^1, R^2, R^3 of the phosphorane reagent (as mentioned previously, these groups can be any combination of alkyl groups since they do not end up in the desired olefin but in the trialkyl phosphine sideproduct), the reaction of semi-stabilized phosphoranes with aldehydes can be directed to yield higher proportions of E olefins in the product. For example, successive replacement of the usual triphenyl (weakly electron-withdrawing) substituents by electron-donating alkyl groups such as cyclohexyl, *n*-butyl or methyl[10–12] results in higher E:Z alkene ratios (equations 2.2–2.4)[12].

					E:Z ratio	
$Ph_3P^+CH_2PhX^-$	+ PhCHO	$\xrightarrow{NaOEt/EtOH}$	PhCH=CHPh	47:53	(2.2)
$Ph_2MeP^+CH_2PhX^-$	+ PhCHO	$\xrightarrow{NaOEt/EtOH}$	PhCH=CHPh	72:28	(2.3)
$PhMe_2P^+CH_2PhX^-$	+ PhCHO	$\xrightarrow{NaOEt/EtOH}$	PhCH=CHPh	87:13	(2.4)

In terms of the mechanism presented earlier for the phosphorane Wittig reaction, the presence of electron-donating groups R^1, R^2 and R^3 increases the electron density on the adjacent phosphorous atom. This results in a decreased tendency of the betaines to cyclize to the oxaphosphetanes which in turn promotes equilibration of the *erythro-* and *threo-* betaines favouring the thermodynamically more stable *threo-* betaine. The final product consequently contains a higher proportion of the E olefin than obtained with the corresponding triphenyl phosphorane.

A potential disadvantage of using dialkyldiphenyl- or trialkylphenyl- phosphonium halide salts, however, is that they may deprotonate at two alkyl groups when using a strong base like *n*-butyllithium (*n*-BuLi), which would result in loss of regioselectivity in the Wittig reaction. This problem can be avoided by replacement of only one of the triphenyl substituents by an alkenyl group which is identical to the CHR^4R^5 portion of the phosphonium salt (equation 2.5)[11].

$$\begin{aligned} &Ph_2[(CH_3)_2C{=}CHCH_2]P{=}CHCH{=}C(CH_3)_2 + PhCHO \\ &\xrightarrow[THF]{NaNH_2} PhCH{=}CHCH{=}C(CH_3)_2 \qquad \text{E:Z ratio} > 94{:}6 \end{aligned} \qquad (2.5)$$

Effect of Other Reaction Conditions

It has been found empirically that other reaction conditions, apart from the structure of the reagent, can affect the stereochemistry of the phosphorane Wittig reaction. These conditions include the solvent used, and the choice of base to generate the phosphorane. The effects of changes of these parameters on the Wittig reaction stereochemistry are usually interpreted in terms of their influence on the equilibrium between the *erythro-* and *threo-* intermediates of the reaction and hence on the yields of Z and E olefins respectively.

The choice of base is important if a lithium base such as *n*-BuLi or lithium hexamethyl disilazide (LiHMDS) is used. In general, for Wittig reactions with unstabilized phosphoranes in a nonpolar solvent like benzene, the presence of lithium salts in the reaction mixture leads to increased yields of E olefin with respect to Z olefin[5,8,13–15] (equations 2.6, 2.7)[13].

$$Ph_3P{=}CHEt + PhCHO \xrightarrow{C_6H_6} PhCH{=}CHEt + Ph_3PO \qquad \text{E:Z ratio } 9{:}91 \qquad (2.6)$$

$$Ph_3P{=}CHEt + PhCHO \xrightarrow[\text{LiBr present}]{C_6H_6} PhCH{=}CHEt + Ph_3PO \qquad \text{E:Z ratio } 40{:}60 \qquad (2.7)$$

This effect has been explained in terms of the decreased ability of the betaine to cyclize to the oxaphosphetane because of the complexation of the oxyanion in the betaine with the lithium cation. This allows an equilibrium to be established between the *erythro-* and *threo-* betaines yielding a greater proportion of the thermodynamically favoured *threo-* diastereomer which in turn results in higher proportions of

E olefin in the product. In reactions involving semi-stabilized and stabilized phosphoranes in nonpolar solvents, the presence of lithium salts favours formation of Z olefins in contrast to the trend observed with unstabilized phosphoranes (equations 2.8, 2.9)[13].

$$Ph_3P{=}CHPh + EtCHO \xrightarrow{C_6H_6} EtCH{=}CHPh + Ph_3PO \quad \text{E:Z ratio } 82{:}18 \quad (2.8)$$

$$Ph_3P{=}CHPh + EtCHO \xrightarrow[LiBr]{C_6H_6} EtCH{=}CHPh + Ph_3PO \quad 73{:}27 \quad (2.9)$$

The reason for this difference in trends is not well understood. It has been suggested that the influence of lithium salts is on the initial carbon-carbon bond forming process and not on betaine or oxaphosphetane reversibility[14,15]. Also, recent evidence[7] has been gained through deuterium labelling studies that E olefins can be obtained under kinetic and not thermodynamic control in reactions of stabilized phosphoranes with aldehydes. Perhaps the opposing trends described above reflect a difference in the kinetically favoured olefin with class of Wittig reagent.

In general, the presence of lithium salts has no effect on the stereochemistry of the phosphorane Wittig reaction if polar solvents like dimethylformamide (DMF) are employed, no matter what class of reagent is used (equations 2.10, 2.11)[13].

$$Ph_3P{=}CHPh + EtCHO \xrightarrow{DMF} EtCH{=}CHPh + Ph_3PO \quad \text{E:Z ratio } 59{:}41 \quad (2.10)$$

$$Ph_3P{=}CHPh + EtCHO \xrightarrow[LiBr]{DMF} EtCH{=}CHPh + Ph_3PO \quad 59{:}41 \quad (2.11)$$

Polar solvents can effectively solvate the lithium salt and hence hinder the formation of a lithium halide-betaine complex such that no change is observed in the steric course of the reaction.

Solvents also play a role in determining the stereochemistry of the phosphorane Wittig reactions apart from their possible ability to solvate lithium salts. Use of polar solvents instead of nonpolar solvents in reactions involving semi-stabilized phosphoranes favours formation of Z olefin (equations 2.8, 2.10)[3,5,13,16]. This has been interpreted by invoking solvation of the oxyanion and phosphonium moieties of the betaine in polar solvents. The electrostatic attraction between the oxygen and phosphorous atoms then ceases to be an important factor in determining the most stable conformation of the betaine. Instead, the most stable conformation

has transoid solvated groups which means that the *erythro*- diastereomer is now of lower energy and Z olefin is preferentially formed (Figure 2.3).

a) In nonpolar solvents

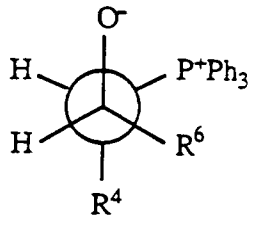

erythro- betaine

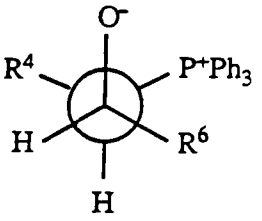

threo- betaine
(lower energy)

b) In polar solvents

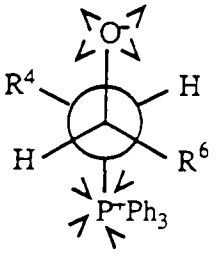

erythro- betaine
(lower energy)

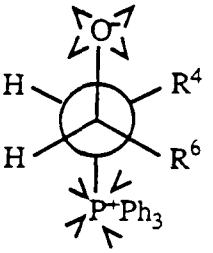

threo- betaine

Figure 2.3: Relative stabilities of *erythro*- and *threo*- betaines in polar and nonpolar solvents.

The stereochemistry, and factors which influence it, are beginning to be understood for phosphorane Wittig reactions with the unstabilized class of reagents, largely because of kinetic studies of oxaphosphetane formation and decomposition by low temperature ^{31}P NMR, and of alkene formation by low temperature ^{1}H NMR[6,17–19]. However, no intermediates have been observed by low temperature NMR in reactions with either the semi-stabilized or stabilized class of reagents[6]. An understanding of the factors influencing the steric course of these latter two classes of phosphorane Wittig reaction is limited mainly to effects of structural changes in the phosphorane.

2.1.2 Stereochemistry of the Phosphonate Wittig Reaction

A variation of the Wittig reaction involves the use of a carbanion generated from a phosphonate of general formula $(R^1O)_2P(O)CHR^2R^3$ as the reagent, instead of a phosphorane (for reviews see Refs. 20–22). It is thought that the mechanism of the phosphonate Wittig reaction is similar to that of the phosphorane Wittig reaction (Figure 2.4), though direct evidence has only been obtained supporting the existence of the cyclic oxyanion[23].

In the case of the semi-stabilizing groups R^2, R^3 as we have here in the synthesis of sterol probes **4a**, **5a** and **6a** from pregnenolone (**1**, R=H) (see Scheme 2.2), the phosphonate carbanion reagent is to be preferred over the phosphorane reagent for a number of reasons.

1. It has been found empirically that semi-stabilized phosphonate carbanions yield high E:Z alkene ratios (usually > 90:10, see equations 2.12, 2.13) compared to the corresponding phosphoranes[22].

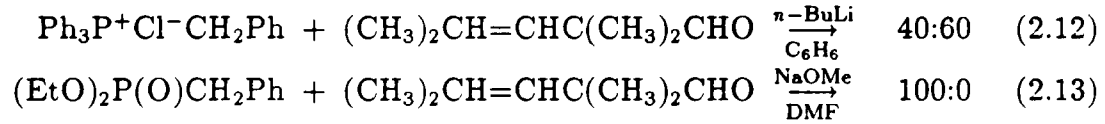

   The reason for this is not clear since the steric course of the reaction has not been followed by low temperature NMR.

2. The phosphonate carbanion is more nucleophilic than its phosphorane counterpart, since the negative charge on the α-carbon atom is not as well stabilized by the phosphorous atom in the phosphonate due to back bonding from the oxygen atom to the phosphorous atom. In practice, this means that phosphonate carbanions should react with both aldehydes and ketones whereas phosphoranes generally only react with aldehydes. Since we wish to retain the 21-methyl group found in the structure of cholesterol, our proposed starting carbonyl compound is pregnenolone (**1**, R=H), a ketone, so the enhanced reactivity of the phosphonate carbanion over the corresponding phosphorane is a definite asset.

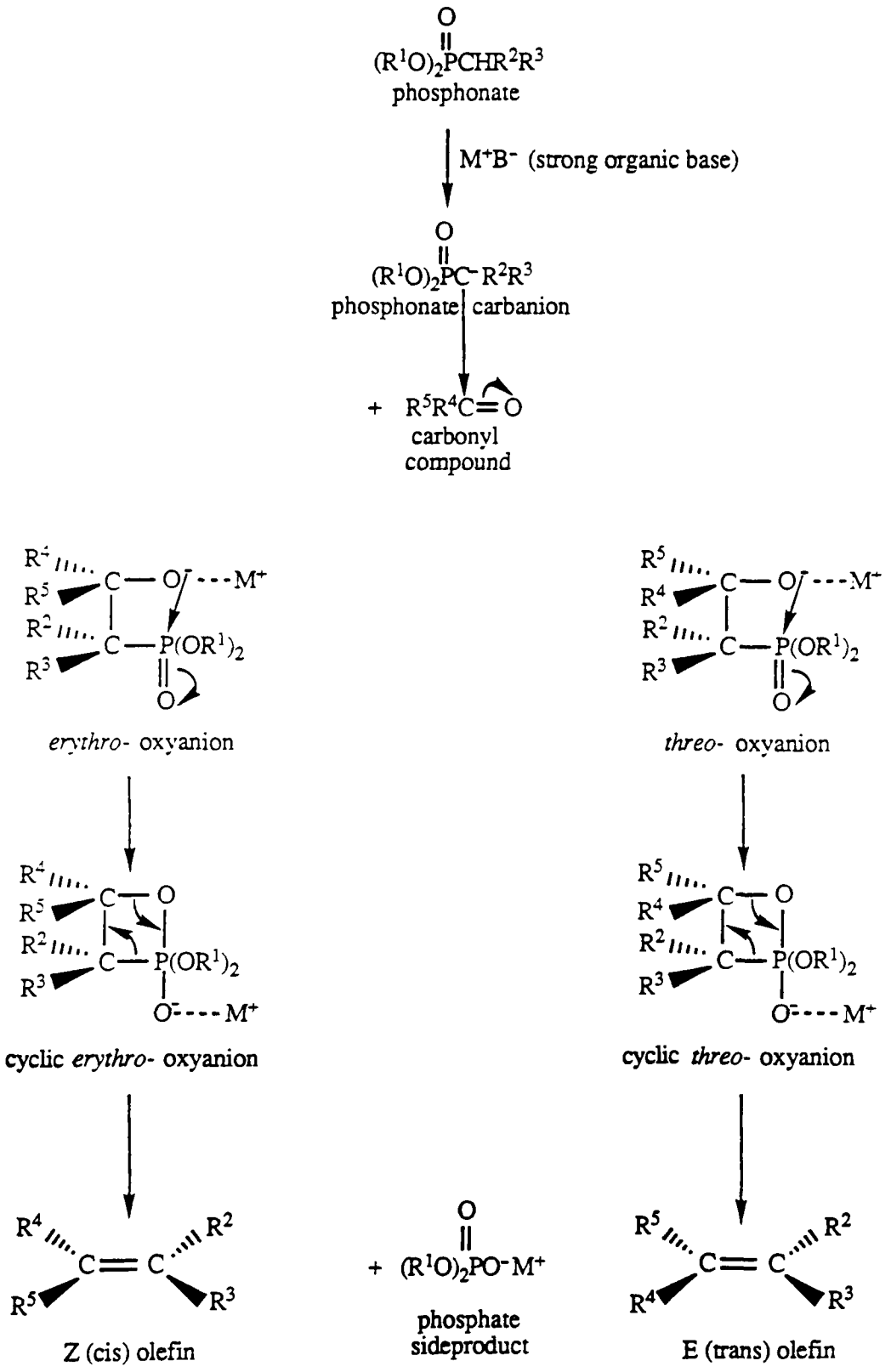

Figure 2.4: Mechanism of the phosphonate Wittig reaction.

Scheme 2.2

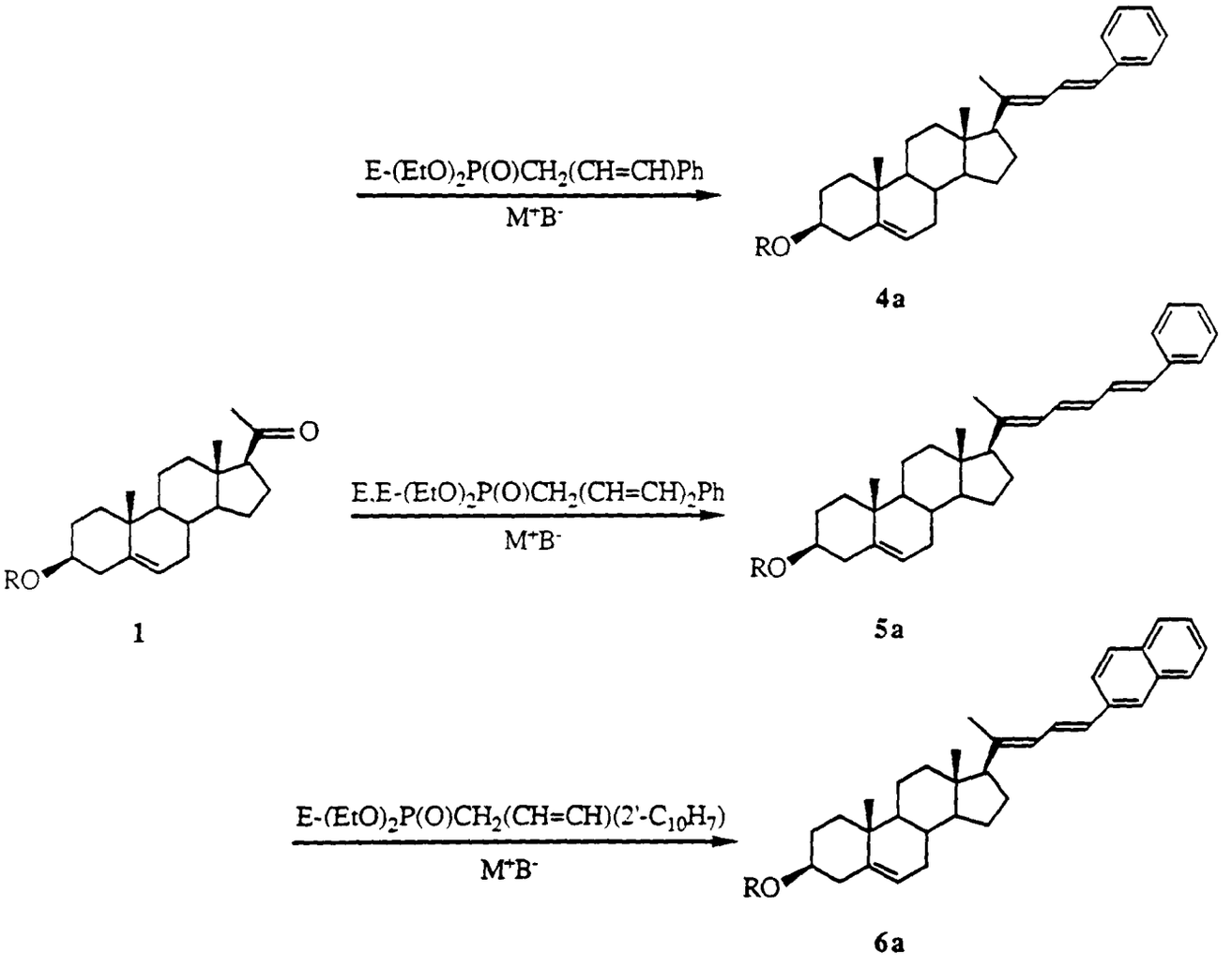
E-(EtO)2P(O)CH2(CH=CH)Ph
M+B-
RO
4a
O
RO
1
E,E-(EtO)2P(O)CH2(CH=CH)2Ph
M+B-
RO
5a
E-(EtO)2P(O)CH2(CH=CH)(2'-C10H7)
M+B-
RO
6a

A possible disadvantage of employing semi-stabilized phosphonate carbanions, however, is that the electrophilicity of the phosphorous atom is decreased compared to that of stabilized phosphonate carbanions. This could result in some difficulty in cyclization of the oxyanion. In fact, the β-hydroxy phosphonate, with little or no olefin, has been isolated from phosphonate Wittig reactions employing unstabilized phosphonate carbanions[24] (Figure 2.5). Hence it can be expected that while phosphonate Wittig reactions with semi-stabilized reagents will exhibit higher E stereoselectivity than their phosphorane counterparts, this could be at the expense of lower overall yields of olefins.

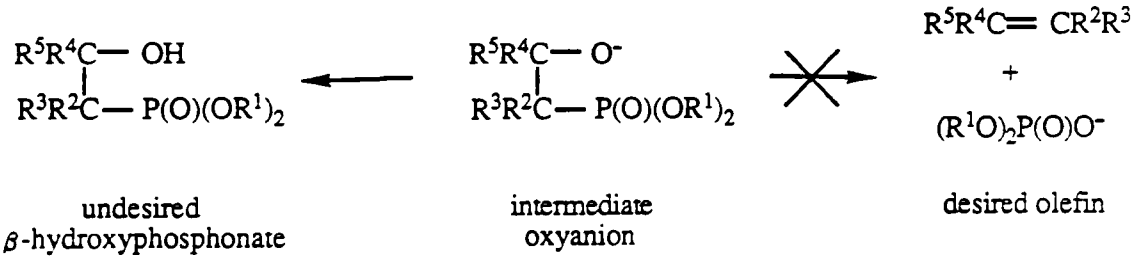

Figure 2.5: Formation of β-hydroxyphosphonate sideproducts from phosphonate Wittig reactions.

A survey of the literature of Wittig reactions performed on pregnenolone (**1**, R=H) is rather surprising in that a number of phosphorane Wittig reactions have been successful[25–34], though none with semi-stabilized ylids. In contrast, only two cases of successful phosphonate Wittig reactions on pregnenolone have been reported, and these are with the activated (stabilized) carbanions of diethylcyanomethyl phosphonate[35–38] and recently triethylphosphonoacetate[39] after a number of unsuccessful attempts[35,37,40].

On balance, it seemed that the best way to proceed with the synthesis of the cholesterol analogues **4a**, **5a** and **6a** was by the phosphonate variation of the Wittig reaction using pregnenolone (**1**, R=H) and the phosphonates shown in Scheme 2.2. Since choice of solvent and base appears to be less critical with regard to final alkene geometry in this variation of the Wittig reactions[20,41,42], solubility factors were the main consideration behind the choice of tetrahydrofuran (THF) as the solvent.

2.2 Results and Discussion

Direct Phosphonate and Phosphorane Reactions on Pregnenolone

The 3β-*t*-butyldimethylsilyl ether of pregnenolone **1** was treated with the carbanion generated from diethyl E-cinnamyl phosphonate (see Scheme 2.2) and despite the history of unsuccessful phosphonate Wittig reactions on pregnenolone and other C-20 steroidal ketones, the desired E,E-diene phenyl compound **4a** (R=$SiMe_2$*t*-Bu) was obtained, albeit in a relatively low yield of 35%. The ratio of isomers formed was 90:10 favouring the E,E-isomer, as determined by high resolution NMR. However, from nuclear Overhauser effect (nOe) experiments, it was apparent that the isomers existed about the C-23,C-24 double bond and not about the C-20,C-22 double bond which was formed in the reaction. Failure to observe a 20(22)Z alkene could be rationalized by steric hindrance from the steroid nucleus to 20(22)Z double bond formation given the bulk of the sidechain being added. On the other hand, observation of the diastereomers about the C-23,C-24 double bond suggests that the negative charge of the phosphonate carbanion was delocalized over the allylic system resulting in loss of geometrical integrity about the eventual 23(24) double bond. Similar isomerization has been observed in the allylic moieties of both ylids[1] and other phosphonate carbanions[20].

The corresponding phosphorane Wittig reaction was attempted on the 3β-*t*-butyldimethylsilyl ether of pregnenolone **1** using the ylid generated from E-cinnamyl triphenyl phosphonium bromide (see Scheme 2.1). Despite the formation of ylid, as witnessed by an intense red colouration of the reaction mixture, no reaction was observed. Considering the precedents for phosphorane Wittig reactions on pregnenolone, this lack of reactivity is probably due to the low nucleophilicity of the semi-stabilized ylid.

Despite the success of the phosphonate Wittig reaction to yield the E,E-diene phenyl compound **4a** (R=$SiMe_2$*t*-Bu), when the 3β-*t*-butyldimethylsilyl ether of pregnenolone **1** was treated with the phosphonate carbanion containing one extra

double bond in order to arrive at the E,E,E-triene phenyl compound **5a** (R=$SiMe_2$t-Bu, see Scheme 2.2), the reaction was unsuccessful. The explanation for this may be that introduction of the extra double bond into the phosphonate reagent stabilizes the carbanion to such an extent as to make it unreactive towards the rather sterically hindered C-20 keto group of pregnenolone. The corresponding phosphonate Wittig reaction to yield the E,E-diene naphthyl compound **6a** (R=$SiMe_2t$-Bu) was not attempted.

2.2.1 Synthesis of 20(22)E-α,β-unsaturated aldehyde 3a

Grignard Reaction on Pregnenolone Followed by Oxidative Rearrangement

Since a more reactive carbonyl compound was needed in order to arrive at the desired olefinic sterol derivatives **5a** and **6a**, it was decided to synthesize the 20(22)E-α,β-unsaturated aldehyde **3a**. Apart from having a more reactive carbonyl function than the 20-keto group of pregnenolone, this aldehyde is less sterically hindered for reaction with a Wittig reagent.

Synthesis of the analogous 3β-acetoxy aldehyde has been reported[43,44], the more efficient route involving a Grignard reaction and then a rearrangement of the tertiary alcohol and subsequent oxidation[43]. We adopted this route except that use of pyridinium chlorochromate[45] enabled us to perform the rearrangement and oxidation in one step (Scheme 2.3).

The *t*-butyldimethylsilyl ether of pregnenolone **1** was treated with vinyl magnesium bromide to obtain the epimeric C-20 alcohols **2a** and **2b**. The ratio of alcohols obtained was determined to be 1:9 by integration of the C-23 ^{1}H NMR peaks centred at δ 5.22 and 5.00 ppm and at δ 5.15 and 4.96 ppm. The major isomer was assigned the 20S configuration (**2b**) in keeping with the stereochemical preference reported for other Grignard reactions on C-20 steroidal ketones[43,46]. The 9:1 ratio of 20S:20R alcohols (**2b**:**2a**) is in good agreement with that observed for the analogous 3β-acetoxy compound (11:1)[43].

Treatment of the 9:1 mixture of 20S,20R-alcohols **2b** and **2a** with pyridinium

Scheme 2.3

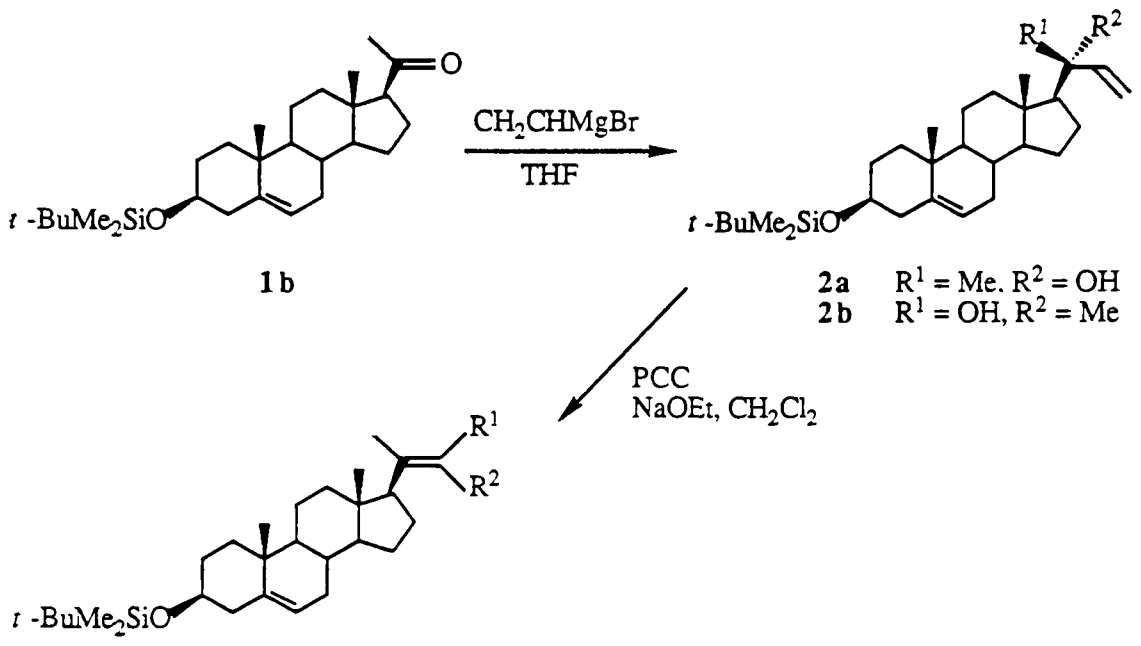

chlorochromate resulted in an 80:20 mixture of the 20(22)E- and 20(22)Z-α,β-unsaturated aldehydes **3a** and **3b** respectively. The 20(22)E- and 20(22)Z-aldehydes were assigned on the basis of their C-21 ^{1}H NMR resonances[47,48]: 20(22)E-isomer **3a**, δ 2.22 ppm; 20(22)Z-isomer **3b**, δ 1.99 ppm. The 80:20 ratio of the aldehydes was determined by integration of the C-23 ^{1}H NMR peaks at δ 10.07 [20(22)E] and δ 9.97 [20(22)Z] ppm and of the C-22 proton peaks at δ 6.05 [20(22)Z] and δ 5.95 [20(22)E] ppm.

In order to obtain some insight into the mechanism of this oxidative rearrangement, the pure 20R- and 20S-alcohols (**2a** and **2b**) were each treated with pyridinium chlorochromate and the resulting ratios of 20(22)E:20(22)Z aldehydes determined by high performance liquid chromatography (HPLC). The results are given in Table 2.1.

It can be seen that the 20R-alcohol **2a** gives the 20(22)E-aldehyde **3a** in a highly stereoselective manner, in contrast to the 20S-alcohol **2b**. This difference in behavior can be attributed to the relative arrangement of the functional groups on C-20 with respect to the D-ring of the steroid nucleus. From an X-ray crystallographic

Table 2.1: Ratios of 20(2)E-/20(22)Z-aldehydes (**3a/3b**) obtained after oxidative rearrangement of various ratios of 20R/20S-alcohols (**2a/2b**) with pyridinium chlorochromate.

2a/2b			**3a/3b**		
10	:	90	80(±1)	:	20(±1)[a]
100	:	0	98(±1)	:	2(±1)[b]
0	:	100	78(±2)	:	22(±2)[b]
10	:	90	80(±2)	:	20(±2)[c]

[a]Determined by 300 MHz ^{1}H NMR.
[b]Determined by HPLC.
[c]Calculated from ratios of aldehydes obtained by starting from pure **2a** and pure **2b**.

study[46] on the analogous 20S-ethyl compound, the position of the ethyl group was determined to be close to 180° from C-13 (when looking along the C-17, C-20 bond). The C-20 C-O bond lies over the D-ring while the 21-methyl group points out the back of the molecule. If we assume that likewise the ethylene group of the 20S- and 20R-alcohols (**2b** and **2a**) adopts an ~180° conformation from C-13 in solution, then the higher stereoselectivity of the 20R-alcohol oxidative rearrangement can be rationalized (Figure 2.6). The hydroxyl group of the 20R-alcohol **2a** would be pointing out the back of the molecule and hence it could be envisaged that the oxidative rearrangement occurs mainly by a concerted mechanism as there is little steric hindrance from neighbouring nuclei. On the other hand, the hydroxyl group of the 20S-alcohol **2b** would lie over the D-ring of the steroid nucleus as in the 20S-ethyl compound and there would be some steric hindrance to a concerted oxidative rearrangement.

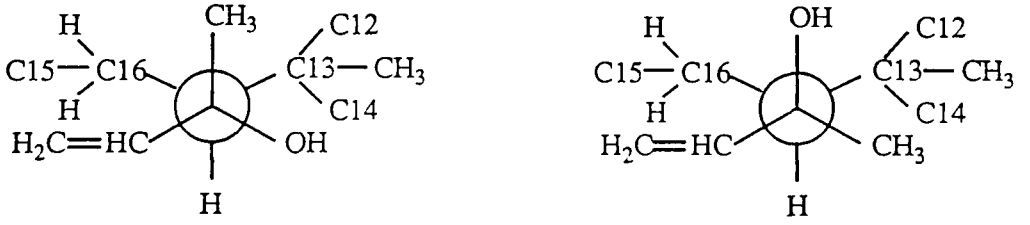

2a **2b**

Figure 2.6: Relative spatial arrangement of C-20 and C-17 substituents in the 20R- and 20S- alcohols (**2a** and **2b**) which could rationalize the difference in stereochemistry of their oxidative rearrangements by PCC.

The difference in stereoselectivities of the oxidative rearrangement of the epimeric alcohols can be seen to account for the ratio difference between the reactants and products [20S:20R alcohols in 9:1 ratio→20(22)E:20(22)Z aldehydes in 4:1 ratio]. As shown in Table 2.1, if 90% of the resultant ratio from the 20S alcohol **2b** oxidative rearrangement is added to 10% of the product ratio from the 20R alcohol **2a** oxidative rearrangement, an aldehyde ratio is arrived at (80:20) which is the same as that found experimentally for the 20S:20R alcohol (9:1) oxidative rearrangement reaction.

Phosphonate Wittig Reaction on Pregnenolone

Another route to the isomeric aldehydes **3a** and **3b** was investigated with the aim of synthesizing the 20(22)E-aldehyde **3a** more stereoselectively since only partial separation of the two diastereomers was possible by flash column chromatography, and long retention times were needed to effect separations by HPLC (see Figure 2.7). It was decided to treat the 3β-*t*-butyldimethylsilyl ether of pregnenolone **1** with the carbanion generated from diethyl 2-(cyclohexylimino)vinyl phosphonate (Scheme 2.4), which has been shown to react with C-3 and C-17 steroidal ketones[49], followed by hydrolysis of the cyclohexylimino function. As expected, this phosphonate Wittig reaction yielded predominantly the 20(22)E aldehyde **3a** (a ratio of 96:4 favouring **3a** over **3b** was determined by HPLC), though with some sacrifice in yield (see Table 2.2).

2.2.2 Phosphonate and Phosphorane Wittig Reactions on 20(22)E-aldehyde 3a

Both phosphonate and phosphorane Wittig reactions were successfully carried out on the 20(22)E-aldehyde **3a** (see Table 2.2 and Scheme 2.5). Treatment of **3a** with the carbanion generated from diethyl (2′-naphthylmethyl) phosphonate resulted in a 90:10 mixture of the E,E- and E,Z- diene naphthyl compounds **6a** and **6b** (R=$SiMe_2$*t*-Bu). The analogous reaction involving the carbanion generated from diethyl E-cinnamyl phosphonate also yielded predominantly the desired E,E,E- triene

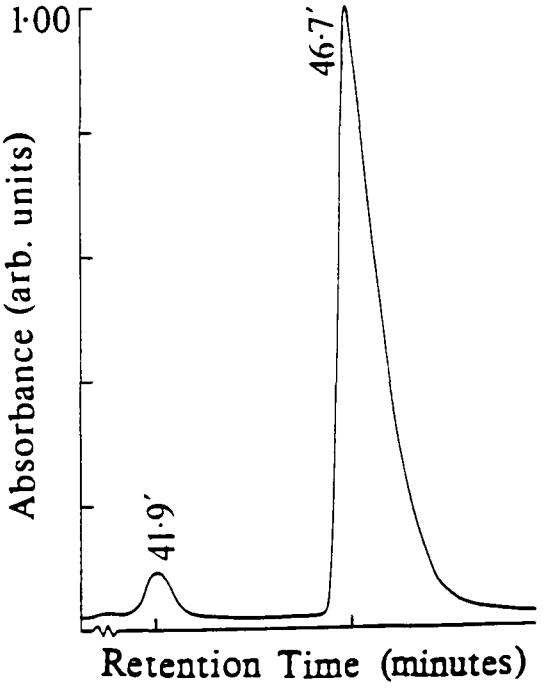

Figure 2.7: HPLC chromatogram showing separation of 20(22)Z- (r_t=41.9′) and 20(22)E- (r_t=46.7′) aldehydes (**3b** and **3a**). Beckman Ultrasphere ODS column, 10 mm × 25 cm, 3 ml/min, 100% CH_3CN, λ = 250 nm.

Scheme 2.4

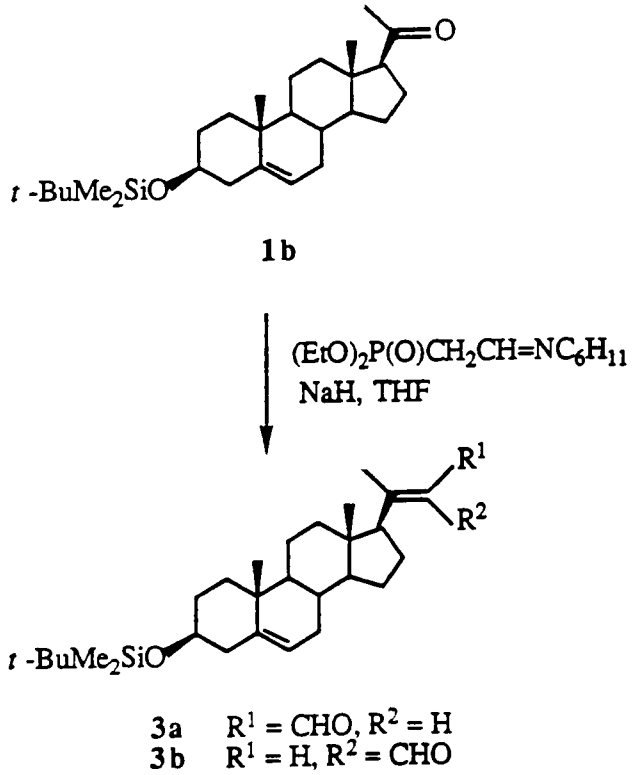

Table 2.2: Yields and E/Z ratios for various Wittig reactions on compounds **1b** and **3a**.

RR'CO	method[a]		product	yield	E/Z ratio[b,c]
		$(EtO)_2P(O)CH_2R''$			
1b	I	R″=(E)-(CH=CH)Ph[d]	**4a,b**	35	90:10[b,e]
1b	I	R″=$(CH=CH)_2$Ph[f]	no reaction		
1b	I	R″=CH=NC_6H_{11}[g]	**3a,b**	45	96:4[c]
3a	I	R″=(E)-(CH=CH)Ph	**5a,b**	40	83:17[c]
3a	I	R″=2-($C_{10}H_7$)[h]	**6a,b**	55	90:10[b]
		$Ph_3P^+CH_2R''X^-$			
1b	II	R″=(E)-(CH=CH)Ph	no reaction		
3a	II	R″=Ph	**4a,b**	75	40:60[b]
3a	II	R″=(E)-(CH=CH)Ph	**5a,b**	75	40:60[b]
3a	III	R″=(E)-(CH=CH)Ph	**5a,b**		1:99[c]

[a]Method I: phosphonate reagent, THF, room temperature for 24h. Method II: phosphorane reagent, THF, reflux for 12h. Method III: phosphorane reagent, 9:1 THF/HMPA, room temperature for 24h.
[b]Determined by 500 MHz ^{1}H NMR.
[c]Determined by HPLC.
[d]See ref 53.
[e]About C-23, C-24 double bond.
[f]90:10 mixture of 2E,4E/2Z,4E isomers.
[g]See ref 49 and 54.
[h]See ref 55.

phenyl compound **5a** with the ratio of E,E,E- to E,Z,E- trienes formed in the reaction being 83:17. The difference in the E:Z alkene ratios for these two reactions could possibly reflect steric effects on the final alkene geometry, the more sterically hindered diethyl (2′-naphthylmethyl) phosphonate carbanion giving rise to a higher proportion of the *all-trans* or E,E-alkene.

Scheme 2.5

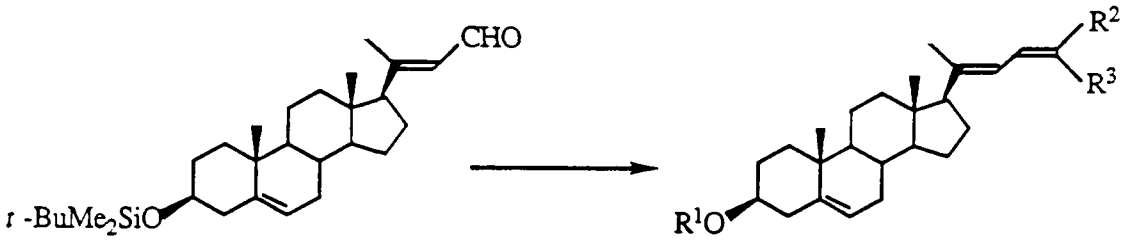

3a

4a	R^2 = Ph, R^3 = H
4b	R^2 = H, R^3 = Ph
5a	R^2 = E-(CH=CH)Ph, R^3 = H
5b	R^2 = H, R^3 = E-(CH=CH)Ph
6a	R^2 = 2′-$C_{10}H_7$, R^3 = H
6b	R^2 = H, R^3 = 2′-$C_{10}H_7$

The phosphorane Wittig reactions carried out on the 20(22)E-aldehyde **3a** gave the expected E:Z alkene product ratios of approximately 1:1, typical of reactions involving semi-stabilized triphenyl phosphoranes (Table 2.2). Through the use of a 1:9 ratio of hexamethylphosphoramide (HMPA)/THF as solvent instead of the usual 100% THF, the Z-stereoselectivity of the reaction between the ylid generated (using *n*-BuLi) from E-cinnamyl triphenylphosphonium bromide, and the 20(22)E-aldehyde **3a**, increased from a 40:60 ratio of E:Z alkenes to a 1:99 ratio. Use of HMPA as a co-solvent has been shown[50–52] to increase Z-stereoselectivity of phosphorane Wittig reactions. It has been postulated that this is due to the ability of HMPA to act as a lithium cation complexing agent, hence accelerating the formation of olefin from the betaine-lithium bromide complex and producing the more kinetically favoured Z-olefin.

2.2.3 Purification and Characterization of the Olefinic Sterol Probes

As with the diastereomeric aldehydes **3a** and **3b**, limited success was achieved by flash column chromatography in separating the isomeric pairs of olefins **4a/4b**, **5a/5b** and **6a/6b** (R=H). HPLC proved to be the method of choice to obtain pure **4a** despite the necessity for long retention times and double passes through the C_{18} reversed phase column (Figure 2.8). The HPLC purification of the E,E,E-triene phenyl probe **5a** was also challenging due to the presence of four diastereomers, the minor isomers perhaps arising from some scrambling of the double bond geometry in the phosphonate carbanion reagent, as witnessed in its reaction with pregnenolone. Separation of the E,E and E,Z diene 2′-naphthyl probes **6a** and **6b** was unsuccessful by HPLC, even when collecting only a portion of the unsymmetrical peak (Figure 2.8). This is possibly due to some aggregation of the naphthalene derivatives as they are passed through a nonpolar C_{18} column with a polar solvent mixture of methanol and water. Perhaps normal phase HPLC would have been successful; however, separation was finally achieved by fractional crystallization.

The double-bond geometry of the olefinic sterols **4a**, **4b**, **5a**, **5b**, **6a** and **6b** (R=H) was determined by high resolution NMR on the basis of ^{1}H-^{1}H shift-correlated spectra (COSY), selected nOe difference experiments and spectral simulation of the olefinic region of a one-dimensional (1D) ^{1}H spectrum of a mixture of the E,E,E- and E,Z,E- triene phenyl sterols **5a** and **5b**. This is presented in detail in the following chapter. Ratios of the isomeric olefins obtained in the various Wittig reactions were determined by a combination of HPLC and high resolution NMR experiments (Table 2.2).

A summary of the overall synthetic pathway to the olefinic sterol probes is presented in Scheme 2.6.

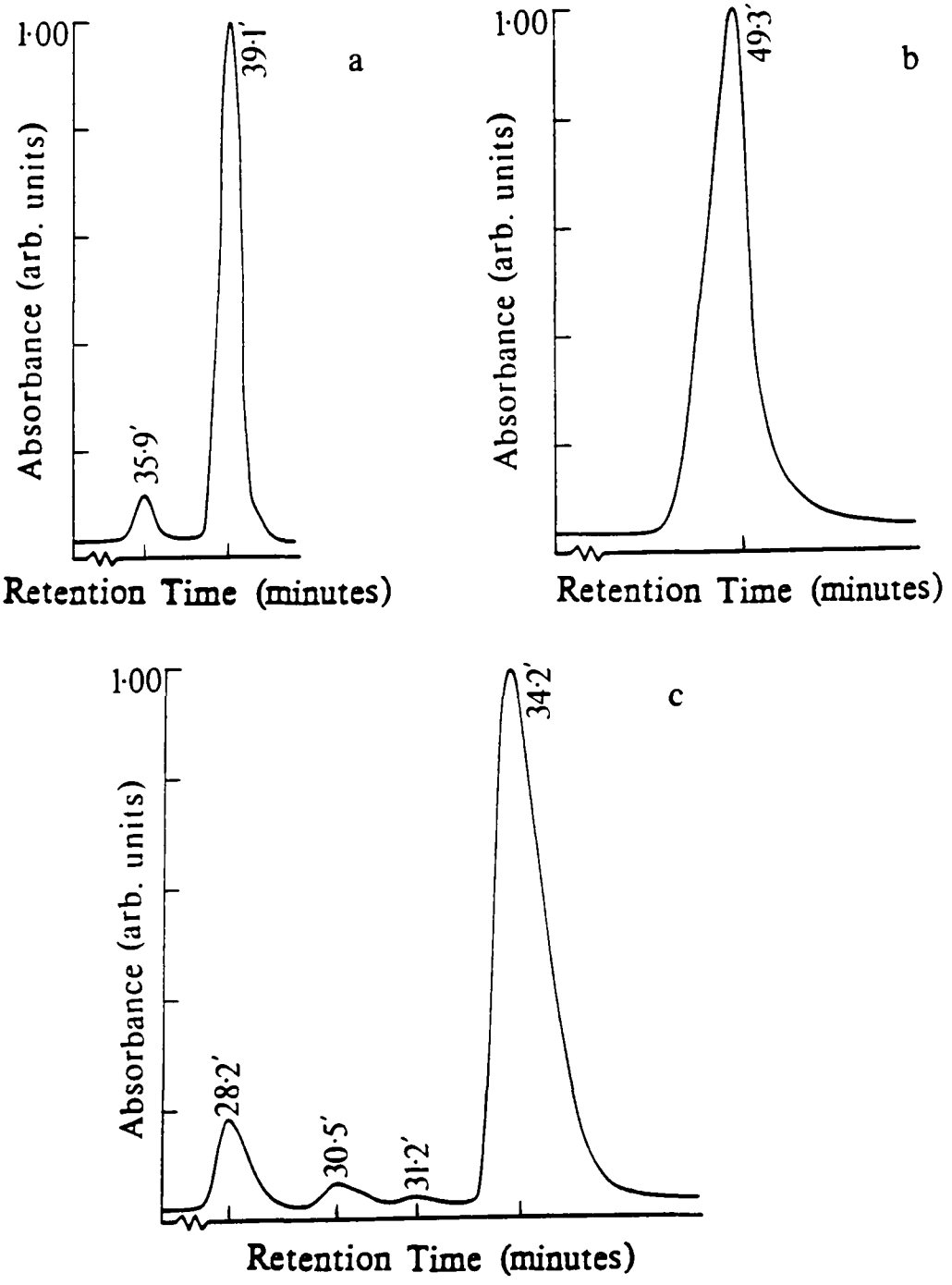

Figure 2.8: HPLC chromatograms for semi-preparative purification of 4a, 5a and 6a using a Beckman Ultrasphere ODS column, 10 mm × 25 cm, 3 ml/min. a) 4a (r_t = 39.1′, 92% MeOH/8% H_2O, λ = 300 nm); b) 6a contaminated with 6b (r_t = 49.3′, 95% MeOH/5% H_2O, λ = 340 nm) – see text; c) 5a (r_t = 34.2′, 98% CH_3CN/2% H_2O, λ = 315 nm).

Scheme 2.6

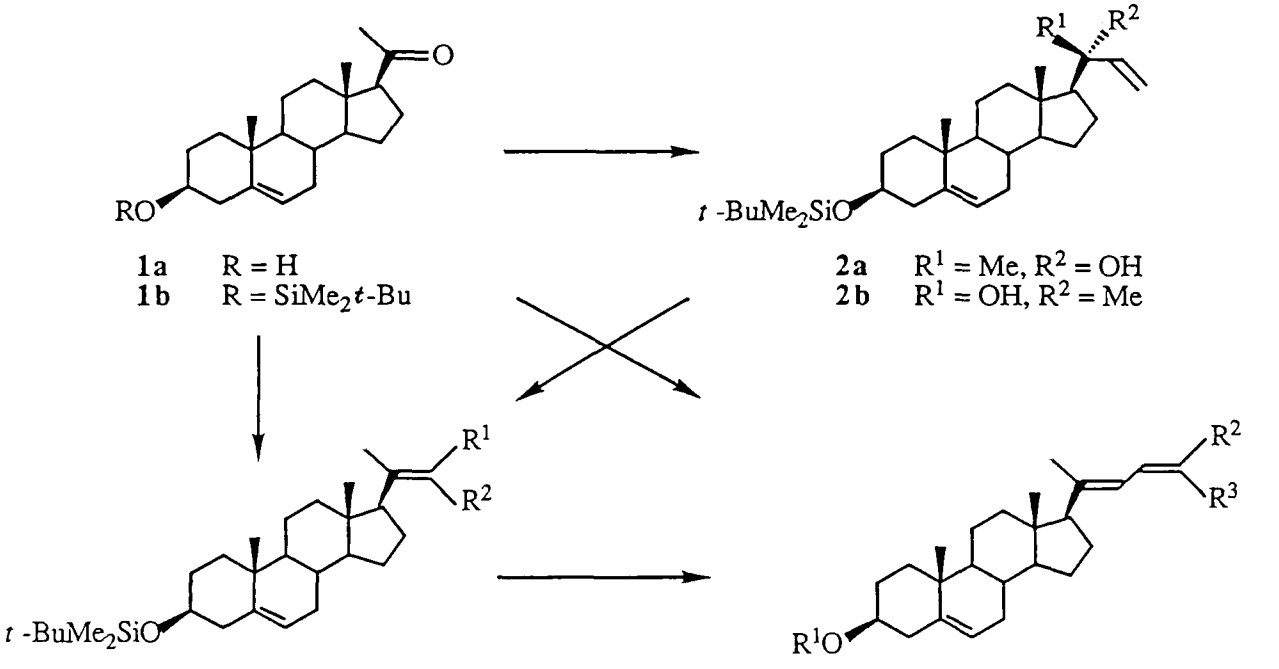

1a R = H
1b R = $SiMe_2t$-Bu

2a R^1 = Me, R^2 = OH
2b R^1 = OH, R^2 = Me

3a R^1 = CHO, R^2 = H
3b R^1 = H, R^2 = CHO

4a R^2 = Ph, R^3 = H
4b R^2 = H, R^3 = Ph
5a R^2 = E-(CH=CH)Ph, R^3 = H
5b R^2 = H, R^3 = E-(CH=CH)Ph
6a R^2 = 2'-$C_{10}H_7$, R^3 = H
6b R^2 = H, R^3 = 2'-$C_{10}H_7$

2.3 Experimental Section

Melting points were determined on a Fisher-Johns melting point apparatus and are uncorrected. Spectra were obtained on the following instruments: Bruker AM-500, AM-200 and Varian XL300 (^{1}H and ^{13}C NMR), Varian Cary 219 (UV), Perkin-Elmer MPF-44A (fluorescence), Perkin-Elmer 23 Polarimeter (rotations) and a Vacuum Generator VG 7070E (MS). The ionizing voltage for MS was 70 eV

For flash column chromatography Terochem Silica Gel 1918 (equivalent to Merck 9385, 20-45 μm) was used. Thin layer chromatography (TLC) was done on Merck 60 nonfluorescent silica gel plates which were visualized by spraying with 5% sulfuric acid in ethanol and heating. Analytical and preparative HPLC was performed on a Varian Vista 5500 Liquid Chromatograph with a Varian DS604 data system.

2.3.1 Preparation of Phosphonates

Diethyl (E)-Cinnamylphosphonate. Equimolar amounts of triethyl phosphite and E-cinnamyl bromide were heated under reflux at 160°C for 10 h. The ethyl bromide evolved was condensed in an acetone/dry ice cold finger and the reaction mixture was distilled to give pure diethyl(E)-cinnamyl phosphonate. bp 147.0-148.5°C (1.0 mm); ^{1}H NMR (300 MHz): δ 1.29 (t, 6H, J = 7.1 Hz, -OCH$_2$C*H*$_3$), 2.74 (d of d of d, 2H, J = 1.2, 7.5, 22.1 Hz, -C*H*$_2$-P), 4.10 (m, 4H, -OC*H*$_2$CH$_3$), 6.15 (m, 1H, -CH=C*H*-CH$_2$P), 6.51 (d of d, 1H, J = 5.0, 15.7 Hz, -C*H*=CH-CH$_2$P), 7.18→ 7.35 (m, 5H, aromatic protons). Anal. Calcd. for $C_{13}H_{19}O_3P$: C, 61.41; H, 7.53. Found: C, 61.19; H, 7.39.

Diethyl (2-naphthylmethyl)phosphonate. This phosphonate was prepared by a reported[55] method. bp 168.0-169.0°C (1.2 mm); ^{1}H NMR (300 MHz): δ 1.22 (t, 6H, J = 7.1 Hz, -OCH$_2$C*H*$_3$) 3.30 (d, 2H, J = 21.7 Hz, -C*H*$_2$-P), 4.00 (m, 4H, -OC*H*$_2$CH$_3$), 7.40→7.47, (m, 3H, aromatic protons), 7.73→7.81 (m, 4H, aromatic protons).

Diethyl (2E,4E)-and (2Z,4E)-2,4-pentadienylphosphonate. This phosphonate was prepared from (E,E)-cinnamylidene acetic acid as outlined below.

Methyl (E,E)-5-Phenyl-2,4-pentadiene-1-oate. (E,E)-Cinnamylidene acetic acid (Pfitzer and Bauer, 10.0 g) was dissolved in anhydrous MeOH (200 ml), and dry HCl (~10 g) was added. The reaction mixture was stirred at room temperature for 20 h, and then the MeOH was evaporated under reduced pressure. The product was extracted with *n*-pentane through a thimble and allowed to crystallize. Total yield of the ester was 96% (10.4 g) after two crops of crystals. mp 67.0–68.0°C (Lit.[56] mp 71°C), m/z = 188 (M^+), 157 (M^+–OCH_3), 129 (M^+–CO_2CH_3). ^{1}H NMR (300 MHz): δ 3.80 (s, 3H, CO_2CH_3), 6.03 (d, 1H, J = 15.9 Hz, H-2), 6.86→6.92 (m, 2H, H-4, H-5), 7.33→7.52 (m, 6H, 5 aromatic protons and H-3). Anal. Calcd for $C_{12}H_{12}O_2$: C, 76.57; H, 6.43. Found: C, 76.53; H, 6.43.

(E,E)-5-Phenyl-2,4-pentadien-1-ol. The 1-methyl ester from above (0.94 g) was added to benzene (Na dried, 11 ml) under nitrogen and then diisobutylaluminum hydride (1.0M solution in toluene, 10.0 ml, 2.0 eq) was added slowly over 1 h. The reaction mixture was then heated at 45 °C for 3 h until no starting material remained. After the mixture was cooled, dry MeOH (1.04 ml in 1.14 ml toluene, 6.0 eq) and then H_2O (0.55 ml in 1.14 ml MeOH, 6.0 eq) were added. The gel which formed upon addition of H_2O was filtered, washed with MeOH, evaporated to dryness, extracted through a thimble with *n*-pentane and allowed to crystallize to yield 0.70 g of the alcohol (87% yield). mp 79.5–81.5°C (Lit.[57] mp 80–81°C, Lit.[58] mp 73–78°C), m/z = 160 (M^+), 142 (M^+–H_2O). ^{1}H NMR (300 MHz): δ 4.26 (d of d, J = 7, 2 Hz, CH_2OH). Anal. Calcd for $C_{11}H_{12}O$: C, 82.46; H, 7.55. Found: C, 82.21; H, 7.43.

1-Bromo-5-phenyl-2,4-pentadiene. (E,E)-5-Phenyl-2,4-pentadien-1-ol (0.95 g) was dissolved in dry ether (20 ml), cooled to 0 °C, and phosphorous tribromide (1.62 ml, 1.05 eq) was added dropwise. After stirring at 0°C for 1.5 h, the reaction mixture was poured onto ice, extracted with ether, washed with $NaHCO_3$, and dried over $MgSO_4$. After evaporation of the solvent under reduced pressure, the cream-coloured residue was ground to a powder and dried under vacuum (over KOH) to

give 1.06 g (80% yield) of slightly contaminated 1-bromo-5-phenyl-2,4-pentadiene, which was used within three days in the following reaction. m/z (under chemical ionization conditions) = 225, 223 (MH^+), 224, 222 (M^+). ^1H NMR (300 MHz): δ 4.09 (d of d, J = 7.7, 2.0 Hz, CH_2Br).

Diethyl 5-Phenyl-2,4-pentadien-1-yldiethyl phosphonate. The slightly contaminated 1-bromo-5-phenyl-2,4-pentadiene (3.48 g) was heated at 160°C with triethyl phosphite (3.00 ml, 1.12 eq) for 20 h. The reaction mixture was distilled [153-158°C (0.1 mm)] to give 2.06 g (47% yield) of a 90:10 mixture of the 2E,4E/2Z,4E isomers as determined by 200 MHz ^1H NMR. This mixture of isomers is suspected to have originated from the bromination reaction above. **2E,4E isomer**: ^1H NMR (200 MHz): δ 1.26 (t, 6H, J = 7.1 Hz, OCH_2CH_3), 2.64 (d of d, 2H, J = 22.9, 7.7 Hz, CH_2P), 4.05 (m, 4H, OCH_2CH_3), 5.72 (m, 1H, H-2), 6.28 (d of d of d, 1H, J = 15.1, 10.2, 5.0 Hz, H-3), 6.44 (d of d, 1H, J = 15.7, 2.4 Hz, H-5), 6.71 (d of d, 1H, J = 15.5, 10.4 Hz, H-4), 7.14→7.38 (m, aromatic protons). **2Z,4E isomer**: ^1H NMR (200 MHz): δ 2.79 (d of d, 2H,J = 23, 8 Hz, CH_2P), 5.48 (d of d, 1H,J = 11, 8 Hz, H-2), 6.96 (d of d, 1H,J = 15, 10 Hz, H-4).

2.3.2 Wittig Reactions

General Conditions of Phosphonate Wittig Reaction for Stereoselective Synthesis of E-Olefins (Method I)

To a cooled solution (-78°C) of the phosphonate (1.1 eq) in THF was added *n*-BuLi (1.1 eq) and, after stirring for 45 min, a solution of the carbonyl compound in THF was added. The reaction mixture was stirred at -78°C for a further 45 min, allowed to come to room temperature and then stirred for 24 h. The solvent was evaporated and the residue taken up in ether and worked up in the usual way. Chromatography of the crude product on silica gel (hexane) gave a mixture of E/Z olefins (see Table 2.2 for isomer ratios).

General Conditions of Phosphorane Wittig Reaction (Method II)

The procedure was identical to that of Method I except that the appropriate phosphonium salt was used instead of the phosphonate, and the reaction mixture was not stirred at room temperature but refluxed for 12 h (see Table 2.2 for isomer ratios).

General Conditions of Phosphorane Wittig Reaction for Stereoselective Synthesis of Z-Olefins (Method III)

The above procedure was followed except that the solvent for the reaction was 90% THF/10% hexamethylphosporamide (HMPA) and the reaction mixture was not refluxed but kept stirring at room temperature for 24 h (see Table 2.2 for isomer ratios).

2.3.3 Preparation of Steroidal Compounds

Pregnenolone 3β-*t*-Butyldimethylsilyl Ether 1,R=SiMe$_2$*t*-Bu from 1,R=H. Pregnenolone (1,R=H, 22.6 g) was treated with *t*-butyldimethyl-silyl chloride (13.1 g, 1.2 eq) and imidazole (11.9 g, 2.4 eq) in dry DMF for 20 h at room temperature. The resulting precipitate was filtered and recrystallized from $CHCl_3$ to give pure 1,R=SiMe$_2$*t*-Bu. The filtrate was extracted with ether, washed with H_2O, dried over $MgSO_4$ and the solvent removed under reduced pressure. The resulting white powder was chromatographed on silica gel (hexane/ethyl acetate, 98:2) to give more protected pregnenolone 1,R=SiMe$_2$*t*-Bu (total yield 28.3 g, 92%). mp 164.5–165.0°C, (Lit.[59] mp 162-164°C); m/z = 415 (M^+–CH_3), 373 [M^+–$C(CH_3)_3$], $[\alpha]_D^{25}$ +23° (c 1.29, CH_2Cl_2); ^{1}H NMR (300 MHz) δ 0.06 [s, 6H, $Si(CH_3)_2$], 0.63 (s, 3H, C-18 methyl), 0.89 [s, 9H, $C(CH_3)_3$], 1.00 (s, 3H, C-19 methyl), 2.12 (s, 3H, C-21 methyl), 3.48 (m, 1H, H-3α), 5.34 (br d, 1H, H-6); ^{13}C NMR (75 MHz) δ -4.61 [$Si(CH_3)_2$], 25.90 [$C(CH_3)_3$], 209.58 (C-20). Anal. Calcd for $C_{27}H_{46}O_2Si$: C, 75.27; H, 10.77. Found: C, 75.02; H, 10.79.

General Deprotection Procedure. The *t*-butyldimethylsilyl ether derivatives of the unsaturated alcohols (**4a**, **4b**, **5a**, **5b**, **6a**, **6b**) were treated with tetra-*n*-butylammonium fluoride[60] (1.0 M solution in THF, 4 eq) in dry THF for 20 h at room temperature. After removal of the solvent, the residue was taken up in ethyl acetate, washed with water, dried over $MgSO_4$ and the ethyl acetate evaporated under reduced pressure. The crude solid was chromatographed over silica gel (hexane/ethyl acetate, 88:12) to give quantitative yields of the corresponding C-3 alcohols.

(20R)- and (20S)-20-Vinylpregn-5-ene-3β,20-diol 3β-*t*-Butyldimethyl Silyl Ether (2a and 2b) from 1(R=SiMe$_2$*t*-Bu). To a cooled solution (-78°C) of the *t*-butyldimethylsilyl ether of pregnenolone (**1**, 15.7 g) in THF was added vinyl magnesium bromide (1 M solution in THF, 90 ml, 2.5 eq) and the reaction mixture was stirred at -78°C for 1 h and then at room temperature for 24 h. Hydrolysis with a saturated solution of NH_4Cl (0 °C), extraction with ether, drying over potassium carbonate and evaporation of the solvent gave the crude product which was purified by chromatography on silica gel (hexane, hexane/ethyl acetate, 98.5:1.5). The fractions containing solely the 20R- and 20S-isomers (**2a** and **2b** respectively) were combined separately; total yield of C-20 alcohol was 14.6 g (87%). ^{1}H NMR (300 MHz) on partially purified reaction product (starting material removed) determined the ratio of the epimers to be 1:9 by integration of the H-23 peaks (RCH=CH_2) centered at δ 5.22 and 5.15 ppm and at δ 5.00 and 4.96 ppm. The major isomer was assigned the 20S configuration (**2b**) in line with reported epimer ratios[43,46] for other Grignard reactions on 20-keto steroids.

20R-Epimer (2a). mp 192–194.5°C; m/z = 443 (M^+–CH_3), 401 [M^+–$C(CH_3)_3$]; $[\alpha]_D^{22}$ -26° (c 0.24, $CHCl_3$); ^{1}H NMR (500 MHz) δ 0.053 [s, 6H, $Si(CH_3)_2$], 0.770 (s, 3H, C-18 methyl), 0.886 [s, 9H, $C(CH_3)_3$], 0.983 (s, 3H, C-19 methyl), 1.538 (s, 3H, C-21 methyl), 3.48 (m, 1H, H-3α), 5.00 (d, 1H, J = 10.7 Hz, H-23), 5.22 (d, 1H, J = 17.2 Hz, H-23), 5.31 (br d, 1H, H-6), 6.03 (d of d, 1H, J = 17.3, 10.7 Hz, H-22); ^{13}C NMR (125 MHz) δ 13.35 (C-18), 22.40 (C-16), 29.93 (C-21), 58.98 (C-17), 75.42 (C-20), 109.78 (C-23), 146.24 (C-22). Anal. Calcd for $C_{29}H_{50}O_2Si$: C, 75.90; H, 10.99. Found: C, 75.75; H, 11.01.

20S-Epimer (2b). mp 157-158°C; m/z = 443 (M^+-CH_3), 401 [M^+-$C(CH_3)_3$]: $[\alpha]_D^{25}$ -52° (c 1.07, CH_2Cl_2); ^{1}H NMR (500 MHz) δ 0.055 [s, 6H, $Si(CH_3)_2$], 0.830 (s, 3H, C-18 methyl), 0.888 [s, 9H, $C(CH_3)_3$], 0.999 (s, 3H, C-19 methyl), 1.542 (s, 3H, C-21 methyl), 3.48 (m, 1H, H-**3a**), 4.96 (d of d, 1H, J = 10.8, 1.3 Hz, H-23), 5.15 (d of d, 1H, J = 17.3, 1.2 Hz, H-23), 5.31 (br d, 1H, H-6), 5.98 (d of d, 1H, J = 17.3, 10.8 Hz, H-22); ^{13}C NMR (125 MHz) δ 13.80 (C-18), 23.21 (C-16), 28.78 (C-21), 59.47 (C-17), 75.73 (C-20), 110.22 (C-23), 146.12 (C-22). Anal. Calcd for $C_{29}H_{50}O_2Si$: C, 75.90; H, 10.99. Found: C, 75.80; H, 11.11.

(20(22)E)- and (20(22)Z)-24-Norchola-5,20(22)-dien-23-al, 3β-*t*-Butyldimethylsilyl Ether (3a and 3b) from 2a and 2b. To a suspension of pyridinium chlorochromate (12.0 g, 2 eq) and sodium acetate (4.5 g, 2 eq) in CH_2Cl_2 was added a solution of the 1:9 mixture of the 20R/20S alcohols (**2a** and **2b**, 12.9 g) in CH_2Cl_2. After stirring at room temperature for 20 h, the solvent was evaporated and the residue taken up in ether, washed with saturated $NaHCO_3$ and brine, and dried over $MgSO_4$. The crude solid obtained after removal of the solvent was chromatographed on silica gel (hexane, hexane/ethyl acetate, 99:1). Those fractions containing solely the 20(22)Z- or 20(22)E-isomers were combined separately giving a total yield of aldehydes of 88% (**3a**, **3b** 11.3 g). The E and Z aldehydes were assigned on the basis of their ^{1}H and ^{13}C 21-methyl NMR resonances: δ 2.20 (E) and 1.99 (Z)[47,48]; δ 19.36 (E) and 24.54 (Z). The ratio of diastereomeric aldehydes was determined by integration of the H-23 peaks at δ 10.07 (E) and 9.97 (Z) and the H-22 peaks at δ 6.05 (Z) and 5.95 (E) to be 80±1:20±1 as E:Z.

The oxidation procedure described above was carried out on both the pure 20R-alcohol (**2a**) and on the pure 20S-alcohol (**2b**) and the ratio of resultant aldehydes determined on the crude products by HPLC (Varian MCH-5NCAP column, 4.6 mm x 15 cm, 100% MeOH, 254 nm). The results are summarized in Table 2.1.

(20(22)E)- and (20(22)Z)-24-Norchola-5,20(22)-dien-23-al, 3β-*t*-Butyldimethylsilyl Ether (3a and 3b) from 1,R=$SiMe_2$*t*-Bu. The *t*-butyldimethylsilyl ether of pregnenolone (**1**, 2.9 g) was treated with diethyl 2-(cyclohexylimino)-vinyl phosphonate[49,54] (1.1 eq) and NaH (50% dispersion in oil, 1.1 eq) in THF initially at 0°C and then at reflux temperature for 12 h. A yellow-green colour

developed upon heating. The reaction mixture was diluted with water and extracted with ether. Hydrolysis of the crude product and chromatography on silica gel (hexane, hexane/ethyl acetate, 96:4) gave a 45% yield of the diastereomeric 20(22)E/20(22)Z-aldehydes (**3a** and **3b**, 1.40 g). The ratio of aldehydes was determined by HPLC (Varian SPC-18 column, 4.6 mm x 15 cm, 100% CH_3CN, 250 nm) to be 20(22)E:20(22)Z = 96:4.

20(22)E-Isomer (3a). mp 145–146.5°C; m/z = 456 (M^+), 441 (M^+–CH_3), 399 [M^+–$C(CH_3)_3$]; λ_{max}^{abs} = 248 nm ($CHCl_3$); ^{1}H NMR (300 MHz) δ 0.06 [s, 6H, $Si(CH_3)_2$], 0.62 (s, 3H, C-18 methyl), 0.89 [s, 9H, $C(CH_3)_3$], 1.01 (s, 3H, C-19 methyl), 2.20 (s, 3H, C-21 methyl), 3.49 (s, 1H, H-3α), 5.35 (br d, 1H, H-6), 5.95 (d, 1H, J = 7.8 Hz, H-22), 10.07 (d, 1H, J = 8.0 Hz, H-23); ^{13}C NMR (125 MHz) δ 19.36 (C-21), 127.99 (C-22), 164.24 (C-20). Anal. Calcd. for $C_{29}H_{48}O_2Si$: C,76.32; H, 10.53. Found: C, 75.80; H, 10.72.

20(22)Z-Isomer (3b). mp 118-119°C; m/z = 456 (M^+), 441 (M^+–CH_3), 399 [M^+–$C(CH_3)_3$]; $[\alpha]_D^{25}$ -102° (c 0.66, $CHCl_3$); ^{1}H NMR (500 MHz) δ 0.059 [s, 6H, $Si(CH_3)_2$], 0.698 (s, 3H, C-18 methyl), 0.890 [s, 9H, $C(CH_3)_3$], 1.009 (s, 3H, C-19 methyl), 1.992 (s, 3H, C-21 methyl), 3.48 (m, 1H, H-3α), 5.33 (br d, 1H, H-6), 6.05 (d, 1H, J = 8.0 Hz, H-22), 9.97 (d, 1H, J = 8.3, H-23); ^{13}C NMR (125 MHz) δ 24.54 (C-21), 131.59 (C-22), 164.11 (C-20), 191.16 (C-23). Anal. Calcd for $C_{29}H_{48}O_2Si$: C, 76.32; H, 10.53. Found: C, 76.06; H, 10.65.

(20(22)E,23E)-24-Phenylchola-5,20(22),23-trien-3β-ol (4a, R^1=H). mp 141.0-142.5 °C; m/z = 416 (M^+); $[\alpha]_D^{25}$ -30° (c 0.19, CH_2Cl_2); λ_{max}^{abs} = 280, 295, 306 nm (MeOH); λ_{max}^{em} = 352 nm (MeOH, λ_{ex} = 300nm); ^{1}H NMR (500 MHz) δ 0.598 (s, 3H, C-18 methyl), 1.009 (s, 3H, C-19 methyl), 1.896 (s, 3H, C-21 methyl), 3.526 (m, 1H, H-3α), 5.365 (br d, 1H, H-6), 6.074 (br d, 1H, J = 11.0 Hz, H-22), 6.466 (d, 1H, J = 15.6 Hz, H-24), 7.083 (d of d, 1H, J = 11.0, 15.6 Hz, H-23), 7.182 (t, 1H, H-4′), 7.295 (t, 2H, H-3′ and H-5′), 7.400 (d, 2H, H-2′ and H-6′); ^{13}C NMR (125 MHz) δ 13.05 (C-18), 18.71 (C-21), 19.44 (C-19), 121.60 (C-6), 125.73 (C-22, C-24), 126.08 (C-2′, C-6′), 126.90 (C-4′), 128.54 (C-3′, C-5′), 130.03 (C-23), 138.18

(C-1′), 139.91 (C-20), 140.84 (C-5). Anal. Calcd for $C_{30}H_{40}O$: C, 86.48; H, 9.68. Found: C, 86.24; H, 9.78.

(20(22)E,23Z)-24-Phenylchola-5,20(22),23-trien-3β-ol (4b, R¹=H). m/z = 416 (M^+); ^{1}H NMR (500 MHz) δ 0.614 (s, 3H, C-18 methyl), 1.014 (s, 3H, C-19 methyl), 1.869 (s, 3H, C-21 methyl), 3.491 (m, 1H, H-3α), 5.357 (br d, 1H, H-6) 6.343 (br d, 1H, J = 11.3 Hz, H-22), 6.444 (d, 1H, J = 11.3 Hz, H-24), 6.506 (d of d, 1H, J = 11.3, 11.3 Hz, H-23), 7.211 (t, 1H, H-4′), 7.32 (t, 2H, H-3′ and H-5′), 7.34 (d, 2H, H-2′ and H-6′). ^{13}C NMR (125 MHz) δ 13.17 (C-18), 18.58 (C-21), 19.44 (C-19), 121.60 (C-6), 121.84 (C-22), 126.52 (C-2′, C-6′), 127.36 (C-4′), 128.13 (C-3′, C-5′), 129.13 (C-23, C-24), 138.06 (C-1′), 140.84 (C-5), 141.49 (C-20). Anal. Calcd. for $C_{30}H_{40}O$: C, 86.48; H, 9.68. Found: C, 86.09; H, 9.70.

(20(22)E,23E,25E)-26-Phenyl-27-norcholesta-5,20(22),23,25-tetraen-3β-ol (5a, R¹=H). mp 171.5–173.0°C; m/z = 442 (M^+); $[\alpha]_D^{25}$ -7° (c 0.15, CH_2Cl_2); λ_{max}^{abs} = 319, 332, 347 nm (THF); λ_{max}^{em} = 390 nm (THF, λ_{ex} = 332 nm); ^{1}H NMR (500 MHz) δ 0.589 (s, 3H, C-18 methyl), 1.013 (s, 3H, C-19 methyl), 1.848 (s, 3H, C-21 methyl), 3.530 (m, 1H, H-3α), 5.361 (br d, 1H, H-6), 6.007 (br d, 1H, J = 11.1 Hz, H-22), 6.322 (d of d, 1H, J = 10.1, 14.7 Hz, H-24), 6.507 (d, 1H, J = 15.2 Hz, H-26), 6.641 (d of d, 1H, J = 11.1, 14.7 Hz, H-23), 6.883 (d of d, 1H, J = 10.1, 15.2 Hz, H-25), 7.189 (t, 1H, H-4′), 7.299 (t, 2H, H-3′ and H-5′), 7.389 (d, 2H, H-2′ and H-6′); ^{13}C NMR (125 MHz) δ 13.05 (C-18), 18.67 (C-21), 19.44 (C-19), 121.59 (C-6), 125.77 (C-22), 126.17 (C-2′, C-6′), 127.13 (C-4′), 128.59 (C-3′, C-5′), 129.85 (C-25), 130.28 (C-23), 130.88 (C-24), 130.93 (C-26), 137.74 (C-1′), 140.20 (C-20), 140.84 (C-5). Anal. Calcd for $C_{32}H_{42}O$: C, 86.82; H, 9.56. Found: C, 86.51; H, 9.60.

(20(22)E,23Z,25E)-26-Phenyl-27-norcholesta-5,20(22),23,25-tetraen-3β-ol (5b, R¹=H). m/z = 442 (M^+); ^{1}H NMR (500 MHz) δ 0.594 (s, 3H, C-18 methyl), 0.997 (s, 3H, C-19 methyl), 1.820 (s, 3H, C-21 methyl), 3.530 (m, 1H, H-3a), 5.361 (br d, 1H, H-6), 6.101 (d of d, 1H, J = 11.2, 11.1 Hz, H-24), 6.343 (d of d, 1H, J = 11.6, 11.2 Hz, H-23), 6.468 (br d, 1H, J = 11.6, H-22), 6.557 (d, 1H, J = 15.1

Hz. H-26), 7.260 (d of d, 1H, J = 11.1, 15.1 Hz, H-25). No C,H analysis due to instability.

(20(22)E,23E)-24-(2′-Naphthyl)-chola-5,20(22),23-trien-3β-ol (6a, R^1=H). mp 190.0-190.5°C; m/z = 466 (M^+), 448 (M^+–H_2O); $[\alpha]_D^{25}$ -25° (c 0.17, CH_2cl_2); λ_{max}^{abs} = (254, **271**, 280), (316, **331**) nm (MeOH); λ_{max}^{em} = 407 nm (MeOH, λ_{ex} = 340 nm); ^{1}H NMR (500 MHz) δ 0.619 (s, 3H, C-18 methyl), 1.014 (s, 3H, C-19 methyl), 1.938 (s, 3H, C-21 methyl), 3.524 (m, 1H, H-3α), 5.363 (br d, 1H, H-6), 6.129 (br d, 1H. J = 10.9 Hz, H-22), 6.622 (d, 1H, J = 15.4 Hz, H-24), 7.206 (d of d, 1H, J = 15.4, 10.8 Hz, H-23), 7.394 (t, 1H, J = 7.0 Hz, H-6′), 7.433 (t, 1H, J = 7.2 Hz, H-7′), 7.638 (d, 1H, J = 8.3 Hz, H-3′), 7.713 (s, 1H, H-1′), 7.76 (m, 3H, H-4′, H-5′ and H-8′). Anal. calcd for $C_{34}H_{42}O$: C, 87.50; H, 9.07. Found: C, 87.29; H, 8.88.

(20(22)E,23Z)-24-(2′-Naphthyl)-chola-5,20(22),23-trien-3β-ol (8b,R^1=H). mp 180.0-181.0°C; m/z = 466 (M^+), 448 (M^+–H_2O); ^{1}H NMR (500 MHz) δ 0.649 (s, 3H, C-18 methyl), 1.018 (s, 3H, C-19 methyl), 1.899 (s, 3H, C-21 methyl), 3.524 (m, 1H, H-3α), 5.363 (br d, 1H, H-6), 6.496 (d, 1H, J = 11.2 Hz, H-24), 6.533 (br d, 1H, J = 11.4 Hz, H-22). 6.593 (d of d, 1H, J = 11.2, 11.4 Hz, H-23). Anal. Calcd. for $C_{34}H_{42}O$: C, 87.50; H, 9.07. Found: C, 87.23; H, 8.99.

2.4 References

1. J. Gosney and A.G. Rowley, in *"Organophosphorous Reagents in Organic Synthesis"*, J.I.G. Cadogan, Ed., Academic: London, **1979**, pp. 17–153.

2. H.J. Bestmann and O. Vostrowsky, *Top. Curr. Chem.*, **1983**, *109*, 85–163.

3. M. Schlosser, *Top. Stereochem.*, **1970**, *5*, 1–30.

4. A.J. Speziale and D.E. Bissing, *J. Am. Chem. Soc.*, **1963**, *85*, 3878–3884.

5. L. Bergelson and M.M. Shemyakin, *Pure Appl. Chem.*, **1964**, *9*, 271–283.

6. B.E. Maryanoff, A.B. Reitz, M.S. Mutter, R.R. Inners, H.R. Almond, R.R. Whittle and R.A. Olofson, *J. Am. Chem. Soc.*, **1986**, *108*, 7664–7678.

7. E. Vedejs, T. Fleck and S. Hara, *J. Org. Chem.*, **1987**, *52*, 4637–4639.

8. M. Schlosser, G. Muller and K.F. Christmann, *Angew. Chem.*, Internat. Ed., **1966**, *5*, 667–668.

9. R.J. Anderson and C.A. Henrick, *J. Am. Chem. Soc.*, **1975**, *97*, 4327–4334.

10. A.W. Johnson and V.L. Kyllingstad, *J. Org. Chem.*, **1966**, *31*, 334–336.

11. E. Vedejs and H.W. Fang, *J. Org. Chem.*, **1984**, *49*, 210–212.

12. Ref. 1, p.82.

13. L.D. Bergelson, L.I. Barsukov and M.M. Shemyakin, *Tetrahedron*, **1967**, *23*, 2709–2720.

14. E. Vedejs, G.P. Meier and K.A.J. Snoble, *J. Am. Chem. Soc.*, **1981**, *103*, 2823–2831.

15. A.B. Reitz, S.O. Nortey, A.D. Jordan, M.S. Mutter and B.E. Maryanoff, *J. Org. Chem.*, **1986**, *51*, 3302–3308.

16. L.D. Bergelson and M.M. Shemyakin, *Tetrahedron*, **1963**, *19*, 149–159.

17. E. Vedejs and K.A.J. Snoble, *J. Am. Chem. Soc.*, **1973**, *95*, 5778–5780.

18. A.B. Reitz, M.S. Mutter and B.E. Maryanoff, *J. Am. Chem. Soc.*, **1984**, *106*, 1873–1875.

19. B.E. Maryanoff, A.B. Reitz, M.S. Mutter, R.R. Inners and H.R. Almond, *J. Am. Chem. Soc.*, **1985**, *107*, 1068–1070.

20. J. Boutagy and R.Thomas, *Chem. Rev.*, **1974**, *74*, 87–99.

21. W.S. Wadsworth, *Org. Reactions*, **1977**, *25*, 73–253.

22. B.J. Walker, in *"Organophosphorous Reagents in Organic Synthesis"*, J.I.G. Cadogan, Ed., Academic: London, **1979**, pp. 155–205.

23. E. Breuer, S. Zbaida and E. Segall, *Tetrahedron Lett.*, **1979**, 2203–2204.

24. E.J. Corey and G.T. Kwiatkowski, *J. Am. Chem. Soc.*, **1966**, *88*, 5654–5656.

25. F. Sondheimer and R. Mechoulam, *J. Am. Chem. Soc.*, **1957**, *79*. 5029–5033.

26. G.R. Pettit, B. Green, G.L. Dunn and P. Sunder-Plassmann, *J. Org. Chem.*, **1970**, *35*, 1385–1389.

27. J.P. Schmit, M. Piraux and J.F. Pilette, *J. Org. Chem.*, **1975**, *40*, 1586–1588.

28. K. Bannai, M. Morisaki and N. Ikekawa, *J. Chem. Soc., Perkin I*, **1976**, 2116–2120.

29. M. Koreeda, N. Koizumi and B.A. Teicher, *Tetrahedron Lett.*, **1976**, 4565–4568.

30. M. Koreeda, N. Koizumi and B.A. Teicher, *J. Chem. Soc., Chem. Commun.*, **1976**, 1035–1036.

31. T.C. McMorris and S.R. Schow, *J. Org. Chem.*, **1976**, *41*, 3759–3760.

32. D.M. Piatak and J.Wicha, *Chem. Rev.*, **1978**, *78*, 199–241.

33. S.R. Schow and T.C. McMorris, *J. Org. Chem.*, **1979**, 44, 3760–3765.

34. A. Furst, L. Labler and W. Meier, *Helv. Chim. Acta*, **1982**, *65*, 1499–1521.

35. A.K. Bose and R.T. Dahill, *J. Org. Chem.*, **1965**, *30*, 505–509.

36. G.R. Pettit, C. Herald and J.P. Yardley, *J. Org. Chem.*, **1970**, *35*, 1389–1392.

37. E.D. Bergmann and A. Solomonovici, *Steroids*, **1976**, *27*, 431–437.

38. G.R. Lenz and J.A. Schulz, *J. Org. Chem.* **1978**, *43*, 2334–2339.

39. M.M. Midland and Y.C. Kwon, *Tetrahedron Lett.*, **1985**, *26*, 5021–5024.

40. W. Fritsch, V. Stache and H. Ruschig, *Justus Liebigs Annal. Chem.*, **1966**, *699*, 195–205.

41. D.H. Wadsworth, O.E. Schuff, E.J. Seus and J.A. Ford, *J. Org. Chem.*, **1965**, *30*, 680–685.

42. B. Deschamps, J.P. Lampin, F. Mathey and J. Seyden-Penne, *Tetrahedron Lett.*, **1977**, 1137–1140.

43. Y. Letourneaux, M.M.L. Lo, N. Chaudhuri and M. Gut, *J. Org. Chem.*, **1975**, *40*, 516–518.

44. A.O. Colonna and E.G. Gros, *J. Steroid Biochem.*, **1973**, *4*, 171–179.

45. E.J. Corey and J.W. Suggs, *Tetrahedron Lett.*, **1975**, 2647–2650.

46. T. Makino, K. Shibata, D.C. Rohrer and Y. Osawa, *J. Org. Chem.*, **1978**, *43*, 276–280.

47. L.M. Jackman and R.H. Wiley, *J. Chem. Soc.*, **1960**, 2881–2886.

48. D.J. Faulkner, *Synthesis*, **1971**, 175–189.

49. W. Nagata and Y. Hayase, *J. Chem. Soc. (C)*, **1969**, 460–466.

50. P.E. Sonnet, *Org. Prep. Proced. Int.*, **1974**, *6*, 269–273.

51. G. Magnusson, *Tetrahedron Lett.*, **1977**, *31*, 2713–2716.

52. E.J. Corey, A. Marfat, G. Goto and F. Brion, *J. Am. Chem. Soc.*, 1980, *102*, 7984–7985.

53. Prepared from triethyl phosphite and cinnamyl bromide by the method used to synthesize diethylbenzyl phoshponate of B.C. Saunders, G.J. Stacey, F. Wild, and I.G.E. Wilding, *J. Chem. Soc.*, **1948**, 699–703.

54. N.D. Dawson and A.Burger, *J. Am. Chem. Soc.*, **1952**, *74*, 5312–5314.

55. Prepared by the method of B.A. Arbuzov and B.P. Lugovkin, *Zhur. Obschchei. Khim.*, **1950**, *20*, 1297–1299, (*CA, 45:* 1567a).

56. A. Riedel, *Justus Liebigs Annal. Chem.*, **1908**, *361*, 96. (*Beilstein*, **1926**, *9*, System No. 950, 639).

57. I.N. Nazarov and L.B. Fisher, *Izvest. Akad. Nauk S.S.S.R., Otdel. Khim. Nauk*, **1948**, *436* (*CA, 43:* 2576f).

58. S. Misumi and M. Nakagawa, *Bull. Chem. Soc. Jpn.*, **1963**, *36*, 399–404.

59. J.H. Dygos and B.N. Desai, *J. Org. Chem.*, **1979**, *44*, 1590–1596.

60. E.J. Corey and A. Venkateswarta, *J. Am. Chem. Soc.*, **1972**, *94*, 6190–6191.

Chapter 3

^{1}H and ^{13}C NMR Assignment of Fluorescent Cholesterol Analogue Probes

3.1 Introduction

In order to simplify the interpretation of data obtained from fluorescence experiments using the sterol probes, it was important to determine the geometry about the double bonds in the synthesized sidechains, and also to verify the presence of only one geometrical isomer. To this end, an analysis of the olefinic proton resonance portion (δ ~6→8 ppm) of the ^{1}H NMR spectra of the sterol probes was performed. It was decided to analyze the upfield (ring proton) region of the spectrum as well (δ ~0.5→2.5 ppm), since few steroids have had their ^{1}H NMR spectrum fully assigned, and analyzed for coupling constants. Comparison of the ring ^{13}C chemical shifts with those reported in the literature for cholesterol[1] could also give an idea of how similar these olefinic sterol probes are to cholesterol.

3.2 Results and Discussion

3.2.1 Olefinic and Aromatic Proton Assignments of 4a→6b

The downfield portion of a one-dimensional (1D) ^{1}H NMR spectrum of a mixture of **5a** and **5b** is shown in Figure 3.1. Due to the presence of the two geometrical isomers, straightforward analysis of the 1D spectrum was not possible. A ^{1}H-^{1}H shift-correlated spectrum (COSY)[2,3] of the same region is shown in Figure 3.2. The 22-H resonances (for a three dimensional representation of **5a** with carbon atom numberings, see Figure 3.3) were recognised due to their coupling with the corresponding 21-methyl resonances at δ ~1.9 ppm (not shown). The connectivities of the olefinic proton resonances in the two isomers was then easily established (for chemical shifts see Table 3.1). The COSY spectrum also confirmed the presence of an olefinic proton resonance under the aromatic envelope, a fact suspected from integration of the 1D spectrum.

By coupling constant analysis (Table 3.2) of the olefinic proton multiplets (J_{trans} ~15Hz, J_{cis} ~11Hz from numerous studies of carotene systems[4,5] for example), and from integration of the 22-H resonance of **5a** versus the identical 6-H resonance of both isomers, it was determined that the isomers **5a** and **5b** were present in

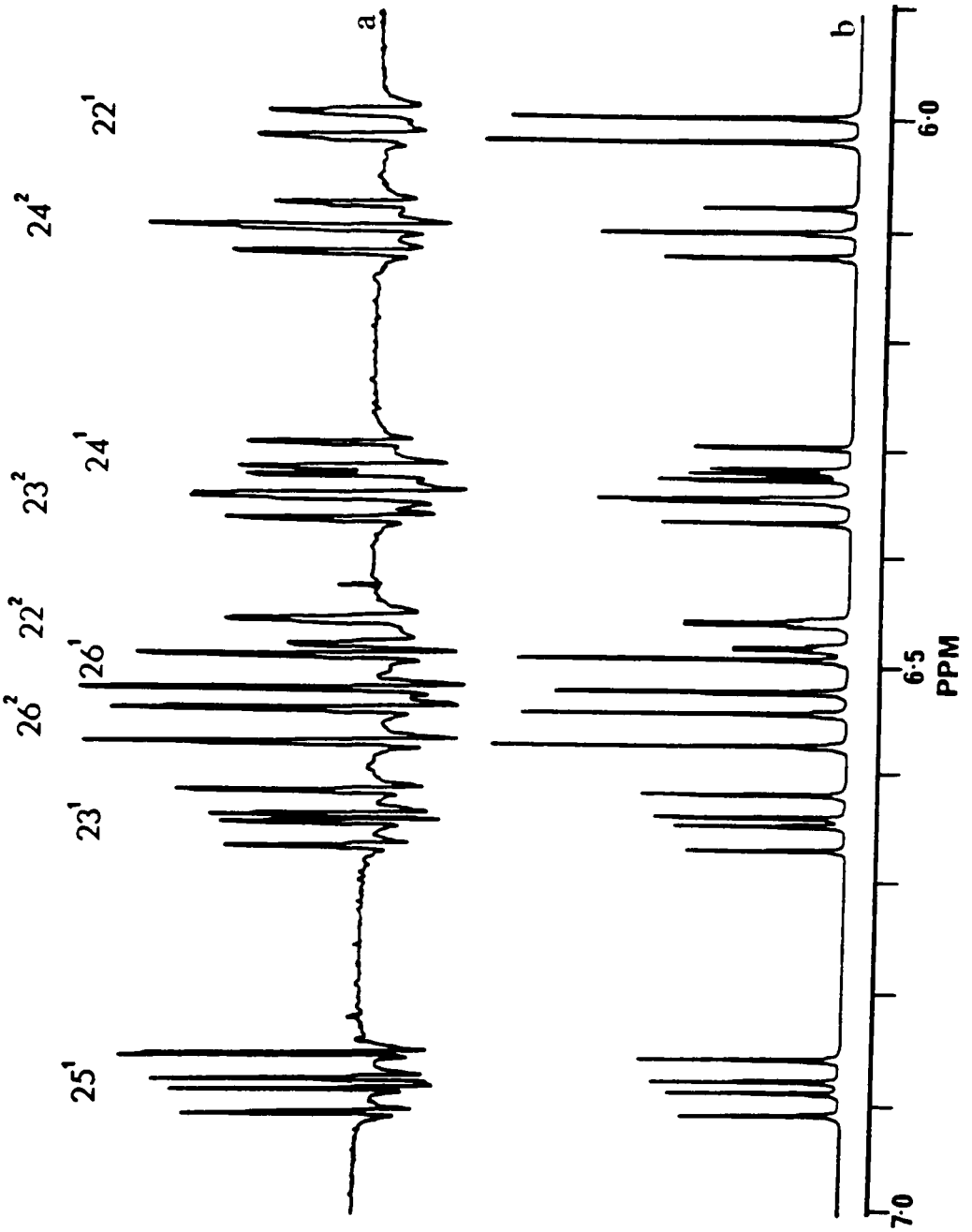

Figure 3.1: Downfield region of the 500 MHz ^{1}H NMR spectrum of a mixture of **5a** and **5b**. a) Experimental Spectrum; b) Simulated Spectrum with parameters given in Tables 3.1 and 3.2.

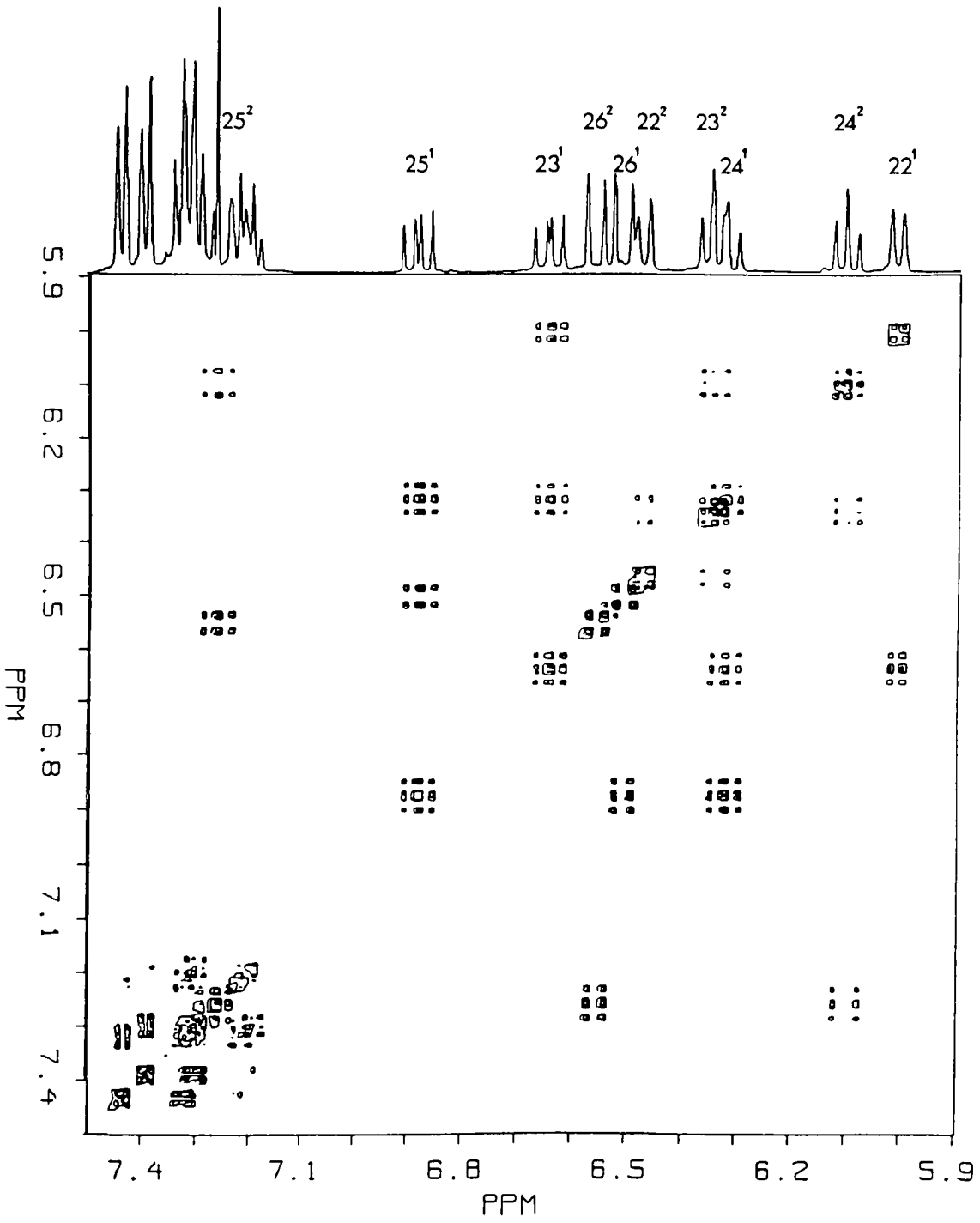

Figure 3.2: Downfield region of the COSY spectrum of a mixture of **5a** and **5b**.

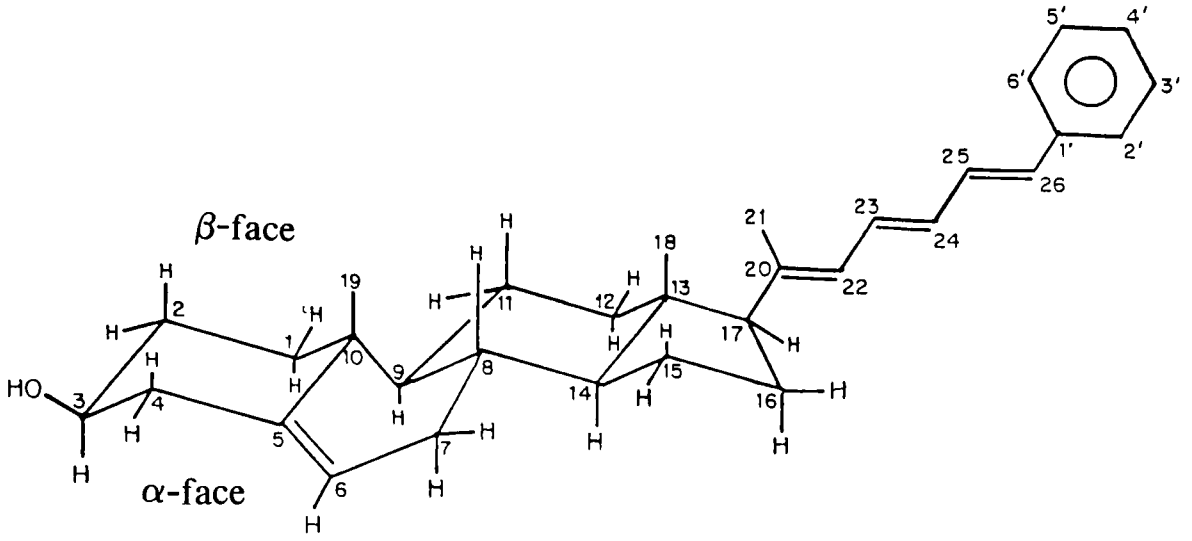

Figure 3.3: 3D representation of **5a** with carbon atom numberings

Table 3.1: ^{1}H NMR chemical shifts (ppm)[a] for the olefinic and aromatic protons of compounds **4a**→**6b** in $CDCl_3$

Proton	**4a**	**4b**	**5a**	**5b**[b]	**6a**	**6b**[b]
22	6.074	6.343	6.007[c]	6.468[c]	6.129	6.533
23	7.083	6.506	6.641[c]	6.343[c]	7.206	6.593
24	6.466	6.444	6.322[c]	6.101[c]	6.622	6.496
25			6.883[c]	7.260		
26			6.507[c]	6.557[c]		
1′	–	–	–		7.713	
2′	7.400	7.34[d]	7.389		–	
3′	7.295	7.32[d]	7.299		7.638	
4′	7.182	7.211	7.189		7.76[d]	
5′	7.295	7.32[d]	7.299		7.76[d]	
6′	7.400	7.34[d]	7.389		7.394	
7′					7.433	
8′					7.76[d]	

[a] ±0.002 ppm
[b] Aromatic ^{1}H chemical shifts not determined
[c] from iterative analysis
[d] ±0.01 ppm due to overlapping resonances

Table 3.2: ^1H–^1H NMR coupling constants (Hz) in the sidechain of compounds **4a**→**6b**[a].

Proton Pair	4a	4b	5a[b]	5b[b]	6a	6b
21,22	<0.5	<0.5	<0.5	1.2	<0.5	<0.5
22,23	11.0	11.3	11.1	11.6	10.9	11.4
23,24	15.6	11.3	14.7	11.2	15.4	11.2
24,25			10.1	11.1		
25,26			15.2	15.1		

[a]Error ±0.2 Hz
[b]Values found from iterative analysis of the spectrum of **5a** and **5b** shown in Figure 3.1

the ratio 40:60. Simulation of the olefinic proton resonances using a 50:50 ratio and the measured chemical shifts and coupling constants, produced a spectrum virtually identical to the experimental 1D spectrum except for the intensity ratios (Figure 3.1). Although **5a** and **5b** had been obtained by a Wittig reaction on the 20(22)E-aldehyde **3a**, the geometry of the C-20,C-22 double bond of the two isomers was not confirmed as being E by the 1D or COSY experiments. This is because the similarity of transoid and cisoid allylic coupling constants does not allow unambiguous assignment[6,7].

Nuclear Overhauser effect (nOe) experiments could allow determination of the C-20,C-22 double bond geometry. This effect involves a through space (not through bonds) interaction via a dipole-dipole mechanism so it is dependent on internuclear distance to the inverse sixth power[8]. However, for nOe experiments to be most effective, they should be performed on systems where either the distance between the two nuclei in question is fixed, or the rates of intramolecular motions affecting the internuclear distance are fast compared with the NMR timescale. The olefinic sterol probes satisfy this criterion since the positions of the 21-methyl group and the 22-H are fixed with respect to each other due to the C-20,C-22 double bond. In a 20(22)Z-isomer of the compounds under study, one would expect to see an nOe enhancement of the 21-methyl resonance upon saturation of the 22-H resonance due to the proximity of these protons. On the other hand, in a 20(22)E-isomer, an nOe enhancement of the 21-methyl resonance should not occur upon saturation of the 22-H resonance since these protons are on opposite sides of a double bond and hence too far apart for an nOe to occur. However, if it assumed that the

conformation about the C-22,C-23 single bond is the sterically more favoured *s-trans* conformation, an nOe enhancement of the 21-methyl resonance should occur upon saturation of the 23-H resonance. NOe experiments were performed on a purified sample of **5a** (Table 3.3) and since an enhancement of the 21-methyl resonance at δ 1.85 ppm was observed upon saturation of the 23-H resonance and not the 22-H resonance, the C-20,C-22 double bond geometry was confirmed as being E, as expected from the synthetic route to this compound.

Table 3.3: ^{1}H nuclear Overhauser enhancements.

Compound	Saturated Signal	Proton Resonance Enhanced (Magnitude of nOe)[a]
4a	18-CH_3	8β,11β(6);15β(2);21-CH_3(2);22(2).
	19-CH_3	2β(1);4β(2);8β,11β(2).
	22	16β(7);17α(3);18-CH_3(2);24(13)
	23	21-CH_3(11);2′,6′(18).
4b	22	16β(6);17α(2);2′,6′(1).
	23	21-CH_3(8);24(10).
5a	18-CH_3	8β,11β(3);15β(1);21-CH_3(2);22(1).
	19-CH_3	2β(1);4β(2);8β,11β(3).
	22	16β(2);17α(3);18-CH_3(2);24(7)
	23	21-CH_3(5);25(6);2′,6′(1).
6a	22	16β(>1)[b];17α(3);24(7).
	23	21-CH_3(6);1′(2);3′(6).

[a]Intensity of saturated signal in difference spectrum set to -100.
[b]overlap with incomplete cancellation of 21-methyl signal.

Analysis of the signals in the olefinic proton region of the 1D ^{1}H NMR spectra of the conjugated dienes **4a**, **4b**, **6a**, and **6b** was straightforward after the geometry of the conjugated trienes **5a** and **5b** had been determined unequivocally. (For a diagram of the nOe experiments performed on **4a** see Figure 3.4.) All that remained was to assign the aromatic proton resonances. The assignment of the *ortho-*, *meta-* and *para-* proton resonances of **4a**, **4b** and **5a** followed from inspection of the multiplicity and integration of the three multiplets in the aromatic region (for **4a**, see Figure 3.4). The identical *ortho-* protons (2′-H, 6′-H) should give a doublet

resonance which integrates to two protons, the identical *meta-* protons (3′-H, 5′-H) should give a triplet resonance which also integrates to two protons while the *para*-proton (4′-H) should give a triplet resonance which only integrates to one proton. Likewise the assignment of the naphthyl proton resonances in **6a** came from multiplicity and integration arguments although the individual chemical shifts of the 4′-, 5′, and 8′- naphthyl protons could not be extracted from the multiplet centred at δ 7.76 ppm. The relative order of the naphthyl proton chemical shifts agreed with that reported for 2-methylnaphthalene[9]. All the downfield ^{1}H chemical shifts determined for compounds **4a**, **4b**, **5a**, **5b**, **6a** and **6b** are given in Table 3.1 while ^{1}H-^{1}H coupling constants are given in Table 3.2.

3.2.2 Ring Proton Chemical Shifts of 5a

The cholesterol ring system with its C-5,C-6 double bond, 3β-OH and 17β substitution, as found in compounds **4a**→**6b**, presents quite a challenge to the NMR spectroscopist for proton assignment as there are 23 proton signals within 1.7 ppm. The only known attempts at ring proton resonance assignment of cholesterol are given in Table 3.4. These assignments were made by comparing spectra of deuterated cholesterol derivatives[10] or by the use of lanthanide shift reagents[11]. Since compounds **4a**→**6b** do not possess the C_8H_{17} saturated sidechain of cholesterol, their ^{1}H NMR assignment was easier, especially with the aid of the recently acquired battery of two-dimensional (2D) NMR techniques[2,3,12]. These 2D NMR techniques have been successfully used to assign ring proton resonances of other steroids, usually those with a larger number of functional groups and/or double bonds resulting in some simplification of the spectrum[13–20].

For a recent ^{1}H and ^{13}C chemical shift assignment, but no ^{1}H-^{1}H coupling analysis, of a cholesterol ring system see Ref. 20. However, in this assignment, the individual chemical shifts of 4α-H and 4β-H, and C-7 and C-8 were not resolved.

The first step in the assignment was to distinguish the methine from the methylene proton resonances. The easiest way to achieve this was to perform a DEPT (Distortionless Enhancement by Polarization Transfer) experiment[3] to identify the methine and methylene carbons (Figure 3.5). Then a ^{13}C-^{1}H shift correlated spectrum[2,3]

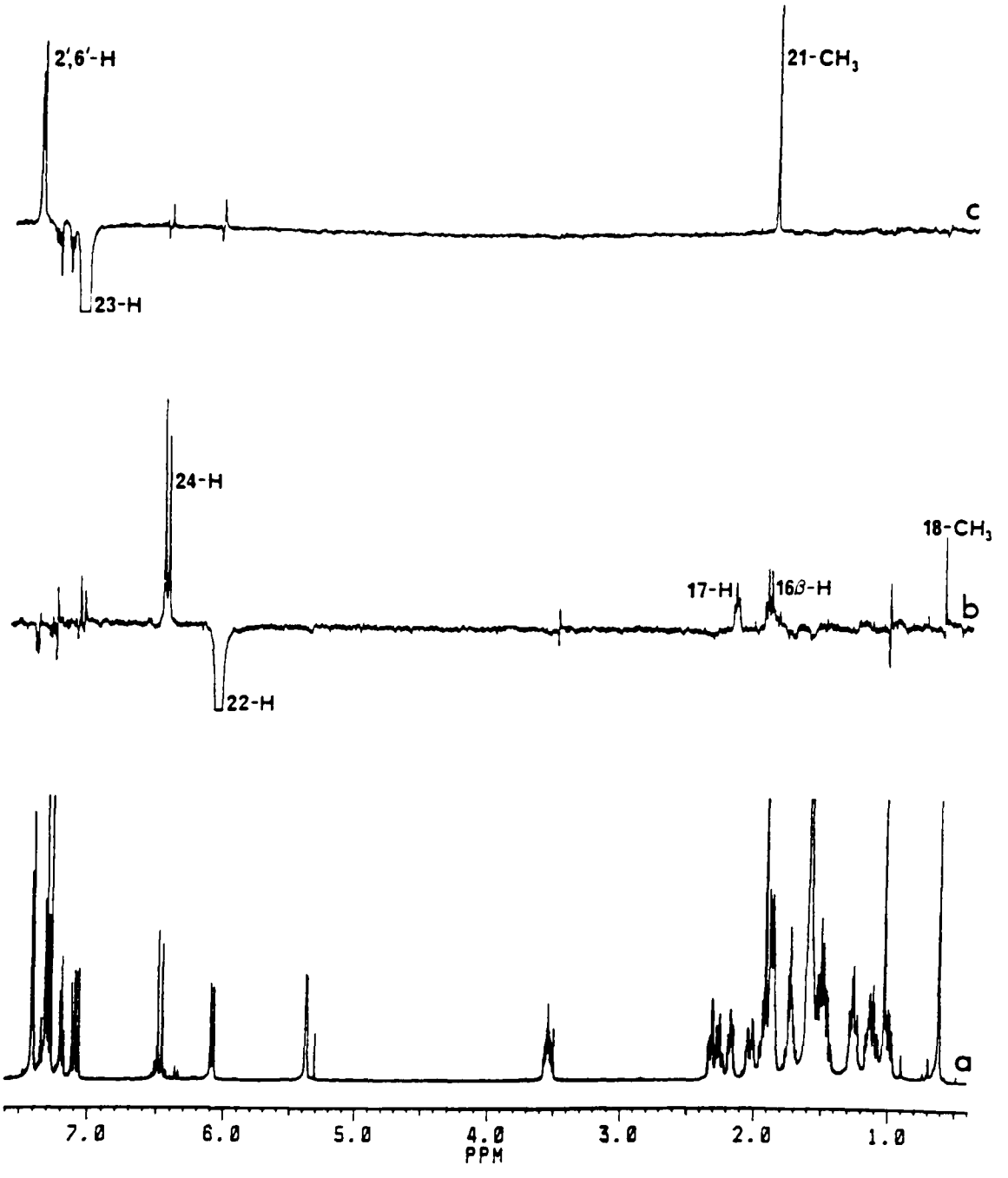

Figure 3.4: a) Complete ^{1}H NMR spectrum of **4a**; b) Nuclear Overhauser effect difference spectrum after saturation of 22-H at δ 6.07; c) Nuclear Overhauser effect difference spectrum after saturation of 23-H at δ 7.08.

Table 3.4: ^{1}H NMR chemical shifts (ppm) for the ring protons and methyl groups of cholesterol and the steroids **4a** and **5a**.

Proton	Cholesterol in pyridine-d_5[c]	Cholesterol in chloroform-d[d]	**4a**[a] (±0.008)	**5a**[b] (±0.005)
1α	1.83	–	1.102	1.088
1β	1.83	–	1.851	1.855
2α	2.07	1.90	1.854	1.845
2β	1.80	1.58	1.516	1.515
3α	3.82	3.47	3.526	3.530
4α	2.60	2.3	2.306[e]	2.303
4β	2.60	2.3	2.235[f]	2.240
6	5.41	5.30	5.362	5.361
7α	2.03	2.05	1.561	1.565
7β	2.03	2.05	2.2002	2.008
8β			1.467	1.468
9α			0.982	0.976
11α			1.566	1.573
11β			1.455	1.447
12α			1.239	1.231
12β			1.841	1.840
14α			1.127	1.119
15α			1.699	1.709
15β			1.236	1.244
16α			1.702	1.687
16β			1.902	1.893
17α			2.152	2.135
18		0.68	0.598	0.589[f]
19		1.02	1.009	1.013[e]
21			1.896	1.848[e]

[a] $CDCl_3$ solution; from CHORTLE analysis
[b] $CDCl_3$ solution; from spin simulation
[c] from reference 10
[d] from reference 11
[e] measured from the 1D spectrum (CHORTLE analysis gave the average chemical shift of the 2 resonances)
[f] measured from the 1D spectrum

with proton decoupling in both dimensions (Figure 3.6) allowed determination of corresponding methine proton chemical shifts. Of the four methine proton resonances, the most downfield one (δ 2.135 ppm) was assigned to 17α-H because of its proximity to the C-20,C-22 double bond. The three remaining methine proton resonances due to 8β-H, 9α-H and 14α-H could only be assigned after analysis of nOe difference experiments and a COSY spectrum.

The second step in the assignment was to distinguish the axial methylene proton resonances from the equatorial proton resonances, since the chemical shifts of axial and equatorial protons in cyclohexyl ring systems differ due to the shielding effect of 1,3-diaxial interactions[17]. This was possible from the proton-decoupled ^{13}C-^{1}H shift correlated spectrum mentioned above since two non-equivalent methylene protons give two peaks in the ^{1}H dimension for each methylene carbon (Figure 3.6). Because of the 1,3-diaxial interaction, the axial proton can be assigned to the more upfield of the two resonances.

The third step was to assign proton numbers to the observed chemical shifts (Table 3.4). This was achieved in large part by analysis of a COSY spectrum (Figure 3.7), with the help of the few known resonances (3α-H, 6-H and 17α-H). For example, the methine proton 14α-H was distinguished from the 8β and 9α methine protons through its coupling with the 15α and β protons (coupled weakly to 17α-H at δ 2.135 ppm). Then since 8β-H but not 9α-H couples with 14α-H, the two remaining methine protons were assigned. However, the spin system 1α, 1β, 2α, 2β could not be easily distinguished from the 12α, 12β, 11α and 11β spin system. Furthermore, the methylene protons of the cyclopentyl D-ring could not be simply assigned as α or β on the basis of the axial/equatorial proton chemical shift difference found for cyclohexyl systems.

Both of these problems were solved by selective nOe difference experiments. The rigid cholesterol ring system, with its two angular methyl groups at C-18 and C-19, is an ideal molecule for nOe experiments. Through saturation of the 18-methyl and 19-methyl resonances, the axial protons on the β face of the molecule can be observed (Table 3.3). Both the 11β and the 2β protons are axial, but while saturation of the 19-methyl resonance will lead to an nOe enhancement of both these resonances, saturation of the 18-methyl resonance will only affect the 11β

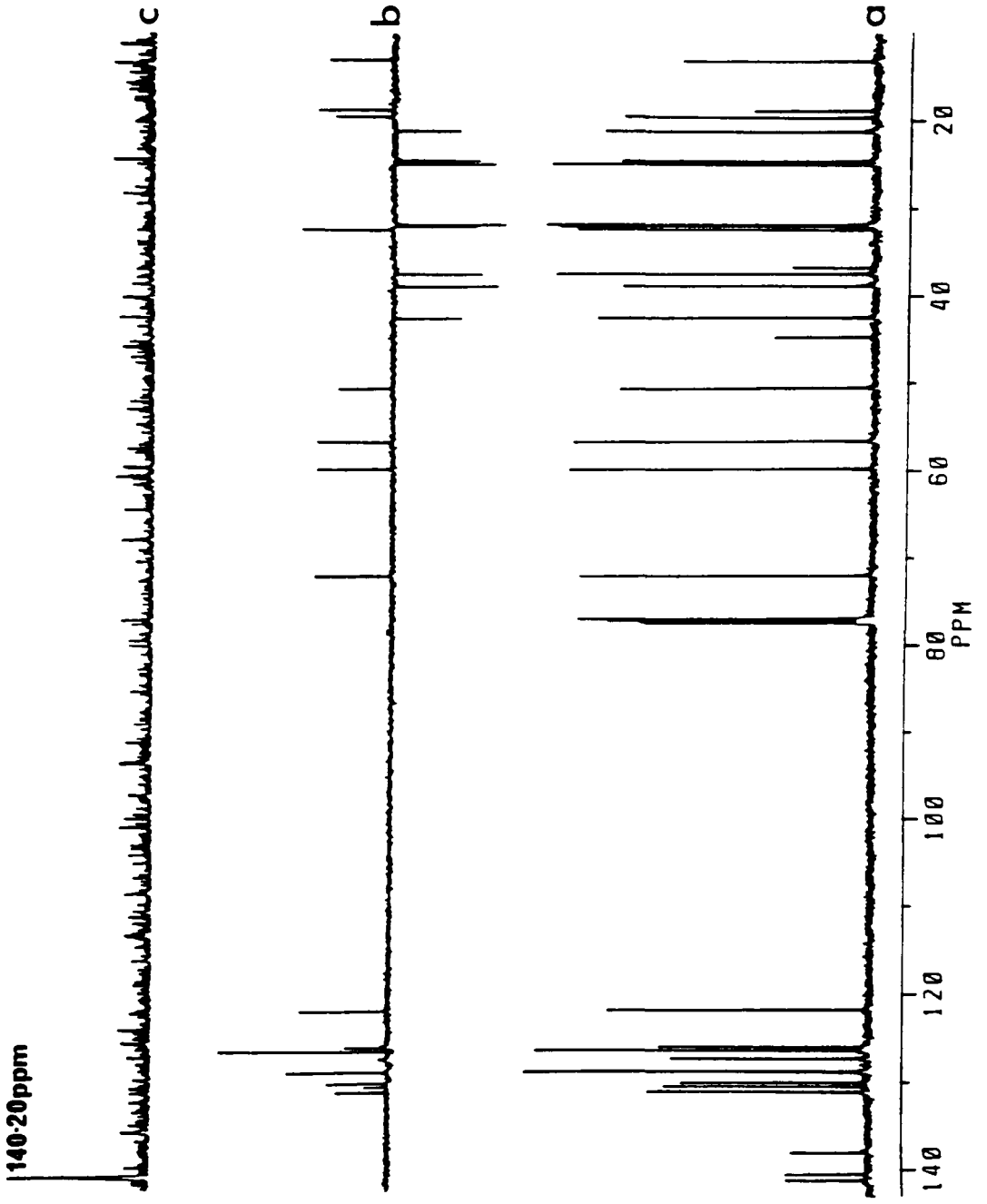

Figure 3.5: a) Complete ^{13}C NMR spectrum of **5a**; b) DEPT spectrum of **5a** (methine, methyl resonances up; methylene resonances down); c) Selective INEPT spectrum of **5a** upon irradiation of 21-CH_3 at δ 1.85.

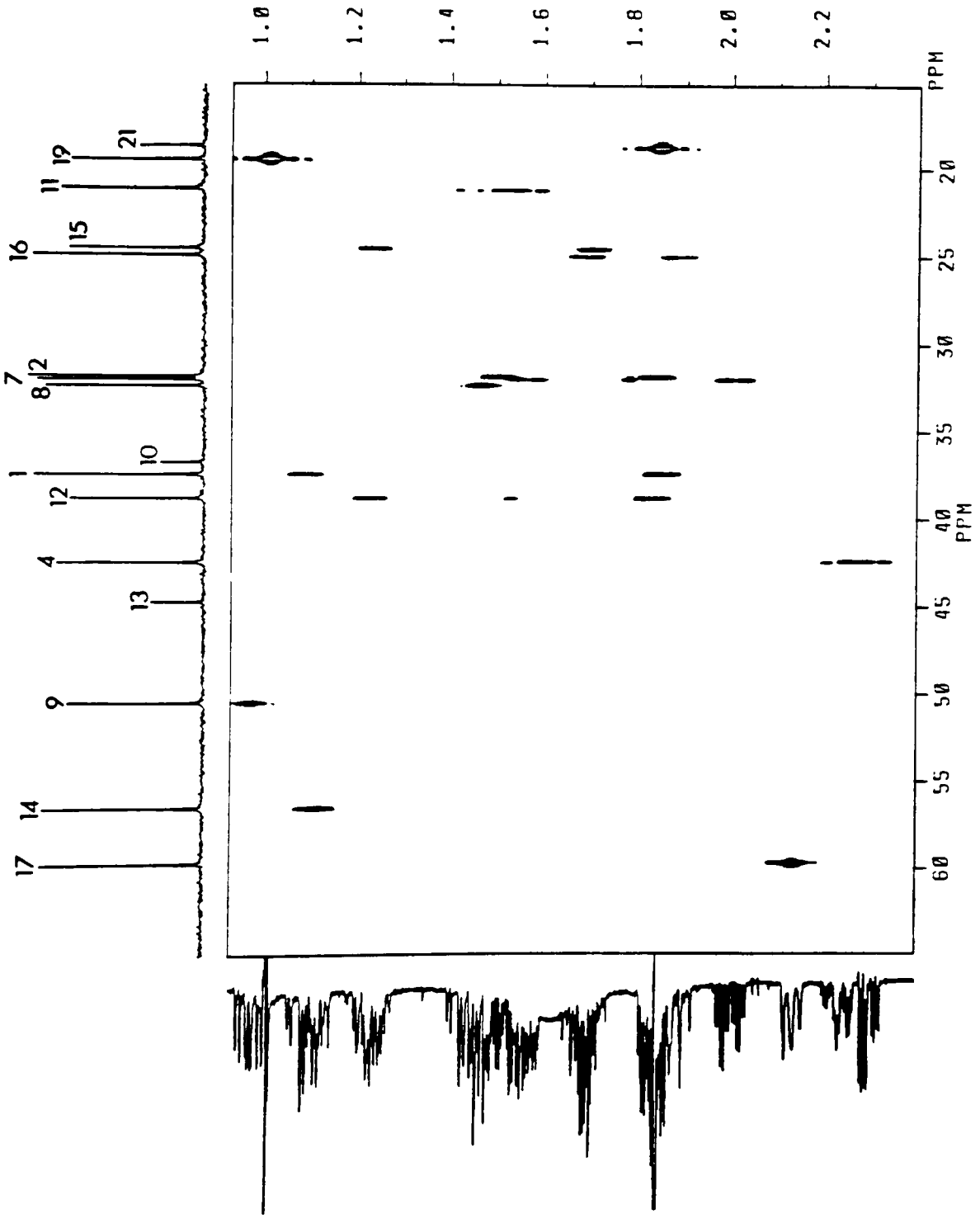

Figure 3.6: Upfield region of the ^{13}C-^{1}H shift-correlated spectrum of **5a**.

Table 3.5: ^{1}H-^{1}H NMR coupling constants (Hz) of **5a**[a]

Proton Pair	$\|^2J\|$	^{3}J	$^3J_{ax-ax}$	$^3J_{ax-eq}$	$^3J_{eq-eq}$	$\|^4J\|$	^{5}J
1α,1β	13.4						
1α,2α				3.5			
1α,2β			13.0				
1β,2α					1.8		
1β,2β				4.9			
2α,2β	14.6						
2α,3α				4.5			
2α,4α						1.2	
3α,4α				4.4			
3α,4β			11.4				
4α,4β	13.0						
4α,6						2.3	
4β,6						2.7	
4β,7α							2.2
4β,7β							2.8
6,7α		3.0					
6,7β		5.2					
7α,7β	17.6						
7α,8β			10.6				
7β,8β				5.2			
8β.9α			11.2				
8β,14α			11.2				
9α,11α				5.4			
9α,11β			12.2				
11α,11β	13.6						
11α,12α				2.5			
11α,12β					2.0		
11β,12α			13.0				
11β,12β				4.2			
12α,12β	12.8						
12α,18						1.2	
17α,18						nm[b]	
1α,19						1.2	
9α,19						0.8	

[a]refined values after spin simulation (±0.5 Hz)
[b]not measurable

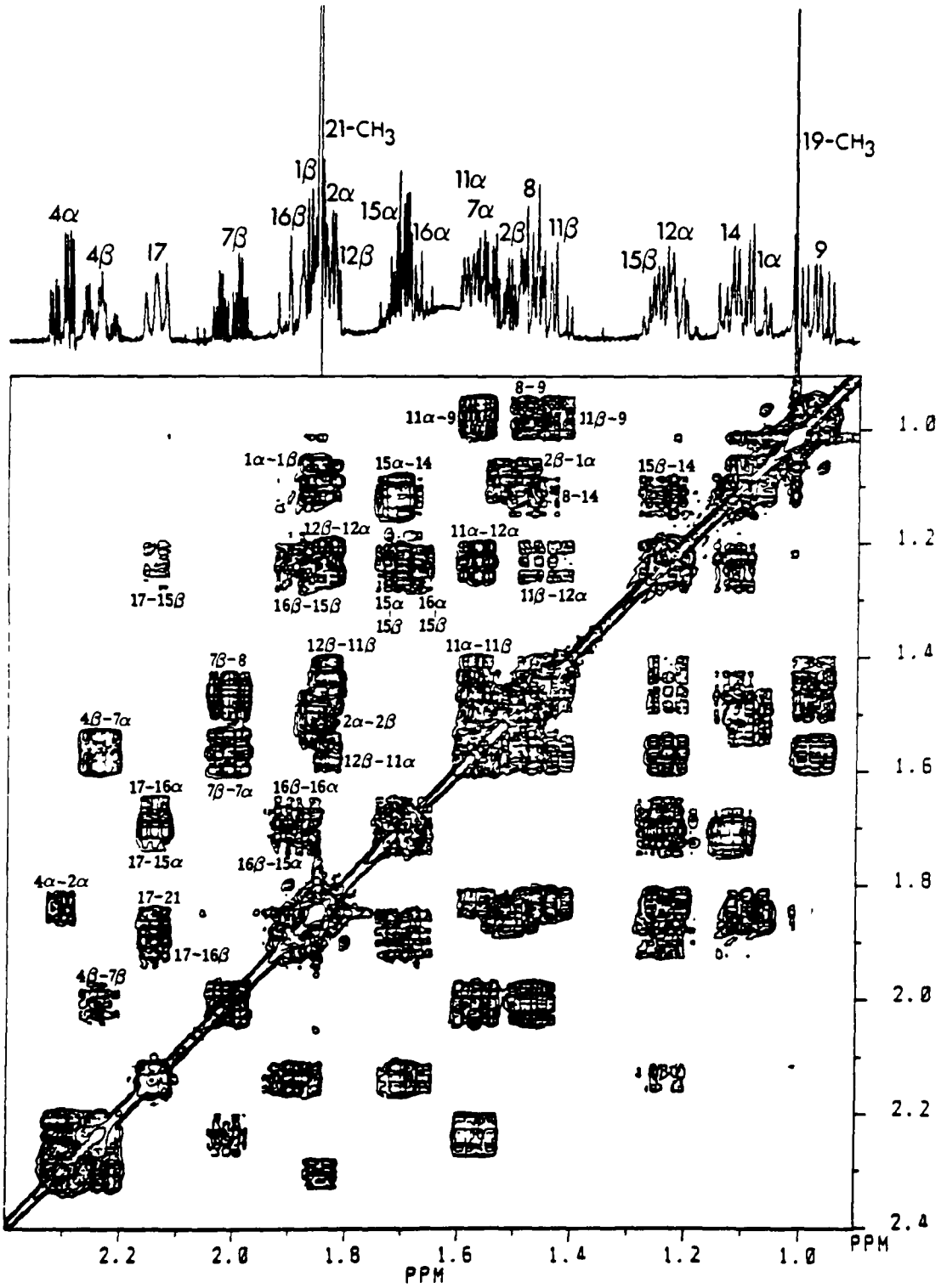

Figure 3.7: Upfield region of the COSY spectrum of **5a**.

Table 3.6: ^{1}H-^{1}H NMR coupling constants (Hz) in the D ring of 5a[a]

	15α	15β	16α	16β	17α
14α	6.8	11.6			
15α		12.0	8.2	0.5	
15β			8.5	10.0	
16α				10.9	8.3
16β					10.2

[a]Refined values from spin simulation; average error ±1Hz.

proton. On this basis, the spin systems 1α, 1β, 2α, 2β and 12α, 12β, 11α, 11β were assigned. These nOe difference experiments also allowed assignment of the 15β-H and confirmation of the assignment of the 4β and 8β axial protons. All that remained was to assign the 16-H resonances since the 16β-H had not been observed by the nOe experiment on the 18-methyl group.

It had been noted from the nOe experiment performed on the 22-H resonance to determine the C-20,C-22 double bond geometry (see section 3.2.1), that enhancements were seen to two ring proton resonances centred at δ 2.15 ppm and δ 1.90 ppm as well as to the 18-methyl group at δ 0.59 ppm (Table 3.3). From a Dreiding model it was determined that upon rotation of the C-17,C-20 bond, the 22-H approaches the 17α and the 16β ring protons most closely. Since the nOe is dependent on internuclear distance to the inverse sixth power[8], the two resonance enhancements must be due to these two protons. The δ 2.15 ppm resonance had already been independently assigned to 17α-H, and the δ1.90 ppm resonance did correspond to one of the 16-H chemical shifts previously determined so the 16β-H and hence 16α-H were assigned.

3.2.3 Ring Proton-Proton Coupling Constants of 5a

Our interest in obtaining proton-proton coupling constants from the multiplets in this crowded region of the spectrum was threefold. Firstly, their determination would provide a further means of confirming assigned proton chemical shifts, particularly for those geminal proton pairs whose axial proton was on the α-face of the molecule and hence had not been confirmed by nOe experiments. Secondly, given

the precedence for allylic and homoallylic coupling[6,7], and the previously observed ^4J coupling to steroid angular methyl groups [6,7,17], it was of interest to determine the extent of long-range coupling in a cholesterol-type ring system. Lastly, due to the dependence of vicinal coupling constants on dihedral angle[21], a coupling constant analysis of the D ring protons could give an idea of the D ring conformation of **5a** in solution.

A ^1H homonuclear J-resolved spectrum[2,3] of **5a** was measured. In such a spectrum, the various proton multiplets are seen as single lines in the second dimension f_2 (in this case allowing confirmation of the chemical shifts), and as separated multiplets in the first dimension f_1 allowing measurement of the various coupling constants. For those resonances that were overlapping in the ^1H 1D spectrum, the f_1 cross-sections of the J-resolved spectrum were plotted and the coupling constants determined. The chemical shifts and coupling constants were used to generate a simulated ^1H 1D spectrum in the region δ 0.9→2.4 ppm, excluding the methyl resonances at δ 1.01 pm and at δ 1.85 ppm (Figure 3.8). The coupling constants obtained after spin simulation are given in Tables 3.5 and 3.6.

The simulated spectrum matched the experimental spectrum well except for the D ring proton resonances which, were line broadened in the latter case. This line broadening is probably due to an intermediate exchange of the chemical shifts of these resonances[22], because of a somewhat hindered rotation about the C17,C20 bond of the sidechain modulating the environment of the ring D protons, in particular the 17α proton ($\delta_{17\alpha-H} = 2.135$ ppm). The line broadening could also be a result of modulation of the coupling constants due to conformational flexibility of the D ring itself. Because of this line broadening and the strong overlap of the resonances due to the 15α and 16α protons, the error associated with the coupling constants of the D-ring protons is larger than for the other ring protons. However, these D-ring coupling constants are quite similar to those determined for other steroids[13,14,16,17], for example there is a large difference in the coupling constants of the geminal protons 15α and 15β with the 16β proton (0.5 and 10.0 Hz respectively). This tends to suggest that the conformation of the D-ring is not altered substantially from D-ring conformations of other steroids by the presence of the triene phenyl sidechain.

As far as long-range coupling is concerned, there was evidence from the COSY

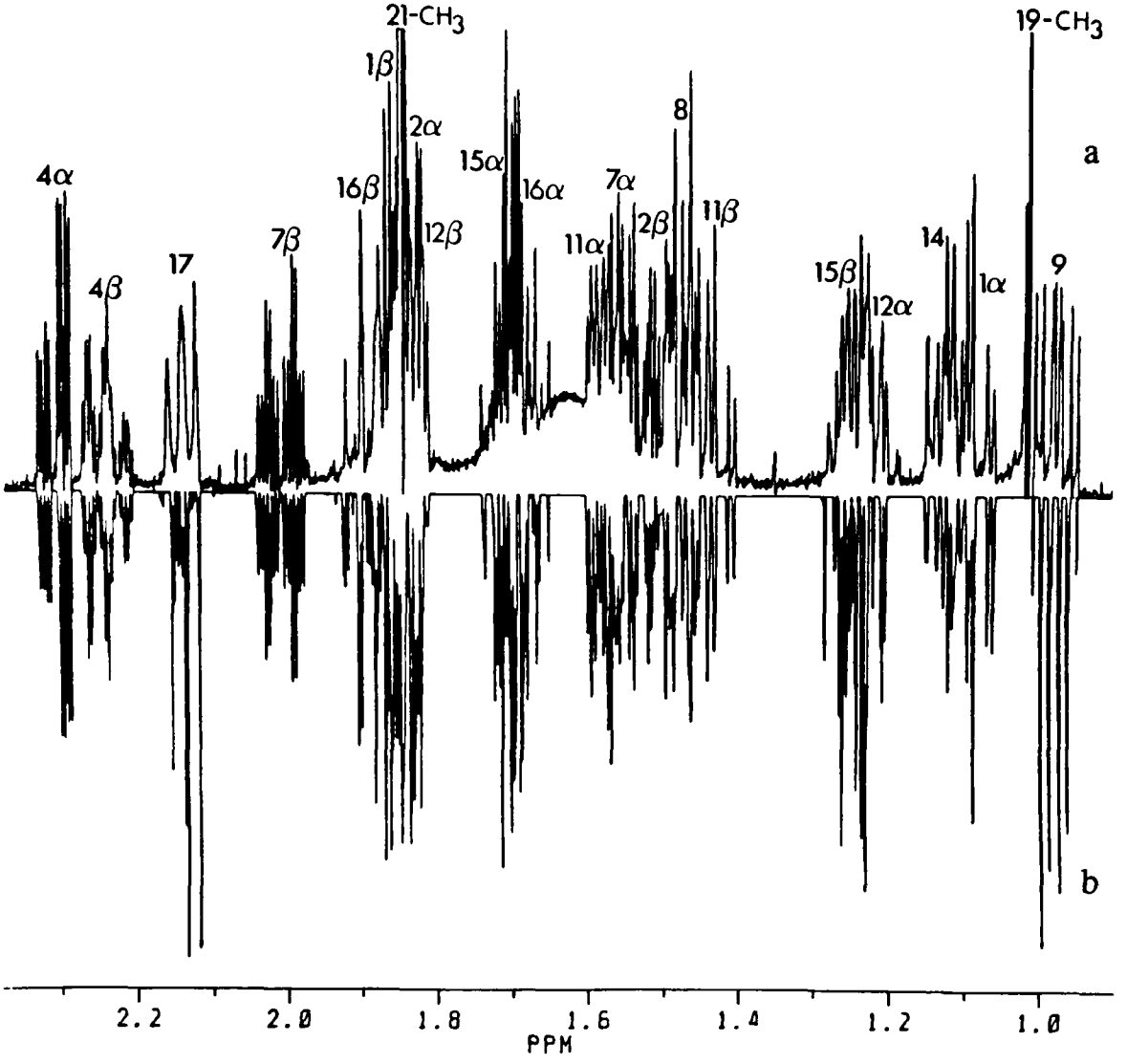

Figure 3.8: Upfield region of the 500 MHz ^{1}H NMR spectrum of **5a**. a) Experimental spectrum; b) Simulated spectrum.

Table 3.7: ^{13}C NMR chemical shifts (ppm) for cholesterol and the steroids **4a**, **4b**, **5a** and **6a**.

Carbon	Cholesterol[a,b]	**4a**[b]	**4b**[b,c]	**5a**[b]	**6a**[b,c]
1	37.3	37.29	37.30	37.29	37.29
2	31.6	31.67	31.68	31.67	31.68
3	71.6	71.80	71.79	71.80	71.77
4	42.2	42.31	42.32	42.31	42.32
5	140.6	140.84	140.84	140.84	140.85
6	121.4	121.60	121.60	121.59	121.58
7	31.9	31.85	31.84	31.85	31.85
8	31.9	32.21	32.21	32.21	32.23
9	50.2	50.36	50.35	50.35	50.37
10	36.5	36.60	36.60	36.60	36.60
11	21.1	21.08	21.08	21.07	21.08
12	39.8	38.67	38.63	38.65	38.69
13	42.3	44.49	44.59	44.57	44.54
14	56.8	56.42	56.40	56.42	56.43
15	24.3	24.40	24.39	24.41	24.42
16	28.3	24.81	24.85	24.80	24.84
17	56.2	59.55	59.72	59.61	59.60
18	11.9	13.05	13.17	13.05	13.07
19	19.4	19.44	19.44	19.44	19.44
20		139.91	141.49	140.20	140.23
21	18.8	18.71	18.58	18.67	18.79
22		125.73		125.77	
23		130.03		130.28	
24		125.73		130.88	
25				129.85	
26				130.93	
1′		138.18		137.74	
2′		126.08		126.17	
3′		128.54		128.59	
4′		126.90		127.13	
5′		128.54		128.59	
6′		126.08		126.17	

[a] from reference 1
[b] $CDCl_3$ solutions
[c] Olefinic and aromatic ^{13}C chemical shifts not determined

spectrum of ^{4}J coupling between the 18-methyl group and both the 12α and 17α proton resonances (not shown in Figure 3.7), and also between the 19-methyl group and the 1α and 9α protons (see Figure 3.7) as found in some other steroids[6,7,17]. However, there was no evidence of coupling between the 18-methyl group and the 14α proton, not even from a long range COSY experiment[2,3]. Long-range coupling between the 2α and 4α protons was also seen in the COSY spectrum (Figure 3.7), and measured from the well-separated 4α proton resonance to be 1.2 Hz. These two protons and the four σ-bonds between them are in the familiar "W" arrangement, a condition found to be necessary for long range coupling not involving a double bond[7]. This is the first known example of non-allylic/non-carbonyl long-range coupling in the steroid nucleus not involving one of the angular methyl groups.

Allylic couplings were seen between protons on either side of the C-5,C-6 double bond, as to be expected from similar studies of Δ^4 steroids[6,7]. The magnitude of the allylic coupling was greater between the 6 and 4β protons than between the 6 and 4α protons (2.7, 2.3 Hz respectively). This is in keeping with theoretical arguments[6,7] where the closer the angle between the plane of the double bond and the vinyl C-H bond is to 90°, the larger the coupling. Homoallylic coupling was also seen, between the 4β proton and both the 7α and 7β protons (see Figure 3.7). However, there was no coupling between the 4α (equatorial) proton and the 7α and 7β protons.

3.2.4 ^{13}C Chemical Shifts of 5a

Since the proton chemical shifts of **5a** were known, assignment of the ^{13}C chemical shifts of **5a** was straightforward from the ^{13}C-^{1}H shift-correlated spectrum (Figure 3.6). However, of the five quaternary carbon resonances, only the C-10 and C-13 resonances could be assigned based on literature values for other steroids[1]. The three remaining quaternary carbon resonances were separated by only 3 ppm (δ 140.85, δ 140.20 and δ 137.74). After measurement of the ^{13}C NMR spectrum for compounds **4a**, **4b** and **6a**, the 140.84 ppm resonance was assigned to C-5 due to its insensitivity to the structure of the sidechain (Table 3.7). The remaining two quaternary carbon resonances of **5a** were due to C-20 and C-1′ and were assigned after performing a Selective INEPT (Insensitive Nuclei Enhanced by Polarization

Transfer) experiment[23]. In this experiment, a specific proton resonance is saturated and the parameters for ^{13}C spectrum acquisition are such that only the carbon atom which is long-range coupled ($J_{CH} \sim 10$ Hz) to the irradiated proton is observed. In this case, upon saturation of the 21-methyl proton resonance, only the quaternary signal at 140.20 was observed and assigned to C-20 (Figure 3.5). Hence the remaining quaternary carbon resonance at 137.74 ppm was assigned to C-1′.

3.2.5 NMR Assignments of 4a, 4b and 6a

Ring ^{13}C resonances of **4a**, **4b** and **6a** were assigned by analogy to those determined for **5a** due to the similarity of the chemical shifts of the carbon signals in the four compounds (Table 3.7). The only small differences (0.17 ppm at most, for C-17) occurred for the chemical shifts of the D-ring carbons, as to be expected from the different sidechain structures.

Olefinic ^{13}C resonances of **4a** were determined from a CHORTLE experiment[24] (not from a ^{13}C-^{1}H shift-correlated spectrum due to low sample concentration) by their correlation with the known olefinic proton resonances (Table 3.7). The CHORTLE experiment also allowed the ring proton resonances of **4a** to be assigned. The resulting proton chemical shifts were very similar to those obtained for **5a** by spin simulation (Table 3.4).

Finally, the ring ^{13}C chemical shifts of cholesterol[1] have been included in Table 3.7. Comparison of these values with those measured in this work for **4a**, **4b**, **5a** and **6a** indicate that the effect of the unsaturated sidechains of these latter compounds on the cholesterol ring system is small. Hence these fluorescent steroids would seem to bear a close resemblance to cholesterol with their free 3β-OH, their cholesterol ring system and their hydrophobic sidechain, and should prove useful in fluorescence studies of cholesterol domains in membranes.

3.3 Experimental Section

All NMR measurements were performed with a Bruker AM-500 instrument at 300K. Chemical shifts are relative to internal TMS. Sample concentrations were typically 3–5 mg/0.5 ml $CDCl_3$ for 1D experiments. The 2D experiments are outlined below.

The ^1H-^1H shift-correlated spectrum (COSY) of a mixture of **5a** and **5b** was acquired and processed using the standard software provided by Bruker. The f_2 spectral width was 4000 Hz or 8 ppm. The initial (t_1,t_2) matrix of 512 × 2K real data points was zero-filled to 2K × 2K data points to give a final resolution of 1.95 Hz/point. Processing was done using sine bell squared functions and a magnitude calculation. For each FID, 32 transients were accumulated requiring a total acquisition time of 16 hours. Sample concentration was 25 mg/0.5ml $CDCl_3$.

The COSY spectrum of **5a** was acquired with an f_2 spectral width of 1400 Hz or 2.8 ppm. The initial (t_1,t_2) matrix of 256 × 1K real data points was zero-filled to 1K × 1K data points to give a digital resolution of 1.37 Hz/point. Data manipulation was done using sine bell functions and a magnitude calculation. For each FID, 64 transients were accumulated. Sample concentation was 40 mg/0.5 ml of $CDCl_3$.

The ^{13}C-^1H shift-correlated spectrum of **5a** with proton decoupling in the f_1 domain was obtained with the usual pulse sequence[25,26,27]. The spectral widths were 4000 Hz (8 ppm) in f_1 and 18500 Hz (~145 ppm) in f_2. The initial (t_1,t_2) matrix of 256 × 1K real data points was zero-filled to 1K × 2K data points to give a digital resolution of 4 Hz/point and 9 Hz/point in the f_1 and f_2 domains respectively. Processing was done using gaussian window functions in both domains and a power spectrum calculation. For each FID, 800 transients were accumulated for a total acquisition time of 60 hours.

NOe difference spectra of **4a**, **4b**, **5a** and **6a** were obtained using spectral widths of 5000 Hz (10 ppm) and 8K real data points, to give a digital resolution of 0.6 Hz/point. Each line in a multiplet was irradiated sequentially[28,28] for a total irradiation time of 2 s per multiplet.

The ^1H J-resolved spectrum of **5a** was acquired with spectral widths of 1000 Hz (2 ppm) and 31.25 Hz in the f_2 and f_1 domains respectively. The initial (t_1,t_2)

matrix of 32K × 2K real data points was zero-filled to 64 × 2K data points to give a digital resolution of 0.49 Hz/point in both dimensions. Processing was done with sine bell window functions and a magnitude calculation.

The CHORTLE analysis of **4a** (5 mg/0.5 ml $CDCl_3$) was performed using the pulse sequence of Pearson[24], with four proton evolution times of 0.24, 1.00, 2.40 and 3.20 ms and 14000 transients per point.

All ^{13}C spectra, including the DEPT spectrum of **5a** (for the pulse sequence used see Ref. 30), were acquired with spectral widths of 31250 Hz (250 ppm), 16K real data points and 12000 transients. The selective INEPT spectrum of **5a** was acquired using the pulse sequence of Bax[23] except that there was no ^{1}H broadband decoupling, and no refocussing of the ^{13}C resonances due to hardware restrictions in switching from high to low power. A total of 1680 transients were accumulated.

Spectral simulations were made using the PANIC program provided by Bruker. The quality of the simulations was judged by visual comparison with the experimental spectra.

3.4 References

1. J.W. Blunt and J.B. Stothers, *Org. Magn. Reson.*, **1977**, *9*, 439–464.

2. A. Bax, *Two-Dimensional Nuclear Magnetic Resonance in Liquids*, D. Reidel, Holland, **1982**.

3. R. Benn and H. Gunther, *Angew. Chem. International Edition*, **1983**, *22*, 350–380.

4. G. Englert, *Pure Appl. Chem.*, **1985**, *57*, 801–821.

5. J. Wernly and J. Lauterwein, *J. Magn. Reson.*, **1986**, *66*, 355–358, and references therein.

6. N.S. Bhacca and D.H. Williams, *"Applications of NMR Spectroscopy in Organic Chemistry"*, Holden-Day, San Francisco, **1966**, p. 108.

7. L.M. Jackman and S. Sternhell, *"Applications of Nuclear Magnetic Resonance Spectroscopy in Organic Chemistry"*, Pergamon, Oxford, **1969**, p. 316.

8. J.H. Noggle and R.E. Schirmer, *"The Nuclear Overhauser Effect"*, Academic Press, N.Y., **1971**.

9. W. Brugel, *"Handbook of NMR Spectral Parameters"*, Heyden, London, **1979**, Vol. 2, p. 455.

10. S.P. Sawan, T.L. James, L.D. Gruenke and J.C. Craig, *J. Magn. Reson.*, **1979**, *35*, 409–413.

11. C.D. Barry, C.M. Dobson, D.A. Sweigart, L.E. Ford and R.J.P. Williams. in *"Nuclear Magnetic Resonance Shift Reagents"*, ed. R.J. Sievers, Academic Press, N.Y., **1973**, pp. 173–195.

12. R. Freeman and G.A. Morris, *Bull. Magn. Reson.*, **1979**, *1*, 5–26.

13. L.D. Hall and J.K.M. Sanders, *J. Am. Chem. Soc.*, **1980**, *102*, 5703–5711.

14. R.D. Farrant, D.N. Kirk, J.D. Mersh and J.K.M. Sanders, *J. Steroid Biochem.*, **1983**, *19*, 181–187.

15. T.C. Wong and V. Rutar, *J. Am. Chem. Soc.*, **1984**, *106*, 7380–7384.

16. A.G.J. Sedee, G.M.J. Beijersbergen Van Henegouwen, W. Guijt and C.A.G. Hasnoot, *J. Chem. Soc., Perkin Trans. II*, **1984**, 1755–1759.

17. H.J. Schneider, U. Buchheit, N. Becker, G. Schmidt and U. Siehl, *J. Am. Chem. Soc.*, **1985**, *107*, 7027–7039.

18. M. Savignac, G.Jaouen, C.A. Rodger, R.E. Perrier, B.G. Sayer, and M.J. McGlinchey, *J. Org. Chem.*, **1986**, *51*, 2328–2332.

19. H. Duddeck, D. Rosenbaum, M. Mani, A. Elgamal and M.B.E. Fayez, *Magn. Reson. Chem.*, **1986**, *24*, 999–1003.

20. R.D. Dawe and J.L.C. Wright, *Can. J. Chem.*, **1987**, *65*, 666-669.

21. M. Karplus, *J. Chem. Phys.*, **1959**, *30*, 11–15.

22. R.A. Dwek, *"Nuclear Magnetic Resonance in Biochemistry"*, Clarendon, Oxford, **1975**, p. 38.

23. A. Bax, *J. Magn. Reson.*, **1984**, *57*, 314–318.

24. G.A. Pearson, *J. Magn. Reson.*, **1985**, *64*, 487–500.

25. A. Bax, *J. Magn. Reson.*, **1983**, *53*, 517–520.

26. V. Rutar, *J. Magn. Reson.*, **1984**, *58*, 306–310.

27. J. Wilde and P.H. Bolton, *J. Magn. Reson.*, **1984**, *59*, 343–346.

28. D. Neuhaus, *J. Magn. Reson.*, **1983**, *53*, 109–114.

29. M. Kinns and J.K.M Sanders, *J. Magn. Reson.*, **1984**, *56*, 518–520.

30. D.M. Doddrell, D.T. Pegg and M.R. Bendall, *J. Magn. Reson.*, **1982**, *48*, 323–327.

Chapter 4

Photophysics of the Aryl Polyene Sidechains of Cholesterol Analogue Probes

4.1 Introduction

An understanding of the photophysics of the sterol probes DPC, TPC and DNC (formerly **4a**, **5a** and **6a** respectively, see Figure 4.1), in well defined systems such as organic solvents, is necessary in order to be able to interpret fluorescence data obtained from the probes incorporated in biological membranes. It is only from studying the response of the fluorescence properties of the three probes to variables such as excitation and emission wavelength, solvent polarity and viscosity, and temperature, that an appreciation can be had of the type of information that each probe could give in a membrane environment.

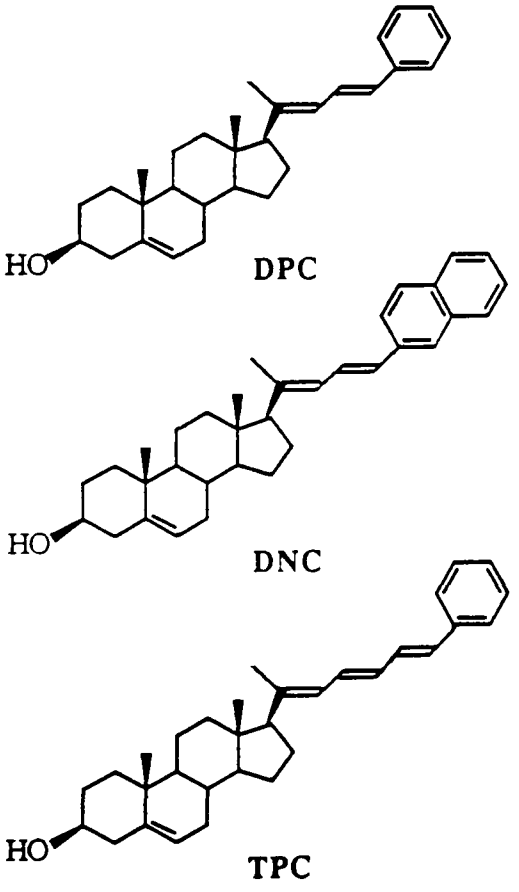

Figure 4.1: DPC, TPC and DNC.

A brief outline follows of the fluorescence process and the various photophysical parameters which can be measured or derived from fluorescence measurements[1-3].

4.1.1 Fluorescence Parameters

Fluorescence is the radiative process that can deactivate an electronically excited molecule, leading to a lower electronic state of the same multiplicity. Usually fluorescence occurs between the first excited singlet state S_1^* and the ground singlet state S_0. S_1^* is generally reached by the absorption of a photon (subject to various selection rules[4]) which promotes an electron from the highest occupied molecular orbital (HOMO) to the lowest unoccupied molecular orbital (LUMO), with the retention of spin orientation such that the two unpaired electrons have opposite spin. In solution, if absorption into S_2^* or higher excited singlet states occurs, vibrational relaxation within a given state and internal conversion between states occur so rapidly that, within a picosecond, the population of excited molecules is generally in the lowest vibrational level of the first excited singlet state S_1^* (see Jablonski diagram, Figure 4.2).

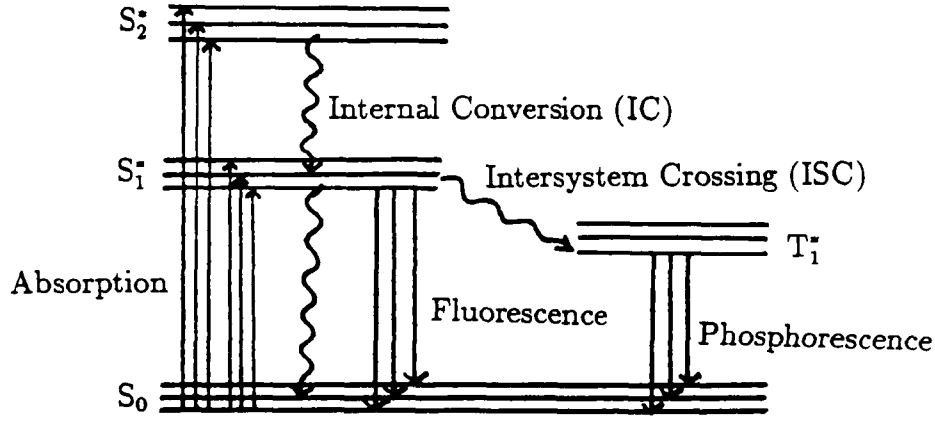

Figure 4.2: Jablonski diagram showing some of the processes which can compete with fluorescence.

Fluorescence is only one of the processes by which electronically excited molecules in S_1^* can lose their excess energy. Other processes include intersystem crossing to an excited triplet state T_n^*, internal conversion to the ground singlet state S_0, collisional deactivation by solvent molecules or by dissolved oxygen in solution, and various photoreactions such as photoisomerization. These various competing processes are

depicted in equations 4.2–4.6.

$$^1M + h\nu \xrightarrow{I_a} {}^1M^* \quad \text{absorption} \tag{4.1}$$

$$^1M^* \xrightarrow{k_f} {}^1M + h\nu' \quad \text{fluorescence} \tag{4.2}$$

$$^1M^* \xrightarrow{k_{ISC}} {}^3M^* \quad \text{intersystem crossing} \tag{4.3}$$

$$^1M^* \xrightarrow{k_{IC}} {}^1M \quad \text{internal conversion} \tag{4.4}$$

$$^1M^* \xrightarrow{k_p} P \quad \text{photoreaction} \tag{4.5}$$

$$^1M^* + Q \xrightarrow{k_q} {}^1M \quad \text{collisional deactivation or quenching} \tag{4.6}$$

The rate of deactivation of the molecules is S_1^* is thus given by equation 4.7

$$\frac{-d[^1M^*]}{dt} = I_a - (k_f + k_{ISC} + k_{IC} + k_p + k_q[Q])[^1M^*] \tag{4.7}$$

where I_a is the intensity in einsteins $dm^{-3}s^{-1}$ of absorbed photons. The fluorescence quantum yield, ϕ_f, is defined as the ratio of the number of photons emitted as fluorescence to the number of photons absorbed (equation 4.8)

$$\begin{aligned} \phi_f &= \frac{\text{number of photons emitted as fluorescence}}{\text{number of absorbed photons}} \\ &= \frac{k_f[^1M^*]}{I_a} \end{aligned} \tag{4.8}$$

Under steady-state conditions ($d[^1M^*]/dt = 0$), it follows that

$$\begin{aligned} \phi_f &= \frac{k_f[^1M^*]}{(k_f + k_{ISC} + k_{IC} + k_p + k_q[Q])[^1M^*]} \\ &= \frac{k_f}{k_f + k_{nr}} \end{aligned} \tag{4.9}$$

where k_{nr} = nonradiative rate constant
= sum of all the rate constants for nonradiative deactivation of the excited state.

Hence the fluorescence quantum yield is a measure of the efficiency of the fluorescence process compared with the other mechanisms for deactivation of the excited state. This parameter is measured under steady-state conditions using a fluorimeter (see section 4.2.1, for details).

A second fluorescence parameter known as the singlet lifetime, τ_s, is measured under transient conditions, in a so-called 'time-resolved' fluorescence experiment.

Upon excitation at time $t = 0$ by an infinitely narrow δ-function light pulse, there exists an initial concentration of excited molecules $[^1M^*]_0$. The rate of deactivation of these molecules at time $t > 0$ is given by equation 4.10.

$$\frac{-d[^1M^*]}{dt} = (k_f + k_{nr})[^1M^*] \tag{4.10}$$

So, at any time t, the concentration of excited molecules $[^1M^*]_t$ is

$$[^1M^*]_t = [^1M^*]_0 e^{-(k_f + k_{nr})t} \tag{4.11}$$

The average singlet lifetime, τ_s, is then defined as the time for the concentration of excited molecules in the excited singlet state to reach $1/e$ of its initial value $[^1M^*]_0$. It can thus be seen that τ_s is equal to the inverse of the sum of all the rate constants for deactivation of the excited state (equation 4.12).

$$\tau_s = \frac{1}{k_f + k_{nr}} \tag{4.12}$$

Singlet lifetimes can be measured using either the time-correlated single photon counting method (for details see section 4.2.2), or frequency domain instrumentation.

Knowledge of the fluorescence quantum yield ϕ_f and the singlet lifetime τ_s enables the radiative rate k_f (and hence the radiative lifetime $\tau_f = 1/k_f$) to be determined (equation 4.13).

$$\begin{aligned} \phi_f &= \frac{k_f}{k_f + k_{nr}} \\ &= k_f \cdot \tau_s \end{aligned} \tag{4.13}$$

This in turn allows the nonradiative rate k_{nr} to be derived (see equation 4.12).

4.1.2 The Utility of Fluorescence Probes

Information from Steady-State Fluorescence Experiments

a) Fluorescence Quantum Yield ϕ_f

The fluorescence quantum yeild, ϕ_f, of a probe is generally desired to be reasonably high, preferably 0.1 or greater. This allows for low levels of incorporation of probe material in the membrane or other biological system under study, thus

minimizing any perturbation of the system by the extrinsic probe. Despite this, a useful property of a fluorescence probe is if its ϕ_f varies markedly with solvent polarity. This is the case for the family of anilino-naphthalene sulphonates and 1,8-anilino-naphthalene sulphonate (ANS) in particular. The fluorescence quantum yield of ANS is negligible in a polar solvent such as water ($\phi_f = 0.009$), whereas it is high in a nonpolar solvent such as dioxane ($\phi_f = 0.68$)[5]. This sensitivity to polarity can be used, for example, to determine the degree of exposure of probe to solvent (i.e. water) in the interiors of bilayer membranes or at binding sites in enzymes[5,6], or to follow changes in membrane surface potential[7].

If the fluorescence quantum yield of a probe varies with excitation wavelength (after correctly accounting for all experimental artifacts, see section 4.2.1), this is an important indication that there may be at least two different probe populations. If the excitation-wavelength dependence of ϕ_f is observed in a homogeneous solvent, then these populations may arise from the presence of single bond conformers/rotamers in the ground state which have slightly different absorption spectra. In a heterogeneous system such as a membrane, two different populations could also arise from the probe existing in two different environments. This is just one example that highlights the need for a careful study of the photophysics of a fluorescence probe in solvents, in order to comment on whether excitation-wavelength dependent fluorescence quantum yields in membranes originate from different conformational states or environmental properties. Note, however, that an excitation-wavelength independent ϕ_f does not necessarily imply that there is only one probe population.

Fluorescence quantum yield measurements of fluorescence probes are also useful in obtaining distance measurements between two non-identical chromophores in various systems[3,8,9]. This is possible due to the phenomenon of resonance energy transfer, which involves the nonradiative transfer of electronic energy from an excited donor molecule to a ground state acceptor molecule, promoting it to an excited singlet state. This process occurs by a dipole-dipole mechanism in which the donor emission oscillator interacts with the acceptor absorption oscillator. Hence, the extent of resonance energy transfer will depend on the separation of the donor and acceptor chromophores to the inverse sixth power. Also important is the extent of spectral overlap of the donor emission spectrum and the acceptor absorption

spectrum (known), a sufficiently long donor singlet lifetime τ_s, and the angular orientation of the two chromophores (this can be satisfactorily approximated).

The energy transfer efficiency, E, can be determined by measuring the change in fluorescence quantum yield of the donor probe in the presence $[\phi_f(da)]$ and absence $[\phi_f(d)]$ of the acceptor chromophore (equation 4.14).

$$E = 1 - \frac{\phi_f(da)}{\phi_f(d)} \tag{4.14}$$

This energy transfer efficiency is then related to the separation or distance r between the two chromophores by equation 4.15

$$E = \frac{R_0^6}{R_0^6 + r^6} \tag{4.15}$$

where R_0 is a constant whose value depends on the spectral overlap and orientation factors mentioned above as well as on $\phi_f(d)$. Such measurements have, for example, allowed studies of the extent of interaction of various proteins and peptides containing tryptophan with model membranes containing fluorescent lipid probes[10-11], or the binding of fluorescent drugs such as adriamycin to both synthetic and natural membranes[12].

b) Spectral Shape and Position

Considerable insight into the photophysics of fluorescence probes can be gained from measurement of their steady-state absorption and fluorescence emission and excitation spectra in organic solvents, as functions of variables such as temperature, solvent polarizability and emission/excitation wavelength. An appreciation of the photophysics of fluorescence probes is required in order to draw conclusions from similar measurements in membranes.

Change in emission spectral shape with temperature can indicate that there is either dual emission from two states in thermal equilibrium, or that a conformeric equilibrium exists in the ground state. For example, the increased importance with increasing temperature of a weak fluorescence band on the high-energy side of the emission spectrum of diphenylhexatriene (DPH, see Figure 4.3) has been attributed to thermal repopulation of S_2^* from S_1^* (see kinetic scheme, Figure 4.4)[13-16] due to

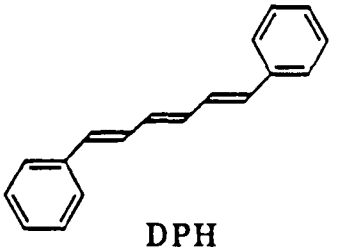

DPH

Figure 4.3: DPH

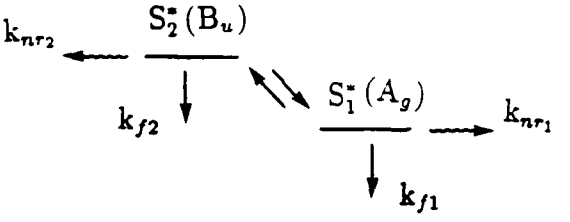

Figure 4.4: Kinetic scheme used to interpret the temperature dependence of the emission spectrum of DPH[16].

the known proximity of these two excited states from one-[17–19] and two-[20,21] photon absorption studies, as well as from molecular orbital calculations[22,23].

Spectra measured at very low temperatures can give additional information. Vibrationally resolved absorption and emission spectra of probes embedded in matrices at 4K can indicate whether a probe is planar or nonplanar by noting the presence (nonplanar) or absence (planar) of low frequency, $\sim 50 cm^{-1}$, vibrational modes in the vibrational development of the spectra. The nature or symmetry of the emitting state can also be determined by studying the high frequency vibrational progressions in a low temperature, highly-resolved emission spectrum.

Absorption, excitation and emission spectra can shift with solvent ***polarizability***, α_s, which is related to the solvent refractive index, η_D, by equation 4.16[13–15].

$$\alpha_s = \frac{\eta_D^2 - 1}{\eta_D^2 + 2} \tag{4.16}$$

This can lead to insight into the nature of the absorbing and emitting states, since spectral shifts are expected with change in α_s only for strongly allowed transitions,

because of their associated large electric dipole moments. For example, the emission maximum of DPH, unlike the absorption maximum, is insensitive to solvent polarizability[15,18,19]. This has been attributed to the presence of a low-lying excited electronic state below the one reached by absorption, whose radiative transition to the ground state is forbidden. Time-resolved fluorescence studies (see below) allowed a further understanding of the photophysics of this molecule.

Emission spectra can also be very sensitive to solvent *polarity*, generally shifting to longer wavelengths (lower energies) with increasing polarity. This sensitivity of emission spectral position with solvent polarity can be used in much the same way as solvent dependent fluorescence quantum yields, in studies of accessibility of membrane bilayer interiors to solvent, for example.

Variation of both emission and excitation spectral shape with excitation and emission wavelengths, respectively, is strong evidence that the fluorescence probe either exists in more than one conformation in the ground state, or in a number of different environments, as mentioned earlier concerning excitation wavelength dependent quantum yields of fluorescence.

Information from Time-Resolved Fluorescence Experiments

Time-resolved fluorescence measurements complement steady-state measurements and together they allow the rate constants for radiative and nonradiative decay of the probe to be determined. The absolute values of these rate constants, and their response to external variables such as solvent polarity and viscosity, and temperature, can give further important insight into the nature of the emitting state and the types of nonradiative processes competing with fluorescence.

The *radiative* rate, k_f, of DPH in organic solvents, for example, was found to be smaller than expected for emission from an excited singlet state of B_u symmetry[18,19]. It is known that the low energy absorption band of DPH is due to a strong, one-photon allowed $\pi \rightarrow \pi^*$ transition from the ground state, S_0, of A_g symmetry, to the lowest B_u excited state. Likewise, the reverse $1B_u \rightarrow 1A_g$ transition is also strongly allowed and should be associated with a high k_f value. So a low k_f value suggested that emission was occurring from an excited state of lower energy than the $1B_u$ state, and whose radiative transition to the $1A_g$ ground state was less allowed or

even forbidden. Subsequent two-photon absorption studies allowed assignment of S_1^* as the $2A_g$ state[20,21], since $A_g \rightarrow A_g$ transitions are two-photon allowed but one photon forbidden. Hence, the fairly long τ_{rad} of S_1^* (i.e. small k_f), and the proximity of S_1^* and S_2^* (ΔE= 630 cm^{-1} in hexane[17]), could allow an excited state equilibrium to be established between the two states. This assignment of the nature of S_1^* and S_2^* of DPH not only accounted for the observed low radiative rate, but also for the dual fluorescence alluded to earlier, and the insensitivity of the maximum of DPH to solvent polarizability.

By studying the dependence of the *nonradiative* rate constant of a probe on solvent viscosity, it can be ascertained whether collisional deactivation or a photoreaction involving twisting, such as photoisomerization, is occurring in the deactivation of S_1^*. Viscosity independent nonradiative rate constants indicate that another mechanism such as intersystem crossing or internal conversion must be invoked as the nonradiative decay channel. If photoisomerization is the only nonradiative process occurring, the internal energy barrier to twisting about the double bond, E_0, can be measured from the temperature dependence of the nonradiative rate constant, obtained at constant viscosity (so-called isoviscosity conditions), using the Arrhenius equation (equation 4.17)[24].

$$k_{nr} = Ae^{E_o/RT} \tag{4.17}$$

Time resolved fluorescence spectroscopy is also a very useful tool in studying heterogeneity of probe conformation or environment, since this is usually manifested in multiexponential fluorescence decay kinetics. With the advent of global analysis techniques (see section 4.2.3), closely spaced singlet lifetime values can be resolved, as well as small contributions to the overall fluorescence. Consequently, time-resolved studies tend to be more definitive than steady-state measurements in unveiling the existence and origin of probe heterogeneity.

4.1.3 Fluorescence Analysis of a Conformeric Mixture

As discussed in the previous section, the presence of multiexponential fluorescence decay kinetics, and excitation wavelength dependent emission spectra and fluorescence quantum yields, is strong evidence that a fluorescence probe exists in more

than one environment and/or conformation.

This has been observed for 1-Phenyl-2-(2′-naphthyl)ethene (PNE, see Figure 4.5) in solution[26–34]. Moreover, the two singlet lifetimes (~25 ns and ~3 ns) obtained for the fit of the fluorescence decay profile of PNE, were seen to be associated with different excitation and emission spectra[27,28,31,32,34]. The longer lifetime component was associated with the main absorption band and a structured emission spectrum. On the other hand, the shorter lifetime was correlated with a relatively weak absorption on the low energy (red edge) side of the total absorption spectrum, and with a lower energy emission band than that associated with the long lifetime. The evidence for this association was obtained from λ_{ex} and λ_{em} dependent pre-exponential factors (equation 4.18), and from quenching studies in which the spectra associated with the longer lifetime were preferentially quenched.

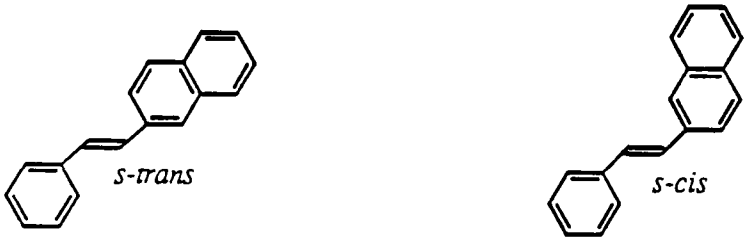

t-PNE *c*-PNE

Figure 4.5: PNE

It was proposed that the above observations were consistent with a ground-state equilibrium between *s-cis (c)* and *s-trans (t)* rotamers of PNE about the single bond connecting the naphthyl and ethylene moieties (Figure 4.5). Support for this hypothesis at first came from low temperature fluorescence studies of PNE at 4K in polycrystalline *n*-hexane matrices[35]. Under these conditions, the emission spectrum was resolved into one quasiline fluorescence, and a second diffuse fluorescence with a lower energy 0-0 transition which was preferentially obtained upon excitation into the red edge of the absorption spectrum. The *s-trans* conformer of PNE was expected to be planar, and hence exhibit sharp line spectra at low temperature. In contrast, the *s-cis* conformer was expected to be nonplanar and hence it would have diffuse low temperature spectra because of progressions in low frequency modes. A difference in planarity of the two conformers was expected due to the difference

in the H-3′,H-1 (longer) and H-1′,H-2 (shorter) distances as a consequence of the different naphthalenic bond lengths (C-1,C-2: 1.37Å; C-2,C-3: 1.43Å)[36,37]. Hence, the long lifetime and its associated structured emission spectrum were attributed to *s-trans* PNE, while the short lifetime, with its associated lower energy (red shifted) absorption and emission spectra, was attributed to *s-cis* PNE.

More conclusive evidence as to the identity of the two PNE species was obtained through a photophysical study of conformationally restricted analogues of PNE, referred to as MPE and BPE (see Figure 4.6)[33]. In MPE, the fluorophore is restricted to the *s-cis* conformation through the presence of a methyl substituent at the 3′ position of the naphthyl group which has an unfavourable steric interaction with H-2 in the *s-trans* conformation. BPE is obviously an analogue for the *s-trans* rotamer of PNE. Both MPE and BPE have λ_{ex} independent emission spectra, while the emission spectrum of BPE is at higher energy than that of MPE (after taking into account a slight red shift due to the presence of the five-membered ring). These emission spectra were compared to pure component emission spectra of PNE obtained through steady-state fluorescence quenching experiments, using principal component analysis. The emission spectrum of MPE closely resembled that associated with the shorter singlet lifetime (i.e. the less quenched spectrum) while the emission spectrum of BPE resembled the more quenched spectrum. On this basis, the conformational assignment reached for the two lifetime components of PNE through the low temperature fluorescence study cited above, was confirmed.

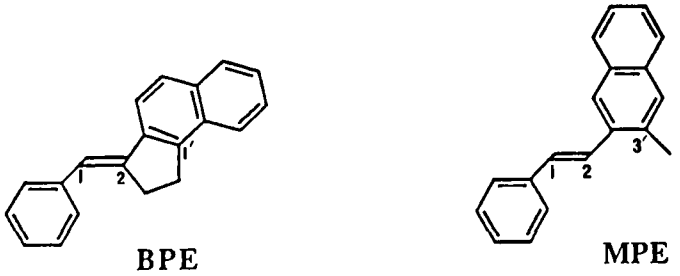

BPE MPE

Figure 4.6: MPE and BPE

Molecular orbital calculations have been made of the energy levels, oscillator strengths and degree of mixing of the lowest excited states of *s-cis* and *s-trans* PNE. Comparison of these results with the experimental data further confirmed the above conformational assignment[32].

It can be expected that, because of the structural similarity of PNE to the fluorophore in DNC, a ground-state conformeric equilibrium will be observed about the C-24,C-2′ single bond of DNC. Consequently, an outline of how fluorescence measurements can be analyzed to yield information about rotameric mixtures is presented below[28,32,38].

If one assumes that there is Non-Equilibration of Excited Rotamers (the so-called NEER principle) upon electronic excitation of a ground state rotamer population[39], then it is possible from the values of the pre-exponential factors α_i, defined by equation 4.18 for a biexponential sample fluorescence decay function $F_s(t)$

$$F_s(t) = \alpha_1 e^{-t/\tau_1} + \alpha_2 e^{-t/\tau_2} \tag{4.18}$$

to calculate the fraction of excited molecules of each conformation, f_i (equation 4.19).

$$F_s(t) = \frac{f_1(\lambda_{ex})F_1(\lambda_{em})e^{-t/\tau_1}}{\tau_1} + \frac{f_2(\lambda_{ex})F_2(\lambda_{em})e^{-t/\tau_2}}{\tau_2} \tag{4.19}$$

F_i = fluorescence intensity of conformer i and is easily determined if there is an isoemissive point in the fluorescence spectrum of the probe; i.e. a particular emission wavelength at which the fluorescence intensity remains constant upon excitation with equal numbers of absorbed quanta at all excitation wavelengths. Otherwise, $F_i(\lambda_{em}')$ can be calculated from the relationships[38]

$$F_1(\lambda_{em}') = \frac{\sigma_1(\lambda_x)\sigma_2(\lambda_y) - \sigma_1(\lambda_y)\sigma_2(\lambda_x)}{\sigma_2(\lambda_y) - \sigma_2(\lambda_x)} \tag{4.20}$$

$$F_2(\lambda_{em}') = \frac{\sigma_1(\lambda_x)\sigma_2(\lambda_y) - \sigma_1(\lambda_y)\sigma_2(\lambda_x)}{\sigma_1(\lambda_x) - \sigma_1(\lambda_y)} \tag{4.21}$$

$$\text{where} \quad \sigma_1(\lambda_{ex}) = \frac{\alpha_1(\lambda_{ex}, \lambda_{em}')\tau_1\overline{F}(\lambda_{ex}, \lambda_{em}')}{\alpha_1(\lambda_{ex}, \lambda_{em}')\tau_1 + \alpha_2(\lambda_{ex}, \lambda_{em}')\tau_2} \tag{4.22}$$

$$\text{and} \quad \sigma_2(\lambda_{ex}) = \frac{\alpha_2(\lambda_{ex}, \lambda_{em}')\tau_2\overline{F}(\lambda_{ex}, \lambda_{em}')}{\alpha_1(\lambda_{ex}, \lambda_{em}')\tau_1 + \alpha_2(\lambda_{ex}, \lambda_{em}')\tau_2} \tag{4.23}$$

$\overline{F}(\lambda_{ex}, \lambda_{em}')$ is the total fluorescence intensity of the probe conformeric mixture at a particular emission wavelength λ_{em}'. In order to compare values of $\overline{F}$ obtained at various excitation wavelengths λ_{ex}, the fluorescence spectra must be measured with the same number of absorbed quanta at each λ_{ex}.

Once the fractions of excited molecules, $f_i(\lambda_{ex})$ have been determined, the fluorescence quantum yield associated with each conformer, ϕ_{fi}, can be calculated

from the total fluorescence quantum yield $\bar{\phi}_f$ at the same excitation wavelengths (equation 4.24).

$$\bar{\phi}_f(\lambda_{ex}) = f_1(\lambda_{ex})\phi_{f1} + f_2(\lambda_{ex})\phi_{f2} \tag{4.24}$$

Then, in conjunction with the singlet lifetime values, the radiative and nonradiative rate constants for deactivation of the individual conformers can be obtained.

Knowledge of the relative excited state concentrations of the conformers allows calculation of their relative abundances, c_1/c_2, in the ground state through equation 4.25

$$\frac{f_1(\lambda_{ex})}{f_2(\lambda_{ex})} = \frac{\varepsilon_1(\lambda_{ex})c_1}{\varepsilon_2(\lambda_{ex})c_2} \tag{4.25}$$

if the absorption or excitation spectrum of each rotamer can be obtained independently (see section 4.2.3, Indirect Excitation Decay Associated Spectra). The enthalpy difference between the conformers in the ground state can be estimated from the Boltzmann distribution (neglecting entropy terms, equation 4.26).

$$\frac{c_1}{c_2} = e^{-(E_1 - E_2)/RT} = e^{-\Delta H_{12}/RT} \tag{4.26}$$

All of the above analysis assumes that each singlet lifetime is associated with only one conformer; in other words that the lifetime value is a function of rate constants for deactivation of a single conformer. This is equivalent to the NEER principle introduced earlier which has been found to hold in the majority of cases including for some molecules in their excited triplet states (for exceptions see refs. 40,41). The general validity of the NEER principle can be intuitively accepted since in electronically excited states of conjugated molecules, the single bonds acquire some double bond character, resulting in a barrier to *s-cis/s-trans* conformational change of typically 5–10 kcal mol^{-1} [29]. Then, since the lifetime of the excited state is very short, there is generally insufficient time for excited state equilibration of the rotamers to occur.

4.2 Experimental Section

The solvents used in the absorption and fluorescence studies were 2,2,4-trimethylpentane (TMP, Caledon), methylcyclohexane (MCH, Caledon), *n*-butanol (*n*-BuOH, Fisher) and methanol (MeOH, Caledon), and were of the highest purity grade available. Heavy (H) and light (L) mineral oils (Drug Trading Company) were purified by silica gel chromatography (two passes) using activated silica gel 60 (70–230 mesh, Merck). Kinematic viscosities and densities of the two oils, and mixtures thereof (heavy oil/light oil 50/50 v/v, designated H1L1; heavy oil/light oil 75/25 v/v, designated H3L1), were measured by technical staff in the Fuels and Lubricants Laboratory, Division of Mechanical Engineering, National Research Council of Canada. All solvents and oils were checked for fluorescent impurities before use.

Volumetric flasks and 1 cm suprasil quartz cells (Hellma) were cleaned successively with chromic acid, ammonium hydroxide, doubly distilled water and spectrograde methanol before use to ensure no contamination of solutions of the sterol probes. If necessary (in order to eliminate oxygen quenching of fluorescence), solutions were degassed by several freeze-pump-thaw cycles or by pumping under vacuum (1 mm) in a dessicator for 1 h (oil solutions only).

4.2.1 Steady-State Absorption and Fluorescence Measurements

Absorption and fluorescence excitation and emission spectra were measured on a Varian DMS-200 UV/visible spectrophotometer and an SLM 8000C spectrofluorimeter (equipped with a Neslab RTE-5DD temperature controller) respectively. Fluorescence excitation and emission spectra were collected with no polarizer in the excitation beam, and with a Glan Thompson polarizer in the emission beam oriented at 35.3° to the vertical, in order to eliminate any polarization bias of the fluorescence (equations 4.27–4.29)[42].

For natural light,

$$I_{total} = I_x + I_y + I_z = 2I_x + I_y \tag{4.27}$$

$$I_{viewed} = I_x \cos^2\theta + I_y \cos^2(90 - \theta) \tag{4.28}$$

and will be proportional to I_{total} if

$$\frac{\cos^2\theta}{\cos^2(90-\theta)} = \frac{1}{\tan^2\theta} = 2, \text{ i.e. } \theta = 35.3°. \tag{4.29}$$

All fluorescence intensity measurements were made relative to a reference photomultiplier with rhodamine in ethylene glycol as the emitter, to correct for any intensity fluctuations of the xenon arc lamp excitation source. Spectra were blank-subtracted to eliminate distortions by solvent Raman bands or scattered light.

It was found that excitation spectra required correction owing to the variation of polarization of the incident beam with excitation wavelength. This was because the polarization varied with wavelength from the excitation double monochromator. This would not be correctly registered by the reference photomultiplier since the light which it monitored was split off from the main excitation beam by a beam splitter which preferentially reflected vertically polarized light. The excitation correction was made by placing an optically dense solution of rhodamine in ethylene glycol in a triangular cell in the sample holder so that excitation was on the hypotenuse and the emission detected through the solution. The excitation spectrum of rhodamine was measured through a Corning 2-62 filter at an emission wavelength of 640 nm. It was reasonably assumed that since the optical density of the rhodamine solution was high, all light that was incident on it was absorbed so that the variation of the intensity of fluorescence was due only to the intensity variation of the excitation light with wavelength. It was also assumed that the fluorescence quantum yield of rhodamine was independent of excitation wavelength. All spectra were then corrected by dividing by this rhodamine excitation spectrum (Figure 4.7).

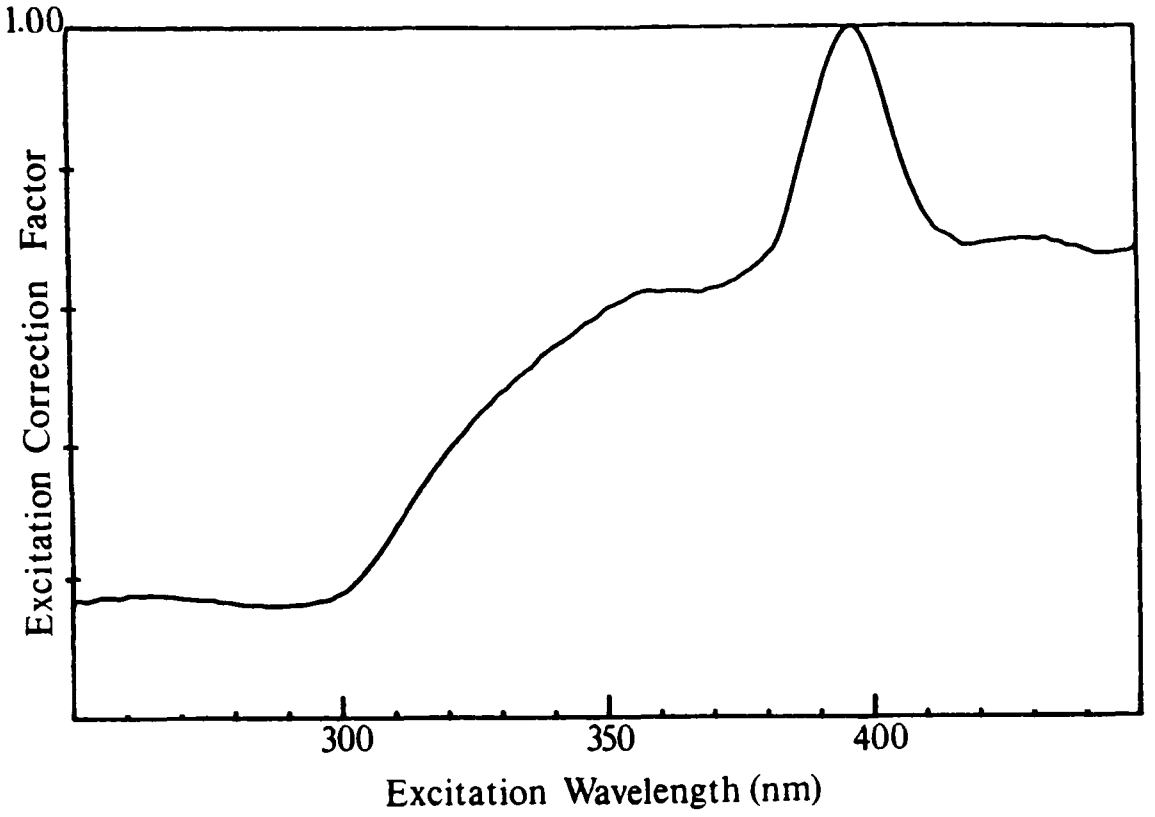

Figure 4.7: Rhodamine excitation spectrum (λ_{em}640 nm, no excitation polarizer, emission polarizer 35.3°), or excitation spectral correction factors.

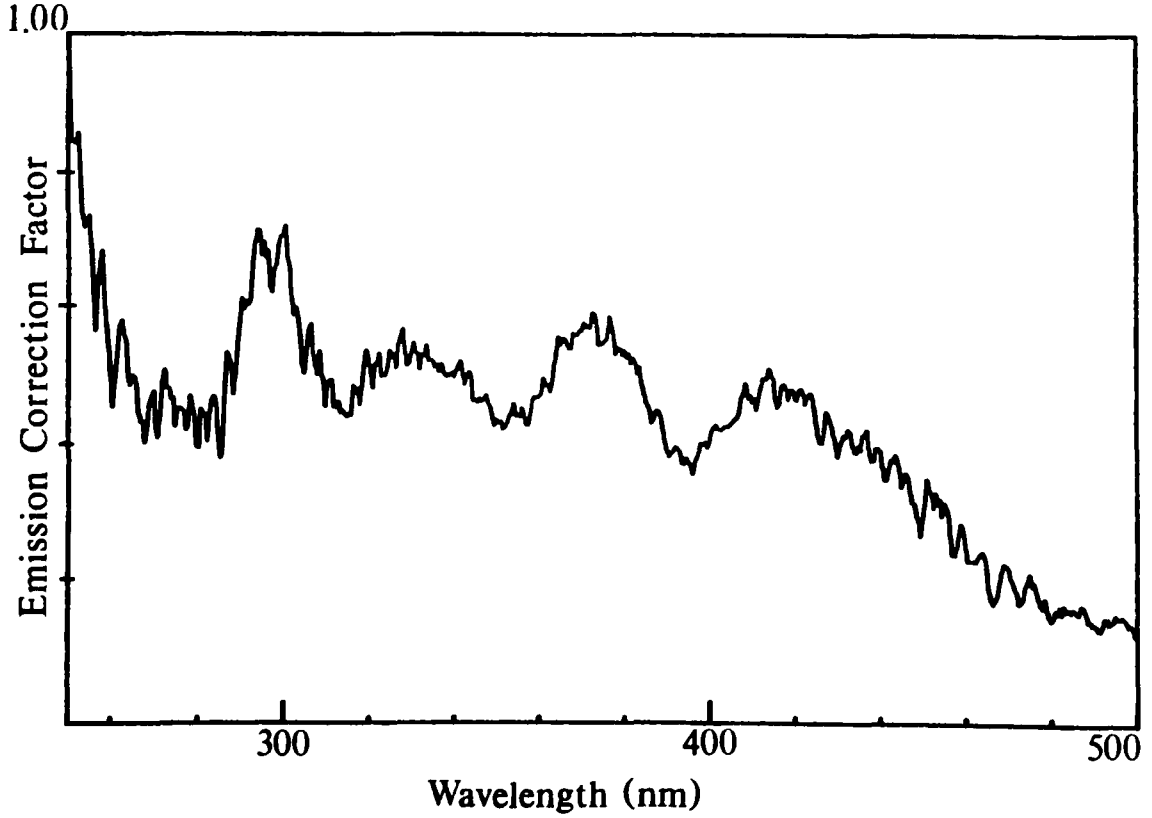

Figure 4.8: Emission spectral correction factors.

Correction factors for emission spectra were supplied with the SLM 8000C spectrofluorimeter software. They were measured with a polarizer in the excitation beam at 54.7° and the emission polarizer set at vertical (0°). These correction factors were determined by SLM by measuring the intensity of a calibrated tungsten lamp at 50 nm intervals at wavelengths greater than 300 nm. Correction factors every 0.2 nm were obtained by interpolation assuming a smooth function between these 50 nm intervals. A more reliable emission correction was measured (with no excitation polarizer and an emission polarizer at 35.3°) by synchronously scanning the excitation and emission monochromators with a diffuse reflector of roughened quartz in the sample compartment. This spectrum was divided by the excitation spectrum of rhodamine measured at 640 nm as indicated above. The synchronous scan provided a lamp/excitation monochromator output spectrum distorted by the variation of emission monochromator throughput and photomultiplier tube sensitivity with wavelength. Hence dividing this spectrum by the rhodamine excitation spectrum resulted in correction factors for emission spectra. These emission correction factors were found to be fairly constant in the region of 350–450 nm (Figure 4.8). Hence no correction of the emission spectra was made.

Fluorescence quantum yields, ϕ_f, were measured relative to fluorescence quantum yield standards and were calculated using equation 4.30[43]

$$\phi_f(x) = \phi_f(y).\frac{1-10^{-A_y}}{1-10^{-A_x}}.\frac{I(\lambda_x)}{I(\lambda_y)}.\frac{D_x}{D_y}.\left[\frac{\eta_D(x)}{\eta_D(y)}\right]^2 \qquad (4.30)$$

where x = sample, y = quantum yield standard, A_i = absorbance of i at the excitation wavelength λ_i used to measure the emission spectrum of i; $\frac{I(\lambda_x)}{I(\lambda_y)}$ = relative intensity of the excitation light at the two excitation wavelengths used to measure the sample and quantum yield standard emission spectra (usually $\lambda_x = \lambda_y$); D_i = area under the emission spectrum of i measured at λ_i; $\eta_D(i)$ = refractive index of the solvent in which i is dissolved.

The absorbances A_i were low and close to 0.1 to avoid errors due to differences in optical geometry (inner filter effect). The fluorescence quantum yield standards were chosen so that they absorbed and emitted in similar spectral regions as the sterol probes. Anthracene (Aldrich, gold label) in ethanol (Commercial Alcohols Limited, distilled twice over KOH), at a low optical density [$A_{340} \simeq$

.01, $\phi_f(\lambda_{ex}340\text{ nm}) = 0.32$[44]] in order to avoid re-absorption, was used as the standard for the determination of the fluorescence quantum yield of both DNC and TPC, while N-acetyltryptophanamide [Aldrich, $\phi_f(\lambda_{ex}295\text{ nm})=0.14$][45] in aqueous cacodylate buffer, pH 7.0, was used to obtain the fluorescence quantum yield of DPC.

Low-temperature fluorescence excitation and emission spectra were measured on solutions in quartz tubes which were placed in a Dewar flask equipped with quartz windows at its base. Cold nitrogen gas, whose temperature was controlled by the rate of heating of a reservoir of liquid nitrogen, was passed over the tubes and the temperature in the vicinity of the samples measured by an iron-constantan thermocouple. The same set-up was used for low temperature time-resolved fluorescence experiments.

4.2.2 Time-Resolved Fluorescence Measurements

Time-resolved fluorescence measurements were made by the method of time-correlated single photon counting (TCSPC, see Figure 4.9)[46,47]. Briefly, this involves measuring the time of arrival of a single photon emitted by the sample after a given excitation flash. In a traditional configuration, this time is measured by sending an electrical pulse, at a *time correlated* with the time of excitation of the sample, to the start input of a time-to-amplitude converter (TAC) where it initiates a linear voltage-time ramp. The optical pulse which excites the sample is attenuated so that only a *single photon* is detected per excitation event after passing through the fluorescence detection optics. The electronic signal resulting from this single photon is sent to the TAC where it acts as a stop pulse for the voltage ramp. The voltage reached on the voltage ramp is proportional to the time difference between the start and stop pulses, or between excitation and emission of the sample, and its amplitude is digitized by means of an analogue-to-digital converter (ADC). A count is then stored in the appropriate channel of a multichannel analyzer (MCA) corresponding to that time difference.

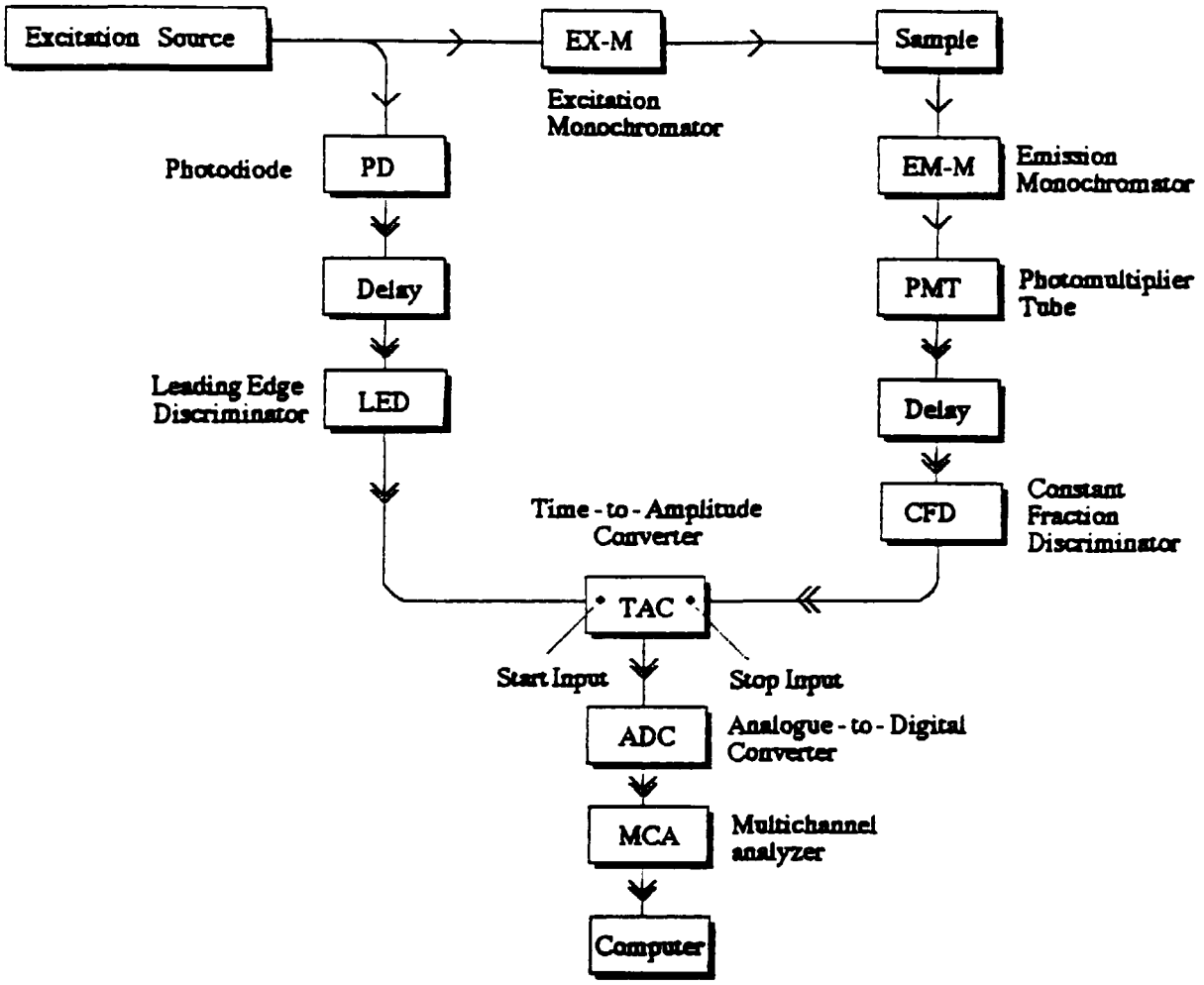

Figure 4.9: Schematic diagram of basic instrumentation required for time-correlated single photon counting (TCSPC) experiments.

This procedure is repeated until a histogram of a sufficient number of counts vs. channel number (time) is acquired in the MCA. Statistically, in order to avoid pulse pile-up, or to achieve an equal probability of observing a fluorescent photon at any time after excitation, the ratio of excitation pulses to single photon events is adjusted to be of the order of 100:1[46,48].

The instrumentation used for the TCSPC experiments described in this work is depicted in Figure 4.10 and is described in detail below.

The excitation source was a mode-locked argon ion laser (Spectra Physics 171–07, beryllium oxide bore; later Spectra Physics 2030, ceramic bore, with Spectra Physics 342 mode-locker head and Spectra Physics 270 power supply) which synchronously pumped a dye laser (Spectra Physics 375). The argon ion laser operated at 81.6 MHz with a pulse-width of 175 ps and average power 470 mW at the 514.5 nm line. Typical operating current was 30A. Both the power supply and the argon ion laser tube were cooled by a closed loop water circulator (Spectra Physics 314) with filtered, deionized and deoxygenated water at a pressure of ~35 psi. flow rate of 3.5 gallons/minute (in line with a small diaphragm to dampen pulsations of the pump), such that the temperature of the water returning from the laser was ~32°C. This water was in turn cooled by passing through a heat exchanger in the water circulator connected to a supply of tap water at a pressure of 75 psi, flow rate of 8–9 gallons/minute. The immediate area around the brewster angle mirrors in the ion laser cavity was purged by air passing through a closed loop system containing molecular sieves (to remove ozone), dessicant (to remove water vapour) and activated charcoal (to remove organic vapours which could deposit on the mirrors).

The dye solution in the dye laser was circulated at a pressure of 100 psi (dye laser circulater, Spectra Physics 376B) and was kept at a temperature of ~30°C (in order to avoid temperature changes of the circulating dye with time), by passing through a heat exchanger connected to Haake water circulator. Rhodamine 6G in ethylene glycol (2mM) provided a tunable range of 570–640 nm[49]. This could be frequency doubled to give ultraviolet light output from 285–320 nm. Excitation of the samples with 295 nm and 320 nm light was achieved using this dye. DCM in benzyl alcohol/ethylene glycol (40:60, 1.5mM) gives an output in the red region of

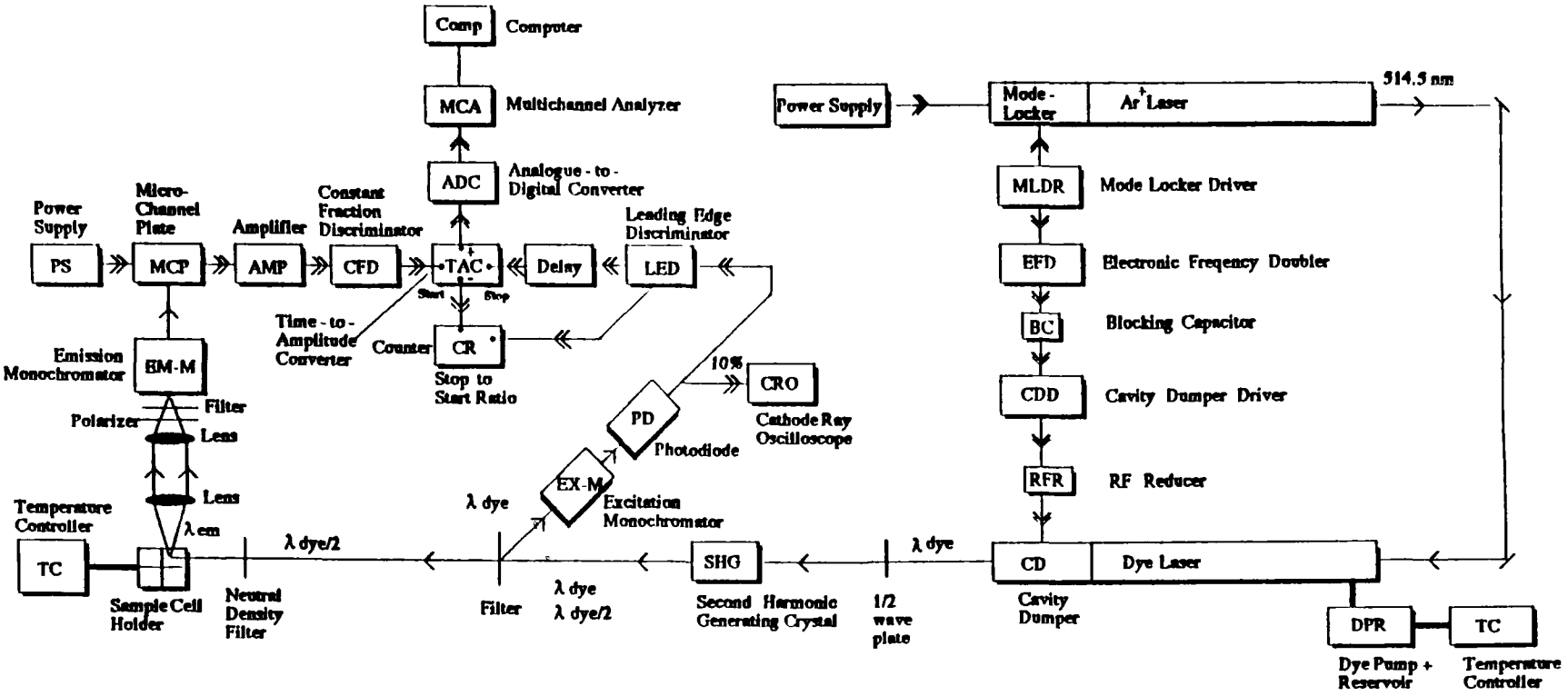

Figure 4.10. Schematic diagram of the instrumentation used for the time-resolved fluorescence experiments reported in this work.

← optical signal

⋘ electronic signal

the spectrum from 640–700 nm[49,50] which can be frequency doubled to wavelengths of 320–350 nm, and so this dye was used for experiments at excitation wavelengths of 340 nm and 350 nm. Wavelength selection of the dye output was made by adjustment of the orientation of a birefringent filter in the dye laser cavity. All mirrors in the dye laser cavity except the input mirror, M_{pump}[51], were changed when the dye was changed [Spectra Physics M_1, G0079-001(R6G) → G0079-004(DCM); M_2, G3852-003(R6G) → G3852-001(DCM); M_3, M_4, G3845-004(R6G) → G3845-008(DCM)].

The output of the dye laser was achieved by passing through a Spectra Physics 344 cavity dumper. This unit reduced the pulse repetition rate so that the peak power of the dye laser pulses was increased to 1.5–2 kW. At the same time the pulse to pulse separation increased thus avoiding the possible overlap of fluorescence signals from successive laser pulses. The output frequency could be selected from 1 Hz to 4 MHz and was typically set at 816 kHz. The operation frequency of the cavity dumper was synchronized with the argon ion laser repetition rate by taking part of the 40.8 MHz radio frequency signal of the mode-locker driver (Spectra Physics 452A), passing it through an electronic frequency doubler, and directing the resulting 81.6 MHz signal to the cavity dumper driver (Spectra Physics 454) via a blocking capacitor. The extinction ratio (the ratio of intensities of the main pulse and the pulse that would have followed it 12.3 ns later had there been no cavity dumper) was adjusted to a maximum (typically 500:1 in the visible region) by adjusting the phase and timing controls of the cavity-dumper driver, and also by the use of an rf reducer to cut down on the lobes of the rf pulse coming out of the cavity dumper driver to the cavity dumper Bragg cell. This ratio was even higher in the UV region (typically 30000:1) owing to the I^2 dependency of the frequency doubling process[52]. A small constant flow of nitrogen gas was passed over the Bragg cell to keep its surfaces free of organic residue buildup.

Fine tuning of the dye laser cavity length was made by adjusting the positions of the mirrors, and the distance between the cavity dumper and dye laser by means of a quartz tube, in order to achieve optimal average power as measured by a power meter (Spectra Physics 404). Typical power at 590 nm was >50 mW; at 640 nm it was 40 mW; while at 700 nm it was 30 mW.

The 20 ps FWHM output pulses from the dye laser were vertically polarized. The non-linear process of frequency doubling (described below) rotated the polarization of the ultraviolet light which it generated by 90°. Hence in order to excite the samples with vertically polarized light, the vertically polarized output from the dye laser was passed through a half-wave plate (Special Optics R8 9012) to rotate the polarization direction to horizontal before passing through an angle-tuned second harmonic generating crystal (for R6G laser lines, Cleveland Crystals KDP1, 25 mm length; for DCM laser lines, Inrad KDP "C", model 542-120, 30 mm length) to give the desired UV light of vertical polarization. The light at the fundamental wavelength which passed through the crystal was filtered from the UV output by a 7-54 Corning filter (295, 320 nm), a UG1 Schott filter (340 nm), or a 7-41 Corning filter and a UG1 Schott filter (350 nm). The filter was also used to reflect the visible light onto the slits of a monochromator (Jobin Yvon H-10) and onto a silicon avalanche photodiode (Texas Instruments TIED 56, operating at 90V DC). 10% of the resulting electronic signal (Tektronix Signal Pickoff CT-3) was directed to a cathode ray oscilloscope (Tektronix 7904 with Amplifier 7A19 triggered internally by a 7B92 dual time base) in order to monitor the performance of the laser system. Fine adjustment of the laser output was made when necessary by adjusting the phase and timing controls of the cavity dumper driver.

The remaining 90% of the signal from the photodiode was passed into a 100 MHz leading edge discriminator (Ortec 436) whose output passed through delay lines (Ortec 425) and then was used as the stop input signal for the biased time-to-amplitude converter (TAC, Ortec 457). This is the opposite configuration to that described earlier in the general description of the TCSPC method, where the signal correlated with the excitation pulse is used as the start pulse for the TAC. In the conventional configuration, the TAC was not able to register all excitation events and hence not all single photon events. This was because the time between successive excitation pulses was 1.2 μs (1/816 kHz) while the TAC conversion time was $\sim$13 μs[53]. Even if no stop pulse was detected, as would happen 99 times out of 100 because of the 100:1 ratio of the excitation events to emission events, the dead time of the TAC was still $\sim$6 μs. By having the detected single photons initiate the voltage ramp and the delayed excitation pulse terminate the ramp, since the ratio of

detected photons to the number of excitation pulses is ~100:1, as mentioned earlier, there is 0.12 ms between successive start pulses and all the detected photons would be registered.

The UV light pulses, after passing through the filters mentioned above, passed through a neutral density filter which had constant thickness but different densities along its 125 mm length. In this way, the intensity of the UV pulses could be attenuated in order to achieve the proper counting statistics mentioned earlier. Following this, the light entered a thermostatted cell compartment (Polyscience 90 Temperature Controller), which could hold up to four 1 cm cuvettes, whose rotation was controlled by a stepping motor (Slo-Syn). The emission was collected at right angles through a collimating lens, and through a second lens which focussed the fluorescence on to the slits of a monochromator (Jobin Yvon H-10) with either 4 nm (0.50 mm slits) or 2 nm (0.25 mm slits) resolution. Immediately in front of the monochromator were positioned a Glan Taylor polarizer set at 54.7° (magic angle) to eliminate time distortions due to rotational relaxation of the fluorophore[42], and a cut-off filter to either block (295 nm, 2 microscope slides; 320/340 nm, 0-52 Corning filter; 350 nm, KV 370 Schott filter) or pass through (for measurement of the instrument response profile) any scattered light. The monochromator was placed on a precision labjack (Newport Research 270) so that its height could be adjusted according to height variation of the UV beam, which resulted from different orientation angles of the doubling crystal.

The fluorescent photon which passed through the monochromator was detected by a proximity-type microchannel plate (MCP)[54] detector (Hamamatsu R1564V-01, operating at -3.2 kV) whose output was amplified (Electronic Navigation Industries 500AP amplifier, 27 dB), passed into a constant fraction discriminator (Tennelec TC 453), and directed to the start input of the TAC. The dark count rate was usually 40 Hz. The ratio of stop to start pulses was measured by a counter (Ortec 9315) using the negative output of the TAC for the number of start pulses and an output of the excitation pulse leading edge discriminator for the number of stop pulses. The stop:start ratio was generally set at 100:1 for the collection of the sample fluorescence decay and instrument response profiles (defined below).

The positive output of the TAC was read into an analogue-to-digital converter

(ADC) (Tracor Northern TN-1211, 50 MHz) and recorded in 1024 or 2048 channels (channel width 5.3 ps/channel to 84.8 ps/channel) of a multichannel analyzer (MCA) (Tennecomp) which was controlled by a Digital 1104 computer. Usually at least 16000 counts were collected in the maximum channel of the sample decay curve. A blank was measured for each sample for the same accumulation time, as controlled by a real time clock in the MCA. The instrument response profile (FWHM $\sim$ 80 ps) was determined by measuring the scattered light from a suspension of rabbit liver glycogen (Sigma) in cacodylate buffer (pH 7.0) having an optical density of $\sim$ 0.1 at the excitation wavelength.

All fluorescence intensity/time profiles were acquired sequentially and were stored on 8″ floppy disks, converted to RT-11 format on a PDP 1134 computer, and transferred to an IBM 3270 VM computer for data analysis.

4.2.3 Fluorescence Decay Data Analysis

Curve Fitting and Quality of Fit

The measured sample fluorescence decay profile, D_s, is a convolution of the impulse function L (i.e. the time profile of the excitation pulse), the true sample fluorescence response function F_s, and an instrument response function H (i.e. the time distortion of an optical signal by the detection and electronic systems), as given by equation 4.31[55].

$$D_s = L * F_s * H \qquad * = \text{convolution} \tag{4.31}$$

F_s is the function of interest and is generally found to be a sum of exponentials consistent with the physical model of fluorescence decay. In order to arrive at F_s, the convolution $L * H$ (equation 4.32) must be known, and can be obtained by measuring the response of the system to scattered light by directing the excitation pulses onto a scattering suspension of rabbit liver glycogen in buffer, under identical optical arrangements.

$$D_l = L * H \tag{4.32}$$

Typical sample fluorescence decay profiles D_s and instrument response profiles (scatterer curve) D_l at channel widths of 5.3 ps/channel and 84.8 ps/channel are shown in Figures 4.11 and 4.12.

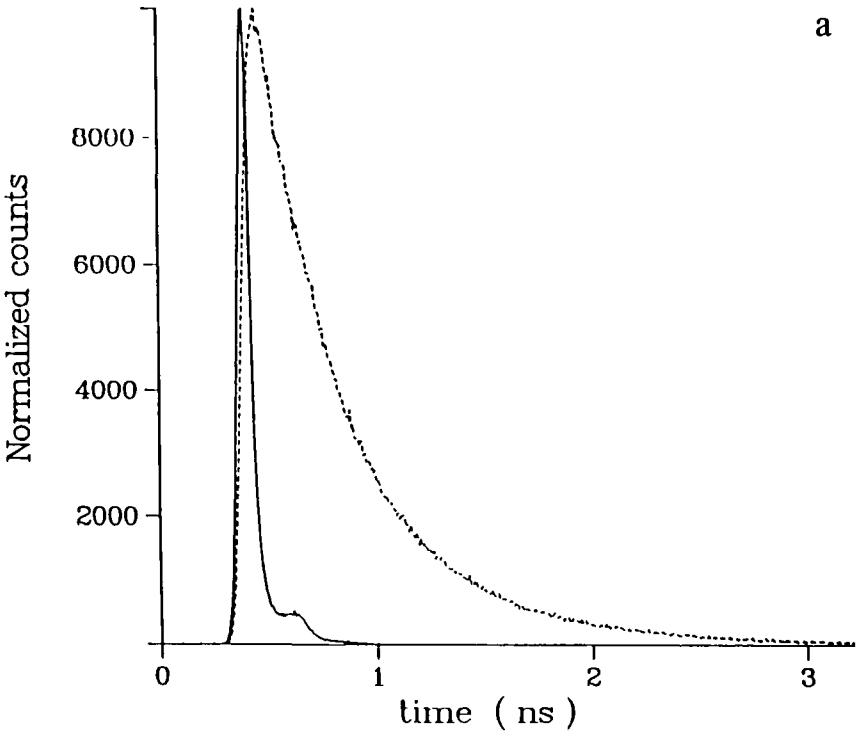

Figure 4.11: a) Fluorescence decay profile of TPC in TMP (λ_{ex}320 nm, λ_{em}410 nm, T=21.5° C) measured at a channel width of 5.3 ps/channel, with the corresponding instrument response profile.

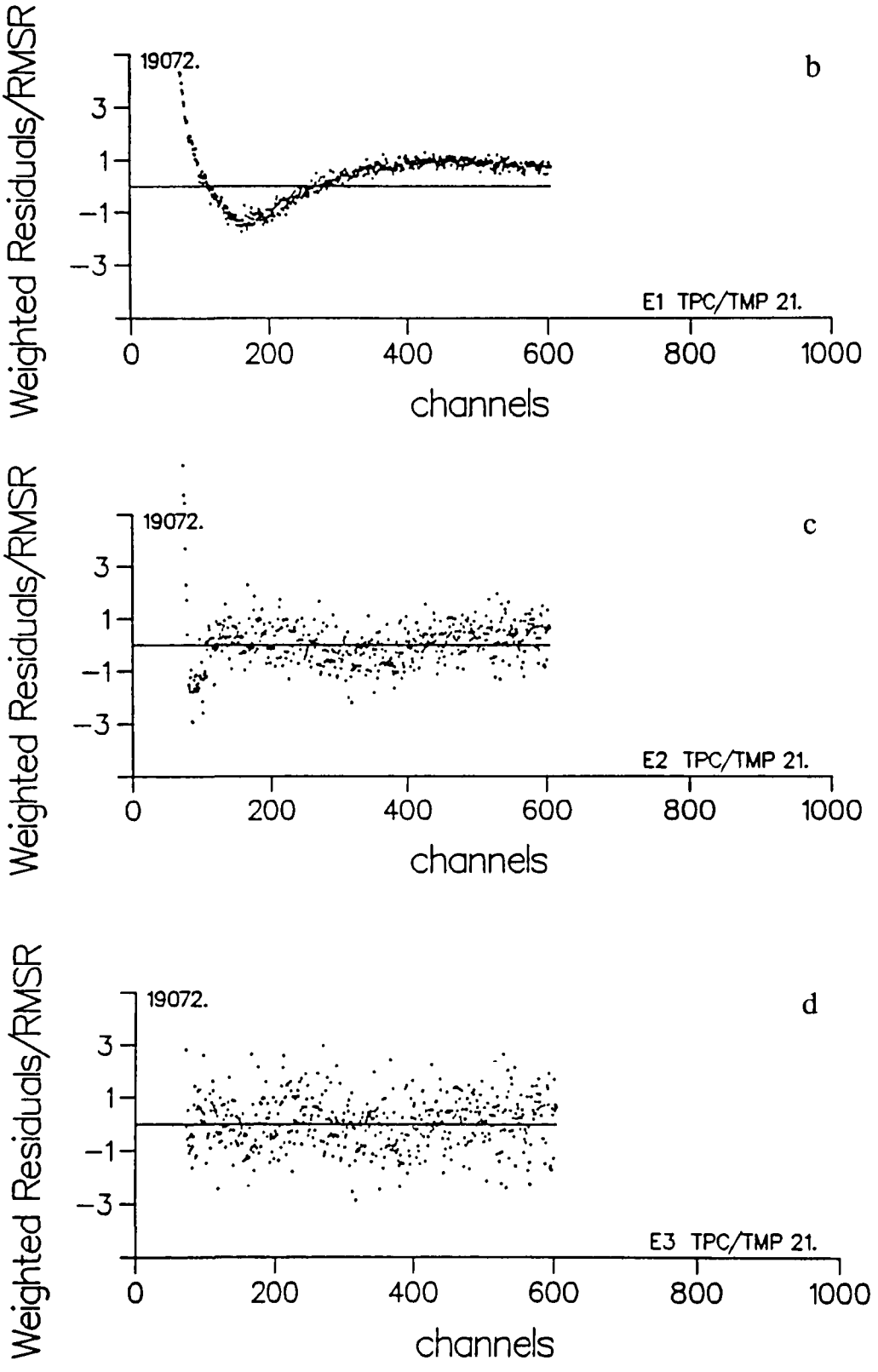

Figure 4.11: Plots of weighted residuals/root mean square of residuals for b) a single exponential fit: $\chi^2 = 5.41$, SVR = 0.05, c) a double exponential fit: $\chi^2 = 1.54$, SVR = 0.77 and d) a triple exponential fit: $\chi^2 = 1.03$, SVR = 1.71, to the fluorescence decay profile in a).

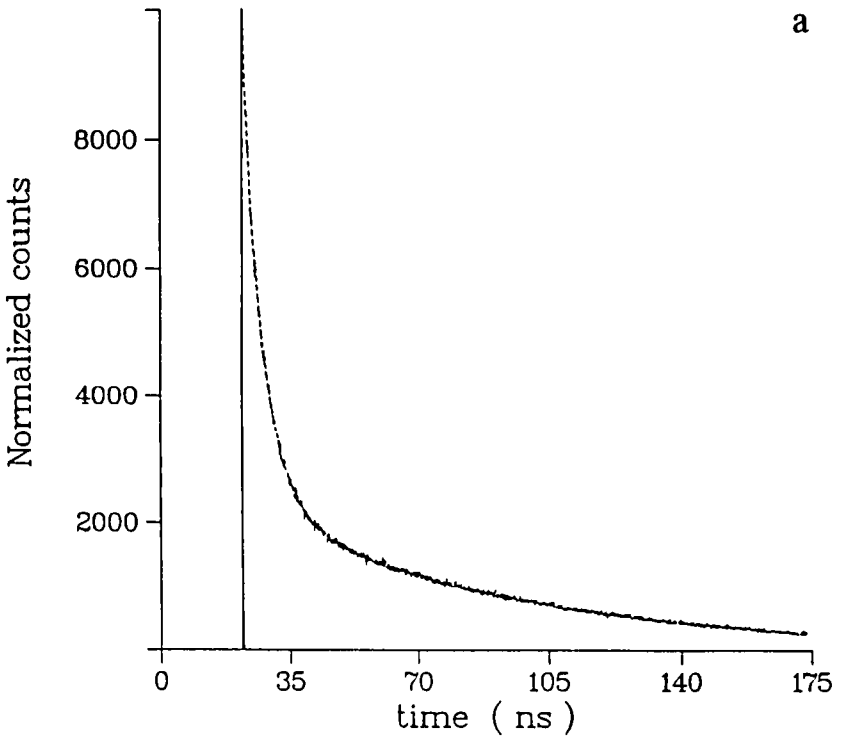

Figure 4.12: a) Fluorescence decay profile of DNC in TMP (λ_{ex}320 nm, λ_{em}410 nm, T=20.5° C) measured at a channel width of 84.8 ps/channel, with the corresponding instrument response profile.

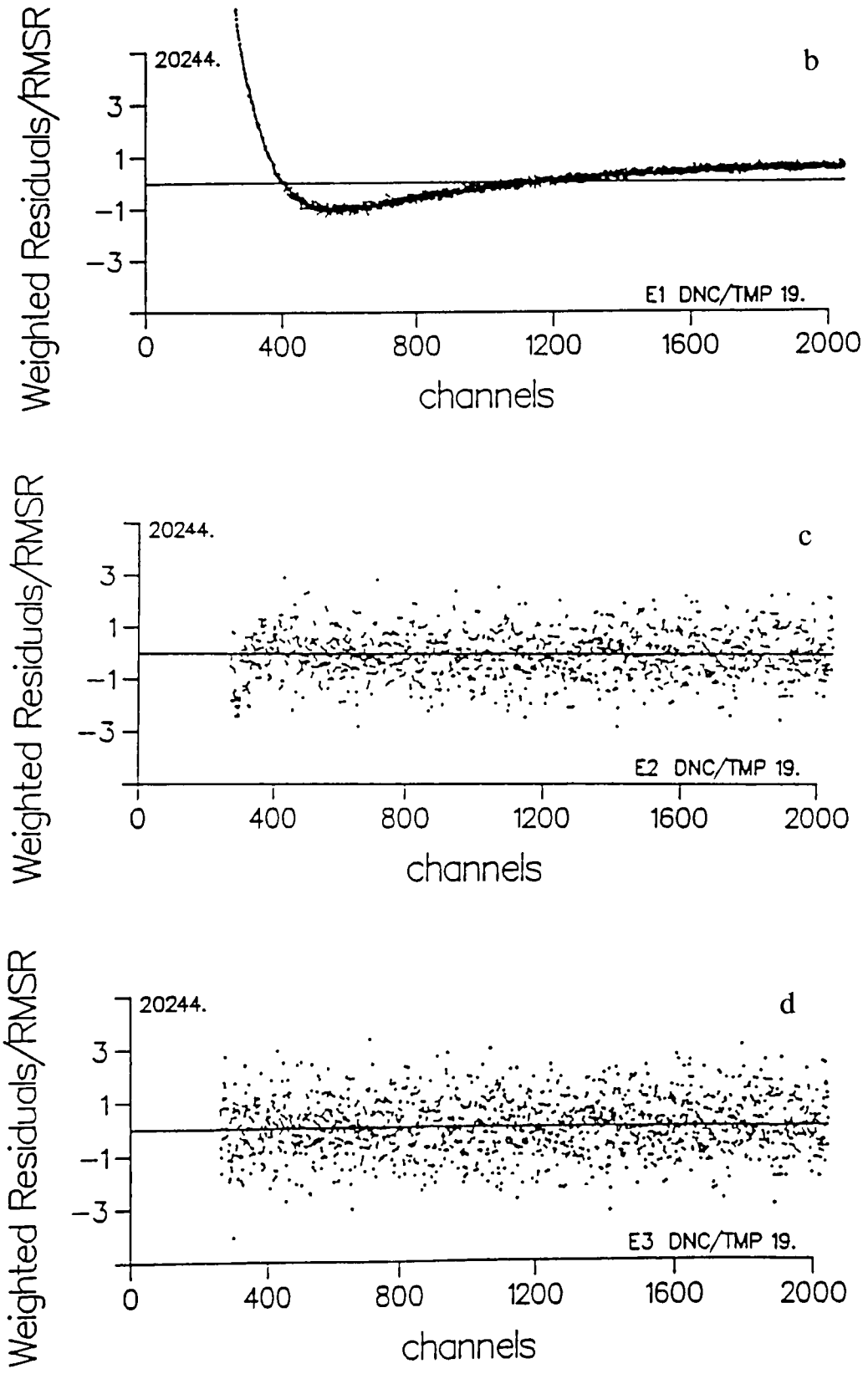

Figure 4.12: Plots of weighted residuals/root mean square of residuals for b) a single exponential fit: $\chi^2 = 11.1$, SVR = 0.02, c) a double exponential fit: $\chi^2 = 1.15$, SVR = 1.52 and d) a triple exponential fit: $\chi^2 = 1.02$, SVR = 1.90, to the fluorescence decay profile in a).

The desired function F_s is determined by convolving the scatterer curve D_l with trial functional forms of F_s (using a weighted nonlinear least squares method[47,56] and the Marquadt algorithm[57]) until there is good agreement with the measured sample fluorescence decay profile D_s. This procedure assumes that the instrument response function H is independent of wavelength, since the scatterer curve D_l is measured at the excitation wavelength λ_{ex}, while the sample fluorescence decay profile D_s is measured at an emission wavelength λ_{em}. Equations 4.31 and 4.32 are more precisely written:—

$$D_s = L * F_s * H_{em} \tag{4.33}$$

$$D_l = L * H_{ex} \tag{4.34}$$

It has been found that the transit time spread of microchannel plate detectors is practically invariant with wavelength of incident light ranging from 300 to 800 nm[54]. If it is assumed that any other possible mechanisms giving rise to the instrument response function are also independent of wavelength (i.e. $H_{ex} = H_{em}$), then the above convolution procedure will yield the correct functional form of F_s.

The best fit between the convolved curve $D_l * F_s$ and the sample fluorescence decay curve D_s was found when the weighted sum of squares of differences or residuals (WSSR) between the experimental points $e(t_i)$ and the calculated points $c(t_i)$ (equivalent to the chi-square value χ^2) was minimized (equation 4.35).

$$\text{WSSR} = \chi^2 = \sum_{i=1}^{n} w_i \left[e(t_i) - c(t_i)\right]^2 \tag{4.35}$$

n = number of data points, channels

w_i = weighting appropriate to data in channel i

Since the counting statistics of the TCSPC method is Poissonian, the correct weighting factor w_i is the reciprocal of the variance σ_i^2, which is equal to the number of counts in channel i (equation 4.36).

$$w_i = \frac{1}{\sigma_i^2} = \frac{1}{e(t_i)} \tag{4.36}$$

So,

$$\text{WSSR} = \chi^2 = \sum_{i=1}^{n} \left\{ \frac{[e(t_i) - c(t_i)]^2}{e(t_i)} \right\} = \sum_{i=1}^{n} [r(t_i)]^2 \tag{4.37}$$

$$r(t_i) \quad = \quad \text{weighted residual}$$

In the convolution procedure, the whole sample fluorescence decay profile D_s was fitted, but the statistical parameters used to judge the quality of the fit were calculated from the point corresponding to 50% of the rising edge of D_s. These statistical parameters included:

1. Sigma value
2. Serial Variance Ratio[58]
3. Inspection of weighted residuals / root mean square of the residuals.

The sigma value is the square root of the reduced chi-square χ_v^2 (equation 4.38)

$$\sum = (\chi_v^2)^{\frac{1}{2}} = \left(\frac{\chi^2}{n_2 - n_1 + 1 - p} \right)^{\frac{1}{2}} \tag{4.38}$$

where χ^2 is the chi-square or WSSR defined earlier, and the term in the denominator represents the number of degrees of freedom. n_1 and n_2 are the start and stop channels used for determination of the statistical parameters and p is the number of variable parameters in the trial function F_s (for a sum of three exponential terms, $p = 6$). Sigma should be close to a value of one for Poisson distributed data.

The serial variance ratio (SVR, equation 4.39) is a measure of the correlation between residuals and is thought to be more sensitive than the sigma value to discrepancies between the calculated and experimental decay curves.

$$\text{SVR} = \frac{\sum_{i=n_1+1}^{n_2} [r(t_i) - r(t_{i-1})]^2}{\sum_{i=n_1}^{n_2} [r(t_i)]^2} \cdot \frac{(n_2 - n_1)}{(n_2 - n_1 - 1)} \tag{4.39}$$

For a good fit, SVR should be in the range 1.7–2.0.

A more subjective test (but quite instructive with experience) of the quality of a fit to the sample fluorescence decay profile, D_s, is an inspection of a plot of the

weighted residuals $r(t_i)$ divided by the root mean square of the residuals (equivalent to the sigma value). Such plots for a single, double and triple exponential fit to the fluorescence decay curves in Figures 4.11a and 4.12a, are shown in Figures 4.11b,c,d and 4.12b,c,d. The points should be randomly distributed about zero, and the majority of them should fall in the range -1 to 1 (equivalent to the standard deviation). Based on this criterion alone, it can be seen that the fluorescence decay curves in Figures 4.11 and 4.12 are both best fit by a sum of three exponential terms. The values of the sigma and SVR parameters for the single, double and triple exponential fits confirm this conclusion (Figures 4.11 and 4.12).

Global/Simultaneous Analysis of Fluorescence Decay Curves

Once satisfactory fits to individual fluorescence decay curves have been obtained, the accuracy of the pre-exponential factor α_i and the lifetimes τ_i can be improved by simultaneously fitting decay curves that are related in some way. For example, decay curves of a particular sample measured at various excitation and emission wavelengths, but at constant temperature, may have identical lifetimes τ_i but different pre-exponential factors α_i. By linking the τ_i values between decay curves, the number of degrees of freedom per decay curve is decreased than in the case when performing individual fits. This allows for an overdetermination of the parameters. Also, such a 'global' analysis allows for more rigorous testing of models since the statistical parameters obtained are more sensitive to the presence of, for example, two close lifetime values ($0.8 < \tau_i/\tau_j < 1$) or terms with small pre-exponential factors, than the statistical parameters obtained from individual analyses[59].

Decay Associated emission Spectra (DAS)

If the values of the pre-exponential factors α_i, obtained for fits of fluorescence decay curves of a particular sample, vary with emission wavelength but the corresponding lifetime values remain constant, then these lifetimes are associated with different emission spectra. These lifetime or decay associated emission spectra (DAS) can be computed by calculating the fractional contributions of the various components to the fluorescence, $\mathcal{F}_i$, at all the emission wavelengths (and constant excitation

wavelength) for which fluorescence decay curves were measured (equation 4.40)[60].

$$\mathcal{F}_i(\lambda_{em}) = \frac{\alpha_i(\lambda_{em})\tau_i}{\sum_i \alpha_i(\lambda_{em})\tau_i} \tag{4.40}$$

If these fractions are then multiplied by the steady-state fluorescence intensities at the appropriate emission wavelengths from an emission spectrum $I(\lambda_{em})$ measured at the same excitation wavelength as used for the lifetime measurements, emission DAS $S_i(\lambda_{em})$ can be obtained (equation 4.41).

$$S_i(\lambda_{em}) = \frac{I(\lambda_{em})\alpha_i(\lambda_{em})\tau_i}{\sum_i \alpha_i(\lambda_{em})\tau_i} = \mathcal{F}_i(\lambda_{em})I(\lambda_{em}) \tag{4.41}$$

These emission DAS represent the emission spectra of different populations (e.g. conformers) of the fluorophore when the lifetimes with which they are associated are simply a function of the rates of the various deactivation processes for one (and only one) of the populations. This is true when the populations arise from ground-state heterogeneity, and do not interconvert in the excited state. This is represented in the kinetic scheme (Figure 4.13, equations 4.42–4.45) below for the case of two ground-state populations. The emission DAS associated with τ_1, τ_2 are the true emission spectra of A*, B*. In the case when the multiexponential decay is a result of excited state reaction(s), the fluorescence decay curves should be analyzed directly for the various rate constants and species associated emission spectra (SAS) $S_A(\lambda), S_B(\lambda)$ computed[61,62]. However, SAS can be extracted from DAS in certain cases[63], for example in the case of an irreversible excited state reaction between A* and B*, or an excited state equilibrium between A* and nonfluorescent B*.

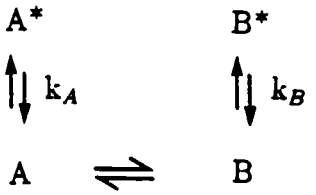

Figure 4.13: Kinetic scheme for two ground state species in equilibrium, which do not interconvert in their excited state lifetimes.

$$\tau_1 = \frac{1}{k_A} = \frac{1}{k_{f1} + k_{nr1}} \tag{4.42}$$

$$\tau_2 = \frac{1}{k_B} = \frac{1}{k_{f2} + k_{nr2}} \tag{4.43}$$

$$\alpha_1 = \alpha_A \tag{4.44}$$

$$\alpha_2 = \alpha_B \tag{4.45}$$

Indirect Excitation Decay Associated Spectra (IEDAS)

Direct excitation DAS (EDAS) can be obtained in a similar way to emission DAS if fluorescence decay measurements are made at closely-spaced excitation wavelengths and at a constant emission wavelength. This is not a trivial task when a synchronously pumped dye laser is used as the excitation source, since the laser optics and detection system need to be optimized at each excitation wavelength, and a number of different dyes would need to be used to span the excitation spectrum of a fluorophore. Instead, EDAS can be obtained indirectly using steady-state excitation spectra $X_j(\lambda_{ex}, \lambda_{em_j})$ measured at certain emission wavelengths λ_{em_j}, and fractional fluorescence contributions $\mathcal{F}_i(\lambda'_{ex}, \lambda_{em_j})$ measured at these same emission wavelengths at a given excitation wavelength $\lambda_{ex}{}'$.[64,65]

The three dimensional surface of fluorescence intensity versus excitation and emission wavelengths $I(\lambda_{ex}, \lambda_{em})$ (for an example see Figure 4.14) can be described as in equation 4.46[64].

$$I(\lambda_{ex}, \lambda_{em}) = \sum_{i=1}^{N} \xi_i(\lambda_{ex}) \alpha_i(\lambda_{ex}, \lambda_{em}) \tau_i = \sum_{i=1}^{N} \xi_i(\lambda_{ex}) \mathcal{F}_i(\lambda_{ex}, \lambda_{em}) \tag{4.46}$$

N = number of components to a fluorescence decay,

$\xi_i(\lambda_{ex})$ = molar absorptivity coefficient of compound i at λ_{ex}

The corresponding expression for a particular excitation spectrum is given in equation 4.47

$$X_j(\lambda_{ex}, \lambda_{em_j}{}') = \sum_{i=1}^{N} \xi_i(\lambda_{ex}) \underbrace{\tilde{\alpha}_i(\lambda_{ex}{}', \lambda_{em_j}) \tau_i}_{M_{ij}} \tag{4.47}$$

$\tilde{\alpha}_i(\lambda_{ex}{}', \lambda_{em_j})$ is the scaled pre-exponential factor $\alpha_i(\lambda_{ex}{}', \lambda_{em_j})$ such that the variation of $\sum \tilde{\alpha}_i(\lambda_{ex}{}', \lambda_{em}) \tau_i$ with emission wavelength reflects the variation of the

steady-state fluorescence intensity with λ_{em_j} measured at the same excitation wavelength $\lambda_{ex}{}'$.

Over the set of emission wavelengths $\lambda_{em_j} = 1, 2, \ldots, n$, at which excitation spectra and fluorescence decay data are obtained, and over the excitation wavelengths $\lambda_{ex_k} = 1, 2, \ldots, m$, of the measured excitation spectra, equation 4.47 becomes

$$\begin{pmatrix} X_{11} & X_{12} & \cdot & X_{1m} \\ X_{21} & X_{22} & \ldots & X_{2m} \\ \vdots & \vdots & \ddots & \vdots \\ X_{n1} & X_{n2} & \ldots & X_{nm} \end{pmatrix} = \begin{pmatrix} \xi_{11} & \xi_{12} & \ldots & \xi_{1N} \\ \xi_{21} & \xi_{22} & \ldots & \xi_{2N} \\ \vdots & \vdots & \ddots & \vdots \\ \xi_{m1} & \xi_{m2} & \ldots & \xi_{mN} \end{pmatrix} \begin{pmatrix} M_{11} & M_{12} & \ldots & M_{1n} \\ M_{21} & M_{22} & \ldots & M_{2n} \\ \vdots & \vdots & \ddots & \vdots \\ M_{N1} & M_{N2} & \ldots & M_{Nn} \end{pmatrix} \tag{4.48}$$

The desired IEDAS are the set of $\xi_i(\lambda_{ex_1} \rightarrow \lambda_{ex_m})$(i.e. the columns of the second matrix above), and can be obtained by linear algebra from the steady-state excitation spectra $X_j(\lambda_{em_1} \rightarrow \lambda_{em_n})$(i.e. the rows of the first matrix above) and the values of $\tilde{\alpha}_i(\lambda_{ex}{}', \lambda_{em_j})\tau_i, i = 1, 2, \ldots, N$ as long as the number of observations or emission wavelengths n is equal to or greater than the number of components N to the fluorescence decay. In the event that $n > N$, the IEDAS were overdetermined by a linear least squares analysis.

Lifetime Distributions

The fluorescence decay profiles measured in this work were not fitted by distributions of lifetime components[84,85] but by sums of two, three or four exponential terms. Successful recovery of up to three decay times, from fluorescence decay profiles obtained using the instrumentation described earlier (see section 2.3), has been demonstrated by simulation studies[86]. The decay times obtained for DNC and TPC, by both single curve and global analysis, were excitation and emission wavelength independent, which supports the use of sums of discrete exponential terms to fit the fluorescence decay profiles. Moreover, the decay times of DNC differed from one another by an order of magnitude, so it is unlikely that a lifetime distribution is a valid model for the photophysics of DNC.

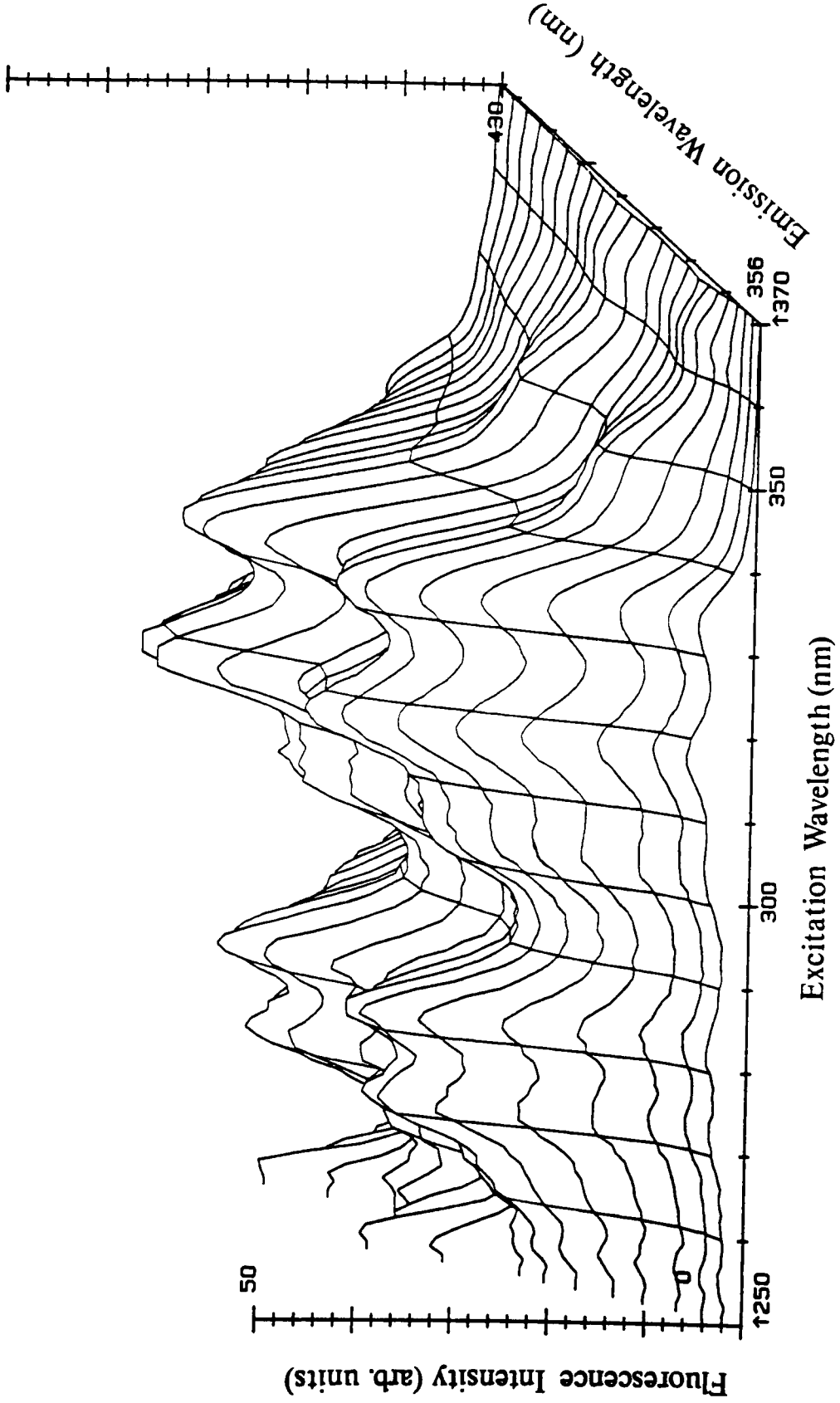

Figure 4.14: The 3D surface of fluorescence intensity versus excitation and emission wavelengths for DNC in TMP at 20.0° C.

4.2.4 Molecular Orbital Computational Methods

For the purposes of calculation, 1-(2'-Naphthyl)-1,3-butadiene (NBD) and 1-Phenyl-1,3,5-hexatriene (PHT) were used as analogues of the fluorophores of DNC and TPC respectively (for structures see Figures 4.31 and 4.36). The excitation patterns, or the positions and oscillator strengths of the low-lying electronic excited states, of NBD and PHT were calculated by the CNDO/S method[66] (Complete Neglect of Differential Overlap/Spectroscopy) using previously optimized geometries for the two molecules. These optimized geometries were obtained using the QCFF/PI method[67] which employs an empirical potential for the σ–electron framework, and a semi-empirical quantum-mechanical self consistent field for the π–electron contribution. The optimized geometries are then the geometries corresponding to the minima in the calculated ground state potential surfaces. This QCFF/PI method has been successful in predicting a number of properties of conjugated molecules such as heats of formation, vibrational frequencies, zero point energies and transition dipole moments[67,68].

The CNDO/S calculations were performed using two different approaches. In order to locate the low-lying A_g-like excited state which is formally one-photon forbidden and two-photon allowed in C_{2h} symmetry from the A_g-like ground state, a Pariser parametrization[69] was used. This calculation includes both singly and doubly excited configurations arising from promotion of one or two electrons from a π orbital to a π^* orbital, and has successfully predicted that the $2A_g$ state is the lowest excited electronic state in a number of (diphenyl) polyenes[70]. However, it has been observed that the excitation energies and oscillator strengths of the main absorption bands are generally predicted better when only singly excited configurations are considered in the calculation. Hence a second CNDO/S calculation, with Mataga-Nishimoto parametrization[71] which neglects doubly excited configurations, was performed in order to predict the main absorption spectral features expected for the various single bond rotamers of NBD and PHT.

4.3 Results and Discussion

4.3.1 Absorption Spectra

The absorption spectra of DPC, DNC and TPC in MeOH and *n*-BuOH are presented in Figures 4.15–4.17 respectively. It can be seen that both DNC and TPC have their longest wavelength absorption band in the 300–360 nm region while the absorption band of DPC is to slightly higher energies (280–320 nm). This is consistent with the empirical observation that the more extensive the conjugated π electron system, as in DNC and TPC, the lower the energy of the first ($\pi \rightarrow \pi^*$) absorption band.

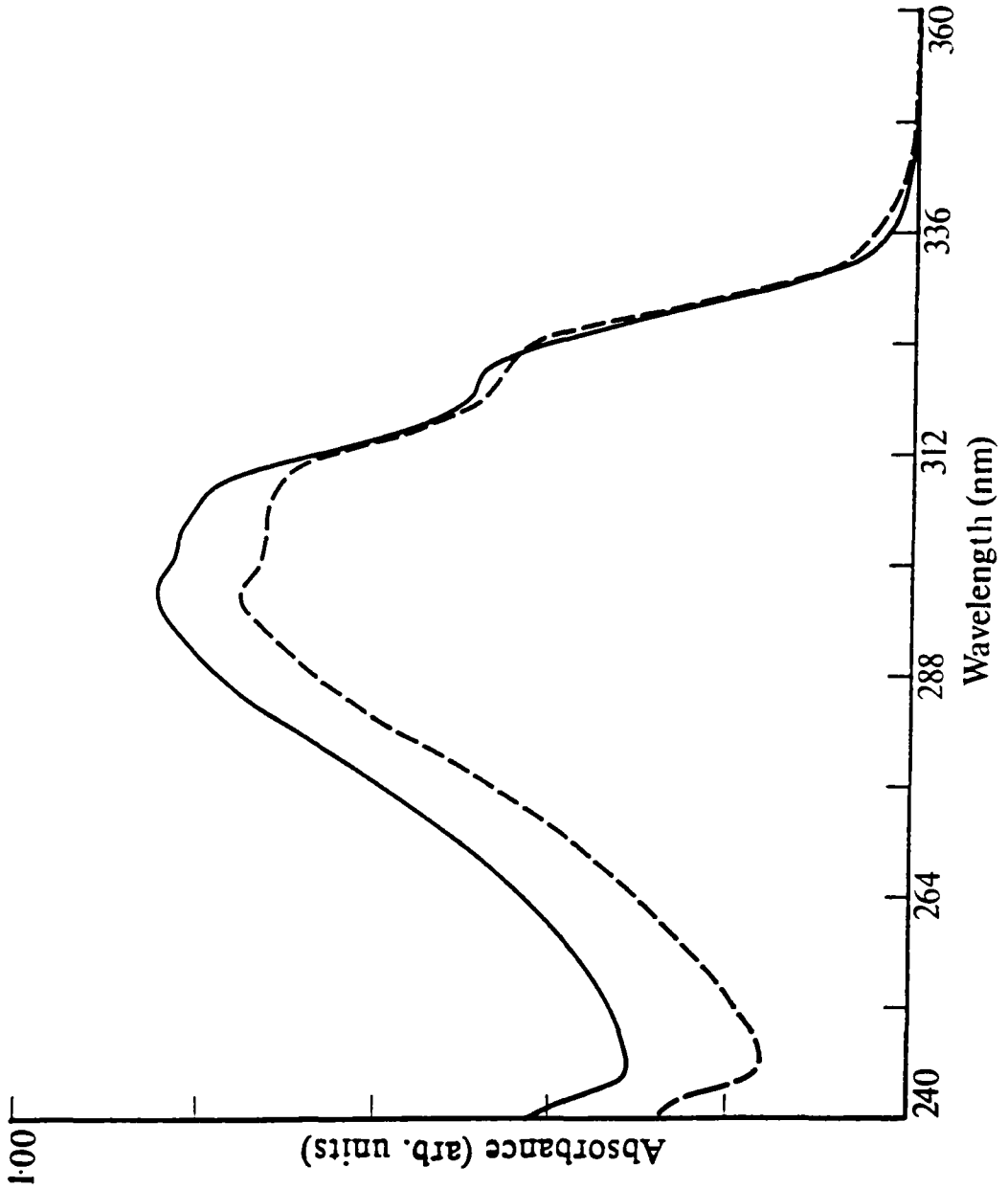

Figure 4.15: Absorption spectra of DPC in MeOH(—) and in *n*-BuOH (---).

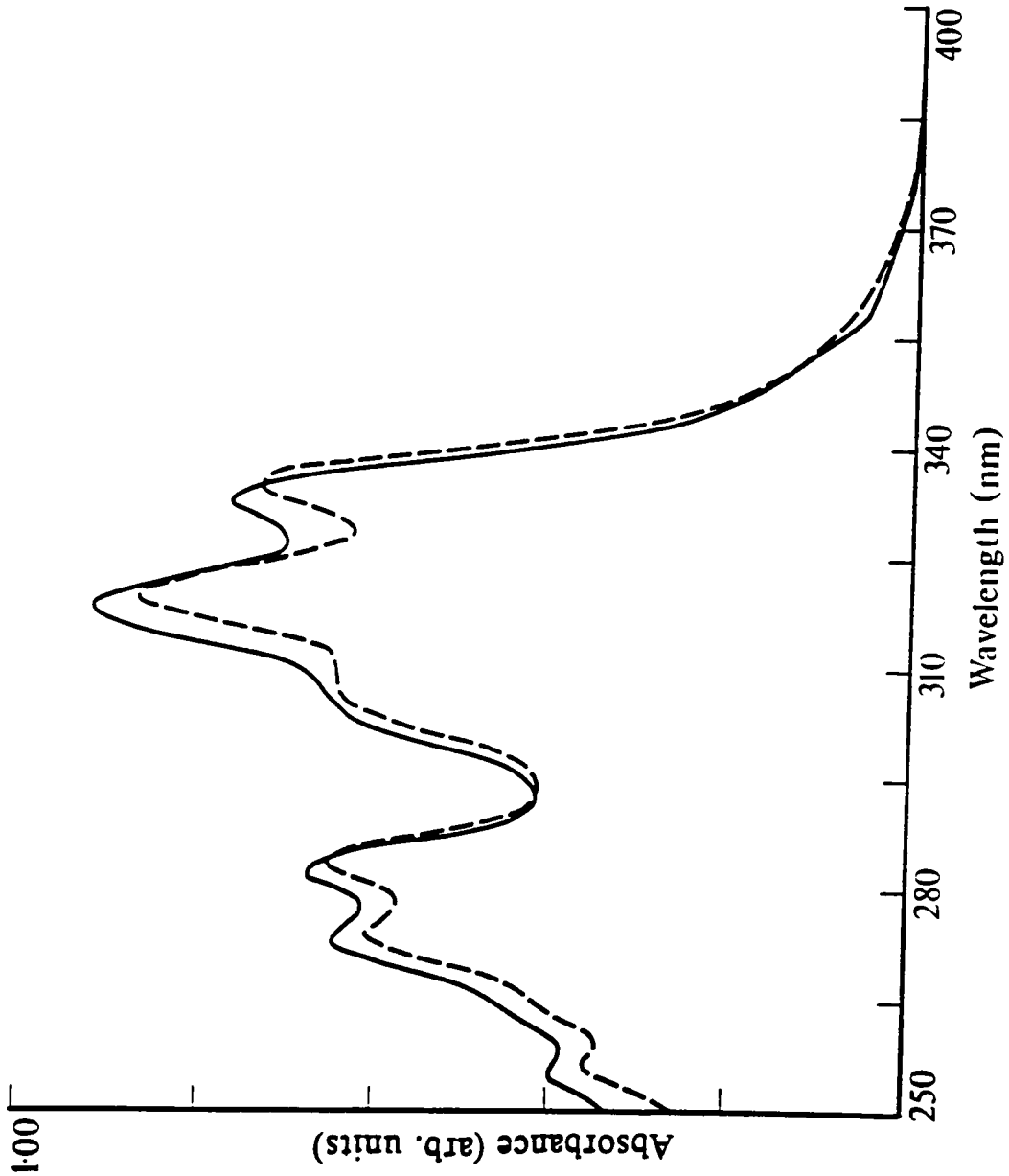

Figure 4.16: Absorption spectra of DNC in MeOH(—) and in *n*-BuOH (---).

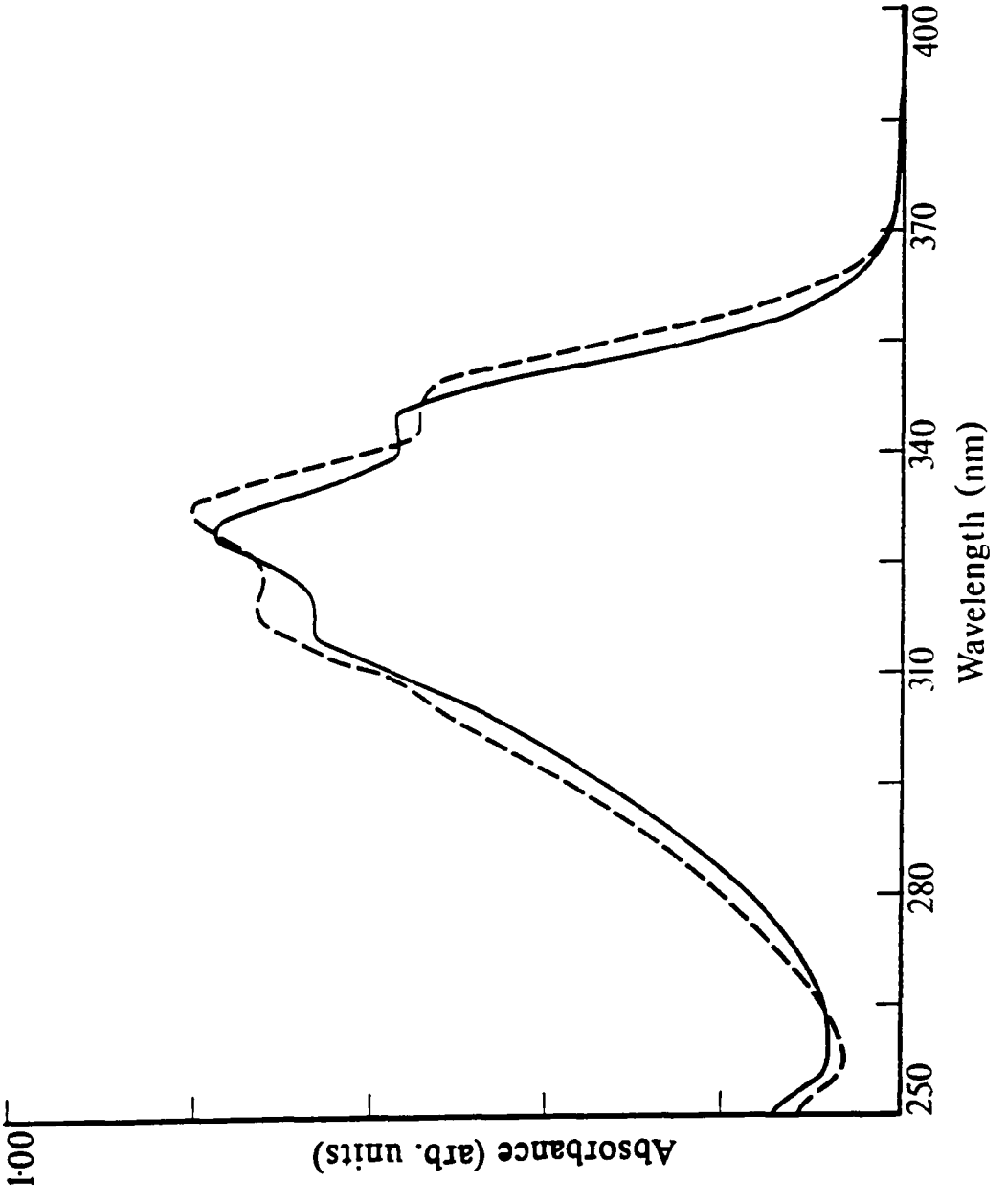

Figure 4.17: Absorption spectra of TPC in MeOH(—) and in *n*-BuOH (---).

The absorption spectra of DNC and TPC are sensitive to solvent polarizability, shifting to longer wavelengths with an increase in solvent refractive index from MeOH (n_D^{20} = 1.3288) to *n*-BuOH (n_D^{20}=1.3993)[72]. On the other hand, change in solvent polarity has little effect on the band positions of these two probes as judged by comparing absorption spectra in two solvents (*n*-BuOH and TMP) of similar refractive indices but different dielectric constants (not shown). The absorption spectral sensitivity to solvent polarizability confirms the expectation that the main low energy absorption in DNC and TPC is the strongly allowed ($\pi \rightarrow \pi^*$) transition from the ground state of A′ symmetry (assuming the fluorophores are planar and belong to the C_s point group)[73] to an excited state of A″ symmetry. The high values obtained for the molar absorptivity coefficient (ϵ ~40,000 $dm^3mol^{-1}cm^{-1}$ at λ_{abs}^{max}, see Table 4.1) provide further evidence supporting the assignment of the main absorption band of the DNC and TPC as the strongly allowed A′ →A″ transition (analogous to the strongly allowed $A_g \rightarrow B_u$ transition in diphenyl polyenes). The smaller molar absorptivity coefficient (ϵ ~15,000 $dm^3mol^{-1}cm^{-1}$ at λ_{abs}^{max}) observed for DPC, as well as the apparent insensitivity of its absorption spectral position to solvent polarizability (Figure 4.15), indicate that the low energy absorption transition of this molecule is not as strongly allowed.

Table 4.1: Molar absorptivity coefficients, ϵ, for DPC, DNC and TPC in chloroform at various absorption wavelengths.

Probe	λ_{max}^{abs} (nm)	ϵ ($dm^3mol^{-1}cm^{-1}$)
DPC	302	17,000
	326	11,000
TPC	336	41,000
	353	30,000
DNC	287	26,000
	323	40,000
	338	34,000
	368	2,300

4.3.2 Fluorescence Excitation and Emission Spectra and Quantum Yields

Fluorescence excitation and emission spectra of DPC, DNC and TPC in TMP are presented in Figures 4.18–4.20. Mirror image symmetry between the excitation and emission spectra, which is to be expected if only one species is present and if it emits from the same excited electronic state as reached upon absorption, is not observed for any of the probes. This is the first indication that the photophysics of these molecules is not straightforward and that there is heterogeneous absorption and/or fluorescence, possibly arising from the involvement of several excited states and/or conformers.

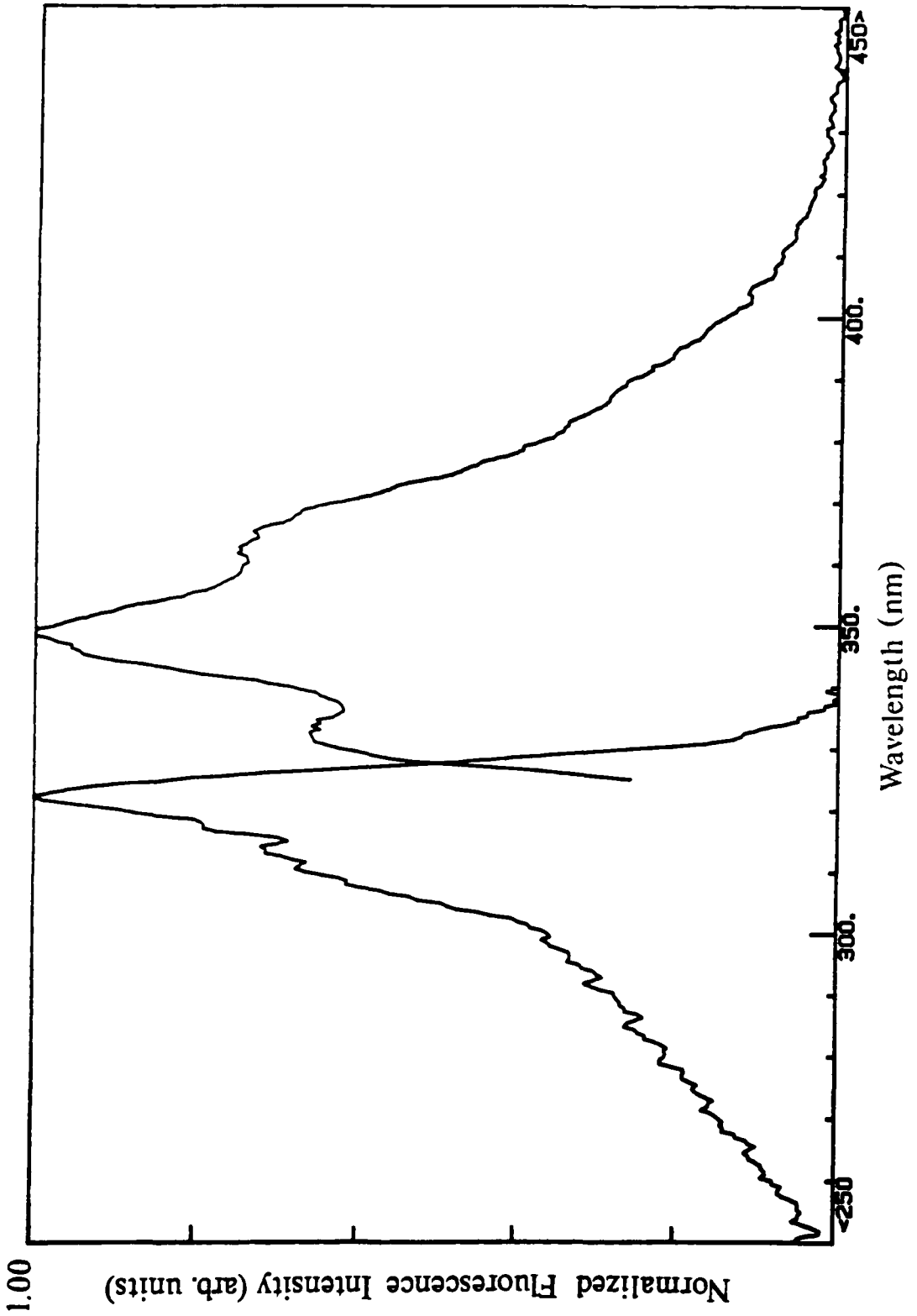

Figure 4.18: Fluorescence excitation (λ_{em} 390 nm) and emission (λ_{ex} 295 nm) spectra of DPC in TMP.

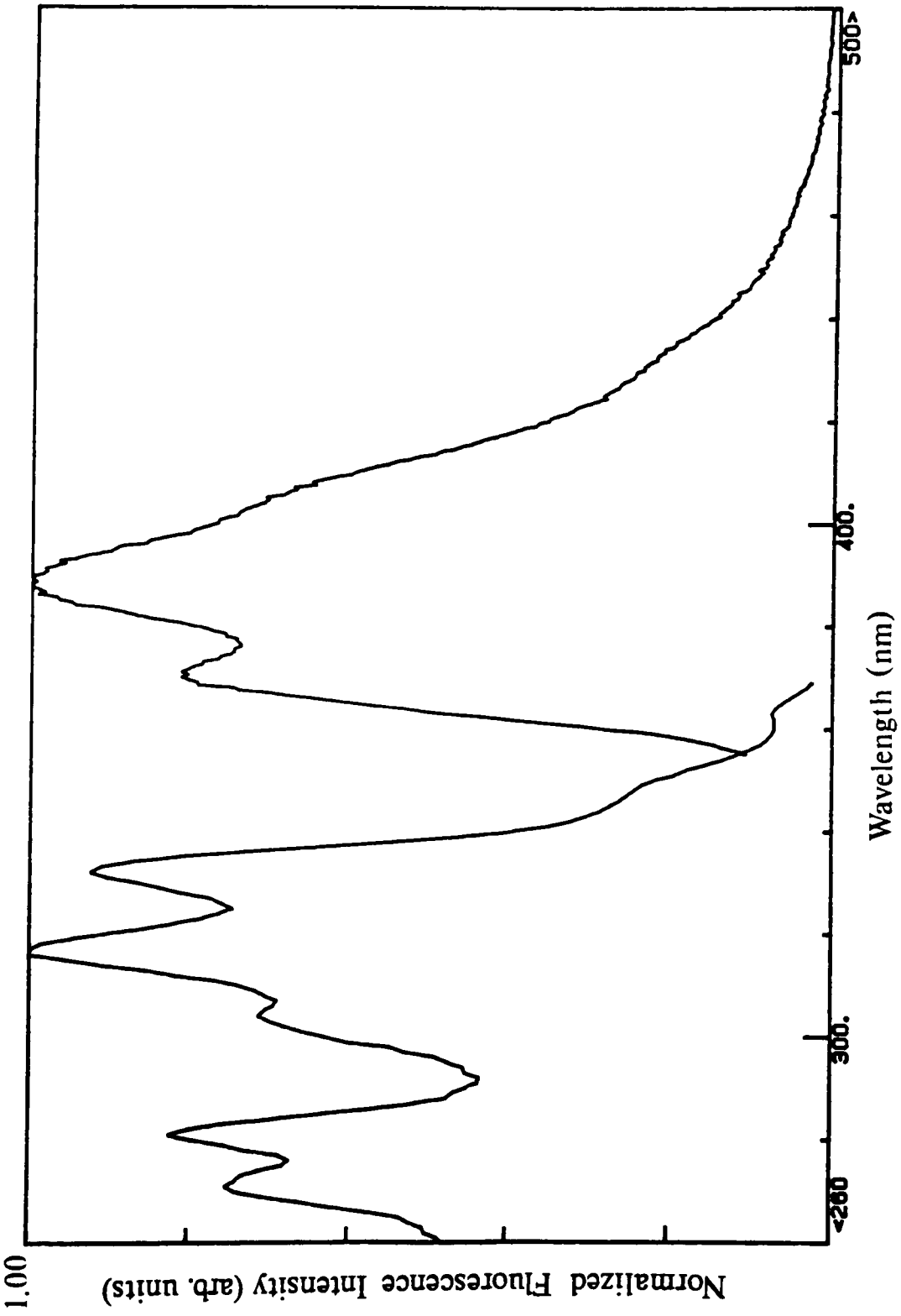

Figure 4.19: Fluorescence excitation (λ_{em} 390 nm) and emission (λ_{ex} 320 nm) spectra of DNC in TMP.

The extent of overlap of the excitation and emission spectra is good for both DPC and DNC. On the other hand, there is a considerable Stokes' shift between the excitation and emission spectra of TPC. The response of the excitation and emission spectra of the three probes to emission and excitation wavelengths (λ_{em},λ_{ex}) respectively (Figures 4.21–4.23), provides further insight into the photophysics of these molecules.

Both DPC and DNC have wavelength dependent excitation and emission spectra. The variation of the emission spectrum of DNC with λ_{ex} is particularly spectacular (Figure 4.22a). A new feature at 370 nm becomes apparent at λ_{ex}=355 nm resulting in an emission spectrum whose relative intensities of the various vibronic bands is altered considerably from the spectrum measured at λ_{ex}=320 nm. The excitation spectrum of DNC also has a pronounced variation with λ_{em}; the weak band at long wavelengths (350–368 nm) and the band at 280 nm contribute most to the excitation spectrum measured at λ_{em}=370 nm. So, it is possible to see that certain features in the excitation and emission spectra of DNC are correlated, which points to the existence of ground-state heterogeneity of this probe, most likely in the form of single bond rotamers as observed for 1–Phenyl–2–(2′–naphthyl) ethene (PNE)[26–35].

The spectral changes of DPC with λ_{ex} and λ_{em} are more subtle and are solvent polarity dependent. For instance, while the emission spectra of DPC in TMP and *n*-BuOH (two solvents of similar refractive indices but differing polarities) at λ_{ex} = 320 nm are different from those measured with λ_{ex}=295 nm and λ_{ex}=305 nm, the difference occurs on the low energy (long wavelength) side of the emission spectrum in TMP (Figure 4.21), while in *n*-BuOH the variation occurs on the high energy side. This suggests either a two state excited state reaction where the position of one of the states varies with solvent polarity, or the presence of two ground-state species whose spectra have different solvent sensitivities.

Unlike the diene aryl sterol probes DNC and DPC, TPC has excitation and emission spectra which are λ_{em} and λ_{ex} invariant (Figure 4.23). A rationale which would seem to be consistent with this wavelength independence, as well as with the lack of mirror image symmetry and the Stokes' shift between the spectra mentioned earlier is that there is only one ground state TPC conformer, but that the photophysics of TPC is governed by an excited state process. Further insight can

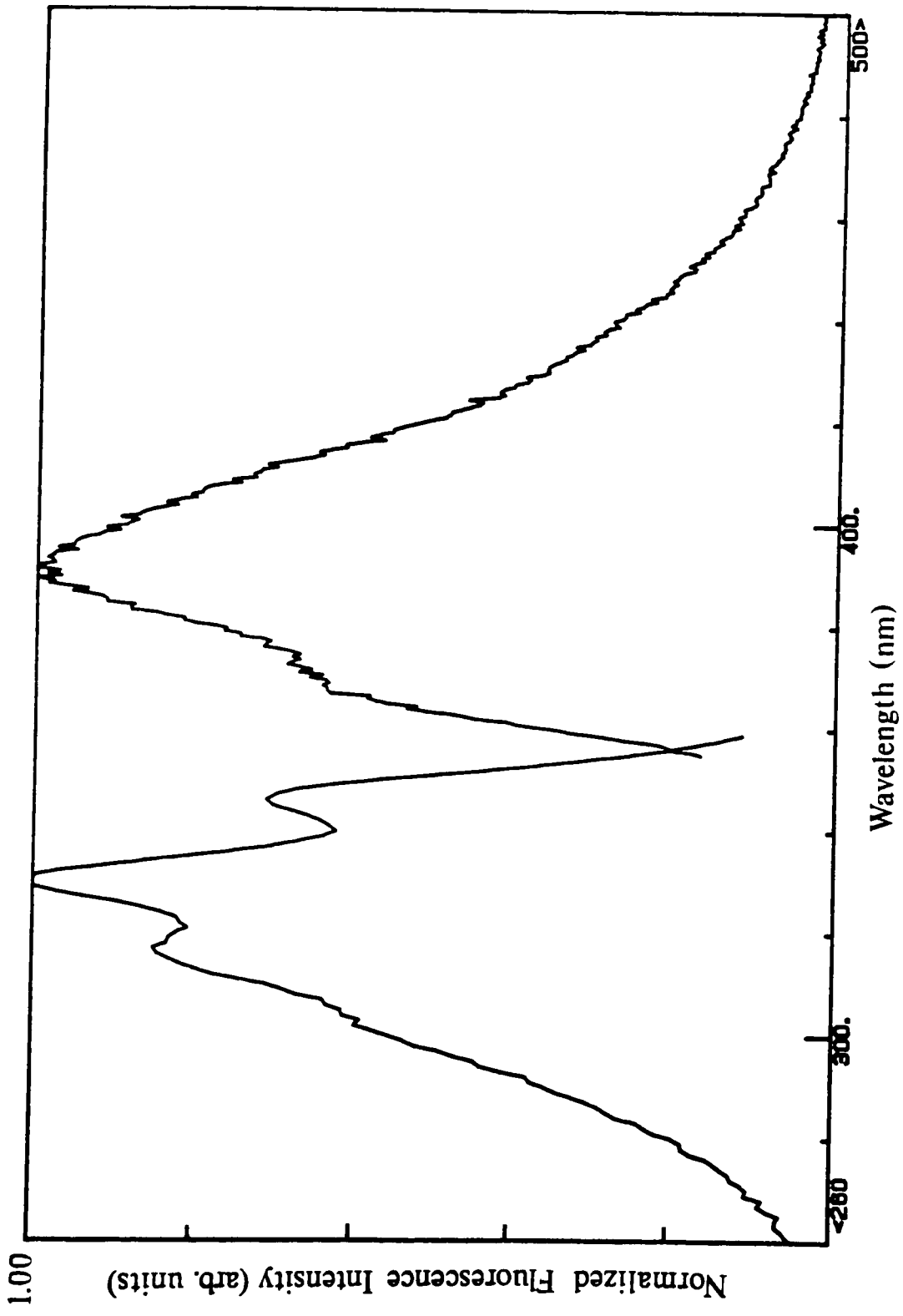

Figure 4.20: Fluorescence excitation (λ_{em} 410 nm) and emission (λ_{ex} 320 nm) spectra of TPC in TMP.

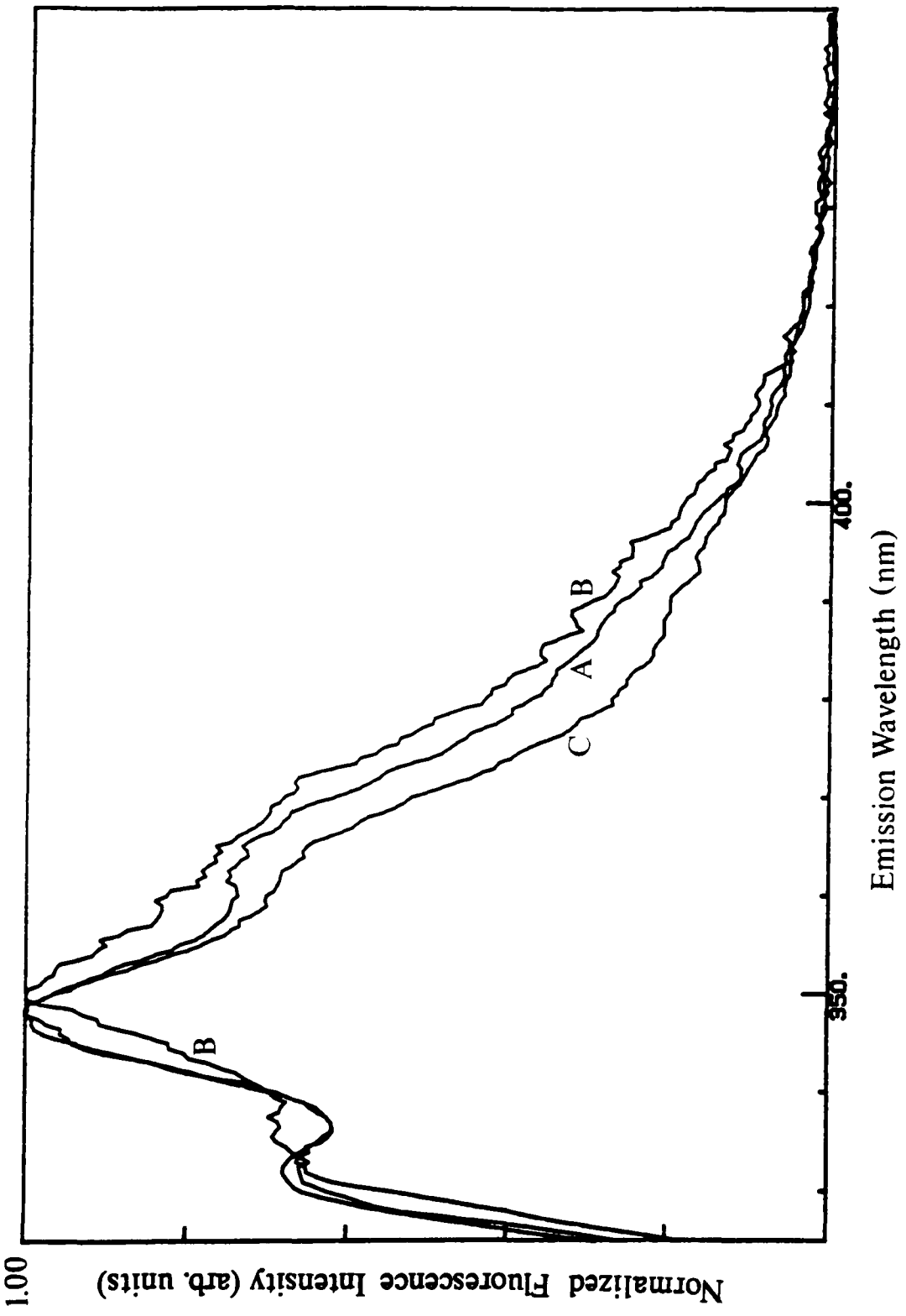

Figure 4.21: Excitation wavelength dependence of the emission spectrum of DPC in TMP (peak normalized); λ_{ex} 295 nm (A), λ_{ex} 305 nm (B), λ_{ex} 320 nm (C).

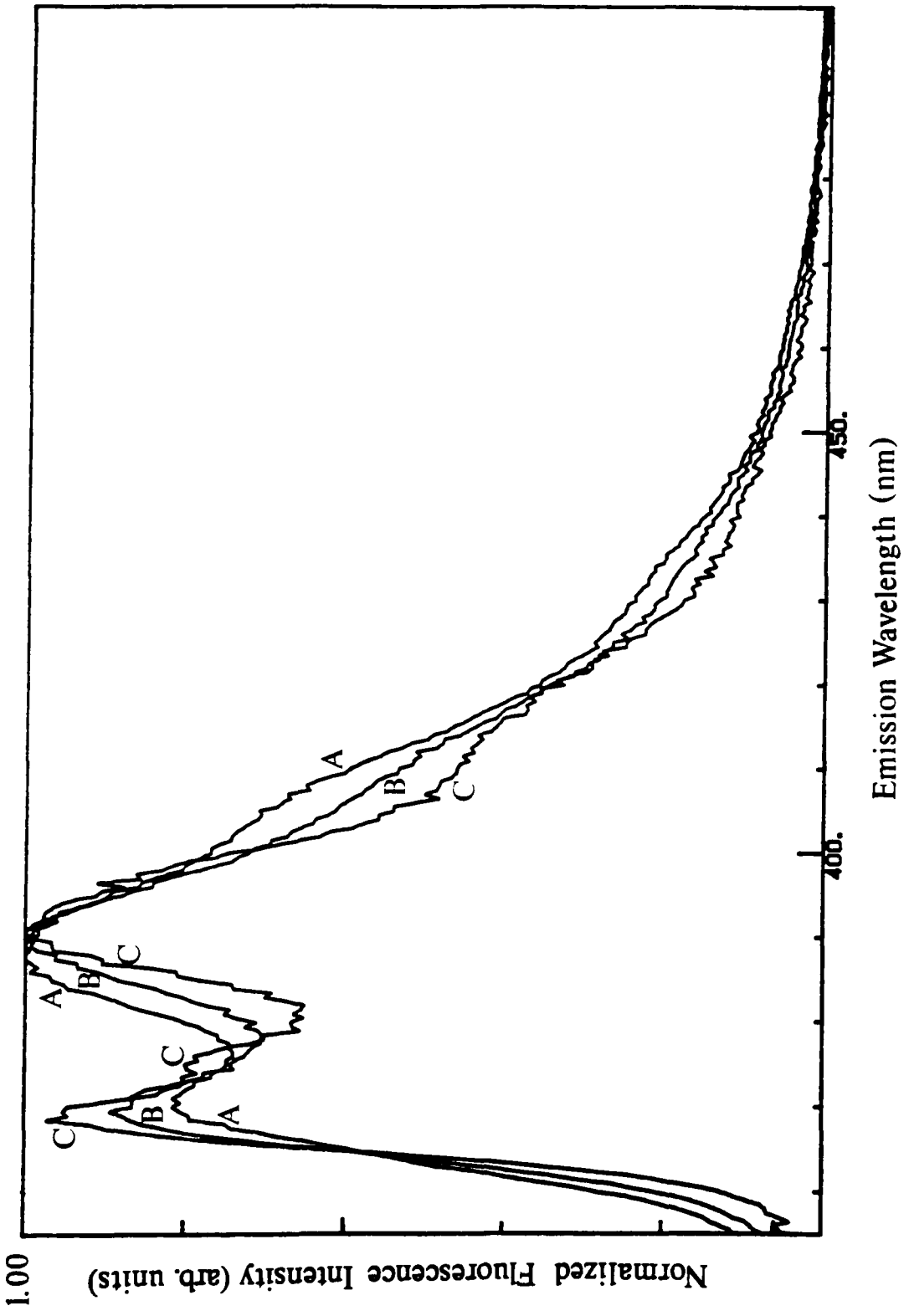

Figure 4.22: a) Excitation wavelength dependence of the emission spectrum of DNC in TMP (peak normalized); λ_{ex}320 nm (A), λ_{ex}340 nm (B) and λ_{ex}355 nm (C).

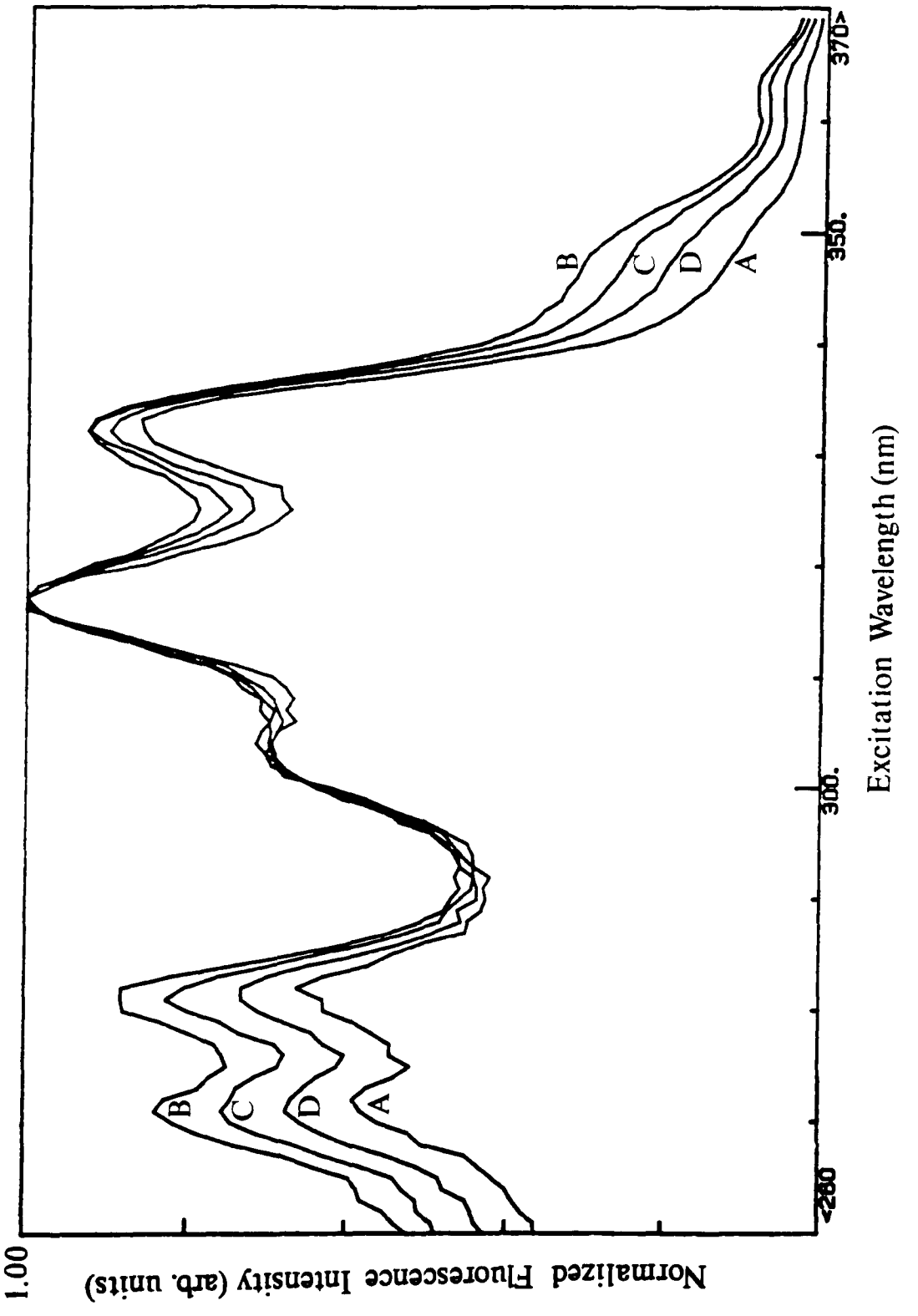

Figure 4.22: b) Emission wavelength dependence of the excitation spectrum of DNC in TMP (peak normalized); λ_{em}360 nm (A), λ_{em}370 nm (B), λ_{em}390 nm (C) and λ_{em}410 nm (D).

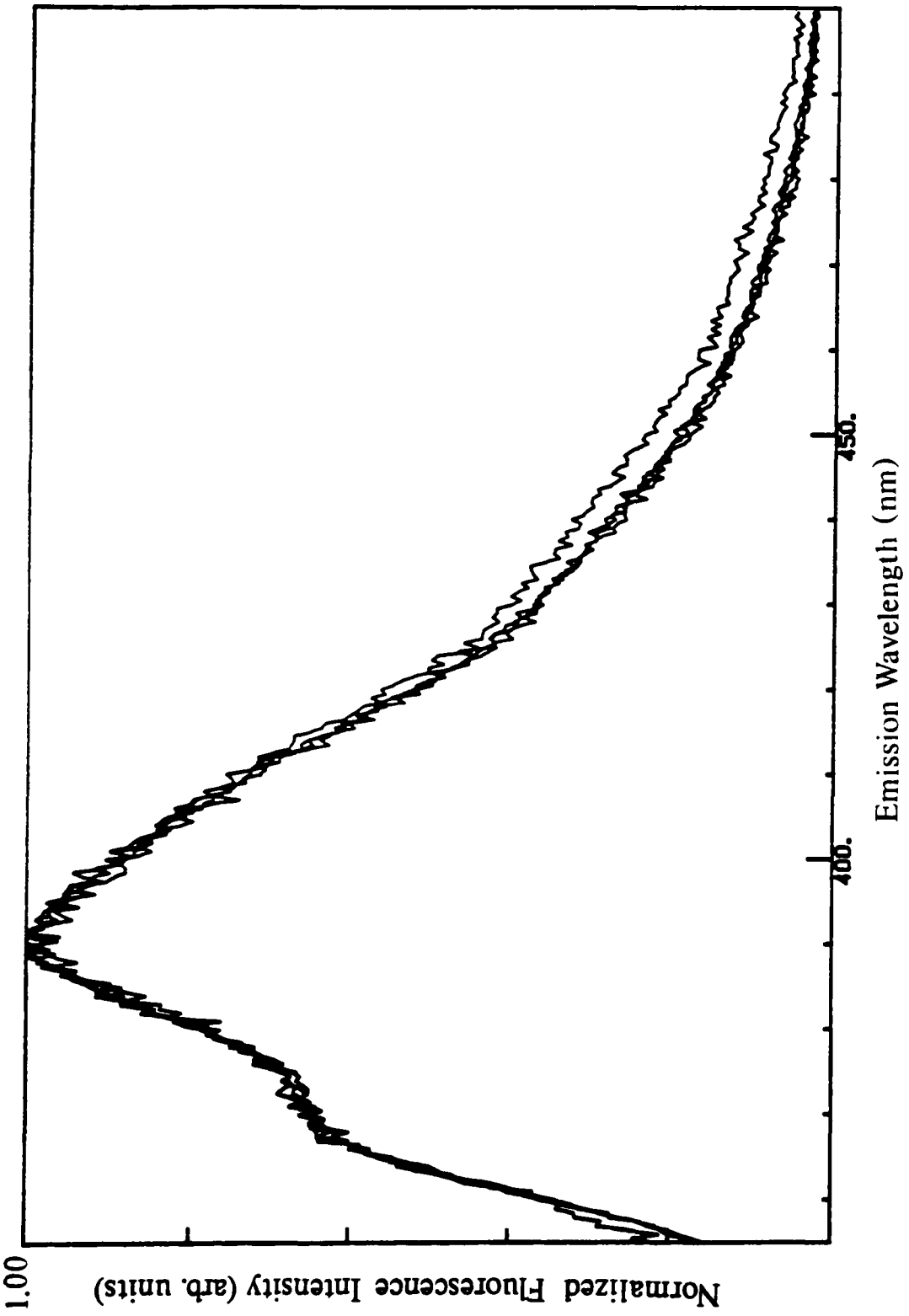

Figure 4.23: a) Invariance of the emission spectrum of TPC in TMP (peak normalized) with excitation wavelength.

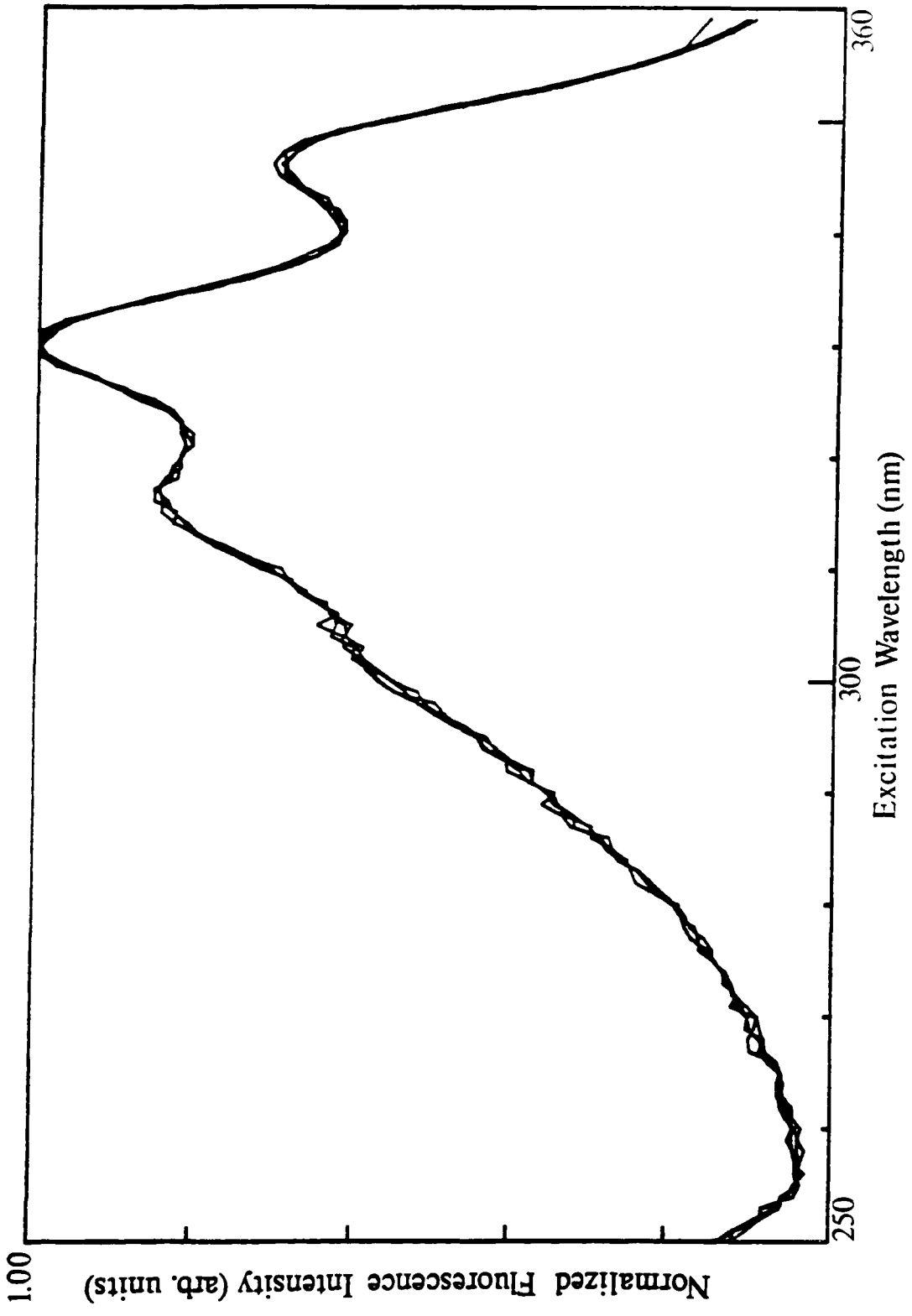

Figure 4.23: b) Invariance of the excitation spectrum of TPC in TMP (peak normalized) with emission wavelength.

be gained from time-resolved fluorescence results presented later.

Fluorescence quantum yield values, ϕ_f, for the three probes in various solvents and at several excitation wavelengths are presented in Tables 4.2–4.4. DNC is the most fluorescent with $\phi_f \sim 0.5$ in nonpolar solvents, while TPC and especially DPC are somewhat less so with ϕ_f's of 0.051 and 0.020 respectively in TMP. Notice that for all three probes, the ϕ_f values in TMP at various excitation wavelengths, λ_{ex}, are within experimental error of each other. Had the ϕ_f values varied with λ_{ex}, this would have been strong corroborative evidence for the existence of more than one ground state species. The observed invariance does not preclude the possibility of a ground state conformational equilibrium, as long as the conformers have similar ϕ_f values. In the case of TPC, however, given the other steady-state fluorescence results mentioned above, the λ_{ex} independence of ϕ_f appears to be a consequence of only one ground state conformer of this molecule.

Table 4.2: Fluorescence quantum yields, ϕ_f, for DPC in various solvents at excitation wavelength, λ_{ex}.

Solvent	Temperature[a] (°C)	λ_{ex} (nm)	ϕ_f[b]
TMP	20.1	295	0.021
	20.1	305	0.019
	20.1	320	0.017
n-BuOH	20.1	295	0.017
MeOH	20.1	295	0.008
H1L0	20.0	295	0.098

[a] ±0.1°C
[b] ±0.005

The ϕ_f of both DNC and TPC is sensitive to solvent polarity as can be illustrated by comparing ϕ_f values in the two solvents of similar refractive index, TMP and *n*-BuOH. There is a twofold increase in ϕ_f of DNC upon passing from *n*-BuOH to TMP, while a fourfold increase is seen in the case of TPC. DPC has low and similar ϕ_f's in both of these solvents. While the ϕ_f's of DNC and TPC display solvent sensitivity, the positions of their emission spectra do not. The emission maxima of DNC/TPC in TMP and *n*-BuOH, for example, are the same (not shown). So, it

Table 4.3: Fluorescence quantum yields, ϕ_f, for DNC in various solvents at excitation wavelength, λ_{ex}.

Solvent	Temperature[a] (°C)	λ_{ex} (nm)	ϕ_f[b]
TMP	20.1	310	0.41
	20.1	320	0.43
	20.1	340	0.45
	20.1	355	0.45
n-BuOH	20.1	310	0.24
	20.1	320	0.26
	20.1	340	0.26
	20.1	350	0.24
MeOH	20.0	340	0.12
H1L0	0.5	340	0.65
H1L0	10.0	340	0.58
H1L0	19.9	340	0.51
H1L0	29.9	340	0.44

[a] ±0.1°C
[b] ±0.005 or 5%, whichever is larger

Table 4.4: Fluorescence quantum yields, ϕ_f, for TPC in various solvents at excitation wavelength, λ_{ex}.

Solvent	Temperature[a] (°C)	λ_{ex} (nm)	ϕ_f[b]
TMP	20.0	310	0.057
	20.0	320	0.051
	20.0	340	0.051
	20.0	355	0.047
MCH	20.2	340	0.073
n-BuOH	20.0	340	0.012
MeOH	20.0	340	0.003
H1L0	20.0	340	0.25

[a] ±0.1°C
[b] ±0.005 or 5%, whichever is larger

appears that only DNC or TPC could be used as polarity probes, if measurements are based on ϕ_f values. However, even then these two probes are orders of magnitude less sensitive to polarity changes than the family of anilino-naphthalene sulphonates discussed earlier.

One other interesting observation is that the ϕ_f of both DPC and TPC increases dramatically with an increase in solvent viscosity. There is a fivefold change in ϕ_f of both compounds between a low viscosity nonpolar solvent like TMP (η = 5.03 cP, T=20°C)[72] and a high viscosity mineral oil, H1L0 (η = 220 cP, T=20.0°C). This reveals that at least one of the nonradiative decay rates of these two probes is viscosity dependent.

In summary then, the steady-state fluorescence measurements performed on DPC, DNC and TPC have allowed the following conclusions to be made so far. DPC is a weakly fluorescent probe whose ϕ_f and spectral maxima are solvent polarity independent but solvent viscosity dependent. Despite the low fluorescence efficiency, it was possible to ascertain that the photophysics of this probe are governed either by an excited state reaction and/or by ground-state conformational heterogeneity. Any pursuit of a further understanding of the photophysical behaviour of DPC would seem to be purely academic given that its low fluorescence quantum yield does not recommend it highly for membrane probe applications.

The relatively low ϕ_f of TPC would seem to put it on the threshold of sensitivity required for membrane studies. However, the marked solvent viscosity dependence of its ϕ_f has the potential of being exploited for studies of membrane fluidity. DNC has reasonably high ϕ_f's and if indeed it is shown by time-resolved fluorescence experiments and subsequent data analysis that the ground state heterogeneity of this probe arises from different rotamer populations, this could prove useful in membrane order studies.

4.3.3 Time-Resolved Fluorescence Results

Since for each of the probes, the steady-state fluorescence results indicated the presence of ground-state and/or excited-state heterogeneity, it was no surprise that the fluorescence decay profiles were not fitted by single exponential decay functions. Values of the lifetimes, τ_i, and the normalized pre-exponential factors, α_i, obtained

for the three probes in various solvents, and at a number of excitation and emission wavelengths, are presented in Tables 4.5–4.7.

Table 4.5: Lifetimes, τ_i, and pre-exponential factors, α_i, of DPC in H1L0.

Temp. (°C)	$\lambda_{ex}/\lambda_{em}$ (nm)	τ_1 (ns)	τ_2 (ns)	τ_3 (ns)	α_1	α_2	α_3	χ^2	SVR
13.3	295/330	0.275	0.109	0.010	0.05	0.24	0.72	1.09	1.59

Table 4.6: Lifetimes, τ_i, and normalized pre-exponential factors, α_i, of DNC in various solvents at excitation and emission wavelengths, λ_{em} and λ_{em}.

Solvent	Temp. (°C)	$\lambda_{ex}/\lambda_{em}$ (nm)	τ_1 (ns)	τ_2 (ns)	τ_3 (ns)	τ_4 (ns)	α_1	α_2	α_3	χ^2	SVR
TMP	20.5	320/360	69.5[a]	5.42	0.34[b]	0.02	0.258	0.409	0.333	1.03	1.99
		320/370	69.5[a]	5.42	0.34[b]	0.02	0.100	0.789	0.111	1.03	1.99
		320/390	69.5[a]	5.42	0.34[b]	0.02	0.170	0.704	0.127	1.03	1.99
	19.9	340/390	66.1[a]	5.29	0.20[b]	0.02	0.032	0.914	0.054	1.01	2.00
	19.9	350/390	63.9[a]	5.30	0.41[b]	0.02	0.005	0.942	0.053	1.03	1.84
n-BuOH	20.2	320/370	27.72	2.54	0.11		0.280	0.406	0.314	1.03	1.97
		320/390	27.72	2.54	0.11		0.264	0.501	0.235	1.03	1.97
	19.9	340/390	27.64	2.57	0.11	0.02	0.107	0.820	0.073	1.02	1.94
	19.9	350/390	27.27	2.56	0.082		0.011	0.614	-0.375	1.25	1.81
MeOH	20	320/390	14.43	1.80	0.41		0.195	0.308	0.498	1.02	1.93
MCH	20	320/390	20.5	4.11	0.20		0.158	0.670	0.172	1.00	1.82
H1L0	20	320/390	55.50	4.68	0.67	0.05	0.154	0.585	0.260	1.01	1.92

[a]The error in each of these values is in the last decimal place shown. The variation between the λ_{ex} could reflect different extents of deoxygenation of the samples.
[b]For discussion about the variation in the value of this lifetime, see text.

The magnitude of the lifetime of DPC was below the resolution limit (~30 ps) of the single photon counting apparatus described earlier (Section 4.2.2) except in a rather viscous environment such as H1L0 (η = 317 cP, T= 13.3°C). In this solvent, the fluorescence decay profile of DPC was fitted by a biexponential function with τ=275 ps and 109 ps, plus a third very short lifetime of 10 ps. This short component may indeed represent a decay parameter of the molecule. However, no definite conclusion about the origin of this component can be made since it could also arise from an instrumental artifact such as the wavelength dependence of the timing

Table 4.7: Lifetimes, τ_i, and normalized pre-exponential factors, α_i, of TPC

Solvent	Temp. (°C)	$\lambda_{ex}/\lambda_{em}$ (nm)	τ_1 (ns)	τ_2 (ns)	τ_3[a] (ns)	α_1	α_2	χ^2	SVR
TMP	21.5	320/360	0.532	0.210	0.001	0.323	0.677	1.01	1.93
		320/370	0.532	0.210	0.001	0.386	0.614	1.01	1.93
		320/390	0.532	0.210	0.001	0.400	0.600	1.03	1.86
		350/390	0.569	0.232	0.001	0.417	0.583	0.96	1.92
MCH	19.7	320/370	0.618	0.302	0.018	0.41	0.59	1.06	1.90
H1L0	20.6	320/370	1.281	0.502	0.024	0.662	0.338	1.07	1.91

[a]fixed

dispersion of the emission monochromator, or from instabilities in the excitation pulse[47]. The lifetimes associated with the fluorescence decay of TPC were also short, 532 ps, 210 ps and 1 ps(fixed) in TMP at 21.5°C, and were again below the resolution limit of the apparatus in solvents like *n*-BuOH and MeOH. However, the lifetimes of TPC in H1L0 were considerably longer at 1.256 ns and 643 ps at 21.3°C, in keeping with the higher ϕ_f observed in this solvent.

Fluorescence decay profiles of DNC were the most complex and could only be adequately described by sums of at least three exponential terms. A fourth lifetime component of ~50 ps was sometimes required in order to improve the statistics of the fitting but the origin of this short component probably lies in an instrumental artifact. Experiments making use of reference deconvolution procedures which correct for distortions introduced by wavelength dependent artifacts, could clarify this point. Unlike the case of DPC and TPC, the lifetimes of DNC differ from each other by at least an order of magnitude: 69.5 ns, 5.42 ns and 0.34 ns in TMP at an excitation wavelength of 320 nm. Notice that the magnitude of the third τ in TMP varies with excitation wavelength (Table 4.6). This probably arises from the fact that the channel widths used for the measurements were either 42.4 or 84.8 ps/channel due to the necessity to characterize the long lifetime component (69.5 ns) over at least two decades of decay. A more reliable value for this third lifetime could be had by using narrower channel widths but more channels in the data acquisition (e.g. 8192 channels instead of the 2048 channels used in this work).

The pre-exponential factors associated with the fluorescence decay of both DNC

and TPC vary with λ_{em}, while only those of DNC are also dependent on the excitation energy (Tables 4.6 and 4.7). This further supports the notion that TPC exists as a single conformer in the ground state, but that upon excitation a reaction occurs such that there are two emitting states or species which give rise to a biexponential fluorescence decay. On the other hand, the time-resolved data for DNC indicate that there is heterogeneity in both the absorption and emission processes of this molecule, which is consistent with the conclusion obtained from steady-state measurements.

Further insight into the nature of the absorption/fluorescence heterogeneity, and even assignment of specific conformations to particular absorbing species, could be had by determining the excitation and emission spectra associated with each lifetime, and also by performing an analysis to arrive at the corresponding photophysical parameters such as k_f, k_{nr} and ϕ_f.

4.3.4 Absorption and Fluorescence Properties of Dimethyl Aryl Polyene Sidechain Analogues

Before embarking on the analysis outlined above in order to gain some understanding of the origin of the observed absorption/fluorescence heterogeneity, it was important to ascertain how the presence of the bulky sterol substituent on the terminal carbon of the polyene chain affected the absorption and fluorescence properties of the sidechains. To this end, studies were carried out on the dimethyl analogues of DPC, DNC and TPC, referred to as DP, DN and TP respectively (Figure 4.24)[74].

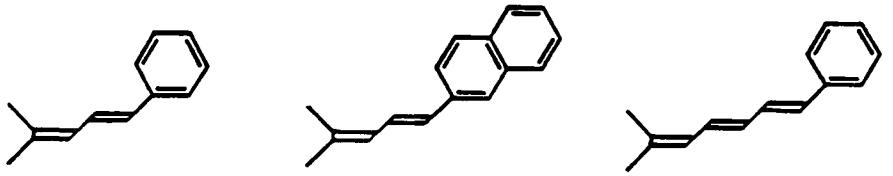

DP DN TP

Figure 4.24: DP, DN and TP.

The absorption spectra of DPC, DNC and TPC and their sidechain analogues, in MeOH, are presented in Figures 4.25–4.27. In all three cases, the cholesterol analogue probes have absorption spectra which are shifted by approximately 8 nm to

longer wavelengths relative to the absorption spectra of the corresponding dimethyl aryl polyenes. This shift in the spectra to lower energy with the presence of alkyl substituents was not surprising given that, for example, the 0–0 band of the $S_0 \rightarrow S_1^*$ transition of benzene in hexane occures at 260 nm while the same band of toluene is at 269 nm; a shift of $\sim$1200 cm^{-1} to lower energy through the addition of a single methyl substituent[75]. The absorption spectral shapes, however, are very similar between a given cholesterol analogue probe and its dimethyl aryl polyene model compound. Likewise, excitation and emission spectra of DP, DN and TP (not shown) are very similar in degree of overlap, and lack of mirror image symmetry, to the spectra of the corresponding cholesterol analogues, except that they are all shifted approximately 8 nm to higher energies.

Fluorescence decay profiles of DP and TP were fitted by the same number of exponential terms as those of DPC and TPC respectively (Table 4.8). DN fluorescence decay profiles, however, could be satisfactorily fitted by sums of two exponential terms with the third short lifetime value of $\sim$0.3 ns not being required to obtain good statistical parameters.

Table 4.8: Lifetimes, τ_i, and normalized pre-exponential factors, α_i, of DP, DN, and TP in various solvents at room temperature.

Probe	Solvent	$\lambda_{ex}/\lambda_{em}$ (nm)	τ_1 (ns)	τ_2 (ns)	τ_3 (ns)	α_1	α_2	α_3	χ^2	SVR
DP[a]	H1L0	295/340	0.25	0.047		0.01	0.99		1.58	0.86
	H1L0	320/390	0.23	0.047	0.001	0.01	0.43	0.56	1.58	0.86
DN	MCH	320/390	31.8	6.97		0.150	0.850		1.04	1.78
	MCH	320/390	32.1	7.04	0.10	0.127	0.725	0.148	1.00	1.94
	MeOH	320/390	28.6	3.75		0.282	0.718		0.99	1.87
	MeOH	320/390	28.7	3.78	0.022	0.222	0.565	0.213	0.98	1.89
TP	H1L0	320/390	1.20	0.63		0.266	0.734		1.94	0.61
	H1L0	320/390	1.73	0.75	0.05	0.049	0.711	0.240	1.09	1.94

[a]These were the best fits obtained for fluorescence decay profiles of this molecule.

All of the above observations are consistent with the presence of the sterol substituent in DPC and TPC as not being a source of heterogeneity in the absorption/fluorescence of these molecules. Very similar spectral shapes and fluorescence

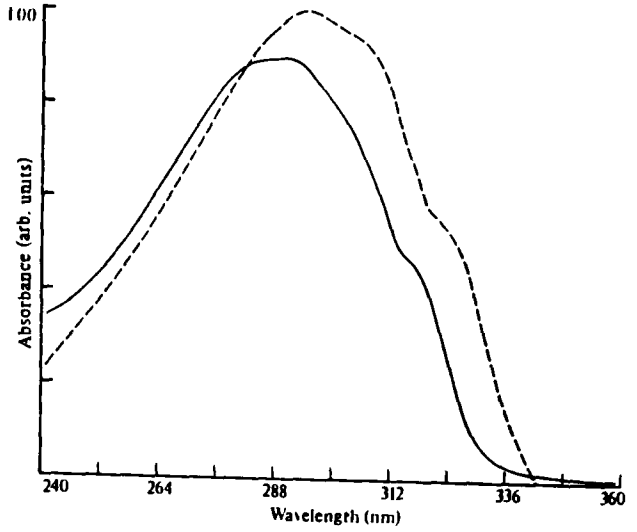

Figure 4.25: Absorption spectra of DP(—) and and DPC(---) in MeOH.

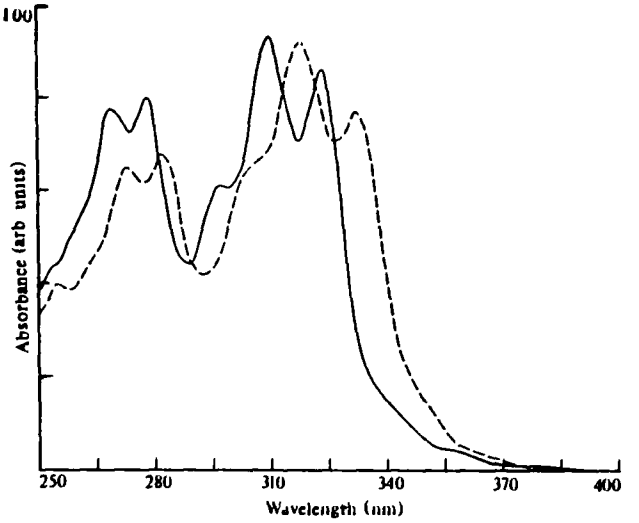

Figure 4.26: Absorption spectra of DN(—) and and DNC(---) in MeOH.

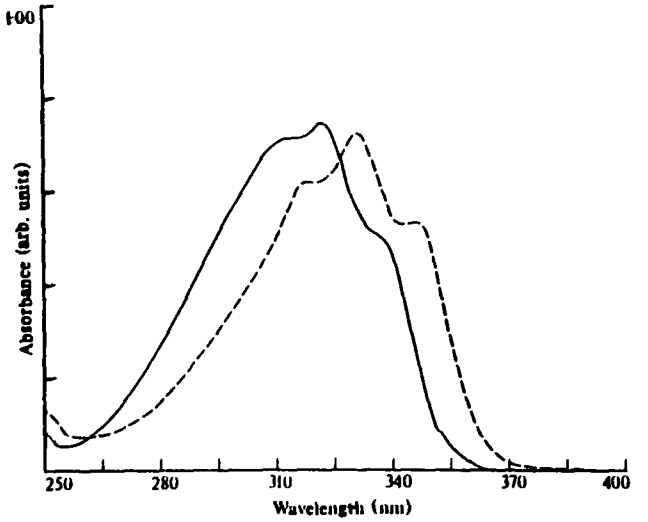

Figure 4.27: Absorption spectra of TP(—) and and TPC(---) in MeOH.

decay laws for these dimethyl aryl probes point to the origin of the heterogeneity as being intrinsic to the fluorophore itself, as opposed to it being due to any substituent. The difference observed in the fluorescence decay laws for DN and DNC will need to be addressed in any model which is put forward to rationalize the photophysical properties of DNC.

4.3.5 Derived Spectra and Photophysical Parameters of DNC

The simplest model which can account for the triexponential decay kinetics and the wavelength dependent excitation and emission spectra of DNC in solvents, is one in which there are as many conformers in the ground state as there are lifetime components, and that these conformers do not establish a new equilibrium within their excited state lifetimes. This model is equivalent to the NEER principle introduced earlier[39], and has been found to be generally valid for diaryl ethylenes, and specifically valid for PNE which is the closest analogue to the DNC fluorophore in the literature.

In such a simple model, the singlet lifetimes are each a function of the rate constants for the deactivation of one of the populations (e.g. conformers) of DNC. DAS and IEDAS then represent the emission and excitation spectra of these various populations, and are presented for each of the three lifetime components in TMP in Figures 4.28 and 4.29. Each of the DAS of DNC in TMP is unique, though the DAS associated with the 69.5 ns and 0.34 ns lifetimes are similar in shape beyond λ_{em}= 390 nm.

The IEDAS of the two longer lifetime components are well resolved, and differ markedly (Figure 4.29d). The long wavelength band between 355 and 370 nm is more prominent in the τ= 5.42 ns IEDAS, while the main band centred at ~320 nm is more intense in the τ= 69.5 ns IEDAS. Also, the main excitation band is shifted to lower energies in the IEDAS associated with the 5.42 ns lifetime. The high energy band around 280 nm is equally intense in both IEDAS. Not suprisingly, the τ=0.34 ns IEDAS is not well resolved since this component accounts for a small percent ($\leq$ 2%) of the fluorescence intensity at any given λ_{em} (Figure 4.29c). It is now possible to confirm that the species which absorbs most on the low energy side of the absorption spectrum does indeed have a maximum in the fluorescence

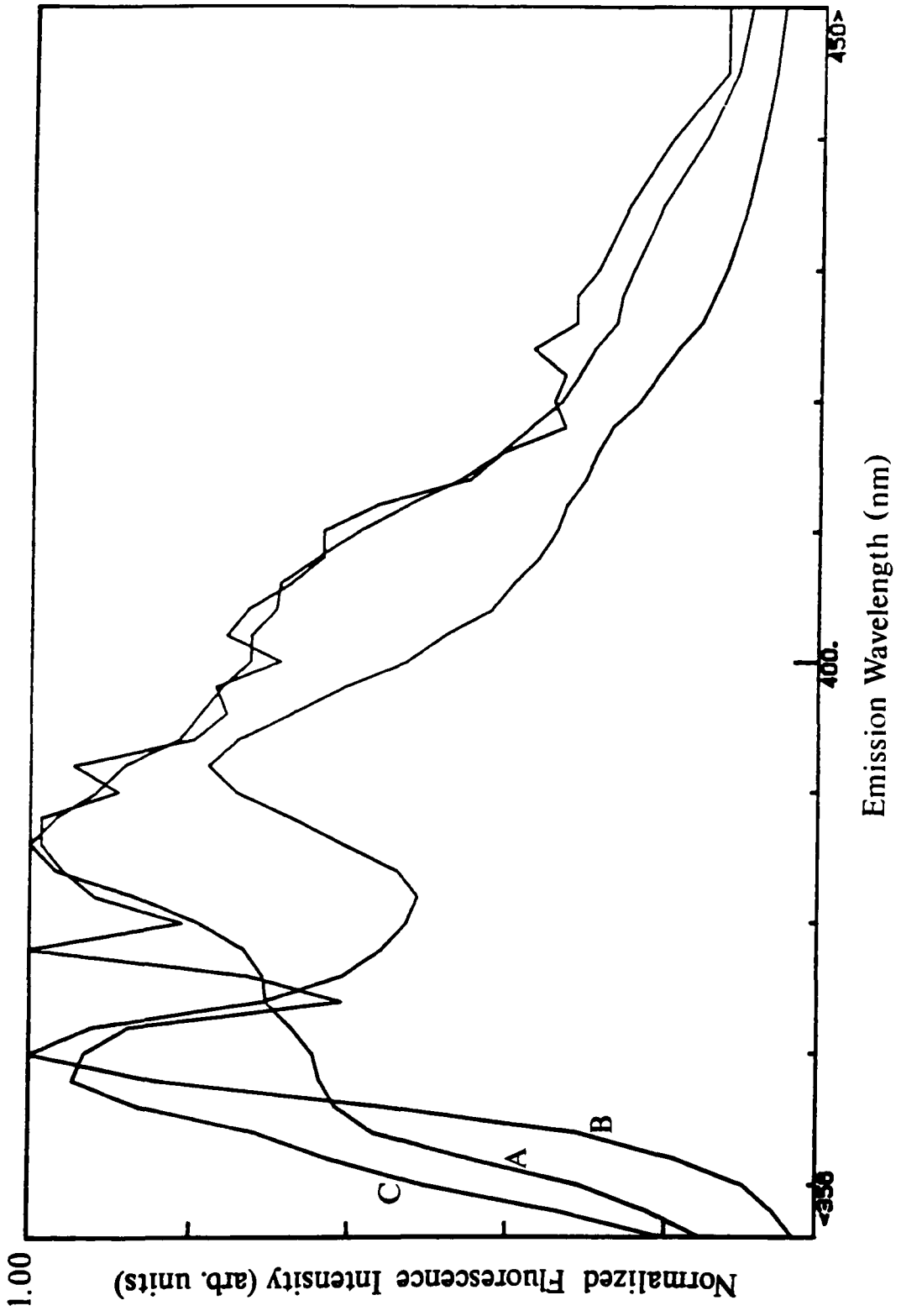

Figure 4.28: Normalized decay associated emission spectra (DAS) for DNC in TMP at λ_{ex}320 nm; τ = 69.5 ns (A), τ = 5.42 ns (B) and τ = 0.34 ns (C).

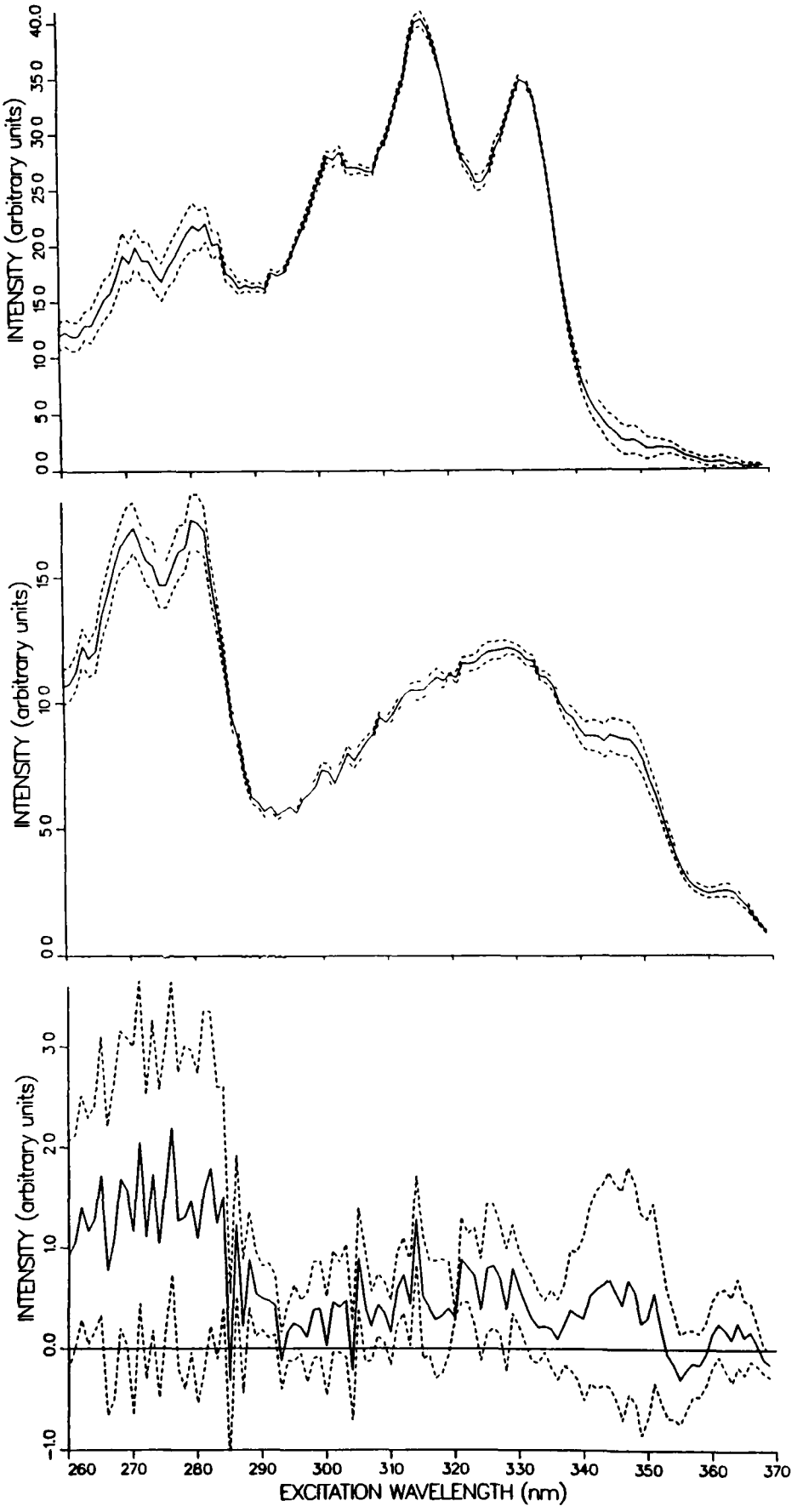

Figure 4.29: Indirect excitation decay associated spectra (IEDAS) for DNC in TMP at λ_{em}390 nm; a) τ = 69.5 ns, b) τ = 5.42 ns, c) τ = 0.34 ns. The dashed lines above and below the solid lines represent the standard error bounds.

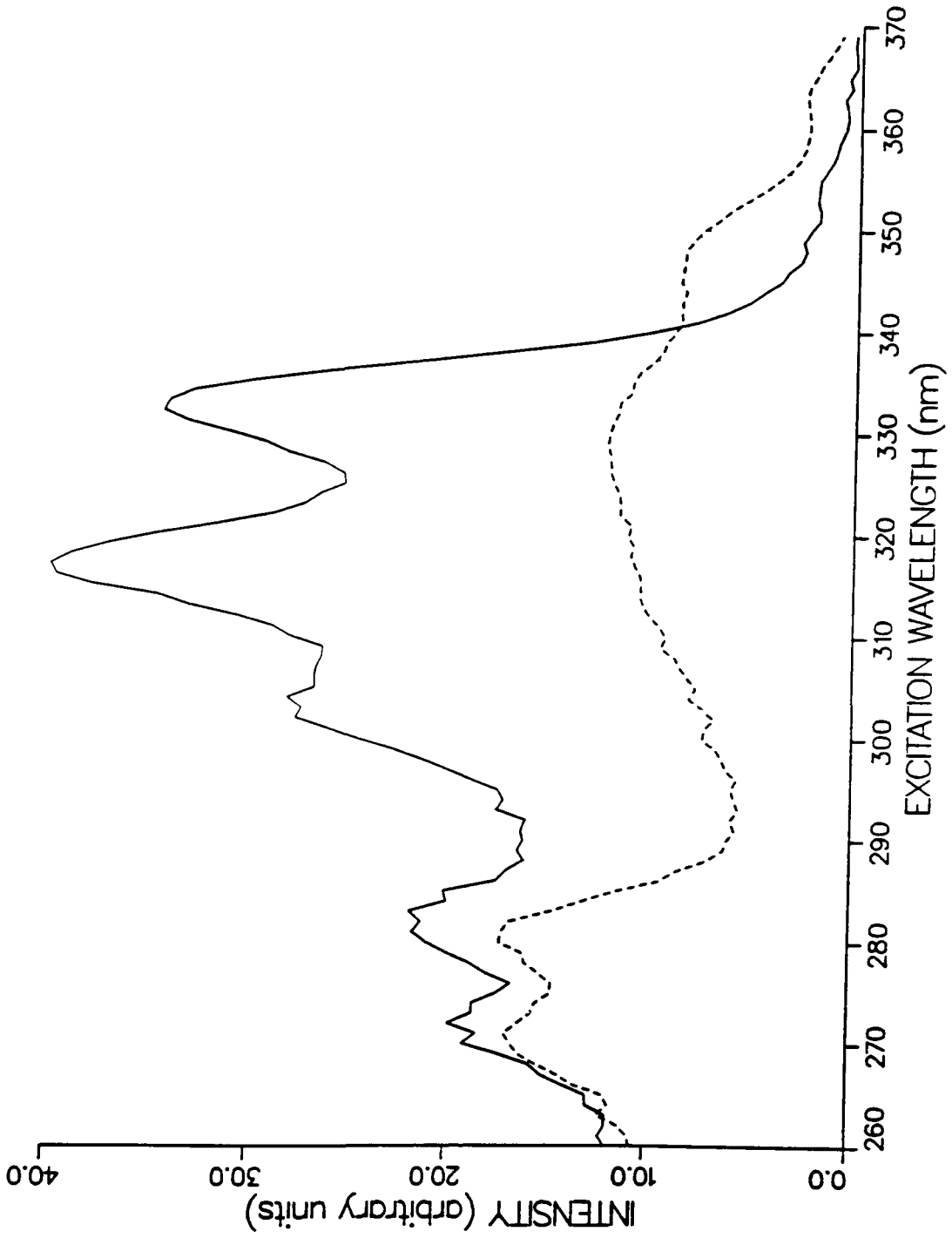

Figure 4.29: Un normalized indirect excitation decay associated spectra (IEDAS) for DNC in TMP at λ_{em}390 nm; τ = 69.5 ns and 5.42 ns

spectrum at 370 nm as suspected from steady-state measurements, and that its singlet lifetime is 5.42 ns in TMP. These observations are very similar to those for *s*-cis PNE[32,34].

Attempts to calculate the various photophysical parameters associated with each lifetime, using the analysis presented in Section 4.1.3 extended to three fluorescence decay components, were unsuccessful since a negative fluorescence intensity, F_3, was obtained for the species associated with the short lifetime. This could be due to the relatively large error in determining the small contribution of this component to the overall fluorescence. Instead, a modified analysis which made use of IEDAS intensities (see below) allowed the excited state fractions of the three species to be directly calculated.

The expression relating the total excitation spectral intensity at a particular λ_{ex} and λ_{em}, $\overline{E}(\lambda_{ex}', \lambda_{em}')$, to the excited state fractions f_i is (equation 4.49)

$$\overline{E}(\lambda_{ex}', \lambda_{em}') = \bar{\epsilon}(\lambda_{ex}')\bar{c}\{f_1(\lambda_{ex}')F_1(\lambda_{em}') + f_2(\lambda_{ex}')F_2(\lambda_{em}') + f_3(\lambda_{ex}')F_3(\lambda_{em}')\} \tag{4.49}$$

The corresponding equation for a particular IEDAS is (equation 4.50)

$$E_i(\lambda_{ex}', \lambda_{em}') = f_i(\lambda_{ex}')F_i(\lambda_{em}')\bar{\epsilon}(\lambda_{ex})\bar{c} \tag{4.50}$$

So, for a given lifetime associated species $i = 1$, the ratio of IEDAS intensities at two different λ_{ex}, ($\lambda_{ex}{}^A$ and $\lambda_{ex}{}^B$), measured at the same λ_{em} is (equation 4.51)

$$\begin{aligned} \frac{E_1(\lambda_{ex}{}^A, \lambda_{em}')}{E_1(\lambda_{ex}{}^B, \lambda_{em}')} &= \frac{f_1(\lambda_{ex}{}^A)}{f_1(\lambda_{ex}{}^B)} \times \frac{F_1(\lambda_{em}')}{F_1(\lambda_{em}')} \times \frac{\bar{\epsilon}(\lambda_{ex}{}^A)\bar{c}}{\bar{\epsilon}(\lambda_{ex}{}^B)\bar{c}} \\ &= \frac{f_1(\lambda_{ex}{}^A)}{f_1(\lambda_{ex}{}^B)} \times \frac{\bar{A}(\lambda_{ex}{}^A)}{\bar{A}(\lambda_{ex}{}^B)} \end{aligned} \tag{4.51}$$

Rearranging,

$$\frac{f_1(\lambda_{ex}{}^A)}{f_1(\lambda_{ex}{}^B)} = \frac{E_1(\lambda_{ex}{}^A, \lambda_{em}')}{E_1(\lambda_{ex}{}^B, \lambda_{em}')} \cdot \frac{\bar{A}(\lambda_{ex}{}^B)}{\bar{A}(\lambda_{ex}{}^A)} \tag{4.52}$$

The ratio of IEDAS intensities for a particular species at different λ_{ex} is known, as is the ratio of total absorption intensities. For triple exponential decay kinetics, the two above ratios can be determined from the absorption spectrum and from IEDAS intensities at three different λ_{ex}, for the three lifetime components. This results in nine unknowns [$f_i(\lambda_{ex}{}^A)$, $i = 1, 2, 3$; $3\lambda_{ex}$], and six equations. However, the sum of

f_i at a particular λ_{ex} must equal unity by definition (equation 4.53).

$$\sum_{i=1}^{n} f_i(\lambda_{ex}{}') = 1 \tag{4.53}$$

This yields three more equations which allows the nine $f_i(\lambda_{ex}{}^A)$ to be determined. Calculation of ϕ_f, k_f and k_{nr} for the individual components follows from equations 4.24, 4.13 and 4.12 respectively.

The derived photophysical parameters associated with the two longest lifetime components of DNC in TMP are listed in Table 4.9. One of the most interesting observations is that the radiative lifetimes associated with the two longest lifetimes are quite different. The long singlet lifetime species has a radiative lifetime of 164 ns while the species with a singlet lifetime of 5.42 ns has a radiative lifetime of 11.7 ns. Insight into the origin of this difference in the radiative lifetimes of the two species can be had by referring back to their respective IEDAS (Figure 4.29d). The 0–0 bands of the $S_0 \rightarrow S_1^*$ and $S_0 \rightarrow S_2^*$ transition of the 69.5 ns lifetime associated species occur at ~363 nm and ~332 nm, while the 0–0 positions of $S_0 \rightarrow S_1^*$ and the $S_0 \rightarrow S_2^*$ transitions of the 5.42 ns lifetime component are ~363 nm and ~345 nm. The energy difference of ~1400 cm^{-1} between S_1^* and S_2^* for this latter species is considerably smaller than that of ~2600 cm^{-1} determined for the long lifetime component. Hence, it can be expected that there will be a greater degree of mixing between S_1^* and S_2^* for the 5.42 ns lifetime associated species, via vibronic (vibroelectronic) coupling. This is because the perturbation induced by vibronic coupling, usually manifested in an intensity redistribution in the absorption and emission spectra, is inversely proportional to the energy difference between the coupled states. So, because of the greater amount of contamination between S_1^* and S_2^* (a B_u–like state based on its sensitivity to solvent polarizability, and its high molar absorptivity coefficient) of the species with $\Delta E(S_2^*–S_1^*)$ ~1400 cm^{-1}, S_1^* is expected to show some B_u character. Indeed, the short τ_{rad} calculated for this species is more typical of a τ_{rad} associated with a B_u state[76] as opposed to the other τ_{rad} value of 164 ns which is more typical of a naphthalene excited state (τ_{rad} ~500 ns[77]). As the emission of this other species should be from a 'purer' S_1^* state, this suggests that S_1^* of DNC is naphthalenic. However, to assess positively the role of vibronic coupling in the emission of DNC, vibrationally resolved spectra of S_1^* are necessary.

Table 4.9: Derived photophysical parameters of DNC in TMP at 20.5°C.

component i	$f_i(\lambda_{ex}340$ nm)	τ_s (ns)	τ_f (ns)	ϕ_{fi}	k_{fi} (s^{-1})	k_{nri} (s^{-1})	c_i[a]
1	0.718	69.5	164	0.42	6.09×10^6	8.30×10^6	0.69
2	0.281	5.42	11.7	0.46	8.55×10^7	9.90×10^7	0.31
3	0.002	0.34					

[a]calculated neglecting component 3.

In summary, the derived photophysical parameters and the derived DAS and IEDAS of DNC have provided insight into the nature of the lowest excited states of this molecule, as well as into the relative positions and intensities of the absorption transitions to these states in the two longest lifetime associated species. Armed with this information, molecular orbital calculations can be very useful in postulating the identity of these species. By calculating the excitation energies and oscillator strengths of the low-lying electronically excited states for the four possible single bond rotamers of a model compound for the fluorescent sidechain of DNC, and comparing these predicted excitation patterns with the observed IEDAS, it should prove possible to assign the lifetime associated species to particular conformers of DNC.

4.3.6 Conformational Assignment for DNC

A partial conformational analysis is possible simply from the relative ground state concentrations, c_i, calculated for DNC in TMP at room temperature (Table 4.9). This is because on steric grounds, the *s-trans, s-trans* conformer of DNC (*tt*-DNC, see Figure 4.30) can be expected to be the most stable due to its more favourable H–H non-bonded interactions. So the species present in the greatest concentration, which is that associated with the 69.5 ns lifetime, can be assigned this conformation. Such an assignment is qualitatively in agreement with the assignment of the longer lifetime of PNE (~25 ns) to its *s-trans* conformer[32,34]. The IEDAS of the 69.5 ns lifetime associated species can then be used as a starting point for comparison of the calculated excitation patterns of the various rotamers of 1-(2′-Naphthyl)-1,3-butadiene (NBD, see Figure 4.31) with the IEDAS for all the lifetime components of DNC.

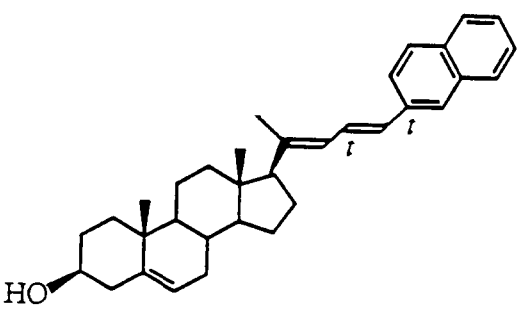

tt -DNC

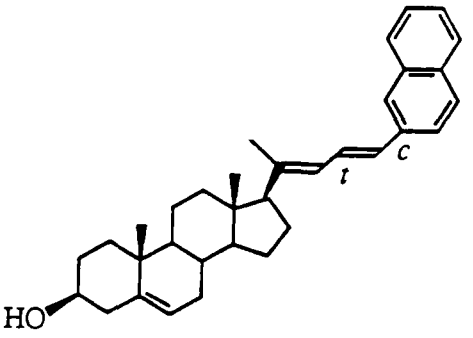

tc -DNC

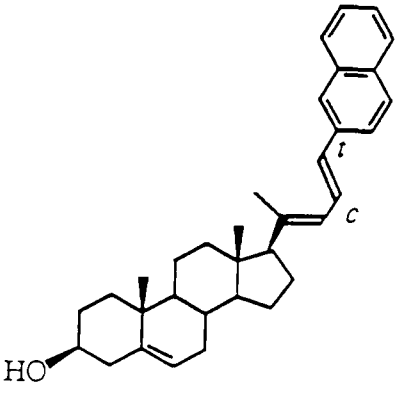

ct -DNC

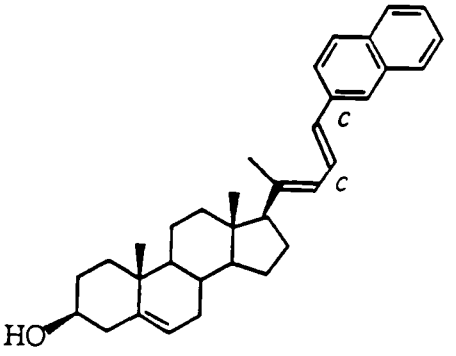

cc -DNC

Figure 4.30: *tt*-,*tc*-,*ct*- and *cc*-DNC.

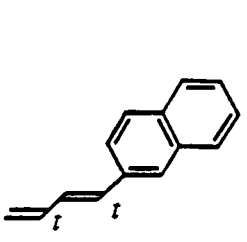

tt -NBD

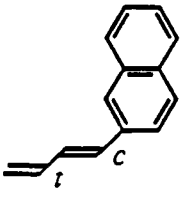

tc -NBD

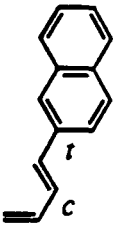

ct -NBD

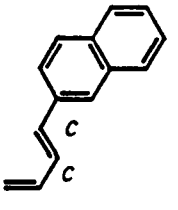

cc -NBD

Figure 4.31: *tt*-,*tc*-,*ct*- and *cc*-NBD.

Molecular Orbital Calculations

The calculated excitation energies and oscillator strengths of the four lowest excited singlet states of *tt*-, *tc*-, *ct*- and *cc*-NBD (see Figure 4.31), including only singly excited configurations (Mataga-Nishimoto parametrization), are presented in Table 4.10. S_1^* is predicted to be a naphthalene L_b-like state, S_2^* a polyene B_u-like state, and S_3^* a naphthalene L_a-like state for all four conformers. The predicted excitation energies for NBD are higher than the experimental values for DNC and DN, which is expected due to the absence of alkyl substituents on the terminal olefinic carbon atom of NBD. However, correlation with the observed excitation pattern is possible. $S_0 \rightarrow S_1^*$ corresponds to the weak red-edge absorption, $S_0 \rightarrow S_2^*$ corresponds to the main absorption band while $S_0 \rightarrow S_3^*$ gives rise to the moderately intense band located at ~280 nm.

The position of the $S_0 \rightarrow S_1^*$ (L_b-like) transition is calculated to be conformer independent, while its oscillator strength is weak but conformer dependent. It is predicted to be stronger for the conformers which have the *s-trans* conformation about the single bond connecting the naphthyl and dienyl moieties. This can be qualitatively understood by considering the electronic interaction between the naphthyl and butadienyl chromophores in the different conformers of NBD. In other words, how do the pure naphthalenic L_b and butadienic B_u excited states interact to yield an L_b–*like* S_1^* and B_u–*like* S_2^* for the four conformers of NBD? The $S_0 \rightarrow S_1^*(L_b)$ transition of unsubstituted naphthalene is long-axis polarized[4]; i.e. the absorption dipole moment is directed along the long-axis (Figure 4.30). For an $S_0 \rightarrow S_2^*$ (A_g–B_u) polyene transition, the absorption dipole moment lies along the C=C framework. So, for a naphthalene molecule substituted in the 2-position with a polyene chain, an *s-trans* conformation of the intervening single bond results in the absorption dipole moments of the two chromophores being roughly parallel (Figure 4.30). On the other hand, an *s-cis* conformation results in an approximate perpendicular arrangement of the two dipole moments. Hence it could be envisaged that there would be less intensity borrowing by the weak $S_0 \rightarrow S_1^*$ (L_b–like) transition from the strong $S_0 \rightarrow S_2^*$ (B_u–like) transition for the *tc* and *cc* conformers of the NBD, as predicted by the molecular orbital calculations.

The trend in S_2^* (B_u-like) oscillator strength with conformation parallels that

Table 4.10: Excitation energies and oscillator strengths, f, predicted for the low-lying excited electronic states of the various rotamers of NBD by CNDO/S calculations (Nishimoto-Mataga parametrization).

Rotamer[a]	State[b]	E (nm)[c]	E (nm)[d]	f	ϵ^e
tt-NBD	S_1^* (L_b)	329	363	0.0113	0.02
	S_2^* (B_u)	303	332	1.1236	1.00
	S_3^* (L_a)	266	281	0.9870	0.63
	S_4^*	238		0.0163	
tc-NBD	S_1^* (L_b)	328	363	0.0022	0.08
	S_2^* (B_u)	310	345	0.7750	0.36
	S_3^* (L_a)	264	280	1.2183	0.50
	S_4^*	239		0.0225	
ct-NBD	S_1^* (L_b)	329		0.0131	
	S_2^* (B_u)	306		0.9906	
	S_3^* (L_a)	269		0.8476	
	S_4^*	239		0.0222	
cc-NBD	S_1^* (L_b)	328		0.0038	
	S_2^* (B_u)	313		0.8788	
	S_3^* (L_a)	267		0.9182	
	S_4^*	240		0.0438	

[a] see Figure 4.31 for a diagram of the various rotamers of NBD.
[b] see reference 4 for general background concerning symmetry designations.
[c] calculated
[d] the positions of the 0-0 bands of the $S_0 \rightarrow S_n^*$ transitions of *tt*-DNC and *tc*-DNC from their respective IEDAS based on the conformational assignment discussed in the text.
[e] relative ϵ at the 0-0 band of the $S_0 \rightarrow S_n^*$ transitions of *tt*-DNC and *tc*-DNC from their IEDAS (λ_{ex}390 nm), arbitrarily assigning $\epsilon(S_0 \rightarrow S_2^*$ 0-0) for *tt*-DNC at 1.00.

of the S_1^* state, as might be expected from the above argument. However, the variation of S_3^* (naphthalene L_a-like) oscillator strength with conformation is quite different. Again, this can be qualitatively understood if one considers that the $S_0 \rightarrow L_a$ transition of naphthalene is short-axis polarized[4]. Using similar arguments to the above, it can be anticipated that the absorption dipole moments of the $S_0 \rightarrow S_3^*$ (L_a–like) transition and the strong $S_0 \rightarrow S_2^*$ (B_u-like) transition of NBD will interact most favourably in their almost parallel arrangement in the *tc* conformer, as predicted by the molecular orbital calculations.

In the assignment of the 69.5 ns and 5.42 ns lifetime associated species of DNC to specific conformers, the main excitation spectral differences which need to be accounted for are (Figure 4.29d):—

1. The shift of the main absorption band ($S_0 \rightarrow S_2^*$) to lower energies for the 5.42 ns lifetime species.

2. The greater intensity of this main absorption band in the IEDAS associated with the longer liftime.

3. The relative intensities of the $S_0 \rightarrow S_3^*/S_0 \rightarrow S_2^*$ absorption transitions are <1 and >1 for the 69.5 ns and 5.42 ns lifetime associated species respectively.

From the relative concentrations of the species at room temperature, it was concluded that the longer lifetime species was the *s-trans*, *s-trans* conformer of DNC (*tt*–DNC). If this result is used as a starting point to compare the predicted excitation patterns with the IEDAS, it can be determined whether a conformational assignment can be made which is consistent with all the data.

Each of the three remaining conformers of NBD, (i.e. *tc, ct* and *cc*) is predicted to have a $S_0 \rightarrow S_2^*$ transition which is red-shifted with respect to that of *tt*-NBD (Table 4.10). This is evidence suggesting that at least the 5.42 ns lifetime associated species of DNC cannot be assigned the *tt* conformation, since its $S_0 \rightarrow S_2^*$ transition is red-shifted from that of the 69.5 ns lifetime associated species. Comparison of the calculated $S_0 \rightarrow S_3^*/S_0 \rightarrow S_2^*$ oscillator strengths of *tt*-NBD (<1), further support the assignment of the *tt* conformation to the 69.5 ns lifetime associated species of DNC. Only two conformations of NBD have $f(S_0 \rightarrow S_3^*)/f(S_0 \rightarrow S_2^*)$ ratios which are greater than one as observed in the 5.42 ns IEDAS, and these are *tc*- and *cc*-NBD. The

ratio predicted for *tc*-NBD of 1.6 is closer to the experimentally observed value of 1.4 from the 5.42 ns IEDAS, than the value of 1.04 calculated for *cc*-NBD. Also, on steric grounds, *tc*-DNC would be expected to be more stable than *cc*-DNC because of the unfavourable 21–CH_3, 24–H interaction in *cc*-DNC (Figure 4.30).

The emerging assignment of the long lifetime species of DNC to the *tt* conformation, and the shorter (5.42 ns) lifetime species to *tc*-DNC, is consistent with the lower intensity $S_0 \rightarrow S_2^*$ absorption band observed in the 5.42 ns IEDAS as this is predicted for *tc*-NBD as opposed to *tt*-NBD (Table 4.10). The only discrepancy between the observed and calculated data with the this conformational assignment is that the intensity of the weak $S_0 \rightarrow S_1^*$ transition appears to be greater for *tc*-DNC than for *tt*-DNC based on the relative IEDAS intensities in this region. This is opposite to what is predicted for *tt*-NBD and *tc*-NBD. The source of this discrepancy could arise from the unknown contribution of the strong $S_0 \rightarrow S_2^*$ band in this region for *tt*-DNC, given that its S_2^* state occurs at a lower energy than that of *tt*-DNC. Alternatively, the discrepancy could be a manifestation of a greater extent of vibronic coupling between S_1^* and S_2^* for *tc*-DNC, as indicated by its small τ_{rad} as discussed earlier.

Nuclear Overhauser Effect (nOe) Experiments

Independent experimental evidence for the existence of a ground-state conformational equilibrium between the *tt*- and *tc*- conformers of DNC was obtained by a high resolution nOe experiment. Upon saturating the 23-H resonance at δ7.21 ppm, an enhancement was seen of the two resonances at δ7.71 ppm and δ7.64 ppm (Table 3.3). These resonances are due to H-1′ and H-3′ respectively on the naphthalene ring (Table 3.1). Since the nOe occurs by a 'through-space' and not 'through-bonds' mechanism, and also since it falls off with distance to the sixth power, observation of an nOe to both of these protons can only be rationalized in terms of a rotation about the C-24,C-2′ single bond on times slower than or approaching the NMR timescale. If rotation occurred faster than on the NMR timescale (i.e. approaching the fluorescence timescale), an average conformation would have been observed and it is unlikely that an nOe to both H-1′ and H-3′ could be observed in such an average conformation. Hence, this NMR result provides strong corroborative evidence as to

the existence of a ground-state equilibrium between the C-24,C-2′ *s-cis* and *s-trans* conformers of DNC. It also upholds the use of the NEER assumption in the conformeric analysis of the fluorescence decay data of DNC, since the interconversion rate between the two rotamers would be expected to be even lower in the excited state due to the acquired partial double bond character of the C-24,C-2′ bond.

The relative magnitudes of the nOe to H-1′ and H-3′ are 2 and 6 respectively, and if it is assumed that the distance of closest approach of the 23-H to these two protons in *tc*- and *tt*-DNC respectively is the same, then an approximate ground-state conformer ratio $c_1/c_2(=c_{tt}/c_{tc})$ of 3 is obtained, corresponding to normalized concentrations of c_1=0.75 and c_2=0.25 (T=300K). These values compare well with those from the fluorimetric analysis (Table 4.9) of c_1=0.69, c_2=0.31 (T=294K). An enthalpy difference between *tt*- and *tc*-DNC in the ground-state can be calculated from these normalized concentrations using the equation for the Boltzmann distribution (equation 4.26). So *tt*-DNC was found to be favoured over *tc*-DNC by 476 cal mol^{-1} in the ground state.

Origin of the Short Lifetime Fluorescence of DNC

One possible rationalization for the third fluorescence component of DNC is that a third rotamer of DNC exists in the ground state. Such a rotamer would have either *s*-cis or *s-trans* geometry about the C-24,C-2′ single bond but would have *s-cis* geometry about the C-22,C-23 single bond (i.e. *ct*- or *cc*-DNC, see Figure 4.30). Unfortunately, the IEDAS is very weak and noisy for this component, precluding any comparison with the calculated excitation pattern of *ct*- or *cc*-NBD. In addition, reliable photophysical parameters for this component could not be obtained.

Little more insight is obtained from NMR studies. NOe experiments might be expected to show an enhancement of the 21-methyl resonance upon saturation of the 24-H resonance for both *ct*-and *cc*-DNC, but this was not observed. Other evidence for an appreciable fraction of a C-22,C-23 *s-cis* conformer could potentially come from the value of the vicinal coupling constant between 22-H and 23-H, $^3J_{22-H,23-H}$. Vicinal coupling constants between protons in a conjugated molecule typically take values of ~11 Hz for an *s-trans* arrangement while the best estimate for an *s-cis* arrangment comes from ^3J values in benzene of ~7 Hz[78]. The value of 10.9 Hz

determined for $^3J_{22-H,23-H}$ (Table 3.2) suggests that if a C-22,C-23 *s-cis* rotamer of DNC is present in the ground-state, its concentration is very small.

Another possible rationalization for the third lifetime component is that it represents fluorescence from an initial excited state/species reached upon excitation of the *tt-/tc*-DNC ground state mixture. The short lifetime associated with this component, as well as the fact that it has its greatest contribution to the overall fluorescence on the high-energy side (blue-edge) of the emission spectrum, lend support to this hypothesis. Also, negative pre-exponential factors, which are indicative of an excited state process, were observed for fits of the fluorescence decay profiles of DNC in *n*-BuOH at λ_{ex} 350 nm (Table 4.6).

Perhaps negative pre-exponential factors were not observed in the other solvents because low enough excitation energies were not used. More information about this excited state process could potentially come from solvent viscosity and temperature studies.

Solvent Viscosity Studies

Viscosity effects on the fluorescence decay parameters of DNC were studied by performing time-resolved measurements at constant temperature in minerals oils of differing viscosity. The data for DNC in H1L0, H3L1 and H1L1 at ~30°C is presented in Table 4.11. At this temperature, the viscosities of H1L0, H3L1 and H1L1 are 100 cP, 59 cP and 38 cP respectively, however τ_1 and τ_2 of DNC remain fairly constant. The value of the short lifetime, τ_3, varies considerably with viscosity, indicating that there is a nonradiative decay channel open to this species/state which is not operative in *tt*- and *tc*-DNC.

Further insight can be gained from the dependence of the pre-exponential factors on viscosity. While the value of α_1 remains constant over an approximate threefold change in solvent viscosity (and even over a narrow temperature range of 13.6–30.7°C), there are changes in α_2 and α_3, with the decrease in α_2 with increasing viscosity being compensated by an increase in α_3. This suggests that the state/species of DNC associated with the short lifetime (and with the negative pre-exponential in *n*-BuOH at λ_{ex}350 nm), is a precursor of *tc*-DNC. Moreover, since the relative proportions of these two species is dependent on viscosity, the process

Table 4.11: Fluorescence decay parameters of DNC in mineral oils as a function of temperature and viscosity; λ_{ex}350 nm, λ_{em}370 nm.

Oil	Temp. (°C)	η (cP)	τ_1 (ns)	τ_2 (ns)	τ_3 (ns)	α_1	α_2	α_3	χ^2	SVR
H1L0[a]	30.3	100	43.4	4.47	0.42	0.011	0.890	0.100	1.04	1.86
H3L1	22.1	95	48.5	4.61	1.14	0.011	0.926	0.063	1.05	1.83
H3L1	30.7	59	42.1	4.42	1.35	0.011	0.945	0.044	1.03	1.90
H1L1	13.6	104	54.6	4.72	1.54	0.010	0.928	0.062	1.03	1.99
H1L1	30.7	38	42.3	4.40	0.83	0.011	0.980	0.009	1.12	1.75

[a]There are large errors associated with the data in the solvent at this temperature, since only ~650 channels at 84.8 ps/channel were used.

which links them appears to involve a conformational change. The insensitivity of the lifetime of *tc*-DNC to viscosity indicates that this conformational change is an *irreversible* excited state process. Also, it is likely that the conformational change involves only a small amplitude motion, because of the significant but small dependence of the α_2 and α_3 on viscosity, and also because of the fact that the interconversion rate for a 180° rotation about the C-24,C-2′ single bond of DNC was found to be slow, even in the ground state, on the basis of nOe experiments.

Temperature Studies

The effect of temperature, and not viscosity, on the fluorescence decay parameters of DNC was monitored under so-called 'isoviscosity' conditions. This involved careful choice of temperatures for each oil solution such that the viscosities were similar. For instance, H1L0, H3L1 and H1L1 have viscosities close to 100 cP at 30.3°C, 22.1°C and 13.6°C respectively, and the fluorescence decay parameters of DNC under these conditions are presented in Table 4.11. The effect of temperature on the lifetime values is large, particularly on the long (τ_1) and short (τ_3) lifetimes, while the pre-exponential factors remain fairly constant.

If it is assumed that the radiative rate constant of DNC rotamers is invariant with temperature, over the range 13.6–30.3°C, and that it is a valid approximation to use k_{f1} and k_{f2} determined for DNC in the nonpolar solvent TMP, to arrive

at k_{nr1} and k_{nr2} for DNC in the mineral oils, then it should prove possible to obtain an activation energy E_0 associated with the nonradiative process of both *tt*- and *tc*-DNC from the slope of an Arrhenius plot (see equation 4.26, Figure 4.32). The E_0 value is the temperature contribution to the barrier for the nonradiative process(es) to occur. The E_0 values obtained were $E_0(1)$ ~3.3 kcal mol^{-1} and $E_0(2)$ ~0.95 kcal mol^{-1}. Temperature dependent nonradiative processes include photoisomerization and collisional deactivation, and it is not clear why the activation energies associated with these processes should be so different for *tt*- and *tc*-DNC. Perhaps this is an indication that the E_0 values are in error because it has been tacitly assumed in the Arrhenius plot that there is only one nonradiative process for each conformer, and that this process is temperature dependent.

Low temperature time-resolved fluorescence experiments were also carried out on DNC in *n*-BuOH, above and below its glass temperature of -88.6°C[79] (Table 4.12). All the lifetime values of DNC increased as the temperature was lowered, particularly τ_3 which changed from 0.23 ns at 19.9°C to 1.20 ns at -105°C. The largest incremental change occurred between room temperature and -50°C, while there were only small differences in the lifetime values just above and below the glass temperature of *n*-BuOH. These lifetime increases are consistent with an increase in ϕ_f due to nonradiative processes becoming less favourable at these low temperatures and high viscosities. In agreement with the room temperature data in mineral oils, viscosity dependent nonradiative processes appear most important for the species associated with τ_3.

Table 4.12: Fluorescence Decay Parameters of DNC in *n*-BuOH at low temperatures; λ_{ex}320 nm, λ_{em}370 nm.

Temp. °C	τ_1 (ns)	τ_2 (ns)	τ_3 (ns)	τ_4 (ns)	α_1 ($\mathcal{F}_1$)	α_2 ($\mathcal{F}_2$)	α_3 ($\mathcal{F}_3$)	χ^2	SVR
19.9	27.70	2.55	0.23	0.03	0.282	0.572	0.146	1.03	1.97
					(0.836)	(0.159)	(0.006)		
-50	43.78	4.08	0.74	0.02	0.346	0.474	0.180	1.43	1.91
					(0.877)	(0.112)	(0.008)		
-81	50.04	4.46	0.90	0.02	0.398	0.380	0.222	1.08	2.03
					(0.911)	(0.078)	(0.009)		
-105	52.67	4.59	1.20	0.02	0.417	0.315	0.268	1.57	1.74
					(0.924)	(0.061)	(0.013)		

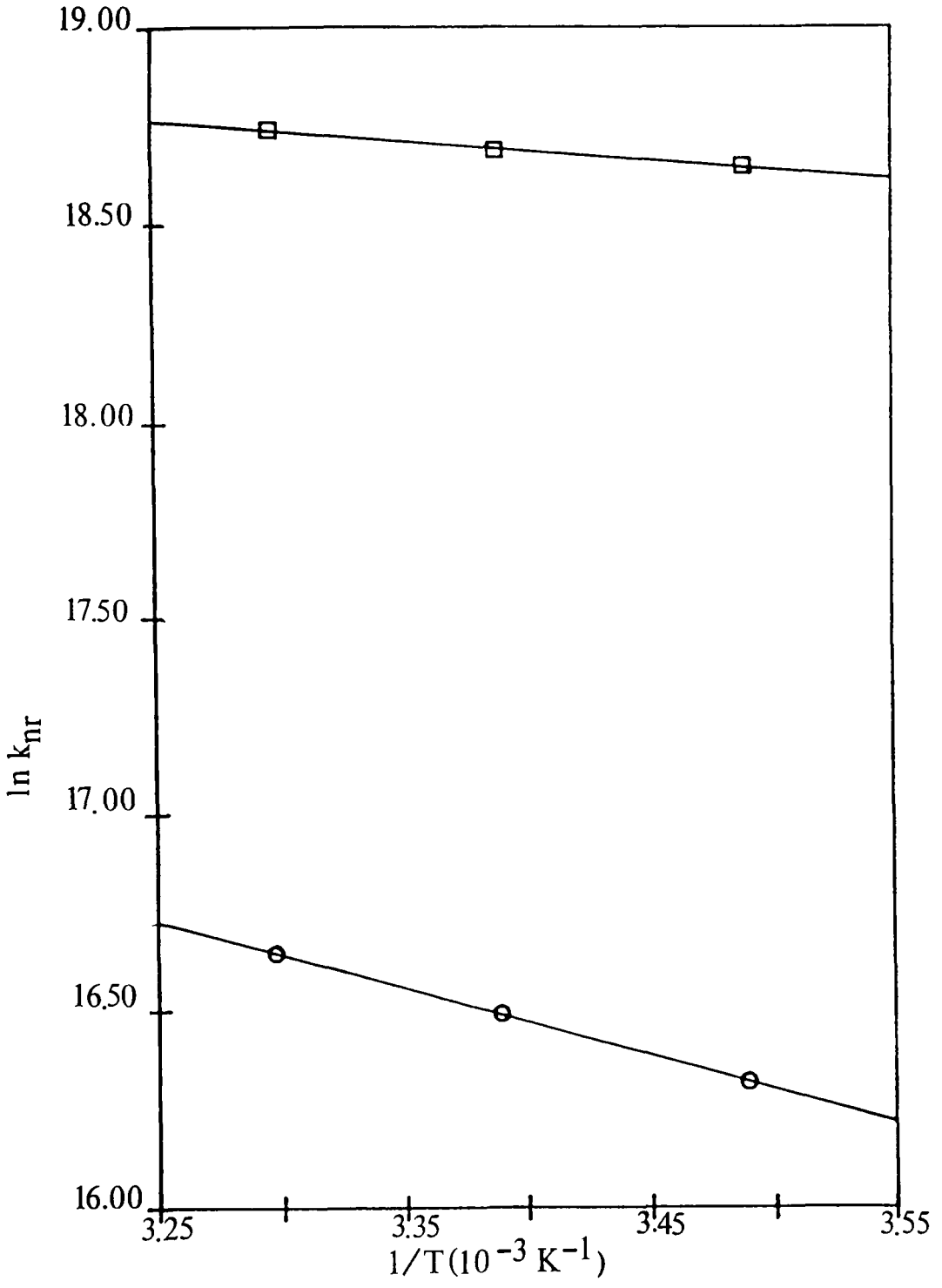

Figure 4.32: Arrhenius plot of $\ln k_{nr}$ versus $1/T$ for DNC in various mineral oils at $\eta \sim$100 cp; k_{nr1} ($\odot$) and k_{nr2} ($\square$).

The variation of the normalized pre-exponential factors, α_i, and fractional fluorescence values, $\mathcal{F}_i$, with temperature is particularly interesting. Since *tt*-DNC is the most sterically stable conformer of DNC due to its more favourable H-H nonbonded interactions, it is expected that the proportion of *tt*-DNC fluorescence will increase at lower temperatures. Indeed, the pre-exponential factor, α_1, associated with the long lifetime which has been assigned to *tt*-DNC, does increase as the temperature decreases. However, α_3 also increases while α_2, which is associated with *tc*-DNC, decreases. This result seems rather surprising at first until it is realised that the species associated with τ_3 is a precursor of *tc*-DNC, and that the sum of $(\alpha_2 + \alpha_3)$ decreases at lower temperatures. Hence these low temperature time-resolved fluorescence results support the notion first advanced by the solvent viscosity studies, that *tc*-DNC is formed by an excited state process whose rate is dependent on the viscosity of the environment.

As mentioned earlier, this process is likely to be a small amplitude conformational change. Insight into the identity of the short lifetime associated species could be had by obtaining DAS and IEDAS of DNC at these low temperatures, where the contribution of this component to the overall fluorescence is considerably enhanced relative to room temperature. However, it can be postulated that this species is a nonplanar (slightly twisted) *tc*-DNC, which upon excitation can become planar because of a more favourable orbital overlap, promoted by delocalization of the electron density in the excited state.

Support for this hypothesis comes from the low temperature (4K) fluorescence studies of PNE in polycrystalline *n*-hexane matrices referred to in the introduction to this chapter[35]. The *s-cis* conformer of PNE was found to be nonplanar at this temperature since it exhibited a broad diffuse fluorescence spectrum consistent with progressions in low frequency bending modes. On the other hand, *s-trans* PNE had a sharp line fluorescence spectrum consistent with a planar geometry. The difference in geometries of the two conformers was attributed to the different naphthalenic bond lengths. No third short lifetime component has been observed for the fluorescence decay of PNE. Perhaps this is due to the fact that the time-resolved studies have for the most part been made with flash lamp as opposed to laser excitation, so the instrument response profiles were typically 2 ns wide. Resolution of

a small amount of ~0.3 ns fluorescence would be difficult under these conditions. Those fluorescence decay profiles of PNE which have been measured with a Nd:YAG laser/streak camera system, which has picosecond resolution[31], have statistical parameters for double exponential fits which are similar to those obtained in this work (χ^2 ~1.5–2.0), but the signal-to-noise ratio characteristics of the data did not allow triple exponential fits to be attempted.

One remaining anomaly is why the fluorescence decay profile of DN, the dimethyl analogue of DNC, is satisfactorily fitted by a sum of two exponential functions. It is conceivable that the value of the third lifetime of DN could be shorter than in DNC such that at room temperature and at low viscosity, it cannot be resolved from the ~0.05 ns component which is thought to be an instrumental artifact. Time-resolved fluorescence studies in high viscosity media and/or at low temperatures could resolve this anomaly since the value of this third lifetime, if it exists, could be expected to lengthen in analogy to what was observed for DNC.

4.3.7 Summary of the Solvent Photophysics of DNC

The photophysical properties of DNC in isotropic solvents are best described by the kinetic scheme presented in Figure 4.33. There is a ground state equilibrium between *tt*-DNC and most likely a nonplanar *tc*-DNC. This equilibrium will be dependent on temperature but not on viscosity. Hence the variation of this equilibrium in a membrane sample at constant temperature, with for example percent cholesterol content, could give information about the change in order of the environment surrounding the probe.

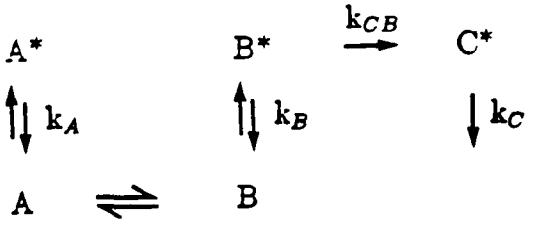

Figure 4.33: Kinetic scheme to describe the photophysics of DNC in solvents. A = *tt*-DNC, B = nonplanar *tc*-DNC, C = planar *tc*-DNC.

In the excited state, there is no interconversion between *tt*- and *tc*-DNC, but

the nonplanar *tc*-DNC appears to become planar. This means that the fluorimetric analysis presented earlier, to arrive at the various photophysical parameters associated with the three lifetime components, is not strictly correct. This is because the underlying assumption in the analysis was that there were three ground state species which did not interconvert in the excited state. However, in the case where one of the species is formed in an irreversible process in the excited state, the lifetime values can still be associated with the three species since each lifetime is simply a function of the rate constants for deactivation of only one species (equations 4.54–4.56).

$$\tau_1 = \frac{1}{k_A} = \frac{1}{k_{f1} + k_{nr1}} \tag{4.54}$$

$$\tau_2 = \frac{1}{k_C} = \frac{1}{k_{f2} + k_{nr2}} \tag{4.55}$$

$$\tau_3 = \frac{1}{k_B + k_{CB}} = \frac{1}{k_{f3} + k_{nr3}} \tag{4.56}$$

$$\alpha_1 = \alpha_A \tag{4.57}$$

$$\alpha_2 = \alpha_C \tag{4.58}$$

$$\alpha_3 = \alpha_B - \alpha_C \tag{4.59}$$

The pre-exponential factors α_1 and α_2 are the true pre-exponential factors associated with *tt*-DNC, (α_A), and planar *tc*-DNC, (α_C), (equations 4.57, 4.58), so the DAS that were previously calculated using α_1 and α_2 are the true emission spectra of these two conformers. However, in order to obtain the true emission spectrum (or SAS, Species Associated Spectrum) associated with nonplanar *tc*-DNC, it can be seen from equation 4.59 that the sum of $(\alpha_2 + \alpha_3)$ will vary with λ_{em} like α_B (the true pre-exponential factor associated with nonplanar *tc*-DNC). So the sum of $(\alpha_2 + \alpha_3)$ was used to generate the SAS of nonplanar *tc*-DNC and this spectrum was found to be very similar in shape and position to the emission spectrum of planar *tc*-DNC (not shown).

Because of the presence of a viscosity dependent excited state reaction in the photophysical behaviour of DNC, the relative amounts of nonplanar and planar *tc*-DNC should be able to be used as a measure of the *dynamical freedom* of membranes.

DNC thus appears to have the potential to report on both aspects of membrane fluidity; *dynamics* and *order*.

4.3.8 Possible Models for the Fluorescence Heterogeneity of TPC

Ground-State Conformational Heterogeneity

The simplest model which can be put forward to account for the biexponential fluorescence decay of TPC is that two conformers of TPC exist in equilibrium in the ground-state, and that they do not have sufficient time to establish an excited state equilibrium during their excited state lifetimes. Such conformers could be rotamers about the C-22,C-23 or C-24,C-25 single bonds (see Figure 4.34). Rotation of 180° about the C-26,C-1′ single bond connecting the triene and phenyl moieties does not lead to a change in the geometry of the chromophore, so it is unlikely that the observed fluorescence heterogeneity arises from rotamerism about this bond.

Support for this model is not forthcoming from the steady-state fluorescence measurements, however, since the excitation and emission spectra are λ_{em} and λ_{ex} independent. If two conformers of TPC do indeed exist in the ground-state, their excitation spectra must be very similar such that a very similar proportion of conformers is always being excited, giving rise to an average emission spectrum which does not vary with excitation wavelength.

Molecular orbital calculations of the excitation patterns of the various rotamers of a model compound, 1-Phenyl-1,3,5-hexatriene (PHT, see Figure 4.35), could allow some insight as to whether large differences in excitation spectra are to be expected for different rotamers of TPC. Results of these calculations using Mataga-Nishimoto parametrization are presented in Table 4.13. The main excitation band is predicted to be due to a transition to a B_u-like excited state, and the 0–0 band position is indeed predicted to be conformer dependent varying from 313 nm in *tt*-PHT to 325 nm in *cc*-PHT.

In spite of the above predictions, and the steady-state fluorescence results, which would seem to indicate that the origin of the fluorescence heterogeneity of TPC lies in an excited state reaction, the DAS and IEDAS associated with the two lifetime

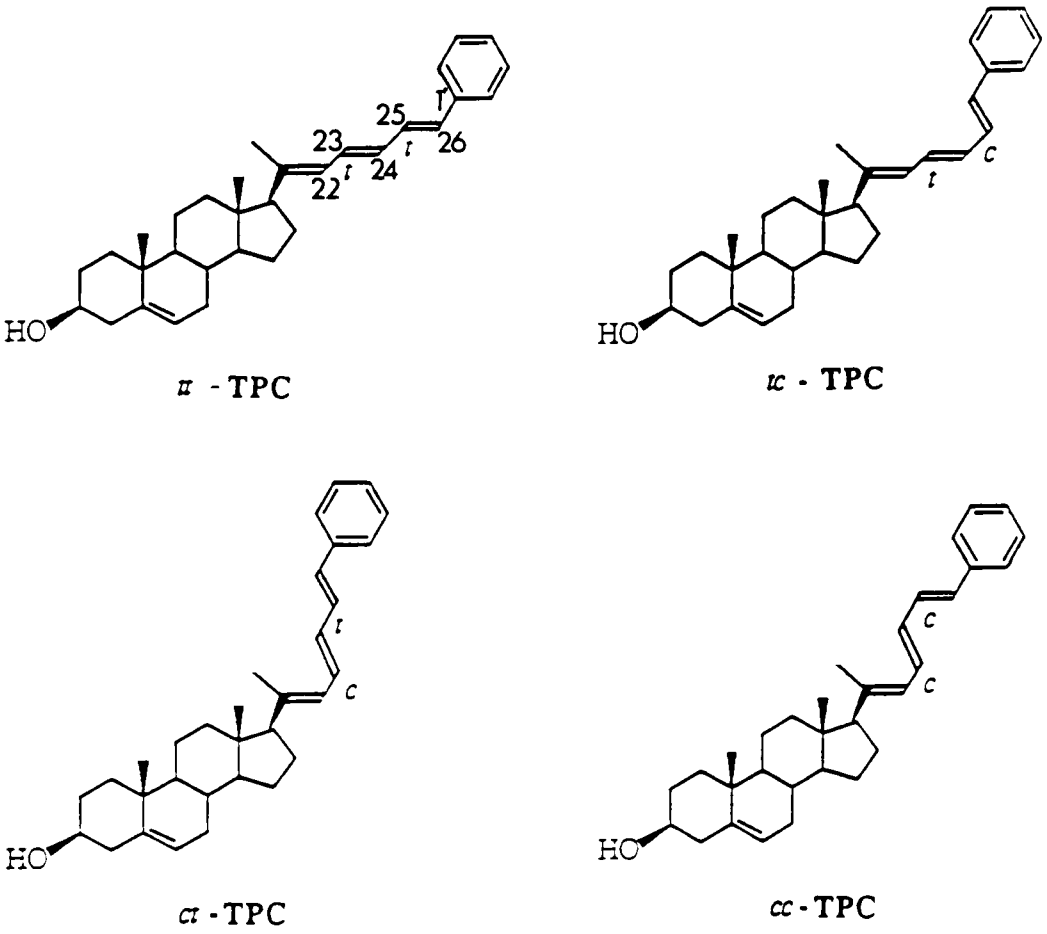

tt - TPC *tc* - TPC

ct - TPC *cc* - TPC

Figure 4.34: *tt*-,*tc*-,*ct*- and *cc*-TPC.

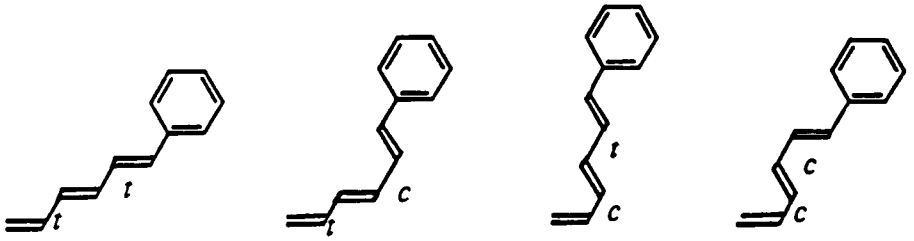

tt -PHT *tc* -PHT *ct* -PHT *cc* -PHT

Figure 4.35: *tt*-,*tc*-,*ct*- and *cc*-PHT.

Table 4.13: Excitation energies and oscillator strengths predicted for the low-lying excited electronic states of the various rotamers of PHT by CNDO/S calculations (Nishimoto-Mataga parametrization).

Rotamer[a]	State[b]	E(nm)	Oscillator Strength, f
tt-PHT	S_1^* (B_u)	313	1.6337
	S_2^* (L_b)	284	0.0102
	S_3^*	243	0.0493
tc-PHT	S_1^* (B_u)	322	1.2886
	S_2^* (L_b)	284	0.0032
	S_3^*	245	0.0361
ct-PHT	S_1^* (B_u)	318	1.4355
	S_2^* (L_b)	284	0.0051
	S_3^*	246	0.0021
cc-PHT	S_1^* (B_u)	325	1.2940
	S_2^* (L_b)	284	0.0037
	S_3^*	247	0.0012

[a]see Figure 4.35 for a diagram of the various rotamers of PHT.
[b]see reference 4 for general background concerning symmetry designations.

components of TPC in TMP were computed and are shown in Figures 4.36 and 4.37. The two DAS are very similar in shape, but are shifted ~390 cm^{-1} with respect to each other. The short lifetime of 210 ps is associated with the more blue-shifted DAS. Very little difference exists between the two IEDAS either, the main difference occurring in the relative intensity of the weak band at ~252 nm. So, the similarity of the IEDAS, as well as the λ_{em} and λ_{ex} independent excitation and emission spectra, indicates that if there is ground-state conformational heterogeneity of TPC, it must reveal itself very subtly, apart from the different DAS and the biexponential fluorescence decay.

Further insight into a possible rotameric equilibrium can be gained from an examination of the magnitudes of ^1H NMR vicinal coupling constants between the protons on either side of the single bonds in question, i.e. $^3J_{22-H,23-H}$, $^3J_{24-H,23-H}$ (see Table 3.2). The value of 11.1 Hz for $^3J_{22-H,23-H}$ is typical of an *s-trans* arrangement of the two protons[78]. The value of 10.1 Hz for $^3J_{24-H,25-H}$, is significantly lower

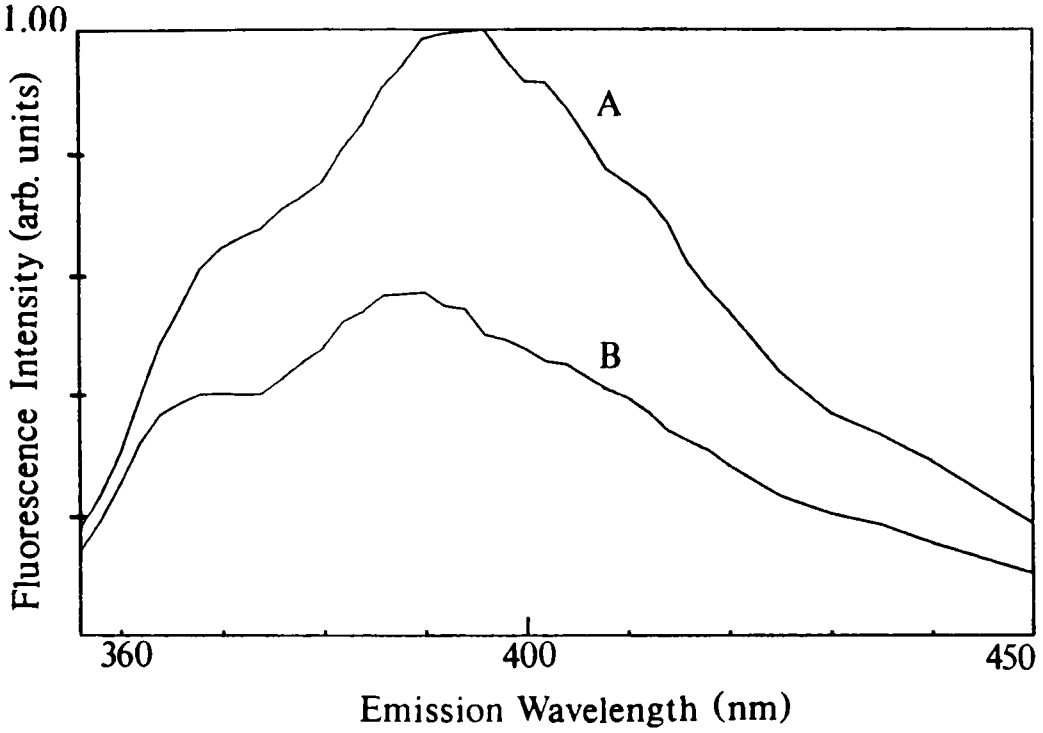

Figure 4.36: a) Unnormalized decay associated emission spectrum (DAS) of TPC in TMP at λ_{ex}320 nm; τ = 0.532 ns (A) and τ = 0.210 ns (B).

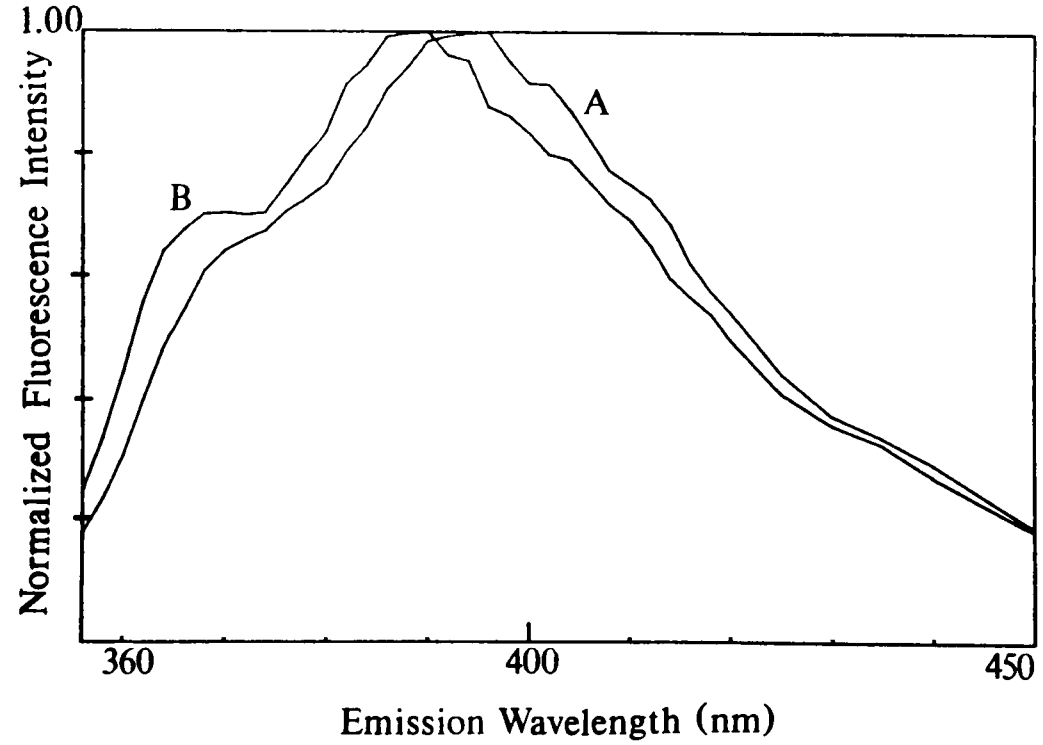

Figure 4.36: b) normalized decay associated emission spectrum (DAS) of TPC in TMP at λ_{ex}320 nm; τ = 0.532 ns (A) and τ = 0.210 ns (B).

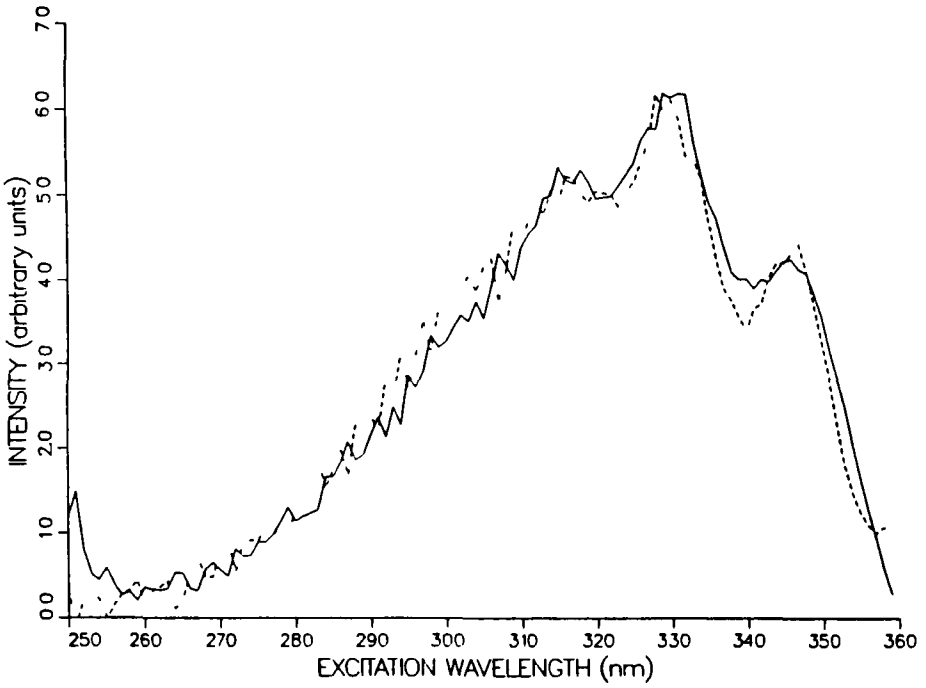

Figure 4.37: Normalized indirect excitation decay associated spectra (IEDAS) of TPC in TMP at λ_{em} = 390 nm; τ = 0.532 ns (—) and τ = 0.210 ns (--).

than the value of 11.1 Hz obtained for $^3J_{24-H,25-H}$ in the 20(22)E,23Z,25E geometrical isomer of TPC (Table 3.2). This latter isomer can be safely assumed to exist entirely in the C-24,C-25 *s-trans* conformation due to the very unfavourable steric interaction between 22-H and 26-H in the *s-cis* conformation. It could be argued, then, that the value of 10.1 Hz for $^3J_{24-H,25-H}$ for TPC is an indication that there is a small proportion of *tc*-TPC in $CDCl_3$ at 300K, since vicinal coupling constants between *s-cis* protons in benzene are ~7.0 Hz. However, due to the scatter in values of vicinal coupling constants, across C-C single bonds, between 10.4–12.6 Hz for substituted butadienes[78], all of which are assumed to exist entirely in the *s-trans* conformation at room temperature, it is not possible to draw any conclusion about the presence or absence of a *tc*-TPC conformer in the ground state. Unfortunately, nOe experiments could not resolve this point since the expected nOe between 23-H and 26-H in *tc*-TPC could not be ascertained due to the very similar chemical shifts of these two protons (δ6.641 and δ6.507 respectively, Table 3.1).

Upon considering both the fluorescence and NMR data, it appears that the photophysical properties of TPC are not a consequence of a ground-state conformational equilibrium, though a more definite conclusion could be reached upon studying the photophysics of conformationally restricted analogues. So, excited state models were investigated to see if any of these were compatible with the observed fluorescence heterogeneity of TPC.

Excited State Heterogeneity

a) Irreversible Excited State Process

The general kinetic scheme for a *reversible* two-state excited state reaction between A* and B*, where only A* is directly excited, is shown in Figure 4.38[80,81].

The expressions for the fluorescence decay of A* and B* are given by equations 4.60 and 4.61[81],

$$i_A(\lambda,t) = [A^*]_0 \cdot \frac{k_{fA}(\gamma_2 - X)}{\gamma_2 - \gamma_1} \cdot S_A(\lambda)(e^{-t/\tau_1} + Ae^{-t/\tau_2}) \qquad (4.60)$$

$$i_B(\lambda,t) = [A^*]_0 \cdot \frac{k_{fB}k_{BA}}{\gamma_2 - \gamma_1} \cdot S_B(\lambda)(e^{-t/\tau_1} + Ae^{-t/\tau_2}) \qquad (4.61)$$

where $[A^*]_0$ = initial concentration of A*,

$$A = (X - \gamma_1)/(\gamma_2 - X) \qquad (4.62)$$

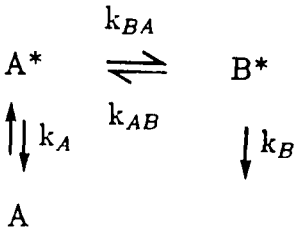

Figure 4.38: Kinetic scheme for a reversible excited state reaction between A* and B*, where only A* is directly excited.

$$X = k_A + k_{BA} \tag{4.63}$$

$$Y = k_B + k_{AB} \tag{4.64}$$

$$\gamma_1 = \tau_1^{-1} = \frac{1}{2}\left\{(X+Y) - \left[(Y-X)^2 + 4k_{BA}k_{AB}\right]^{1/2}\right\} \tag{4.65}$$

$$\gamma_2 = \tau_2^{-1} = \frac{1}{2}\left\{(X+Y) + \left[(Y-X)^2 + 4k_{BA}k_{AB}\right]^{1/2}\right\} \tag{4.66}$$

k_{fA}, k_{fB} = radiative rates of A*, B* and $S_A(\lambda)$,$S_B(\lambda)$ = emission spectra associated with the decay of species A*, B* (i.e. species associated spectra or SAS). Equations 4.60 and 4.61 can be rewritten as

$$i_A(t) = \alpha_1 S_A(\lambda) e^{-t/\tau_1} + \alpha_2 S_A(\lambda) e^{-t/\tau_2} \tag{4.67}$$

$$i_B(t) = \beta_1 S_B(\lambda) e^{-t/\tau_1} + \beta_2 S_B(\lambda) e^{-t/\tau_2} \tag{4.68}$$

where

$$\alpha_2/\alpha_1 = A \tag{4.69}$$

and

$$\beta_2 = -\beta_1 \tag{4.70}$$

It can be seen that for an *irreversible* excited state reaction, $k_{AB} = 0$, and the above expressions simplify to

$$\gamma_1 = \tau_1^{-1} = k_A + k_{BA} = X \tag{4.71}$$

$$\gamma_2 = \tau_2^{-1} = k_B = Y \tag{4.72}$$

$$i_A(\lambda, t) = [A^*]_0 k_{fA} S_A(\lambda) e^{-t/\tau_1}, i.e.\ \alpha_2 = 0 \tag{4.73}$$

$$i_B(\lambda, t) = [A^*]_0 \frac{k_{fB} k_{BA}}{Y - X} S_B(\lambda)(e^{-t/\tau_1} - e^{-t/\tau_2}) \tag{4.74}$$

When deactivation from A* is faster than from B* (i.e. $X > Y$ and $\tau_1 < \tau_2$), β_1 is negative and β_2 is positive. The total fluorescence decay profile is then given by equation 4.75

$$i(\lambda,t) = i_A(\lambda,t) + i_B(\lambda,t) = [\alpha_1 S_A(\lambda) - \beta_1 S_B(\lambda)]e^{-t/\tau_1} + \beta_2 S_B(\lambda)e^{-t/\tau_2} \quad (4.75)$$

or

$$i(\lambda,t) = S_1(\lambda,t)e^{-t/\tau_1} + S_2(\lambda)e{-t/\tau_2} \quad (4.76)$$

where $S_i(\lambda)$ = DAS associated with lifetime τ_i, and

$$S_1(\lambda) = \alpha_1 S_A(\lambda) - \beta_1 S_B(\lambda) \quad (4.77)$$

$$S_2(\lambda) = \beta_2 S_B(\lambda) \quad (4.78)$$

Hence $S_i(\lambda)$ are the DAS that have already been calculated (Figure 4.36) and the DAS associated with the longer lifetime τ_2 should always be positive (equation 4.78). Meanwhile the DAS associated with the shorter lifetime τ_1 will become negative when $\beta_1 S_B(\lambda)$ exceeds $\alpha_1 S_A(\lambda)$, or in other words when the emission intensity of species B exceeds that of species A by a factor greater than α_1/β_1 [see Figure 2, ref. 81 for simulated $S_1(\lambda)$, $S_2(\lambda)$].

In the opposite case when deactivation from B* is faster than from A* (i.e. $Y > X$ and $\tau_1 > \tau_2$), β_1 is positive and β_2 is negative. Under these circumstances, the total fluorescence decay profile is given by equation 4.79

$$i(\lambda,t) = [\alpha_1 S_A(\lambda) + \beta_1 S_B(\lambda)]e^{-t/\tau_1} - \beta_2 S_B(\lambda)e^{-t/\tau_2} \quad (4.79)$$

and the DAS by equations 4.80 and 4.81.

$$S_1(\lambda) = \alpha_1 S_A(\lambda) + \beta_1 S_B(\lambda) \quad (4.80)$$

$$S_2(\lambda) = -\beta_2 S_B(\lambda) \quad (4.81)$$

Hence, in this case, the DAS associated with the short lifetime τ_2 will always be negative, while the long lifetime DAS will be positive (see Figure 2, ref. 81).

The DAS observed for TPC in TMP were always positive (Figure 4.36) so if an irreversible excited state reaction is occurring, clearly the deactivation of species B* which is formed in the reaction, cannot be faster than that of the initial species

A*. Even so, it might have been expected that the short lifetime DAS would have gone negative at long emission wavelengths when the contribution of B* to the fluorescence sufficiently exceeded the contribution of A*. In other words, it was surprising that no negative pre-exponential factors were ever seen for fits of the fluorescence decay profiles of TPC, especially at long emission wavelengths where B* fluorescence would be expected to be considerably more intense than A* fluorescence if an excited state process was occurring. It is possible that the energy difference between A* and B* is so small that a negative portion of the DAS would not be seen until wavelengths corresponding to the red edge of the emission spectrum. If this is indeed the case, as would seem to be indicated by the data, then it is unlikely that an excited process between A* and B* would be irreversible if A* and B* are two different excited states (i.e. S_2^* and S_1^*) of TPC. Alternatively, A* and B* could be two conformers of TPC which differ only by a small degree of twist, similar to what was observed for *tc*-DNC. If this model is correct then solvent viscosity and low temperature studies, presented later, should show that the relative amount of A* fluorescence increases as viscosity increases.

b) Reversible Excited State Process

The scheme and associated kinetic equations for the reversible two-state excited state reaction, in which only A* is directly excited, were presented earlier (Figure 4.38, equations 4.60–4.70). Assuming the excited state process is reversible, these equations will only simplify if either A* or B* is nonfluorescent, implying k_{fA} or k_{fB} $\sim$0. Since A* is the initial excited state/species formed by a radiative transition from the ground state, A* will only be nonfluorescent when nonradiative deactivation is very efficient. However, it is conceivable that B* could be nonfluorescent since in this model we have assumed that the reverse process of absorption to B* does not occur. The total fluorescence decay profile is then simply the fluorescence decay profile of A* as given by equation 4.60. Under these conditions the DAS which have already been calculated for TPC, $S_i(\lambda)$, are the SAS of species A* multiplied by a scaling constant (equations 4.82, 4.83).

$$S_1(\lambda) = \alpha_1 S_A(\lambda) \tag{4.82}$$

$$S_2(\lambda) = \alpha_2 S_A(\lambda) \tag{4.83}$$

The two DAS are thus related by a scalar (from equations 4.62, 4.69)

$$\frac{S_2(\lambda)}{S_1(\lambda)} = \frac{\alpha_2}{\alpha_1} = A = \frac{X - \gamma_1}{\gamma_2 - X} \tag{4.84}$$

and should have the same shape.

Referring back to the DAS of TPC in TMP (Figure 4.36), it can indeed be seen that they have the same shape but that they are shifted by approximately 390 cm^{-1} from one another. The short lifetime DAS occurs at the slightly higher energy. This slight energy difference between the two DAS could perhaps be accounted for by a slight relaxation of A* between its prompt and delayed emissions.

One possibility for A* and B* in this model is that they are two conformers of TPC which differ from one another by a small amplitude conformational change, such that they can interconvert within $\tau_1 = 0.5$ ns in TMP. In other words, TPC could be undergoing a 'wobbling' in the excited state. It could be envisaged that TPC could undergo an irreversible small amplitude comformational change in the excited state, because of a tendency for planarity (better orbital overlap) due to increased delocalization of electron density. However, it is unclear what mechanism could account for an equilibrium between the preferred ground state and excited state geometries, or between any two geometries in general which differ to such a small degree that the equilibrium is established within the short lifetime of TPC.

Another possibility is that A* and B* are two different excited states in close proximity (i.e. S_2^* and S_1^*), with $B^* \rightarrow S_0$ being a weak radiative transition. As pointed out in the introduction to this chapter, it is known that S_2^* and S_1^* of DPH (the closest analogue to the TPC fluorophore in the literature) are very close in energy and are of B_u and A_g symmetry respectively, such that $S_2^* \rightarrow S_0$ is a strongly-allowed transition while $S_1^* \rightarrow S_0$ is a weak radiative transition. Biexponential fluorescence decay has been observed for DPH in solution on the blue edge of the emission band[82], so it is possible that a reversible excited state reaction between S_2^* and S_1^* of TPC could explain its biexponential fluorescence decay if $S_1^* \rightarrow S_0$ is forbidden or only weakly allowed.

CNDO/S calculations of the lowest excited states of PHT rotamers, using a Mataga-Nishimoto parameterization, predicted that S_1^* is B_u-like, and that the oscillator strength of the $S_0 \rightarrow S_1^*$ transition is quite high. However, this calculation

neglects doubly excited configurations and so does not allow for low-lying A_g-like states which are one-photon forbidden but two-photon allowed from S_0. It was decided to perform CNDO/S molecular orbital calculations on *tt*-PHT using the Pariser parameterization which allows for both singly and doubly excited configurations, and which has been found to predict the correct ordering of the strongly allowed $A_g \rightarrow B_u$ and forbidden $A_g \rightarrow A_g$ transitions in a number of polyenes[70]. The results of this calculation are presented in Table 4.14. Unlike the case for unsubstituted hexatriene[70,83] and DPH[22,23], S_1^* is not predicted to be A_g-like but instead to be a benzene L_b-like state. The oscillator strength of the $S_0 \rightarrow S_1^*$ transition was calculated to be very small.

Table 4.14: Excitation energies and oscillator strengths predicted for the low-lying excited electronic states of *tt*-PHT by CNDO/S calculations (Pariser parametrization).

State	E(nm)	Oscillator Strength, f
S_1^* (L_b)	378	0.0021
S_2^* (B_u)	344	1.2184
S_3^* (A_g)	333	0.0998
S_4^*	282	0.0084

So, according to molecular orbital calculations on *tt*-PHT, *tt*-TPC has S_2^* and S_1^* in close proximity with S_1^* being an essentially nonfluorescent state. Hence, it seems that the fluorescence heterogeneity of TPC could be rationalized in terms of one ground-state conformer (most likely *tt*-TPC based on steric arguments and ^{1}H NMR vicinal coupling constants) which undergoes a reversible excited state reaction between its closely spaced S_2^* and S_1^* excited states, with S_1^* being a nonfluorescent benzene L_b-like state.

Solvent Viscosity Studies

The decay parameters of TPC in mineral oils of different viscosities, at ~5.0°C, are presented in Table 4.15. The viscosities of the oils at this temperature vary by a factor of ~10, from 69 cP (H0L1) to 638 cP (H1L0). As the viscosity is increased, there is a concomitant increase in τ_1 and α_1, while α_2 decreases and τ_2 remains almost constant. This sensitivity of the decay parameters to viscosity is not compatible with the irreversible excited state reaction (conformational change)

model put forward to rationalize the fluorescence heterogeneity of TPC. In this model, the short lifetime, τ_2, is associated with the initial excited state species A*, and the conformational change that it must undergo to form B* should be viscosity dependent. Hence τ_2 should increase as the viscosity increases, through the dependence of k_{BA} on viscosity. Moreover, it would be expected that the proportion of fluorescence from A* (i.e. α_2) would increase at higher viscosities. This is the opposite trend to what is observed.

Table 4.15: Fluorescence decay parameters of TPC in mineral oils as a function of temperature and viscosity; λ_{ex}350 nm, λ_{em}370 nm.

Oil	Temp. °C	η (cP)	τ_1 (ns)	τ_2 (ns)	τ_3 (ns)	α_1	α_2	χ^2	SVR
H1L0	5.2	638	1.64	0.73	0.013	0.763	0.237	1.01	1.91
H3L1	4.8	324	1.57	0.76		0.780	0.220	1.04	1.89
H3L1	30.9	58	1.04	0.53	0.005	0.615	0.385	1.03	2.00
H1L1	4.8	187	1.50	0.71	0.003	0.752	0.248	1.04	1.97
H1L1	21.7	64	1.15	0.53	0.001	0.651	0.349	1.02	1.83
H0L1	5.2	69	1.38	0.70	0.014	0.691	0.309	1.00	1.90

For models involving multiple excited states as opposed to conformers, the viscosity dependence of the decay parameters is determined by the nature and relative importance of nonradiative decay processes from each of the states, which is difficult to predict. So, the solvent viscosity studies presented here cannot give any insight into whether the photophysics of TPC is governed by a reversible two-excited state model.

Temperature Studies

The effect of temperature, and not viscosity, on the fluorescence decay parameters of TPC was determined under isoviscosity conditions. The three mineral oils H3L1, H1L1 and H0L1 have viscosities close to 65cP at 30.9°C, 21.7°C and 5.2°C respectively, and the lifetimes and normalized pre-exponential factors of TPC under these conditions are presented in Table 4.15. All of the parameters are very temperature dependent, with α_2 increasing and the values of the other parameters decreasing as

the temperature is raised.

Low temperature time-resolved fluorescence experiments were also performed on TPC in MCH, above and below its glass temperature of -126.6°C[79] (Table 4.16). These results largely confirm the trends observed over the narrow temperature range of 5.2°C–30.9°C in the oil solutions. Notice the dramatic increase in α_1 from 0.41 at 19.9°C to 0.93 at -142°C and the accompanying decrease in α_2 from 0.59 to 0.07. The lifetime value, τ_1, increases by a factor of ~3 over this same temperature range while the value of τ_2 increases at first but then appears to shorten again below -50°C, though this could be an artifact arising from the decreasing contribution of this component to the overall fluorescence, coupled possibly with increased background scatter at these lower temperatures. No background scatter was measured and subtracted from the sample fluorescence decay curve, due to the difficulty in aligning quartz tubes in the Dewar flask with identical collection geometries.

Table 4.16: Fluorescence Decay Parameters of TPC in MCH at low temperatures; λ_{ex}320 nm, λ_{em}370 nm.

Temp. °C	τ_1 (ns)	τ_2 (ns)	τ_3 (ns)	α_1	α_2	$\mathcal{F}_1$	$\mathcal{F}_2$	χ^2	SVR
19.7	0.618	0.302	0.018	0.41	0.59	0.59	0.41	1.06	1.90
-47	1.60	0.93		0.71	0.29	0.81	0.19	1.02	1.99
-72	1.67	0.49		0.88	0.12	0.96	0.04	1.09	1.83
-105	1.75	0.28		0.90	0.10	0.98	0.02	1.04	1.96
-142	1.73	0.4		0.93	0.07	0.98	0.02	0.99	1.93

Generally, lifetime values of fluorescence probes increase at lower temperatures, as observed for τ_1 of TPC, and this is usually attributed to the effect of temperature/viscosity on the nonradiative decay processes. These processes become less efficient in the overall deactivation of the probe if they are associated with an activation barrier, while the radiative decay rate, k_f, is usually independent of temperature. Consequently, the τ_i and ϕ_f values generally increase to the same extent as the temperature is lowered (see equation 4.13). This was not observed for TPC.

The unnormalized emission spectra of TPC in MCH at various temperatures,

ranging from room temperature to -136°C, are presented in Figure 4.39. The change in area under these spectra reflect the change in ϕ_f of TPC with temperature, assuming the molar absorptivity coefficient is temperature independent and that changes in solvent refractive index only account for a small proportion of the increase. So, ϕ_f of TPC in MCH increases by a factor of ~3 between 22.4°C and -54°C, and by another factor of ~2 upon reaching -112°C. At the same time, τ_1 increases twofold between 19.9°C and -47°C which is not too different from the change in ϕ_f over this temperature range, but there is only a further increase in τ_1 of ~10% down to a temperature of -105°C.

This difference in temperature sensitivity of τ_1 and ϕ_f could be accounted for by an increase in k_{f1} at lower temperatures. Changes in k_f with temperature are not to be expected for emission from an excited state which is well separated from other excited states. Even if there are two excited states in close proximity, k_f would not be temperature dependent unless there was some interaction between the two states such as an excited state equilibrium, as well as a temperature dependent spacing between them. The change of solvent refractive index, and hence solvent polarizability, with temperature leads to a concomitant shift in the positions of spectra associated with strongly-allowed transitions. The positions of forbidden or weakly-allowed transitions are not affected.

Excitation spectra of TPC in MCH (Figure 4.40) were observed to shift by ~500 cm^{-1} to lower energies between 22.4°C and -150°C. Clearly this must be the consequence of a lowering of the energy of the B_u-like excited state of TPC relative to the A_g-like ground state. However, if S_1^* of TPC was B_u-like, a lowering of its energy with temperature should not lead to a change in k_f. However, if S_2^* is B_u-like and S_1^* is L_b-like, as predicted by the CNDO/S (Pariser) molecular orbital calculations, a change in k_f could be rationalized. The spacing between S_2^* and S_1^* would decrease at lower temperatures due to the temperature dependence and independence of the positions of S_2^* and S_1^* respectively. In the case of the model of an equilibrium between B_u-like S_2^* and a nonfluorescent L_b-like S_1^*, this decrease in separation of the two states would lead to more of the longer lifetime fluorescence component, as observed, through an increase in the rate constant k_{AB} of the back reaction from S_1^* to S_2^*. However, a change in k_f would not be expected since the two

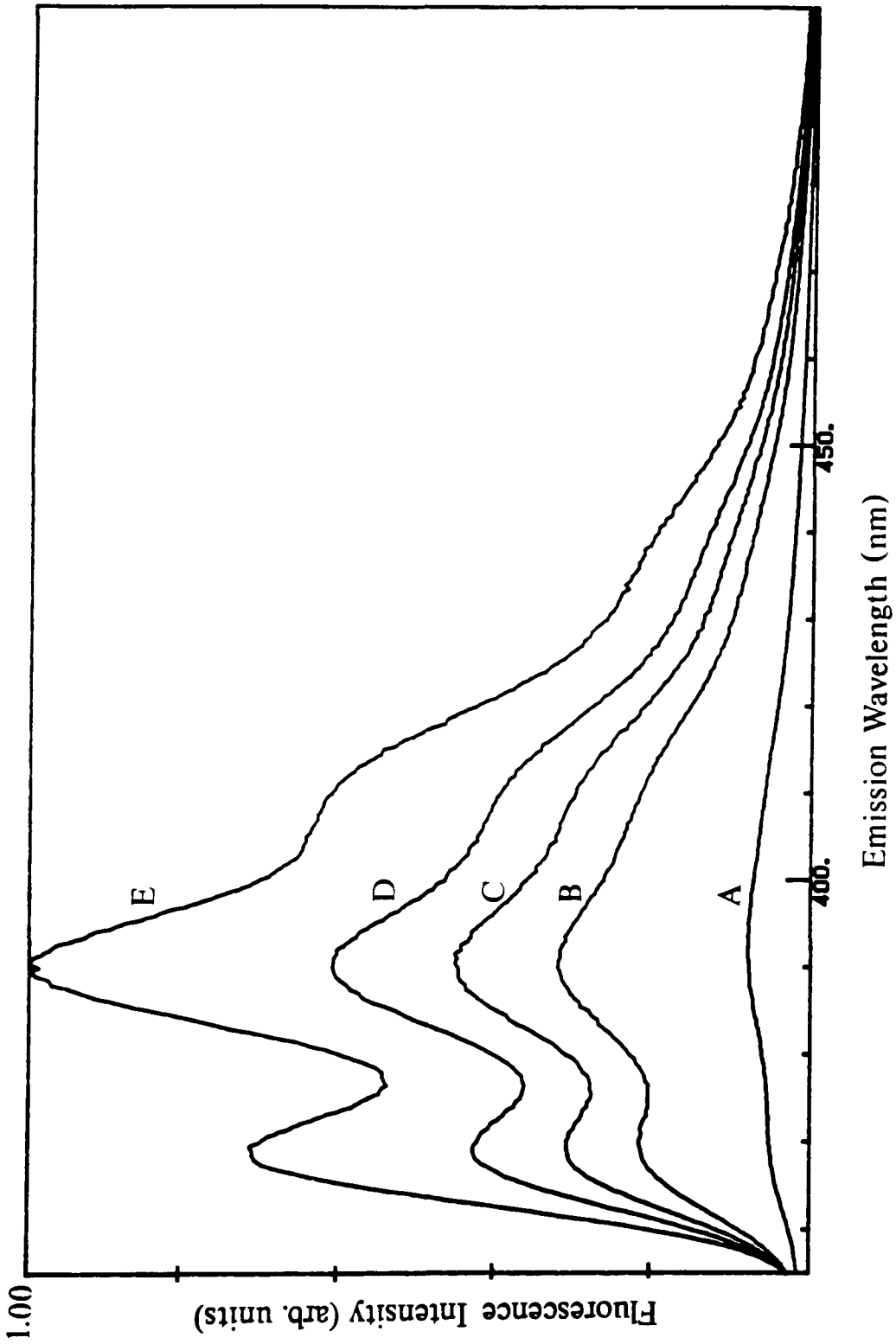

Figure 4.39: Unnormalized emission spectra of TPC in MCH (λ_{ex} 320 nm) at low temperatures; 22.4°C(A), -54°C(B), -82°C(C), -112°C(D) and -136°C(E).

fluorescence components in this case are prompt and delayed emissions from B_u-like S_2^*, whose high radiative transition probability (=k_f) should not be affected by interaction with a nearby excited state with a low radiative transition probability.

So it appears that the photophysics of TPC in solvents is best described by the general reversible two-excited state model in which both S_1^* and S_2^* are fluorescent. Thus both fluorescence decay times, τ_1 and τ_2, have contributions from $S_2^* \rightarrow S_0$ and $S_1^* \rightarrow S_0$ emissions (equations 4.67, 4.68). The low temperature fluorescence measurements confirm $S_1^* \rightarrow S_0$ is a weak radiative transition consistent with the prediction of a L_b-like S_1^* by CNDO/S (Pariser) molecular orbital calculations. The changes in k_{f1} and k_{f2} with temperature reflect the increased radiative transition probability of S_1^* upon its greater interaction with B_u-like S_2^* at lower temperatures. It is interesting to note that the lifetime of DPH actually decreases as the temperature is lowered, while ϕ_f increases[15], and this too can be rationalized by an excited state equilibrium between a strong S_2^* (B_u)$\rightarrow S_0$ radiative transition and a formally forbidden S_1^* (A_g)$\rightarrow S_0$ radiative transition. It is possible that the A*/nonfluorescent B* model could be valid around room temperature since there was a fairly good correspondence between $\Delta\tau$ and $\Delta\phi_f$ between room temperature and ~-50°C. This is an indication that the variation of these two parameters over this temperature range is due to the effect of viscosity and temperature changes on the nonradiative processes of TPC. Perhaps at these temperatures, S_1^* and S_2^* are sufficiently far apart that there is no vibronic coupling between them, and under these conditions S_1^* could be a truly nonfluorescent state. At lower temperatures, S_1^* likely gains some S_2^* character and the more general reversible two-excited state model applies.

4.3.9 Summary of the Solvent Photophysics of TPC

The kinetic scheme which best accounts for the photophysical properties of TPC in isotropic solvents is presented in Figure 4.41. It is possible that at higher temperatures, S_1^* is nonfluorescent, i.e. $k_{fB} \sim 0$. The excited state equilibrium is dependent on viscosity, as manifested through viscosity dependent pre-exponential factors and lifetimes at constant temperature. This sensitivity to viscosity is most likely the result of differences in the relative importance of viscosity dependent nonradiative processes from the two states. The ϕ_f of TPC is also sensitive to solvent viscosity,

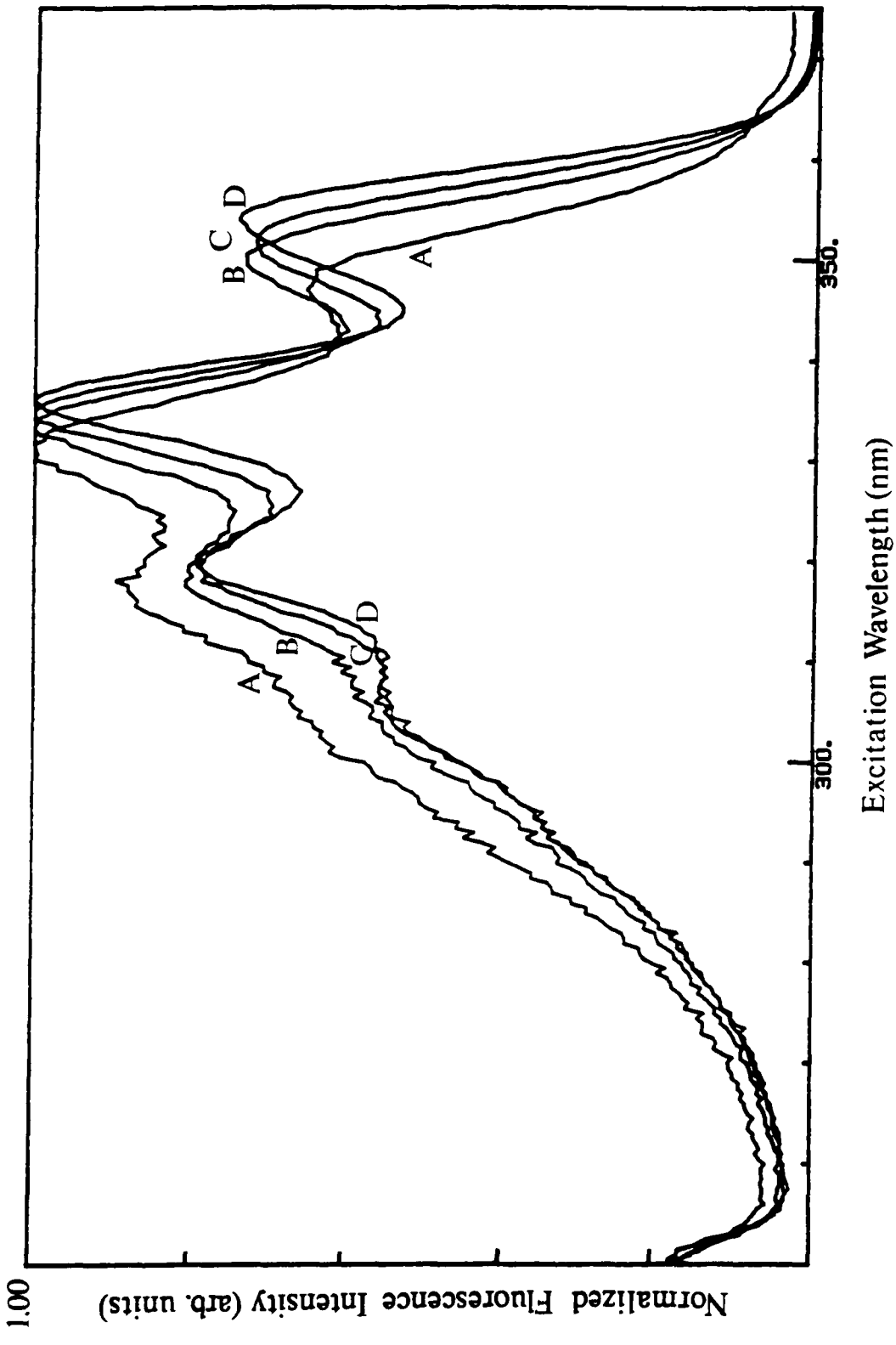

Figure 4.40: Normalized excitation spectra of TPC in MCH (λ_{ex} 410 nm) at low temperatures; 22.4°C(A), -52°C(B), -112°C(C), -150°C(D).

so TPC is potentially a useful probe of the dynamical aspect of membrane fluidity. Also, TPC should be very useful in resonance energy transfer studies from tryptophan (the intrinsic fluorophore of proteins and peptides) because of its optical transparency between ~255–300 nm where tryptophan absorbs, and its strong absorption between ~300–360 nm where tryptophan emits.

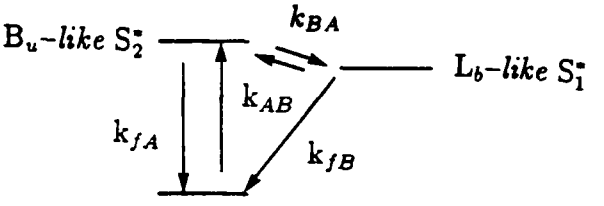

Figure 4.41: Kinetic scheme to describe the photophysics of TPC in solvents.

4.4 References

1. J.B. Birks, *"Photophysics of Aromatic Molecules"*, Wiley, London, **1970**.

2. A.J. Pesce, C-G. Rosen and T.L. Pasby, *"Fluorescence Spectroscopy. An Introduction for Biology and Medicine"*, Marcel Dekker, New York, **1971**.

3. J.R. Lakowicz, *"Principles of Fluorescence Spectroscopy"*, Plenum, New York, **1983**.

4. H.H. Jaffé and M. Orchin, *"Theory and Applications of Ultraviolet Spectroscopy"*, Wiley, New York, **1962**.

5. D.C. Turner and L. Brand, *Biochem.*, **1968**, *7*, 3381–3390.

6. L. Brand and J.R. Gohlke, *Ann. Rev. Biochem.*, **1972**, *41*, 843–868.

7. J. Vanderkooi and A. McLaughlin, in *"Biochemical Fluorescence Concepts"*, R.F. Chen and H. Edelhoch eds., Marcel Dekker, New York, **1976**, Vol. 2, pp. 737–765.

8. P.W. Schiller, in *"Biochemical Fluorescence Concepts"*, R.F. Chen and H. Edelhoch eds., Marcel Dekker, New York, **1976**, Vol. 1, pp. 285–303

9. N.J. Turro, *"Modern Molecular Photochemistry"*, Benjamin / Cummings, California, **1978**.

10. A.M. Kleinfeld and M.F. Lukacovic, *Biochem.*, **1985**, *24*, 1883–1890.

11. S. Wang, E. Martin, J. Cimino, G. Omann and M. Glaser, *Biochem.*, **1988**, *27*, 2033–2039.

12. E.A. Griffin, J.M. Vanderkooi, G. Maniara and M. Erecinska, *Biochem.*, **1986**, *25*, 7875–7880.

13. P.C. Alford and T.F. Palmer, *Chem. Phys. Lett.*, **1982**, *86*, 248–253.

14. T.C. Felder, K-J. Choi and M.R. Topp, *Chem. Phys.*, **1982**, *64*, 175–182.

15. P.C. Alford and T.F. Palmer, *J. Chem. Soc., Faraday Trans. II*, **1983**, *79*, 433–447.

16. T. Itoh and B.E. Kohler, *J. Phys. Chem.*, **1987**, *91*, 1760–1764.

17. B.S. Hudson and B.E. Kohler, *J. Chem. Phys.*, **1973**, *59*, 4984–5002.

18. B.S. Hudson and B.E. Kohler, *Ann. Rev. Phys. Chem.*, **1974**, *25*, 437–460.

19. B.S. Hudson, B.E. Kohler and K. Schulten, in *"Excited States"*, E.C. Lim ed., Academic, New York, **1982**, Vol. 6, pp. 1–95.

20. H.L-B. Fang, R.J. Thrash and G.E. Leroi, *Chem. Phys. Lett.*, **1978**, *57*, 59–63.

21. J.S. Horowitz and B.E. Kohler and T.A. Spiglanin, *J. Phys.*, **1985**, *46*, C7-381–C7-389.

22. K. Schulten and M. Karplus, *Chem. Phys. Lett.*, **1972**, *14*, 305–309.

23. R.A. Goldbeck, A.J. Twarowski, E.L. Russell, J.K. Rice, R.R. Birge, E. Switkes and D.S. Kliger, *J. Chem. Phys.*, **1982**, *77*, 3319–3328.

24. S.P. Velsko and G.R. Fleming, *J. Chem. Phys.*, **1982**, *76*, 3553–3562.

25. B.S. Hudson, D.L. Harris, R.D. Ludescher, A. Ruggiero, A. Cooney-Freed and S.A. Cavalier, in *"Applications of Fluorescence in the Biomedical Sciences"*, D.L. Taylor, A.S. Waggoner, R.F. Murphy, F. Lanni and R.R. Birge eds., Alan R. Liss, New York, **1986**, pp. 159–202.

26. Y.B. Sheck, N.P. Kovalenko and M.V. Alfimov, *J. Lumin.*, **1977**, *15*, 157–168.

27. E. Haas, G. Fischer and E. Fischer, *J. Phys. Chem.*, **1978**, *82*, 1638–1643.

28. J.B. Birks, G. Bartocci, G.G. Aloisi, S. Dellonte and F. Barigelletti, *Chem. Phys.*, **1980**, *51*, 113–120.

29. E. Fischer, *J. Molec. Struct.*, **1982**, *84*, 219–226.

30. U. Mazzucato, *Pure Appl. Chem.*, **1982**, *54*, 1705–1721.

31. A.C. Matthews, R. Sakurovs and K.P. Ghiggino, *J. Photochem.*, **1982**, *19*, 235–244.

32. G. Bartocci, F. Masetti, U. Mazzucato and G. Marconi, *J. Chem. Soc., Faraday Trans. II*, **1984**, *80*, 1093–1105.

33. J. Saltiel and D.W. Eaker, *J. Am. Chem. Soc.*, **1984**, *106*, 7624–7626.

34. G. Bartocci, U. Mazzucato, F. Masetti and G.G. Aloisi, *Chem. Phys.*, **1986**, *101*, 461–466.

35. K.A. Muszkat and T. Wismontski-Knittel, *Chem. Phys. Lett.*, **1981**, *83*, 87–90.

36. D.W.J. Cruickshank, *Acta Cryst.*, **1957**, *10*, 504–508.

37. C.P. Brock and J.D. Dunitz, *Acta Cryst.*, **1982**, *B38*, 2218–2228.

38. G. Bartocci, F. Masetti, U. Mazzucato, A. Spalleti and M.C. Bruni, *J. Chem. Soc., Faraday Trans. II*, **1986**, *82*, 775–788.

39. H.J.C. Jacobs and E. Havinga, *Adv. Photochem.*, **1979**, *11*, 305–373.

40. Y.T. Mazurenko, V.S. Udaltsov and A.S. Cherkasov, *Opt. Spectrosc.* (USSR), **1979**, *46*, 389–391.

41. S.R. Flom, V. Nagarajan and P.F. Barbara, *J. Phys. Chem.*, **1986**, *90*, 2085–2092.

42. M.G. Badea and L. Brand, *Meth. Enzymol.*, **1979**, *61*, 378–425.

43. J.N. Demas and G.A. Crosby, *J. Phys. Chem.*, **1971**, *75*, 991–1024.

44. C.M. Himel and R.T. Mayer, *Anal. Chem.*, **1970**, *42*, 130–132.

45. A.G. Szabo and D.M. Rayner, *J. Am. Chem. Soc.*, **1980**, *102*, 554–563.

46. A.E.W. Knight and B.K. Selinger, *Aust. J. Chem.*, **1973**, *26*, 1–27.

47. D.V. O'Connor and D. Phillips, *"Time-Correlated Single Photon Counting"*, Academic, London, **1984**.

48. C.M. Harris and B.K. Selinger, *Aust. J. Chem.*, **1979**, *32*, 2111-2129.

49. *Exciton Laser Dye Catalogue*, Exciton Chemical Company, Daytona, Ohio, **1986**.

50. E.G. Marason, *Opt. Commun.*, **1981**, *37*, 56–58.

51. Model 344S, High-Efficiency Cavity Dumper, Instruction Manual, Laser Products Division, Spectra Physics, Mountain View, California, **1984**, p. 3-42.

52. W. Demtröder, *"Laser Spectroscopy. Basic Concepts and Instrumentation"*, Springer-Verlag, Berlin, **1982**, pp. 362–364.

53. G.R. Haugen, B.W. Wallin and F.E. Lytle, *Rev. Sci. Instrum.*, **1979**, *50*. 64–72.

54. I. Yamazaki, N. Tamai, H. Kume, H. Tsuchiya and K. Oba, *Rev. Sci. Instrum.*, **1985**, *56*, 1187–1194.

55. M. Zuker, A.G. Szabo, L. Bramall, D.T. Krajcarski and B. Selinger, *Rev. Sci. Instrum.*, **1985**, *56*, 14–22.

56. A. Grinwald and I.Z. Steinberg, *Anal. Biochem.*, **1974**, *59*, 583–598.

57. D.W. Marquadt, *J. Soc. Indust. Appl. Math.*, **1963**, *11*, 431–441.

58. J. Durbin and G.S. Watson, *Biometrika*, **1971**, *58*, 1–19.

59. J.R. Knutson, J.M. Beechem and L. Brand, *Chem. Phys. Lett.*, **1983**, *102*, 501–507.

60. B. Donzel, P. Gauduchon and P. Wahl, *J. Am. Chem. Soc.*, **1974**, *96*, 801–808.

61. J.M. Beechem, M. Ameloot and L. Brand, *Anal. Instrum.*, **1985**, *14*, 379–402.

62. J.M. Beechem, M. Ameloot and L. Brand, *Chem. Phys. Lett.*, **1985**, *120*, 466–472.

63. J.R. Knutson, D.G. Walbridge and L. Brand, *Biochem.*, **1982**, *21*, 4671–4679.

64. J.R. Knutson, L. Davenport, J.M. Beechem, D.G. Walbridge, M. Ameloot and L. Brand, in *"Excited State Probes in Biochemistry and Biology"*, L. Masotti and A.G. Szabo eds., Plenum, New York, in press.

65. M.D. Barkley, S. Cheatham, D.E. Thurston and L.D. Hurley, *Biochem.*, **1986**, *25*, 3021–3031.

66. J. Del Bene and H.H. Jaffé, *J. Chem. Phys.*, **1968**, *48*, 1807–1813.

67. A. Warshel and M. Karplus,*J. Am. Chem. Soc.*, **1972**, *94*, 5612–5625.

68. A. Warshel, in *"Modern Theoretical Chemistry"*, A. Segal ed., Plenum, New York, **1977**, Vol. 7, part A, pp. 133–172.

69. P. Pariser, *J. Chem. Phys.*, **1953**, *21*, 568–569.

70. G. Orlandi and F. Zerbetto, *Chem. Phys.*, **1986**, *108*, 187–195.

71. G. Klopman and R.C. Evans, in *"Modern Theoretical Chemistry"*, A. Segal ed., Plenum, New York, **1977**, Vol. 7, part A, pp. 29–67.

72. A.J. Gordon and R.A. Ford, *"The Chemist's Companion"*, Wiley, New York, **1972**.

73. D.M. Bishop, *"Group Theory and Chemistry"*, Clarendon, Oxford, **1973**.

74. M. Letellier, B.Sc. Hons. thesis, University of Ottawa, **1987**.

75. Reference 1, Table 3.1, p. 70.

76. D.J.S. Birch and J.B. Birks, *Chem. Phys. Lett.*, **1976**, *38*, 432–436.

77. J.B. Birks, *"Organic Molecular Photophysics"*, Wiley, London, **1973**, Vol. 1, p. 15.

78. A.A. Bothner-By, *Adv. Magn. Reson.*, **1965**, *1*, 195–309.

79. S.L. Murov, *"Handbook of Photochemistry"*, Marcel Dekker, New York, **1973**.

80. W.R. Laws and L. Brand, *J. Phys. Chem.*, **1979**, *83*, 795–802.

81. L. Davenport, J.R. Knutson and L. Brand, *Biochem.*, **1986**, *25*, 1186–1195.

82. S. Yamashita, A.G. Szabo, P. Cavatorta and C. Zannoni, unpublished results.

83. R.J. Cave and E.R. Davidson, *J. Phys. Chem.*, **1988**, *92*, 614–620.

84. D.R. James and W.R. Ware, *Chem. Phys. Lett.*, **1986**, *126*, 7–11.

85. J.R. Alcala, E. Gratton and F.G. Prendergast, *Biophys. J.*, **1987**, *51*, 925–936.

86. A.G. Szabo, D.T. Krajcarski, J. Ridgeway and M. Zuker, unpublished results.

Chapter 5

Model Membrane Studies Employing the Novel Fluorescent Cholesterol Analogues

5.1 Introduction

DNC and TPC appear to have considerable potential as probes of membrane fluidity, particularly in cholesterol domains, because they possess both viscosity sensitive photophysical parameters as well as a structural similarity to cholesterol. In order to test this prediction, it was decided to perform steady-state and time-resolved fluorescence studies on the two sterols incorporated into model membranes.

The systems which have been most often employed as model membranes are lipid vesicles or liposomes[1-3]. Vesicles are closed lipid bilayers (see Figure 5.1) and they are the structures which are typically formed by phospholipids upon their dispersion in aqueous media. Generally vesicles consist of several lamellae of bilayers arranged in an 'onion-skin' like structure, unless special preparative procedures are employed. Such vesicles are termed multilamellar vesicles (MLVs). This class of vesicle is not well suited as a model membrane since cell membranes are composed of only a single lipid bilayer, and also the location of probes in MLVs is likely to be heterogeneous which makes interpretation of their physical parameters difficult. Consequently, methods have been developed to obtain unilamellar (single bilayer) vesicles.

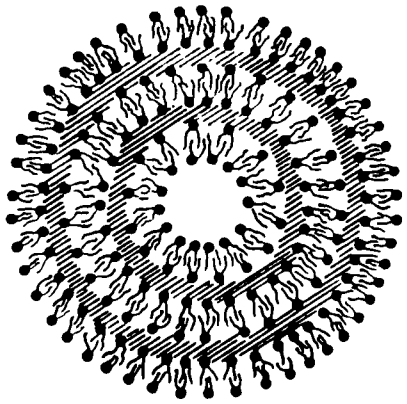

Figure 5.1: A schematic diagram of a multilamellar vesicle (MLV) showing only three concentric lipid bilayers (from "Biological Membranes. Their Structure and Function", R. Harrison and G.C. Lunt, Blackie, Glasgow, **1975**, p. 94).

Small unilamellar vesicles (SUVs) can be prepared from MLVs either by subjecting the MLVs to sonication followed by high-speed centrifugation or by passing them through a French press[2-5]. SUVs typically have diameters of 25-40 nm which limits their use as model membranes due to their high radii of curvature. This results in a ratio of outer to inner monolayer lipid of ~2:1[2], and packing restraints which could lead to asymmetric distribution of lipids between the monolayers as compared with less highly curved systems, such as cell membranes. Moreover, the aqueous volume enclosed by SUVs is often too small to allow studies of permeability or ion distributions between the internal and external aqueous compartments.

Large unilamellar vesicles (LUVs), which have diameters from 100–500 nm, are more suitable as model membranes since the distribution of lipid between the monolayers is close to 1:1, and the internal aqueous (encapsulation) volume is considerably higher than for SUVs[1-4]. In fact the encapsulating ability of LUVs, as well as their natural lipid composition which renders them nontoxic and allows them to escape removal by the body's immune system, has been exploited in the use of LUVs as drug delivery systems[3-6]. This is an active field of research since LUVs not only protect drugs against dilution and degradation in the blood, but they also have the potential to be targetted to deliver drugs to specific tissues through the presence of antibodies attached to their outer surfaces.

LUVs can be prepared directly by methods which employ organic solvents or detergents[1-4,7]. These methods have the disadvantage, however, that they involve removal of the solvent or detergent from the lipid/aqueous buffer system. This is very difficult to achieve completely, even if lengthy dialysis or vacuum pumping procedures are followed. Alternatively, LUVs can be formed by fusion of SUVs through a cycle of quick-freezing, gradual thawing and brief sonication[1,3], or by repeated extrusion of MLVs through inert polycarbonate membranes of 100 nm pore size or less[8]. The former method yields a heterogeneous population of vesicles with diameters of 20-200 nm, while the latter gives vesicles whose diameters approximate the pore size of the membrane filter. Increased homogeneity of size can be achieved by extrusion through two stacked polycarbonate membrane filters.

The model membranes used in this work, to study the potential of DNC and

TPC as cell membrane probes, were LUVs prepared by the above extrusion procedure. The phospholipid chosen was dimyristoylphosphatidylcholine (DMPC, see Figure 5.2) partly because of its two saturated acyl chains which renders it less susceptible to degradation (e.g. oxidation) than unsaturated lipids[9], and also since its gel-liquid crystalline phase transition temperature T_m (=23.9°C), is around room temperature[10]. This allows fluorescence studies to be conveniently performed both in the gel and the physiologically relevant liquid crystalline phase. It is obviously of interest to determine how the incorporation of DNC and TPC in these two distinct phases is manifested in their photophysical properties. In addition, DMPC/cholesterol binary mixtures are one of the better characterized phospholipid/cholesterol systems in the literature. This should enable comparison of the results obtained using the novel fluorescent cholesterol analogues, DNC and TPC, with conclusions that have been made on this system from other studies.

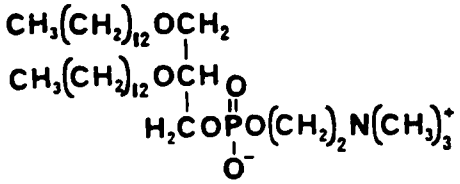

Figure 5.2: DMPC

5.2 Materials and Methods

5.2.1 Large Unilamellar Vesicle (LUV) Preparation

Aliquots of stock solutions of cholesterol (Sigma, ~10 mM), DMPC (Avanti Polar Lipids, ~3 mM), DNC (~0.1 mM) and TPc (~0.1 mM) in chloroform were combined so as to arrive at mole percent cholesterol levels of 0, 4, 7, 12 and 20%, and lipid:probe ratios of 200:1 and 500:1. The purity of the DMPC had previously been checked by HPLC (Beckman Hypersil column, 100% MeOH, 220 nm) and was found to be 99.4%. All traces of chloroform were first removed by rotary evaporation and then under vacuum in a dessicator for 12 h. The dried lipid film was taken up in TRIS buffer (Boehringer-Mannheim, 0.01 M, adjusted to pH 7.2 with HCl) and vortexed for approximately 1 minute to ensure complete suspension. The resulting MLVs (1.0 mg DMPC/ml buffer) were transformed into LUVs by extrusion through polycarbonate membrane filters of successively smaller pore size [Nucleopore, 25 mm diameter, pore sizes 0.4 μm (1 pass), 0.2 μm (1 pass) and 2 stacked, 0.1 μm filters (3 passes)] under moderate pressures (150–200 psi, nitrogen), based on a literature method[8]. The membrane filters were supported in the bottom half of a Millipore membrane holder (XX 30025 00) equipped with two stainless steel mesh grids, in order to avoid buckling of a single grid under the moderately high pressures. A homebuilt (Mechanical Workshop, Division of Biological Sciences, NRC) stainless steel chamber was screwed into the Millipore holder and could hold up to 50 ml of lipid suspension above the filter. This chamber was thermostatted above the gel-liquid crystalline phase transition temperature, T_m, of DMPC (23.9°C) through contact with coiled brass tubing which was connected to a Polysciences Polytemp 90 temperature controller (see Figure 5.3).

Due to the relatively little manipulation of the lipid sample in the above procedure, for example, the absence of a centrifugation step such as in the preparation of small unilamellar vesicles, and the low adsorption and high chemical resistance characteristics of polycarbonate membranes[11], it was expected that there would be minimal loss of material and hence that the lipid:probe ratio and mole percent

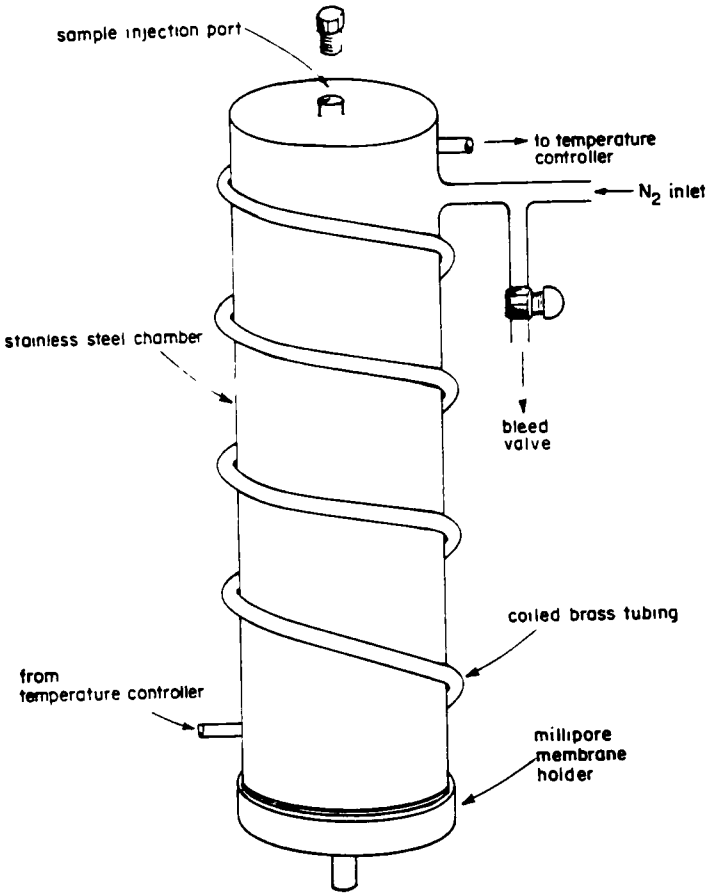

Figure 5.3: A schematic diagram of the extrusion apparatus used to prepare LUVs.

cholesterol content would be very close to their initial input values. However, it was attempted to quantify these parameters through HPLC. An aliquot of each of the preparations was diluted 1:1 with tetrahydrofuran (THF) in order to disrupt the vesicles[12], and the resulting solutions injected onto three different types of HPLC column, a Dupont Zorbax C_8 column, a Beckman Hypersil normal phase column and a Varian SP C_{18} reversed phase column. The best separation of peaks was achieved with the latter column using 100% MeOH as eluant, and gave retention times of ~2.1′ (DMPC), ~9.5′ (cholesterol) and ~11.9′ (DNC or TPC). Accurate quantitation of the area under the DMPC peak, however, was difficult due to its proximity to the solvent front. In addition, use of an internal standard (e.g. another sterol[13]) could improve the accuracy of cholesterol level determinations by this method. Time-resolved fluorescence results of DNC in the DMPC/cholesterol LUVs, to be presented later, show a consistent trend with input cholesterol content which indicates that final cholesterol levels are similar to their input levels. Fluorescence intensity differences between samples with 200:1 as opposed to 500:1 lipid:probe ratios are also consistent with no loss of probe material in the LUV preparation procedure.

5.2.2 Characterization of the LUV preparations by electron microscopy

The size distribution of the LUVs was checked by both negative stain and thin section electron microscopy[14,15]. In the negative staining procedure, a drop of the LUV preparation was allowed to settle on a formvar coated copper grid for 1 minute and the excess liquid was then drawn off with filter paper. One drop of a 1% aqueous uranyl acetate staining solution was then placed on the grid for 1 minute and excess again drawn off with filter paper. Four grids were prepared for each LUV sample and were visualized under a Phillips 201 electron microscope.

The LUVs appeared in the electron micrographs as approximate circular projections on the grid, each with an opaque periphery that corresponds to the outer headgroup region of the vesicle since this region is accessible to the aqueous staining solution (see Figure 5.4). The vesicle sizes determined from the diameters of these

projections tend to be overestimated due to distortions introduced by flattening of the vesicles on the grid. For this reason, size distributions were also obtained by the thin sectioning technique. This involved a lengthy sample preparation procedure described below[5].

The LUV samples were first treated with a fixative (2% OsO_4, pH 7.4) for at least 48 hrs at 4°C, in order to preserve the vesicle structure. 1 ml of the fixed samples was mixed with 0.1 ml of freshly prepared 2% gelatin solution and then filtered onto a filter (Sartorius) of pore size 0.01 μm. The filter and deposited sample were transferred to 10 ml of 5% aqueous uranyl acetate for staining, and left in the dark for 48 h at 37°C. Dehydration of the filter and sample was achieved by treating with 70, 80, 90 and 100 (×3)% EtOH for 10 minutes each, and then with propylene oxide (3×10 minutes) which also dissolved the filter. The samples were embedded by placing them in a propylene oxide/epon araldite mixture (3:1) for 24 h, in 100% epon araldite for a further 24 h and then baking this preparation in flat moulds at 68°C for 48 h. Thin sections were cut with a Reichert-Jung ultra microtome, stained with 5% uranyl acetate (15 minutes) and lead citrate (15 minutes), and then visualized under a Phillips 420 electron microscope (see Figure 5.4).

Unlike the negative staining technique, thin sectioning tends to underestimate the average vesicle diameter since only the sections which are taken through the centre of vesicle will yield the correct diameter. The average size of the LUVs was taken as the average of the vesicle diameters determined by these two techniques (see Table 5.1).

Table 5.1: Size characterization of the DMPC/cholesterol LUV preparations.

% Cholesterol	d (nm)[a,b] (thin sectioning)	d (nm)[a,b] (negative staining)	average d (nm)
0	73±22	107±25	90±25
7	84±11	111±17	98±17
12	120±20	114±31	117±31
20	108±12	117±12	113±12

[a]determined by taking the average of the long and short axis diameters of approximately 50 vesicles.
[b]error = average error

The unilamellar character of the vesicles was checked by thin section electron

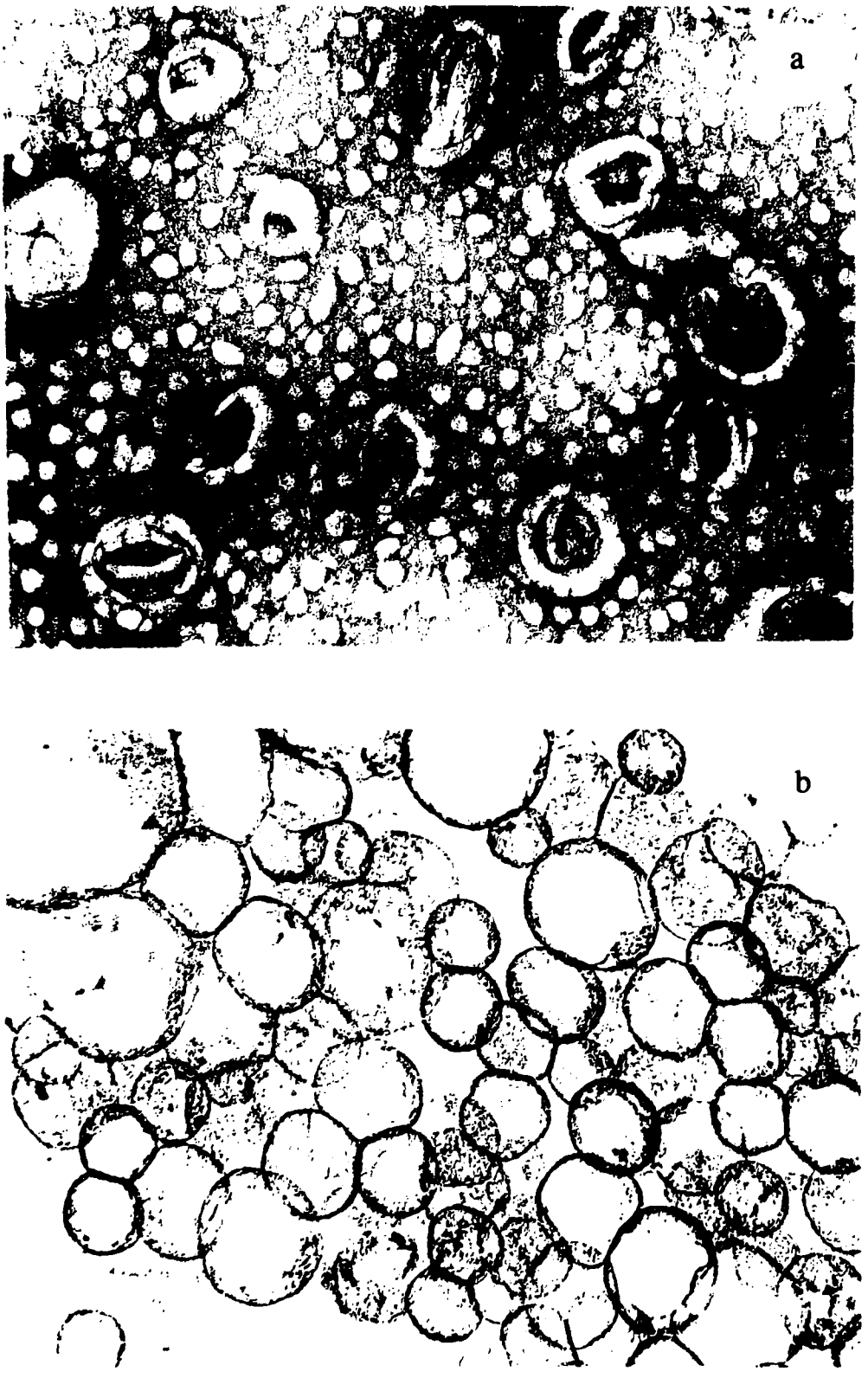

Figure 5.4: Electron micrographs, of a DMPC/12% cholesterol LUV preparation, obtained by a) negative staining and b) thin sectioning techniques.

microscopy, since sections of unilamellar vesicles treated with staining agent are characterized by two closely-spaced dark circles on their perimeter (see Figure 5.4). These correspond to the inner and outer headgroup regions of the single lipid bilayer.

5.2.3 Steady-state and time-resolved fluorescence measurements on the LUV preparations

The instrumentation and data analysis methods used in the steady-state and time-resolved fluorescence studies of the LUVs were identical to those described in the previous chapter.

5.3 Results and Discussion

5.3.1 Fluorescence Excitation and Emission Spectra

Fluorescence excitation and emission spectra of DNC and TPC incorporated into DMPC/cholesterol LUVs were measured above and below the gel-liquid crystalline phase transition temperature (T_m=23.9°C) as a function of mole percent cholesterol content (0, 4, 7, 12 and 20%) and lipid:probe ratio (200:1 and 500:1). Both excitation and emission spectral shapes of TPC were invariant within this range of probe and cholesterol levels (not shown), as well as with the phase state of the model membrane. There was, however, a significant amplitude change in the spectra of TPC between 20.1°C and 31.1°C, but this is probably due to temperature dependent nonradiative decay processes rather than a sensing of the different phases of the DMPC/cholesterol LUVs. This could be checked by measuring the steady-state fluorescence spectra of TPC through the phase transition.

Likewise, there were no excitation or emission spectral shape changes of DNC as the lipid:probe ratio in the LUVs was varied from 500:1 to 200:1. This confirmed the expectation that, at these low DNC concentrations, there would be no perturbation of the LUVs through DNC dimer or excimer formation. There were, however, subtle changes in the ratio of the peak heights at the red edge at and the maximum of the excitation spectrum of DNC as a function of cholesterol content (Figure 5.5). Even though DNC exists in a conformational equilibrium in the ground state, this result is

not expected since the excitation spectra were measured under identical conditions of temperature and emission wavelength. The intensity ratio change most likely arises from a slight shift in the position of the strongly allowed $S_0 \rightarrow S_2^*$ transition compared with the weakly allowed $S_0 \rightarrow S_1^*$ transition, due to a small refractive index change. Further investigation, such as the determination of IEDAS, could ascertain whether this is a real effect or an artifact.

The sensitivity of the fluorescence spectral shapes of DNC to the DMPC phase transition was even more subtle than the above effect noted for different cholesterol levels. The implication is that both DNC and TPC appear to be insensitive membrane fluidity probes as far as their steady-state fluorescence spectra are concerned.

5.3.2 Time-resolved Fluorescence Results

Above the Gel-Liquid Crystalline Phase Transition

The decay parameters of DNC and TPC in the various DMPC/cholesterol LUV preparations, above T_m, are presented in Tables 5.2 and 5.3 respectively. The fluorescence decay of DNC was fitted by a sum of three exponential terms with lifetime amplitudes similar to those determined for DNC in mineral oils. Consequently, comparison of the viscosity effects on the ground and excited state conformation equilibria of DNC in mineral oils, with the observed changes in the decay parameters of DNC in the LUV preparations, should allow conclusions to be made of the effect of cholesterol on the order and dynamics of DMPC LUVs in the liquid crystalline (physiologically relevant) phase. Note that the pre-exponential factor, α_1, associated with the longest lifetime (*tt*-DNC) remains constant between 0 and 7% cholesterol content but decreases in amplitude between 7, 12 and 20% cholesterol levels. In the context of the discussion in section 4.3.7, this signifies a change in the ground state conformational equilibrium of DNC between *tt*-DNC and nonplanar *tc*-DNC, favouring the less stable *tc*-DNC at higher cholesterol levels. Since the decay parameters were obtained under identical conditions of temperature and excitation wavelength, this shift in the ground state equilibrium towards the less stable conformer must be a result of an increase in the order of DMPC acyl chains in the liquid crystalline phase upon incorporation of greater than 7% cholesterol.

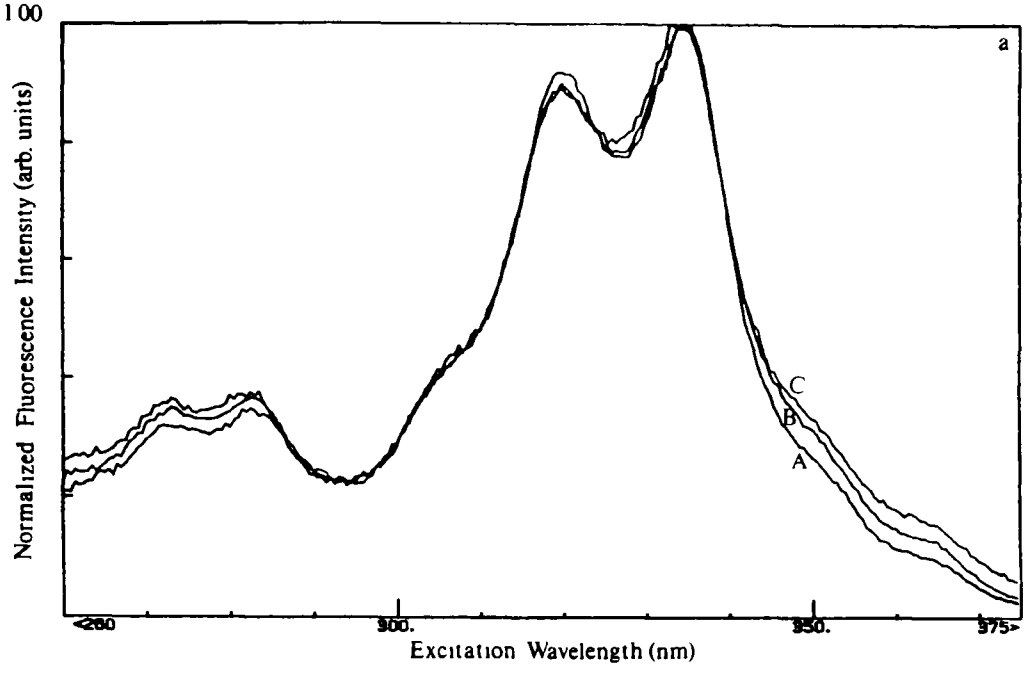

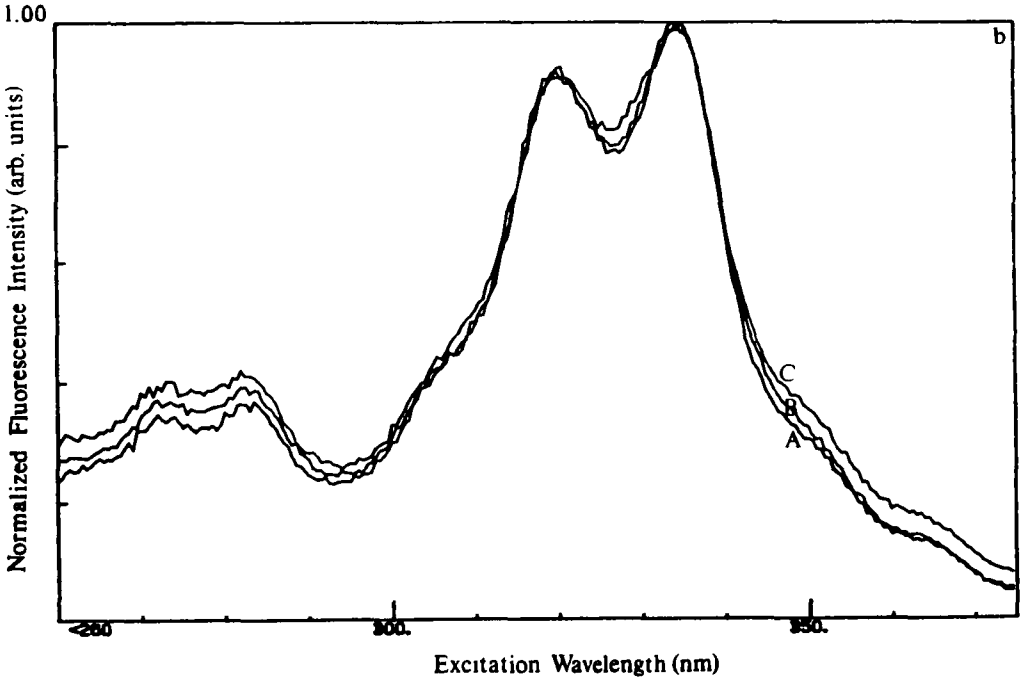

Figure 5.5:
Uncorrected fluorescence excitation spectra of DNC in DMPC/cholesterol LUVs with 0(A), 12(B) and 20(C) mole percent cholesterol; a) 20.6°C and b) 31.0°C.

Of course, due to the position of the naphthyl butadiene chromophore in DNC, and the expected alignment of DNC in the DMPC bilayer with its 3β-OH group in the vicinity of the carbonyl oxygen in the acyl chain, DNC only reports on the lipid acyl chain order and dynamics towards the centre of the bilayer (see Figure 5.6).

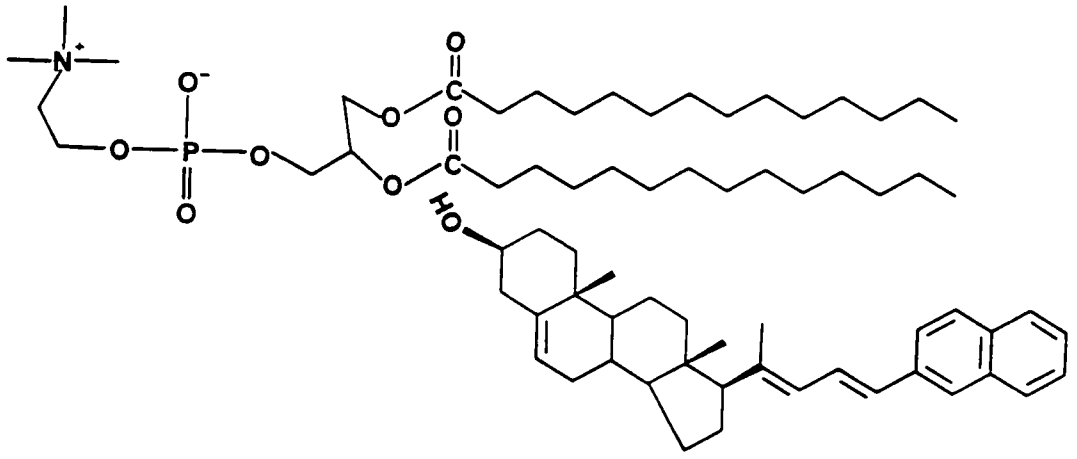

Figure 5.6: A 2D representation of the expected relative vertical positions of the DMPC acyl chains and the DNC fluorophore.

Table 5.2: Time-resolved fluorescence parameters of DNC in DMPC/cholesterol LUVs above the gel-liquid crystalline phase transition (T=31.1°C, λ_{ex}320 nm, λ_{em}410 nm).

% Cholesterol	lipid: probe ratio	τ_1 (ns)	τ_2 (ns)	τ_3 (ns)	α_1	α_2	α_3	χ^2	SVR
0	500:1	38.4	4.74	0.33	0.197	0.427	0.376	1.03	1.99
7	500:1	40.6	3.89	0.39	0.203	0.493	0.305	1.05	1.95
12	200:1	39.0	5.09	0.44	0.166	0.418	0.416	1.09	1.71
20	500:1	40.6	4.29	0.53	0.129	0.450	0.421	1.03	1.85

The observed increase in order above T_m with added cholesterol is in general agreement with established ideas about cholesterol's effect on membrane fluidity[16]. However, the fact that the increase was not observed until greater than 7 mole percent cholesterol tends to support the hypothesis of an onset of liquid-liquid immiscibility at around 10 mole percent cholesterol, as concluded from freeze-fracture electron microscopy and EPR studies[17–19]. This hypothesis is certainly not universally accepted. For example, recent neutron scattering results have been cited as

Table 5.3: Time-resolved fluorescence parameters of TPC in DMPC/cholesterol LUVs above the gel-liquid crystalline phase transition (T=31.4°C, λ_{ex}320 nm, λ_{em}410 nm).

% Cholesterol	lipid: probe ratio	τ_1 (ns)	τ_2 (ns)	τ_3 (ns)	α_1	α_2	α_3	χ^2	SVR
0	500:1	0.621	0.22		0.69	0.31		0.95	1.91
0	200:1	0.578	0.15		0.70	0.30		1.05	1.61
7	200:1	0.745	0.284		0.71	0.29		1.00	2.02
12	200:1	0.698	0.236		0.59	0.41		1.03	2.00
20	200:1	0.911	0.488	0.114	0.24	0.41	0.36	0.95	1.93
20 (E2 fit)	200:1	0.770	0.231		0.51	0.49		1.14	1.34
20	500:1	0.671	0.169		0.62	0.38		1.06	1.88

evidence of complete miscibility in the liquid crystalline phase of DMPC up to 14 mole percent cholesterol, and possibly even up to 45 mole percent[20]. Recently, a phase diagram has been constructed which accounts for the proposed liquid-liquid immiscibility by invoking the existence of a liquid disordered (ld) phase below ~10% cholesterol, a liquid ordered (lo) phase above ~20% cholesterol, and a co-existence of the two phases between these two cholesterol concentrations[21]. If this is the case, it might be expected that there would be a gradual increase in order between 10% and 20% cholesterol levels, as indicated by the DNC time-resolved fluorescence results, and that at around 20% cholesterol, there would be no further increase in order and hence no further reduction in the value of α_1 for DNC. Clearly, additional experiments at cholesterol levels of 20% and higher are required to test this hypothesis.

Regarding cholesterol's effect on the dynamics of DMPC acyl chains in the liquid crystalline phase, the discussion in section 4.3.7 indicated that at constant temperature, the ratio of the pre-exponential factors α_2 and α_3, associated with planar and nonplanar *tc*-DNC respectively, can yield dynamical information due to the viscosity dependence of the excited state conformational change. The α_2/α_3 ratio of DNC in the DMPC LUVs is greatest at 7 mole percent cholesterol content, compared with 0, 12 and 20% cholesterol levels (Table 5.2). This result could be interpreted in terms of maximal dynamical freedom of the lipid acyl chains at

the phase boundary between the postulated liquid disordered (ld) and liquid disordered (ld)/liquid ordered (lo) phases. Notice also that the α_2/α_3 ratio is greater at 20% cholesterol than at 12% cholesterol, possibly a reflection of the ld/lo–lo phase boundary around 20% cholesterol content. Any such conclusions must be tempered by the fact that there is considerable variation in the value of τ_2 with cholesterol content, which could affect the value of α_2. From the mineral oil studies reported for DNC in the previous chapter (Table 4.11), τ_2 was found to be insensitive to viscosity changes, so the origin of the τ_2 variation could be a polarity change in the environment and/or collisional quenching by Cl^- since HCl was used to adjust the TRIS buffer to physiological pH. LUVs of mean diameter 150 nm, prepared by a combination of a solvent vapourization technique and extrusion through polycarbonate membranes, have indeed been found[22] to be permeable to Cl^- though they are impermeable to other ionic species such as Na^+, K^+, SO_4^{2-} and PO_4^{2-}. Hence, the smaller values for τ_2 at 7 and 20 mole percent cholesterol could be an indication of increased membrane permeability at these cholesterol levels due to the presence of phase boundaries. If indeed Cl^- quenching, or a more polar environment (i.e. a greater extent of water penetration), can account for the variation in τ_2 (associated with planar *tc*-DNC), it is surprising that the longer lifetime value τ_1 (associated with *tt*-DNC) is not affected. Perhaps this is an indication that *tt*-DNC is located in a more ordered domain of the membrane and is not as accessible to Cl^- or water molecules. This could be because its structure is more elongated than that of *tc*-DNC so that it intercalates more closely between the lipid acyl chains. Further insight will have to await repetition of these preliminary experiments, both in the presence and absence of Cl^-.

TPC also has the potential to report on the dynamical freedom of its environment, through the different viscosity dependencies of the nonradiative rate constants associated with its S_2^* (B_u-like) $\rightarrow S_0$ and S_1^* (L_b-like) $\rightarrow S_0$ transitions, as discussed in section 4.3.9. This is manifested in a change in the ratio of pre-exponential factors, α_2/α_1, at constant temperature. The α_2/α_1 ratio of TPC in DMPC LUVs above T_m remains constant between 0 and 7% cholesterol levels, and again between 12 and 20% levels, but undergoes an increase between 7 and 12 mole percent cholesterol (Table 5.3). From the results presented earlier for TPC is mineral oils at constant

temperature (Table 4.15), this increase in α_2/α_1 signifies increased mobility of the lipid acyl chains between 7 and 12% cholesterol levels which could be consistent with a phase boundary in this temperature-composition region of the DMPC/cholesterol phase diagram, as suggested by the time-resolved fluorescence results obtained using DNC.

Below the Gel-Liquid Crystalline Phase Transition

The decay parameters of DNC and TPC in the DMPC/cholesterol LUVs, below T_m, are presented in Tables 5.4 and 5.5 respectively. Note that the fluorescence decay profiles of both probe molecules are fitted by an extra exponential term than was necessary for satisfactory fits of fluorescence decays obtained above the phase transition (except for TPC in DMPC/20% cholesterol, see later), or in mineral oils. Consequently, until it is known where this extra lifetime fits into the kinetic scheme describing the photophysics of these molecules, no conclusions can be made regarding changes in ratios of their pre-exponential factors. It does appear, however, that the extra lifetime of ~0.14 ns observed for TPC occurs at the expense of the longest lifetime of ~1.2 ns, since the pre-exponential factor α_2 associated with the intermediate lifetime remains constant between 0 and 7 mole percent cholesterol, while the fluorescence decay kinetics of TPC over this cholesterol concentration range changes from double to triple exponential behaviour (Table 5.5). At 20 mole percent cholesterol and a lipid:probe ratio of 200:1, the decay parameters of TPC are very similar above and below the gel-liquid crystalline phase transition. This is consistent with the recent phase diagram postulated for DMPC/cholesterol, mentioned earlier, which indicates that above 20 mole percent cholesterol there is only a single (liquid ordered) phase down to temperatures substantially lower than T_m[21]. Notice, though, that a satisfactory double exponential fit was obtained for the fluorescence decay of TPC in DMPC/20% cholesterol LUVs above T_m, at a lipid:probe ratio of 500:1. The reason for this discrepancy with the triple exponential fluorescence decay determined at a lipid:TPC ratio of 200:1 is not clear, but it could arise from a slight difference in the cholesterol levels of the two LUV preparations. Clearly, repetition of these preliminary experiments, as well as studies at higher mole percent cholesterol levels, could resolve this issue and could also provide insight into

the origin of the third fluorescence component of TPC.

Table 5.4: Time-resolved fluorescence parameters of DNC in DMPC/cholesterol LUVs below the gel-liquid crystalline phase transition (T=20.5°C), λ_{ex}320 nm, λ_{em}410 nm)

% Cholesterol	lipid: probe ratio	τ_1 (ns)	τ_2 (ns)	τ_3 (ns)	τ_4 (ns)	α_1	α_2	α_3	α_4	χ^2	SVR
0	500:1	49.0	12	4.4	0.52	0.18	0.06	0.42	0.35	1.02	1.98
4	200:1	49.5	13	4.3	0.44	0.13	0.08	0.39	0.41	1.03	2.03
7	500:1	51.9	10	3.9	0.59	0.13	0.13	0.35	0.38	1.00	2.08
12	200:1	51.6	10.0	3.8	0.49	0.11	0.13	0.33	0.43	1.06	1.97
20	500:1	52.3	8.1	3.1	0.52	0.10	0.19	0.32	0.39	1.00	2.03
20	200:1	51.0	8.9	3.2	0.49	0.10	0.20	0.33	0.37	1.03	1.91

Table 5.5: Time-resolved fluorescence parameters of TPC in DMPC/cholesterol LUVs below the gel-liquid crystalline phase transition (λ_{ex}320 nm, λ_{em}410 nm).

% Cholesterol	lipid: probe ratio	T (°C)	τ_1 (ns)	τ_2 (ns)	τ_3 (ns)	α_1	α_2	α_3	χ^2	SVR
0	500:1	19.8	0.963	0.252		0.54	0.46		1.02	1.88
0	200:1	19.8	0.883	0.218		0.55	0.45		1.09	1.60
4	200:1	19.8	1.26	0.58	0.14	0.27	0.44	0.29	0.95	1.92
7	200:1	20.1	1.30	0.59	0.14	0.25	0.45	0.30	0.98	1.98
12	200:1	19.8	1.14	0.52	0.15	0.35	0.37	0.28	1.00	1.97
20	200:1	20.1	1.16	0.53	0.12	0.34	0.38	0.28	1.03	2.02

In the case of DNC, the extra ~10 ns lifetime observed below T_m is known not to be due to a population of DNC molecules which can self-quench, since very similar decay parameters were obtained with lipid:probe ratios of 200:1 and 500:1 (Table 5.4). It is possible, however, that it could reflect a population of DNC molecules which differs in its vertical position in the DMPC bilayer with respect to the usual vertical displacement of cholesterol. Perhaps due to the disparity in the lengths of DNC and the DMPC acyl chains (see Figure 5.6), a proportion of the DNC molecules in the DMPC/cholesterol 'solid-ordered' phase are situated with their 3β-OH groups in the lipid headgroup region rather than in the vicinity of the acyl chain linkages. It would be interesting to measure the fluorescence decay parameters of both DNC and TPC in LUVs composed of either dipalmitoylphosphatidylcholine

(DPPC) or distearoylphosphatidylcholine (DSPC). Studies with these lipids which possess two saturated C_{16} and C_{18} acyl chains respectively, as opposed to the C_{14} chains of DMPC, could ascertain whether the lipid acyl chain length is a determining factor in the presence of the additional fluorescence components for both molecules, below T_m. Furthermore, determination of the DAS and IEDAS (or SAS) associated with the extra lifetime component would help in the elucidation of the photophysics of TPC and DNC in the gel phase of lipid bilayers.

Once an appreciation of the photophysics is obtained, both sterols should prove to be powerful probes of membrane fluidity since their decay parameters are clearly sensitive to both the lipid phase state and the level of incorporation of cholesterol. For example, the amplitudes of both the ~10 ns and ~4 ns lifetimes of DNC decrease by ~33% between 0 and 20% cholesterol levels (Table 5.4). This could be an indication of a gradual increase in the permeability of the LUVs with increasing cholesterol content, if the decrease in the lifetime values can be attributed to Cl^- quenching or the presence of a more polar environment, as discussed earlier concerning the time-resolved fluorescence results of DNC obtained above T_m.

5.4 Conclusions and Future Directions

The potential of DNC and TPC as membrane fluidity probes has been clearly demonstrated on the basis of the sensitivity of their fluorescence decay parameters (but not steady-state fluorescence spectra) to the phase state and the cholesterol level of lipid bilayers. Further insight into the order and dynamics of model membranes, with and without cholesterol, could be provided by experiments already outlined. These include studying the effect of acyl chain length and the degree of acyl chain unsaturation on the fluorescence decay parameters; monitoring these parameters through both the pretransition and gel-liquid crystalline phase transition, as well as at higher cholesterol levels; and performing controlled quenching experiments. In addition, fluorescence depolarization or anisotropy experiments can quantify trends in order and dynamics observed by the fluorescence decay studies, in terms of order parameters and rotational correlation times. If it proves possible to obtain anisotropy decay associated spectra (ADAS), in other words if particular decay times can be linked to specific rotational correlation times, the relative mobilities of DNC rotamers in membranes could be established which would provide unique information on membrane order and dynamics.

Both DNC and TPC should prove amenable to FRAP experiments, not only for the study of membrane fluidity, but also to gain insight regarding cholesterol transfer within cells by monitoring the movement of these fluorescent cholesterol analogues. Conclusions from this latter experiment could only come after characterization of the similarity of DNC and TPC to cholesterol in terms of, for example, their effect on the endothermic phase transition and glucose permeability of membranes, and their effectiveness as substrates for enzymes such as lecithin:cholesterol acyltransferase and cholesterol oxidase.

One important aspect of the role of cholesterol in membranes is its interaction with membrane bound proteins. TPC will be especially useful in this regard due to its absorption spectral characteristics which allow it to participate in resonance energy transfer from the aromatic amino acids tryptophan and tyrosine. This should

enable TPC to provide insight into the proximity and possible significance of tryptophan and tyrosine residues near or in the binding sites of sterol carrier proteins, for example. Resonance energy transfer between TPC (or 3β-ester derivatives of TPC) and tryptophan could also be exploited to study the binding of LDL to its receptor, which is of importance in determining the factors which contribute to atherosclerosis. TPC and DNC have the potential to report both on the polarity of protein binding sites through the sensitivity of their fluorescence quantum yields and decay parameters to solvent polarity, as well on their own fluidity in these binding sites. Moreover, an exciting possibility exists for DNC to yield structural information if some proteins bind, or interact preferentially with, a particular rotamer of DNC.

In short, the fluorescent cholesterol analogues DNC and TPC synthesized and characterized in this work, hold great promise as a means to attain a better understanding of sterol-lipid and sterol-protein interactions, and the role of cholesterol in membrane structure and function.

5.5 References

1. D.W. Deamer and P. Uster, in *"Structure and Properties of Cell Membranes"*, G. Benga ed., CRC, Florida, **1985**, Vol. 3, pp. 103–122 and references therein.

2. P.R. Cullis and M.J. Hope, in *"Biochemistry of Lipids and Membranes"*, D.E. Vance and J.E. Vance eds., Benjamin/Cummings, California, **1985**, pp. 25–72.

3. D. Lichtenberg and Y. Barenholz, in *"Methods of Biochemical Analysis"*, D. Glick ed., Wiley, New York, **1988**, Vol. 33, pp. 337–462.

4. F. Szoka and D. Papahadjopoulos, *Ann. Rev. Biophys. Bioeng.*, **1980**, *9*, 467–508 and references therein.

5. R. L. Hamilton, J. Goerke, L.S.S. Guo, M.C. Williams and R.J. Havel, *J. Lipid Res.*, **1980**, *21*, 981–992.

6. M.J. Ostro, *Sci. Am.*, **1987**, *256*(1), 103–113.

7. D.W. Deamer, in *"Liposome Technology"*, G. Gregoriadis ed., CRC, Florida, **1984**, Vol. 1, pp. 29–35.

8. M.J. Hope, M.B. Bally, G. Webb and P.R. Cullis, ***Biochim. Biophys. Acta***, **1985**, *812*, 55–65.

9. R.A. Klein, ***Biochim. Biophys. Acta***, **1970**, *210*, 486–489.

10. S. Mabrey and J.M. Sturtevant, ***Proc. Natl. Acad. Sci. USA***, **1976**, *73*, 3862–3866.

11. Nucleopore Catalogue, Nucleopore Corporation, Pleasanton, California, **1984**.

12. M.S. McCracken and N.J. Holt, *J. Chromat.*, **1985**, *348*, 221–227.

13. A.B. Kier, W.D. Sweet, M.S. Cowlen and F. Schroeder, *Biochim. Biophys. Acta*, **1986**, *861*, 287–301.

14. W.F. Voorhout and A.J. Verkleij, in *"Modern Physical Methods in Biochemistry, Part B"*, A. Neuberger and L.L.M. van Deenen eds., Elsevier, Amsterdam, **1988**, pp. 267–300.

15. A.H. Merrill and J. Wylie Nichols, in *"Phospholipids and Cellular Regulation"*, J.F. Kuo ed., CRC, Florida, **1985**, Vol. 1, pp. 61–96.

16. see references in Chapter 1.

17. B.R. Lentz, D.A. Barrow and M. Hoechli, *Biochem.*, **1980**, *19*, 1943–1954.

18. E.J. Shimshick and H.M. McConnell, *Biochem. Biophys. Res. Commun.*, **1973**, *53*, 446–451.

19. D.J. Rectenwald and H.M. McConnell, *Biochem.*, **1981**, *20*, 4505–4510.

20. W. Knoll, G. Schmidt, K. Ibel and E. Sackmann, *Biochem.*, **1985**, *24*, 5240–5246.

21. H.J. Ipsen, G. Karlström, O.G. Mouritsen, H. Wennerström and M.J. Zuckermann, *Biochim. Biophys. Acta*, **1987**, *905*, 162–172.

22. L. Louni, J.L. Rigaud and C.M. Gary-Bobo, in *"Physical Chemistry of Transmembrane Ion Motions"*, **1983**, *24*, 319–326.

Appendix A

Claims to Original Research

1. The synthesis and characterization of

   Pregnenolone 3β-*tert*-butyldimethylsilyl ether (**1b**)

   (20R)- and (20S)-20-Vinylpregn-5-ene-3β,20-diol 3β-*tert*-butyldimethylsilyl ether (**2a** and **2b**)

   (20(22)E)-and (20(22)Z)-24-Norchola-5,20(22)-dien-23-al,3β-*tert*-butyldimethylsilyl ether (**3a** and **3b**)

   (20(22)E,23E)- and (20(22)E,23Z)-24-Phenylchola-5,20(22),23-trien-3β-ol and their 3β-*tert*-butyldimethylsilyl ether derivatives (**4a** and **4b**, R=H or $SiMe_2t$-Bu).

   (20(22)E,23E,25E)- and (20(22)E,23Z,25E)-26-Phenyl-27-norcholesta-5,20(22),-23,25-tetraen-3β-ol and their 3β-*tert*-butyldimethylsilyl ether derivatives (**5a** and **5b**, R=H or $SiMe_2t$-Bu).

   (20(22)E,23E)- and (20(22)E,23Z)-24-(2'-Naphthyl)chola- 5,20(22),23-trien-3β-ol and their 3β-*tert*-butyldimethylsilyl ether derivatives (**6a** and **6b**, R=H or $SiMe_2t$-Bu).

   1-Bromo-5-phenyl-2,4-pentadiene.

   (2E,4E)- and (2Z,4E)-Diethyl 5-Phenyl-2,4-pentadien-1-ylphosphonate.

2. Elucidation of the stereochemistry of

   (a) the oxidative rearrangement of mixtures of **2a** and **2b** by PCC;

(b) two phosphonate Wittig reactions on pregnenolone (**1a**). These are the first known successful reactions of pregnenolone with semi-stabilized phosphonate carbanions, and represent a 100% increase in the number of reported phosphonate Wittig reactions of this rather unreactive steroidal ketone;

(c) two phosphonate and two phosphorane Wittig reactions on **3a**.

3. Complete assignment of the ^{1}H and ^{13}C NMR spectra of **4a** and **5a** which represents the first total analysis of ^{1}H and ^{13}C chemical shifts and ^{1}H-^{1}H coupling constants (**5a**) for the cholesterol ring system.

4. Characterization of the UV absorption spectra of **4a**, **5a** and **6a** at room temperature, and the response of these spectra to changes in solvent polarity and polarizability (refractive index).

5. Characterization of the fluorescence excitation and emission spectra of **4a** (DPC) at different emission and excitation wavelengths in isotropic solvents at room temperature.

6. Determination of the fluorescence quantum yield of **4a** in organic solvents at room temperature, and the fluorescence decay parameters of **4a** in a heavy mineral oil at 13.3°C.

7. Characterization of the fluorescence excitation and emission spectra, and fluorescence decay parameters, of **5a** (TPC) at different emission and excitation wavelengths: in various isotropic solvents around room temperature; in MCH at low temperatures; and in DMPC/cholesterol large unilamellar vesicles below and above the gel-liquid crystalline phase transition.

8. Determination of the fluorescence quantum yield of **5a** in organic solvents at room temperature.

9. Elucidation of a kinetic scheme to account for the photophysical properties of **5a** in organic solvents.

10. Demonstration of the utility of **5a** as a probe of membrane dynamics through viscosity studies with mineral oils and preliminary model membrane experiments.

11. Characterization of the fluorescence excitation and emission spectra, and fluorescence decay parameters, of **6a** (DNC) at different emission and excitation wavelengths: in various solvents around room temperature; in *n*-BuOH at low temperatures; and in DMPC/cholesterol large unilamellar vesicles below and above the gel-liquid crystalline phase transition.

12. Determination of the fluorescence quantum yield of **6a** in organic solvents at and around room temperature.

13. Resolution of the fluorescence excitation and emission spectra of three rotamers of **6a** (*tt*-DNC, planar and nonplanar *tc*-DNC) in TMP.

14. Development of a linear least squares method to resolve excitation decay associated spectra from steady-state excitation spectra and fluorescence decay parameters (in collaboration with M. Zuker, A. Szabo and J. Ridgeway).

15. Elucidation of a kinetic scheme to account for the photophysical properties of **6a** in organic solvents.

16. Demonstration of the utility of **6a** as a probe of membrane dynamics and order, through viscosity studies with mineral oils and preliminary model membrane experiments.

17. Measurement of the fluorescence decay parameters of sidechain analogues of **4a**, **5a** and **6a** in a limited number of solvents at room temperature.

Appendix B

Publications Arising from this Research

1. J. Drew, G. Gowda, P. Morand, P. Proulx, A.G. Szabo and D. Williamson, "Synthesis of an Olefinic Sterol Derivative for use as a Membrane Probe", *J. Chem. Soc., Chem. Comm.*, **1985**, 901–902.

2. P. Morand, J. Drew, A.G. Szabo and P. Proulx, "Conjugated Polyene Sterol Derivatives as Membrane Probes", *U.S. Patent Application, 867,565*, May 28, 1986.

3. J. Drew, J.-R. Brisson, P. Morand and A.G. Szabo, "^{1}H and ^{13}C NMR Assignment of Fluorescent Olefinic Sterol Derivatives for use as Membrane Probes", *Can. J. Chem.*, **1987**, *65*, 1784–1794.

4. J. Drew, M. Letellier, P. Morand and A.G. Szabo, "Synthesis from Pregnenolone of Fluorescent Cholesterol-Analogue Probes with Conjugated Unsaturation in the Sidechain", *J. Org. Chem.*, **1987**, *52*, 4047–4052.

5. J. Drew, A.G. Szabo and P. Morand, "Fluorescence Studies of a Cholesterol Analogue Probe", in *Time-Resolved Laser Spectroscopy in Biochemistry*, J.R. Lakowicz ed., *Proc. SPIE*, **1988**, *909*, 299–300.

6. P. Morand, J. Drew, A.G. Szabo and P. Proulx, "Conjugated Polyene Sterol Derivatives as Membrane Probes", *Canadian Patent 1,241,947*, 13 September 1988.

7. J. Drew, F. Zerbetto, A.G. Szabo and P. Morand, "Ground and Excited State Conformational Heterogeneity of the 2′-Naphthyl-butadiene Chromophore of

a Fluorescent Cholesterol Analogue Membrane Probe", *J. Phys. Chem.*, to be submitted.

8. J. Drew, F. Zerbetto, A.G. Szabo and P. Morand, "Dual State Fluorescence from the Phenylhexatriene Chromophore of a Cholesterol Analogue Membrane Probe", *J. Phys. Chem.*, to be submitted.

9. J. Drew, A.G. Szabo and P. Morand, "Time-Resolved Fluorescence Studies of Cholesterol Analogue Probes in DMPC/Cholesterol Large Unilamellar Vesicles", in preparation.

10. J. Drew, A.G. Szabo, J. Ridgeway and M. Zuker, "Linear Least-Squares Method for obtaining Fluorescence Excitation Decay Associated Spectra", in preparation.

Appendix C

Presentations

J. Drew, G. Gowda, P. Morand, A.G. Szabo, P. Proulx and D. Williamson, "Synthesis and Characterization of Sterols with Fluorescent Sidechains", *Chemistry Institute of Canada (CIC) Conference*, Montreal, June 1984.

J. Drew, "Synthesis and Characterization of a Conjugated Triene Sterol Derivative for use as a Membrane Probe", *Physics Department, University of Utrecht*, December 1984.

J. Drew, P. Morand and A.G. Szabo, "Synthesis and Characterization of a Conjugated Triene Sterol Derivative for use as a Membrane Probe", *CIC Conference*, Kingston, June 1985.

J. Drew, "Synthesis and NMR Analysis of Fluorescent Sterol Probes", *Division of Biological Sciences, National Research Council of Canada*, Ottawa, January 1987.

J. Drew, P. Morand and A.G. Szabo, "Synthesis and Characterization of Fluorescent Cholesterol Analogue Probes", *American Chemical Society 30th National Organic Symposium*, Vancouver, June 1987.

J. Drew, P. Morand and A.G. Szabo, "Fluorescence Studies of Cholesterol Analogue Probes in Lipid/Cholesterol Systems", *9th International Biophysics Congress*, Jerusalem, August 1987.

J. Drew, A.G. Szabo and P. Morand, "Fluorescence Studies of a Cholesterol Analogue Probe", *SPIE Symposium on Time-resolved Laser Spectroscopy in Biochemistry*, Los Angeles, January 1988.

J. Drew, F. Zerbetto, A.G. Szabo and P. Morand, "Rotamerism in Aryl Polyene Sidechains of Cholesterol Analogue Probes", *Euchem Conference on Photoisomerism and Rotamerism in Organic Molecules*, Assisi, July 1988.